Effective Field Theories to Probe Physics Beyond the Standard Model at Colliders

Thesis submitted for the degree of Doctor of Philosophy by

Abhik Sarkar

under the supervision of

Prof. Subhaditya Bhattacharya

Department of Physics
Indian Institute of Technology Guwahati
May, 2026

Effective Field Theories to Probe Physics Beyond the Standard Model at Colliders

Thesis submitted in partial fulfillment of the requirements for the award of the degree of Doctor of Philosophy in Physics by

Abhik Sarkar

under the supervision of

Prof. Subhaditya Bhattacharya

Department of Physics
Indian Institute of Technology Guwahati
May, 2026

To my sister, Ankita.

"Truth is much too complicated to allow anything but approximations."
John von Neumann

Declaration

This is to certify that the thesis entitled "**Effective Field Theories to Probe Physics Beyond the Standard Model at Colliders**", submitted by me to the *Indian Institute of Technology Guwahati*, for the award of the degree of Doctor of Philosophy, is a bonafide work carried out by me under the supervision of Prof. Subhaditya Bhattacharya. The content of this thesis, in full or in parts, have not been submitted to any other University or Institute for the award of any degree or diploma. I also wish to state that to the best of my knowledge and understanding nothing in this report amounts to plagiarism.

Signed: Abhik Sarkar

Abhik Sarkar
Department of Physics,
Indian Institute of Technology Guwahati,
North Guwahati-781039, Assam, India.

Date: 01/05/2026

Certificate

This is to certify that the thesis entitled "**Effective Field Theories to Probe Physics Beyond the Standard Model at Colliders**", submitted by Abhik Sarkar (216121001), a research scholar in the *Department of Physics*, *Indian Institute of Technology Guwahati*, for the award of the degree of Doctor of Philosophy, is a record of an original research work carried out by him under my supervision and guidance. The thesis has fulfilled all requirements as per the regulations of the institute and in my opinion has reached the standard needed for submission. The results embodied in this thesis have not been submitted to any other University or Institute for the award of any degree or diploma.

Signed: 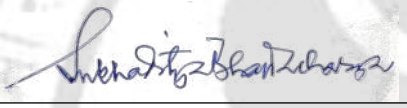

Prof. Subhaditya Bhattacharya
Department of Physics,
Indian Institute of Technology Guwahati,
North Guwahati-781039, Assam, India.

Date: 01/05/2026

Acknowledgements

I would like to begin by expressing my sincere gratitude to my supervisor, Subhaditya Bhattacharya, for his unwavering support and guidance through the many phases of this journey. At times when this path felt like merely a means of livelihood, conversations with him rekindled my scientific curiosity and restored a deeper sense of purpose. His clarity of thought, fluency of expression, and exceptional command over presentation skills will remain a lasting source of admiration for me.

Next, I would like to express my gratitude to my Doctoral Committee members: Meduri C. Kumar, Soumitra Nandi, Arunansu Sil, and Poulose Poulose, for their valuable comments and suggestions during the annual progress seminars, which significantly contributed to improving the quality and direction of this thesis. I would also like to sincerely thank my research collaborators: Subhaditya Bhattacharya, Soumitra Nandi, Sanjoy Biswas, Basabendu Barman, Jayita Lahiri, Sahabub Jahedi, Anupam Ghosh, Amir Subba, Dipankar Pradhan, Lipika Kolay, Indrajit Saha, Niloy Mondal, Soumyajit Dutta, Lopamudra Mukherjee, Shashwat Sharma, and Mathew Thomas Arun for generously sharing their expertise. Without their contributions, none of these projects would have reached publication-worthy quality. I am also grateful to ILANCE, Japan for supporting my international travel to Tokyo for attending their conference.

I would like to express my heartfelt gratitude to my friends and colleagues at IIT Guwahati: Niloy Mondal, Sourav Mondal, Subhasis Maiti, Hrishikesh Deka, Saswata Jana, Arpita Deb Singha, Rajesh Mondal, Rony Boral, Amir Subba, Dipankar Pradhan, Sahabub Jahedi, Gargi Sen, Anupam Ghosh, Partha Das, Swarup Kanti Sarkar, Avishek Sarkar, Shantanu Sahoo, Seshadri Majumdar, Chinmoy Dey, Lipika Kolay, Sunil Kumar Moharana, Sovan Sau, Subhankar Patra, Ankan Pramanik, Ayan Chakraborty, Indrajit Saha, Camelia Jana, Dipendu Bhandari, Snehasish Das, Amit Kumar, Sanjib Ray, Nayan Das, Jnana Ranjan Das, Bhoomika Das, Koustav Roy, Shailesh Pincha, Joya Ghosh Dastider, Vaibhav Pandey, Vishal, Urmimala Dewan, Arkodip Biswas, Disha Bandyopadhyay, Niraj Koirala, Nihar Ranjan Ghosh, Jitumani Kalita, Rajat Kumar Mandal, Subhajit Kala, Sandip Naskar, and many others, for making this journey truly memorable. I would also like to thank a few dear friends who have been part of different phases of my life and to whom I owe a great deal: Lakhan Paul, Kripanka Sundi, Priyanka Dey, Joybrata Sarkar, Pallabi Biswas, Shubham Choudhury, Anupam Deka, Victor Dey, Sajal Chakrabarty, Supriya Dutta, Prabhat Kumar Singh, Rohit Kumar, and, Surojit Kayal. I would like to especially thank Anindita Talukdar for her constant support through both good and challenging times.

Most importantly, I would like to express my deepest gratitude to my father, Ajit Kumar Sarkar, my mother, Amita Sarkar, and my sister, Ankita Datta, for their constant support and for standing by me during the times when I needed them the most. Finally, I would like to thank LGBRIMH, Tezpur, for providing me with psychiatric and psychological support, thereby keeping me sane, throughout this journey.

Abstract

Physics beyond the Standard Model (BSM) is motivated from several observations like that of tiny but non-zero neutrino masses, evidences of a dark matter, matter-anti-matter asymmetry, stability of the Higgs vacuum, heirarchy problem, and many more. But, since the discovery of the Higgs boson, searches for TeV-scale New Physics (NP) at the Large Hadron Collider (LHC) have largely yielded null results, thereby placing significant constraints on fundamental theories that predict new resonances at the TeV scale. In this context, where no substantial increase in the LHC energy is expected in its future run, and relatively lower energy but high precision lepton colliders are on the horizon, Effective Field Theories (EFTs) emerge as a powerful and pragmatic framework for probing the effects of NP that remain kinematically inaccessible and thus manifest only virtually. The thesis explores the prospects of applying EFTs, with particular emphasis on the Standard Model Effective Field Theory (SMEFT), wherein the Standard Model (SM) is extended by higher dimensional effective operators constructed from its fields abiding by the SM gauge symmetry. We study several applications of SMEFT, where the deperture from the SM observation can hint towards the existence of NP. We investigate modifications to the Higgs boson couplings with SM gauge bosons, as well as flavor violating effects that are highly suppressed in the SM. In addition, we employ the Dark Matter Effective Field Theory (DMEFT) framework, which extends the SM by introducing a Dark Matter (DM) candidate whose interactions with SM fields are mediated by higher dimensional operators. While accounting for the observed DM relic abundance such operators can also encode imprints of the early Universe when produced during the reheating era, which may be probed through their signatures at the future collider experiments.

Publications

This thesis is based on the following works:

[1] ***Higgs couplings in SMEFT via Zh production at the HL-LHC***; Subhaditya Bhattacharya, Sanjoy Biswas, **Abhik Sarkar**; *Phys.Rev.D 111 (2025) 11, 11* (e-Print: 2403.03001 [hep-ph]).

[2] ***Optimal estimation of Higgs-gauge boson couplings at the future e^+e^- colliders***; Subhaditya Bhattacharya, Amir Subba, **Abhik Sarkar**; *Phys.Rev.D 112 (2025) 11, 11* (e-Print: 2508.08893 [hep-ph]).

[3] ***Probing CP-violating Higgs-gauge couplings with Higgsstrahlung at e^-e^+ colliders***; Amir Subba, Subhaditya Bhattacharya, **Abhik Sarkar**; *Phys.Rev.D 113 (2026) 5, 055018* (e-Print: 2511.18541 [hep-ph]).

[4] ***Exploring optimal sensitivity of lepton flavor violating effective couplings at the e^+e^- colliders***; Sahabub Jahedi, **Abhik Sarkar**; *Phys.Rev.D 110 (2024) 9, 9* (e-Print: 2408.00190 [hep-ph]).

[5] ***Lepton flavor violating top quark FCNC processes at the μTRISTAN***; **Abhik Sarkar**; *Phys.Rev.D 113 (2026) 9, 095010* (e-Print: 2506.18015 [hep-ph]).

[6] ***Lepton collider as a window to reheating via freezing in dark matter detection. Part I***; Basabendu Barman, Subhaditya Bhattacharya, Sahabub Jahedi, Dipankar Pradhan, **Abhik Sarkar**; *Phys.Lett.B 869 (2025) 139863* (e-Print: 2406.11963 [hep-ph]).

[7] ***Lepton collider as a window to reheating via freezing in dark matter detection. Part II***; Basabendu Barman, Subhaditya Bhattacharya, Sahabub Jahedi, Dipankar Pradhan, **Abhik Sarkar**; *JHEP 07 (2025) 157* (e-Print: 2410.18198 [hep-ph]).

Other works not included in the thesis:

[1] ***Probing flavor constrained SMEFT operators through tc production at the muon collider***; Subhaditya Bhattacharya, Sahabub Jahedi, Soumitra Nandi, **Abhik Sarkar**; *JHEP 07 (2024) 061* (e-Print: 2312.14872 [hep-ph]).

[2] ***The influence of lepton portal on the WIMP-pFIMP framework***; Jayita Lahiri, Dipankar Pradhan, **Abhik Sarkar**; *JHEP 08 (2025) 019* (e-Print: 2410.19734 [hep-ph]).

[3] ***Up-type FCNC in presence of Dark Matter***; Subhaditya Bhattacharya, Lipika Kolay, Dipankar Pradhan, **Abhik Sarkar**; *JHEP 02 (2026) 239* (e-Print: 2504.20045 [hep-ph]).

[4] ***Probing $\Delta L = 2$ lepton number violating SMEFT operators at the same-sign muon collider***; Subhaditya Bhattacharya, Soumyajit Dutta, **Abhik Sarkar**; *Phys.Rev.D 113 (2026) 5, 055043* (e-Print: 2505.20936) [hep-ph].

[5] ***Lepton Collider as a Window to Reheating via Freezing Out Dark Matter Detection***; Subhaditya Bhattacharya, Anupam Ghosh, Niloy Mondal, **Abhik Sarkar**; (e-Print: 2509.14340 [hep-ph]).

[6] ***Electroweak phase transition in SMEFT: Gravitational wave and collider complementarity***; Sahabub Jahedi, Indrajit Saha, **Abhik Sarkar**; (e-Print: 2512.04168 [hep-ph]).

[7] ***Connecting Dark Matter Signals at Lepton Colliders to Reheating Temperature***; Basabendu Barman, Subhaditya Bhattacharya, Sahabub Jahedi, Dipankar Pradhan, **Abhik Sarkar**; *Springer Proc.Phys. 432 (2026) 314-317*; Contribution to 26th DAE-BRNS High Energy Physics Symposium 2024.

[8] ***Probing anomalous quartic gauge couplings via vector boson scattering at the same-sign muon collider***; Lopamudra Mukherjee, **Abhik Sarkar**; (e-Print: 2605.03116 [hep-ph]).

[9] ***From WIMP to FIMP during reheating: collider vs non-collider probes for p-wave annihilation***; Dipankar Pradhan, Niloy Mondal, **Abhik Sarkar**, Anupam Ghosh, Shashwat Sharma, Mathew Thomas Arun, Basabendu Barman; (e-Print: 2605.27521 [hep-ph]).

Permissions

The content of Chapter 4 is based on the following works:

- ***Higgs couplings in SMEFT via Zh production at the HL-LHC***; *Phys.Rev.D 111 (2025) 11, 11* (e-Print: 2403.03001 [hep-ph]); in collaboration with Subhaditya Bhattacharya, and Sanjoy Biswas.
- ***Optimal estimation of Higgs-gauge boson couplings at the future e^+e^- colliders***; *Phys.Rev.D 112 (2025) 11, 11* (e-Print: 2508.08893 [hep-ph]); in collaboration with Subhaditya Bhattacharya, and Amir Subba.
- ***Probing CP-violating Higgs-gauge couplings with Higgsstrahlung at e^-e^+ colliders***; *Phys.Rev.D 113 (2026) 5, 055018* (e-Print: 2511.18541 [hep-ph]); in collaboration with Subhaditya Bhattacharya, and Amir Subba.

The content of Chapter 5 is based on the following works:

- ***Exploring optimal sensitivity of lepton flavor violating effective couplings at the e^+e^- colliders***; *Phys.Rev.D 110 (2024) 9, 9* (e-Print: 2408.00190 [hep-ph]); in collaboration with Sahabub Jahedi.
- ***Lepton flavor violating top quark FCNC processes at the μTRISTAN***; *Phys.Rev.D 113 (2026) 9, 095010* (e-Print: 2506.18015 [hep-ph]).

The content of Chapter 6 is based on the following works:

- ***Lepton collider as a window to reheating via freezing in dark matter detection. Part I***; *Phys.Lett.B 869 (2025) 139863* (e-Print: 2406.11963 [hep-ph]); in collaboration with Basabendu Barman, Subhaditya Bhattacharya, Sahabub Jahedi, and Dipankar Pradhan.
- ***Lepton collider as a window to reheating via freezing in dark matter detection. Part II***; *JHEP 07 (2025) 157* (e-Print: 2410.18198 [hep-ph]); in collaboration with Basabendu Barman, Subhaditya Bhattacharya, Sahabub Jahedi, and Dipankar Pradhan.

List of Figures

List of Tables

Contents

Chapter 1

Introduction and Motivation

"Somewhere, something incredible is waiting to be known."
Carl Sagan

Contents

In a broader sense, the goal of particle physics extends beyond the mere discovery of new particles or forces. Its deeper objective is to uncover the fundamental principles of physics. This involves identifying the underlying concepts, symmetries, and mathematical structures that organize the seemingly complex phenomena of the universe into a coherent framework described by a small set of physical laws. From this perspective, particle physics may be viewed as a program of reductionism, seeking to explain diverse phenomena in terms of a minimal number of physical principles. Over the past century, remarkable theoretical and experimental evidences have led to the formulation of the Standard Model (SM) of particle physics [17], which is based on the principles of quantum field theory and local gauge symmetry. It successfully describes three of the four known fundamental interactions of nature: electromagnetic (EM), weak and strong forces, through the gauge symmetry structure: $SU(3)_C \times SU(2)_L \times U(1)_Y$.

The SM has been extensively tested in a wide variety of experiments and has achieved remarkable agreement with observations across different energy scales. A major milestone in the validation of the SM was the discovery of the Higgs boson in 2012 by the

ATLAS [18] and the CMS [19] experiments. This discovery confirmed the mechanism of electroweak symmetry breaking (EWSB) [20] and the generation of masses for elementary particles within the SM. Despite its tremendous success, there are several issues which the SM cannot address, rendering it to be an incomplete description of nature. Such observations suggest the existence of physics beyond the Standard Model (BSM). Understanding the nature of these new physics (NP) remains one of the central challenges in particle physics.

1.1 The Standard Model of Particle Physics

The modern formulation of the SM did not emerge as a single construct, but evolved over the century through gradual synthesis of distinct theoretical ideas and experimental ventures. An important development in this progression was the α-particle scattering experiment by Rutherford [21], which demonstrated the existence of a compact atomic nucleus and established scattering as a powerful tool to probe internal structure. The quest for fundamental particles started in 1897 with the discovery of electron (e^-) at the Cavendish Laboratory by J.J. Thompson in the Cathode Ray Tube Experiment [22]. Although the idea of the EM force carrier photon (γ) was conceptualized by Albert Einstein in his paper explaining photoelectric effect [23] in 1905, the formal discovery is attributed to discovery of Compton scattering in 1923 at the Washington University (WashU). Muons (μ^-) were discovered in cosmic rays by Anderson and Neddermeyer in 1936-1937. Electron neutrino (ν_e) was discovered at Savannah River Plant (SRP) in 1956, followed by muon neutrino (ν_μ) in 1962 at Brookhaven National Laboratory (BNL). The third generation leptons tau (τ^-) and tau neutrino (ν_τ) were discovered in 1975 and 2000, respectively, thereby completing the lepton family. Concept of quarks were conceptualized by Gell-Mann and Zweig to explain hadronic structure in 1964. Following that the light quarks: up (u), down (d) and strange (s) were discovered via deep inelastic scattering (DIS) experiments at SLAC in 1968. The charm (c) quark was discovered from J/Ψ discovery in 1974, followed by bottom (b) quark discovery in 1977. The heaviest of them all, the top (t) quark was discovered in 1995 by the CDF [24] and D$\emptyset$ [25] collaborations at Fermilab. The mediator of strong forces, gluon (g) was discovered in 1979 at DESY. The heavy gauge bosons: $W^\pm$ and Z, were discovered by UA1/UA2 collaboration in 1983 at CERN [26–28]. With the discovery of the Higgs boson in 2012,

the final missing ingredient of the SM, the particle content is now complete, summarized in Tab. 1.1.

Particle	Q_{EM}	m **(GeV)**	τ **(s)**	**Discovery**
Fermion: Quarks				
u	$+2/3$	2.16×10^{-3}	–	SLAC; 1968
d	$-1/3$	4.70×10^{-3}	–	SLAC; 1968
s	$-1/3$	93.5×10^{-3}	–	SLAC; 1968
c	$+2/3$	1.2730	–	BNL, SLAC; 1974
b	$-1/3$	4.183	–	Fermilab; 1977
t	$+2/3$	172.56	4.2×10^{-25}	Fermilab; 1995
Fermion: Leptons				
e^-	-1	$510.99895000 \times 10^{-6}$	–	Cavendish Lab; 1897
ν_e	0	$< 0.8 \times 10^{-9}$	–	SRP; 1956
μ^-	-1	$105.6583755 \times 10^{-3}$	2.2×10^{-6}	Caltech; 1937
ν_μ	0	$< 0.19 \times 10^{-3}$	–	BNL; 1962
τ^-	-1	1.77693	2.9×10^{-13}	SLAC; 1975
ν_τ	0	$< 18.2 \times 10^{-3}$	–	Fermilab; 2000
Boson: Gauge				
g	0	0	–	DESY; 1979
γ	0	$< 1.0 \times 10^{-27}$	–	WashU; 1923
$W^\pm$	± 1	80.3692	3.0×10^{-25}	CERN UA1/UA2; 1983
Z	0	91.1880	3.0×10^{-25}	CERN UA1/UA2; 1983
Boson: Scalar				
h	0	125.20	1.6×10^{-22}	CERN LHC; 2012

TABLE 1.1: The SM particles with corresponding EM charge (Q_{EM}), mass (m), lifetime (τ) and discovery information [9].

The mathematical construction of the SM was developed over stages. The unification of electricity and magnetism through Maxwell's equations marked the first step toward a unified description of fundamental forces. In the early 20^{th} century, the development of quantum theory provided a framework to describe phenomena at short distances, where classical physics fails. With the advent of the Dirac equation, the unification of quantum physics and special relativity was initiated. This program reached full maturity with the

development of the quantum electrodynamics (QED) in the 1940s by Schwinger, Tomonaga, and Feynman. This was further extended through the development of non-Abelian gauge theories, by Yang and Mills, providing the formulation of the weak interaction, building upon Fermi's theory. The understanding of strong interactions advanced following the development of the quark model by Gell-Mann and Zweig, leading to an $SU(3)$ gauge description known as quantum chromodynamics (QCD). These ideas were ultimately combined together by Glashow, Salam, and Weinberg into the modern SM, based on the gauge group $SU(3)_C \times SU(2)_L \times U(1)_Y$. The SM Lagrangian is defined as follows:

$$\begin{aligned}\mathcal{L}_{\rm SM} = &-\frac{1}{4}G^A_{\mu\nu}G^{\mu\nu A} - \frac{1}{4}W^I_{\mu\nu}W^{\mu\nu I} - \frac{1}{4}B_{\mu\nu}B^{\mu\nu} + |D_\mu H|^2 - \mu^2(H^\dagger H) \\ &- \lambda(H^\dagger H)^2 + \overline{\ell_p} i\not{D}\ell_p + \overline{q_p} i\not{D} q_p + \overline{e_p} i\not{D} e_p + \overline{u_p} i\not{D} u_p + \overline{d_p} i\not{D} d_p \\ &- (y_e^{pr}\overline{\ell_p} H e_r + y_u^{pr}\overline{q_p}\widetilde{H} u_r + y_d^{pr}\overline{q_p} H d_r + \text{h.c.})\,.\end{aligned} \tag{1.1}$$

Here, $\widetilde{H} = i\sigma_2 H^*$, where H is the SM Higgs doublet. The terms in the final row of Eq. (1.1) are referred to as Yukawa terms. The index p, r runs over the flavor generations of the SM fermions, $p, r = \{1, 2, 3\}$. In addition, the $SU(2)_L$ doublet fields, ℓ, q, and H, carry indices that are implicitly summed over their components. Similarly, the $SU(3)_C$ color triplet quarks, q, u, and d, carry color indices that are summed over the three colors: r, g, and b. The field strength tensors are defined as

$$\begin{aligned} B_{\mu\nu} &= \partial_\mu B_\nu - \partial_\nu B_\mu\,, \\ W^I_{\mu\nu} &= \partial_\mu W^I_\nu - \partial_\nu W^I_\mu + g\epsilon^{IJK} W^J_\mu W^K_\nu\,, \\ G^A_{\mu\nu} &= \partial_\mu G^A_\nu - \partial_\nu G^A_\mu + g_s f^{ABC} G^B_\mu G^C_\nu\,, \end{aligned} \tag{1.2}$$

where, B_μ, W^I_μ and G^A_μ are the gauge bosons corresponding to the groups $U(1)_Y$, $SU(2)_L$, and $SU(3)_C$, respectively. ϵ^{IJK} and f^{ABC} are the structure constants for $SU(2)_L$ and $SU(3)_C$, respectively. The indices run as follows, $I, J, K = \{1, 2, 3\}$ ($SU(2)_L$ triplet indices)[1], and $A, B, C = \{1, 2, \cdots, 8\}$ ($SU(3)_C$ octet indices). The covariant derivative is defined as

$$D_\mu = \partial_\mu - ig_s\delta_s T^A G^A_\mu - ig\,\delta_w\,\tau^I W^I_\mu - iY g' B_\mu\,. \tag{1.3}$$

[1] Also, M, N denote $SU(2)_L$ indices in Sec. 2.2, when more than three doublets appear in an operator.

T^A and τ^I are the $SU(3)$ and $SU(2)$ generators, respectively. The SM fermion representations, with their generations, are defined as follows:

$$\begin{aligned} &\ell_p^{(0,1,-\frac{1}{2})} : \left\{ \begin{pmatrix} \nu_e \\ e^- \end{pmatrix}_L, \begin{pmatrix} \nu_\mu \\ \mu^- \end{pmatrix}_L, \begin{pmatrix} \nu_\tau \\ \tau^- \end{pmatrix}_L \right\}, \quad q_p^{(1,1,+\frac{1}{6})} : \left\{ \begin{pmatrix} u \\ d \end{pmatrix}_L, \begin{pmatrix} c \\ s \end{pmatrix}_L, \begin{pmatrix} t \\ b \end{pmatrix}_L \right\}, \\ &e_p^{(0,0,-1)} : \{e_R^-,\, \mu_R^-,\, \tau_R^-\}, \quad u_p^{(1,0,+\frac{2}{3})} : \{u_R,\, c_R,\, t_R\}, \quad d_p^{(1,0,-\frac{1}{3})} : \{d_R,\, s_R,\, b_R\}. \end{aligned} \tag{1.4}$$

The numbers in the superscript correspond to the gauge parameters (δ_s, δ_w, Y). The left (L) and right (R) chiral fermions are defined as $\psi_{L,R} = P_{L,R}\,\psi$, where, P_L and P_R are the chiral projection matrices $\frac{1}{2}(1-\gamma_5)$ and $\frac{1}{2}(1+\gamma_5)$, respectively. Further, for the $SU(2)_L$ doublets, ℓ_p and q_p have weak isospins $I_3 = \frac{1}{2}$ and $I_3 = -\frac{1}{2}$ for the upper and lower components, respectively. Correspondingly, the $U(1)_Y$ hypercharge (Y) is defined as $Y = Q_{\rm EM} - I_3$, where, $Q_{\rm EM}$ is the EM charge of the fermion. The Higgs doublet, H has $Y = \frac{1}{2}$, hence the doublet can can be decomposed as follows:

$$H = \frac{1}{\sqrt{2}} \begin{pmatrix} H_1 + iH_2 \\ H_4 + iH_3 \end{pmatrix} = \begin{pmatrix} H^+ \\ H^0 \end{pmatrix}. \tag{1.5}$$

1.1.1 Electroweak Symmetry Breaking

In the SM, the constituent particles acquire mass through the mechanism of EWSB, also known as Higgs mechanism. The mechanism induces a spontaneous breakdown of electroweak symmetry $SU(2)_L \times U(1)_Y \to U(1)_{\rm EM}$, leaving electromagnetism unbroken and the photon massless. Also, the $SU(3)_C$ color symmetry is left untouched in this mechanism. For $\mu^2 < 0$, $\lambda > 0$, the Higgs potential in Eq. (1.1) has has an infinite set of degenerate minima satisfying

$$(H^\dagger H) = \frac{1}{2}(H_1^2 + H_2^2 + H_3^2 + H_4^2) = \frac{v^2}{2} = -\frac{\mu^2}{2\lambda}. \tag{1.6}$$

One possible way to adhere to Eq. (1.6) is to provide a non zero vacuum expectation value (VEV) v to H_4 component, while the remaining components acquire zero VEV. The H_4 component can be expanded around the VEV as $H_4(x) = v + h(x)$, where $h(x)$ denotes the physical Higgs boson field. The corresponding Higgs potential exhibit the *Mexican Hat* shape. This is demonstrated for the H^0 component in Fig. 1.1. After EWSB, in addition to this massive scalar field, there are three massless Goldstone fields, which ultimately gives the longitudinal degrees of freedom (DOFs) to the $W^\pm$ and Z

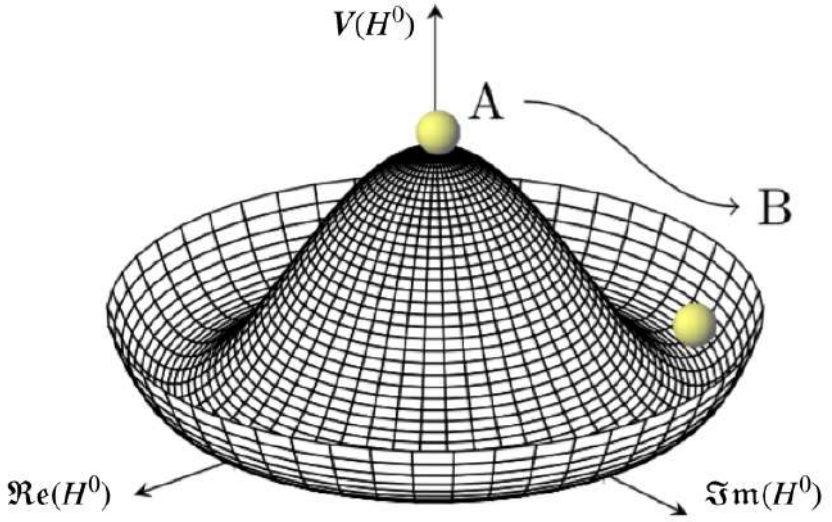

FIGURE 1.1: The Higgs potential exhibiting the popular *Mexican Hat* shape. We demostrate it for the H^0 component. The transition from $A \rightarrow B$ indicates the shift of VEV from $\langle H^0 \rangle = 0 \rightarrow \langle H^0 \rangle = v$.

bosons, rendering them massive. The photon is still left massless due to the unbroken $U(1)_{\rm EM}$ symmetry, and the gluon is massless as $SU(3)_C$ remains unbroken. Gauging away the Goldstone bosons, the Higgs doublet can be written in the unitary gauge as

$$H = \frac{1}{\sqrt{2}}\begin{pmatrix} H_1(x) + iH_2(x) \\ v + h(x) + iH_3(x) \end{pmatrix} \quad \longrightarrow \quad \frac{1}{\sqrt{2}}\begin{pmatrix} 0 \\ v + h(x) \end{pmatrix}. \tag{1.7}$$

Upon redefining the electroweak gauge bosons in terms of their physical fields

$$W_\mu^\pm = \frac{1}{\sqrt{2}}\left(W_\mu^1 \mp iW_\mu^2\right), \quad \begin{aligned} Z_\mu &= W_\mu^3 \cos\theta_W - B_\mu \sin\theta_W, \\ A_\mu &= W_\mu^3 \sin\theta_W + B_\mu \cos\theta_W, \end{aligned} \tag{1.8}$$

and expanding the Higgs kinetic term, one obtains the masses and interaction terms of the Higgs and gauge bosons. Here, $\theta_W = \tan^{-1}(g'/g)$, is called the Weinberg angle, with $\sin^2\theta_W \simeq 0.23$ following W and Z mass measurements. Similarly, the Higgs potential gives rise to the physical Higgs boson mass, $m_h = \sqrt{2\lambda}\, v$, as well as Higgs self-interactions. The Yukawa sector generates the fermion masses and governs the Higgs-fermion Yukawa interactions. The Feynman diagrams for Higgs boson interactions with SM particles, along with the corresponding Feynman rules, are shown in Tab. 1.2.

Quark Mixing and Flavor Violation The origin of quark mixing in the SM arises from the Yukawa terms and is manifested in the $W^\pm$ boson mediated charged current (CC) interactions. For the flavor eigenstates, we use the notation $u'_{L,R}$ and $d'_{L,R}$, while

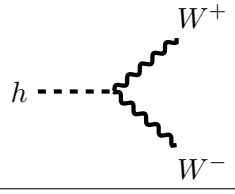	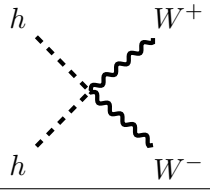
$i\frac{g^2 v}{2} g_{\mu\nu} = 2i\frac{m_W^2}{v} g_{\mu\nu}$	$i\frac{g^2}{2} g_{\mu\nu} = 2i\frac{m_W^2}{v^2} g_{\mu\nu}$
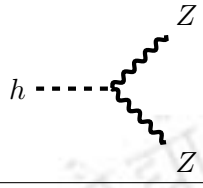	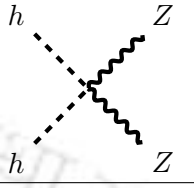
$i\frac{(g^2+g'^2)v}{2} g_{\mu\nu} = 2i\frac{m_Z^2}{v} g_{\mu\nu}$	$i\frac{(g^2+g'^2)}{2} g_{\mu\nu} = 2i\frac{m_Z^2}{v^2} g_{\mu\nu}$
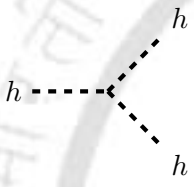		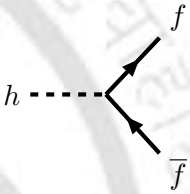
$-6i\lambda v = -3i\frac{m_h^2}{v}$	$-6i\lambda = -3i\frac{m_h^2}{v^2}$	$-i\frac{y_f}{\sqrt{2}} = -i\frac{m_f}{v}$

TABLE 1.2: Tree level Feynman diagrams of Higgs boson interactions with SM gauge bosons, itself and SM fermions, with corresponding Feynman rules.

$u_{L,R}$ and $d_{L,R}$ denote the corresponding mass eigenstates. After EWSB, the quark Yukawa Lagranian looks like

$$\begin{aligned} \mathcal{L}_q^Y &= -\overline{(u'_L)_p}\left(\frac{y_u^{pr} v}{\sqrt{2}}\right)(u'_R)_r - \overline{(d'_L)_p}\left(\frac{y_d^{pr} v}{\sqrt{2}}\right)(d'_R)_r - \text{h.c.}\,, \\ &= -\overline{(u_L)_p}\,(M_u)_{\rm D}^{pr}\,(u_R)_r - \overline{(d_L)_p}\,(M_d)_{\rm D}^{pr}\,(d_R)_r - \text{h.c.}\,, \end{aligned} \tag{1.9}$$

where, the flavor and the mass eigenstates and eigenvalues are connected as follows:

$$\begin{aligned} &(u_L)_p = (V_L^u)^{pr}(u'_L)_r\,, \quad (u_R)_p = (V_R^u)^{pr}(u'_R)_r\,, \quad (M_u)_{\rm D}^{pr} = (V_L^u)^{ps}\left(\frac{y_u^{st} v}{\sqrt{2}}\right)(V_R^{u\dagger})^{tr}\,, \\ &(d_L)_p = (V_L^d)^{pr}(d'_L)_r\,, \quad (d_R)_p = (V_R^d)^{pr}(d'_R)_r\,, \quad (M_d)_{\rm D}^{pr} = (V_L^d)^{ps}\left(\frac{y_d^{st} v}{\sqrt{2}}\right)(V_R^{d\dagger})^{tr}\,. \end{aligned} \tag{1.10}$$

Here, $V_{L,R}^{u,d}$ are unitary matrices. Now, the quark CC Lagrangian can be written as

$$\begin{aligned}\mathcal{L}_q^{\rm CC} &= \frac{g}{\sqrt{2}}\,\overline{(u'_L)_p}\,\gamma^\mu W_\mu^-(d'_L)_p + \frac{g}{\sqrt{2}}\,\overline{(d'_L)_p}\,\gamma^\mu W_\mu^+(u'_L)_p\,,\\ &= \frac{g}{\sqrt{2}}\,\overline{(u_L)_p}\,\gamma^\mu W_\mu^-(V_L^u V_L^{d\dagger})^{pr}(d_L)_r + \frac{g}{\sqrt{2}}\,\overline{(d_L)_p}\,(V_L^d V_L^{u\dagger})^{pr}\gamma^\mu W_\mu^+(u_L)_r\,,\end{aligned} \tag{1.11}$$

Here, $(V_{\rm CKM})^{pr} = (V_L^u V_L^{d\dagger})^{pr}$ is the Cabibbo-Kobayashi-Maskawa (CKM) mixing matrix [29]. By convention, the flavor and the mass eigenstates are chosen to be same for u quarks i.e. $u'_p = u_p$, whereas the d quarks are chosen to be rotated, going from the flavor basis to the mass basis:

$$d'_p = (V_{\rm CKM})^{pr} d_r \quad \Longrightarrow \quad \begin{pmatrix} d' \\ s' \\ b' \end{pmatrix} = \begin{pmatrix} V_{ud} & V_{us} & V_{ub} \\ V_{cd} & V_{cs} & V_{cb} \\ V_{td} & V_{ts} & V_{tb} \end{pmatrix} \begin{pmatrix} d \\ s \\ b \end{pmatrix}. \tag{1.12}$$

From the definition of $V_{\rm CKM}$, the transition from a d quark to an u quark is described by V_{ud}, whereas the transition from an u quark to a d quark is described by V_{ud}^*. We now discuss some features of the CKM matrix:

- For $n \times n$ complex matrix, there are n^2 complex elements, and hence $2n^2$ real parameters. Unitary ($V^\dagger V = \mathbb{I}$) imposed n^2 constraints, n on diagonal entries and $n^2 - n$ off-diagonal orthogonality conditions. Since overall phases are irrelevant, $2n - 1$ relative phases can be removed. So, the overall number of free parameters is $2n^2 - n^2 - (2n - 1) = (n - 1)^2$. These parameters are divided into $n(n - 1)/2$ Euler angles and $(n - 1)(n - 2)/2$ phases. For the 3×3 $V_{\rm CKM}$ matrix, there are 4 free parameters: 3 Euler angles and 1 complex phase.

- Using three Euler angles: θ_{12}, θ_{13}, θ_{23}, and the complex phase: δ, the CKM matrix can be parameterized as:

$$\begin{aligned} V_{\rm CKM} &= \begin{pmatrix} c_{12} & s_{12} & 0 \\ -s_{12} & c_{12} & 0 \\ 0 & 0 & 1 \end{pmatrix} \begin{pmatrix} c_{13} & 0 & s_{13}e^{-i\delta} \\ 0 & 1 & 0 \\ -s_{13}e^{i\delta} & 0 & c_{13} \end{pmatrix} \begin{pmatrix} 1 & 0 & 0 \\ 0 & c_{23} & s_{23} \\ 0 & -s_{23} & c_{23} \end{pmatrix}, \\ &= \begin{pmatrix} c_{12}c_{13} & s_{12}c_{13} & s_{13}e^{-i\delta} \\ -s_{12}c_{23} - c_{12}s_{23}s_{13}e^{i\delta} & c_{12}c_{23} - s_{12}s_{23}s_{13}e^{i\delta} & s_{23}c_{13} \\ s_{12}s_{23} - c_{12}c_{23}s_{13}e^{i\delta} & -c_{12}s_{23} - s_{12}c_{23}s_{13}e^{i\delta} & c_{23}c_{13} \end{pmatrix}, \end{aligned} \tag{1.13}$$

where, c_{ij} and s_{ij} refers to as $\cos\theta_{ij}$ and $\sin\theta_{ij}$, respectively. The complex phase δ carries the seed of CP violation in the SM.

- The elements of $V_{\rm CKM}$ are determined from a global fit to a wide range of experimental data [9]. The magnitude $|V_{ud}|$ is primarily extracted by comparing nuclear β decay and neutron decay rates with that of μ decay. The elements $|V_{us}|$ and $|V_{cs}|$ are obtained from semileptonic $K \to \pi$ and $D \to K$ decays, respectively. The value of $|V_{cd}|$ is obtained from neutrino and antineutrino-induced charm production from valence d quarks in nucleons. The elements $|V_{ub}|$ and $|V_{cb}|$ are extracted from semileptonic $B \to \pi$ and $B \to D$ decays, respectively. The magnitudes $|V_{td}|$ and $|V_{ts}|$ are determined indirectly through loop-induced processes involving top quark mediated box diagrams. Finally, $|V_{tb}|$ is obtained from measurements of top quark decay branching fractions at collider experiments. The best-fit values and hierarchical structure of these elements are shown in Fig. 1.2.

$$\begin{pmatrix} V_{ud} & V_{us} & V_{ub} \\ V_{cd} & V_{cs} & V_{cb} \\ V_{td} & V_{ts} & V_{tb} \end{pmatrix} \approx \begin{pmatrix} 0.97435 & 0.22501 & 0.00373 \\ 0.22487 & 0.97349 & 0.04183 \\ 0.00858 & 0.04111 & 0.99912 \end{pmatrix} \approx$$

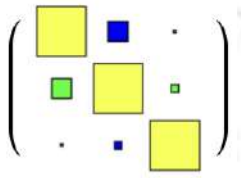

FIGURE 1.2: The magnitudes of the different elements of the CKM matrix along with their pictorial representation, where the area of the boxes indicate the sizes of the respective elements.

1.2 Need for Physics Beyond the Standard Model

Despite its enormous success, the SM is unable to address several important issues, indicating that it provides only an approximate description of nature. These include the existence of non-luminous dark matter (DM) [30–34], the observation of non-zero neutrino masses [35–38], the hierarchy problem [39–41], the question of Higgs vacuum stability at high scales [42–45], the strong CP problem [46, 47], the origin of the matter-antimatter asymmetry [48, 49], and various flavor anomalies [50–54], among others. We briefly discuss some of these issues in the following sections.

1.2.1 Existence of Dark Matter

Anisotropies in the Cosmic Microwave Background (CMB) indicate that DM constitutes $\sim$ 26% of the total energy density of the Universe [34], which corresponds to a relic abundance of $\Omega h^2 = 0.1200 \pm 0.0012$. Ω is defined as (ρ/ρ_c) with

$$\rho_c = \frac{3H^2}{8\pi G_N} \sim 1.054 \times 10^{-5}\, h^2 \text{ GeV/cm}^3\,, \tag{1.14}$$

where, H and G_N are the Hubble and the Gravitational constants, respectively. h is the reduced Hubble parameter, defined as $h = H_0/(100 \text{ km}/s/\text{Mpc})$, with $H_0 = (73 \pm 1)$ km$^{-1}s^{-1}$Mpc^{-1}. However, the SM does not provide a viable DM candidate, thereby strongly motivating the existence of BSM physics. Evidence for DM primarily arises from astrophysical and cosmological observations. Early indications include the stellar motions in the Milky Way and galaxy velocity dispersions in clusters [31], both pointing to the presence of unseen mass. Stronger evidence emerged from galaxy rotation curve measurements [32] in the 1970s, which showed flat rotation profiles at large radii instead of the expected classical behaviour, implying the existence of unknown matter. Gravitational lensing provides another compelling evidence for DM by mapping the total gravitating mass through the deflection of light. In context of the *Bullet Cluster* observation [33], gravitational lensing measurements indicate a clear separation between visible matter and collisionless, non-luminous DM, shown in Fig. 1.3 (*left*).

DM Properties Recent Planck [34] results indicate that the total matter density of the Universe is $\Omega_m \sim 0.31$, while the baryonic component contributes only $\Omega_b \sim 0.04$, with visible matter accounting for an even smaller fraction, implying the existence of a dominant non-luminous component. Although baryonic dark matter candidates have been considered, constraints from big-bang nucleosynthesis (BBN) strongly favor dark matter being predominantly non-baryonic [55] and composed of fundamental particles. Below we state some properties of DM:

- DM should be electromagentically neutral, and thereby have minimal interaction with photons, as indicated by CMB. However, feeble effective interactions [56–58] or interaction with *dark photons* [59] is possible, although strongly constrained [60].

- DM must be stable on the scale of the lifetime of the Universe, as any significant decay into lighter particles would deplete its abundance and hence fail to account for the observed relic density.

- DM should be massive, as its presence is inferred through gravitational effects and it significantly contributes to the energy density of the Universe. The allowed mass range spans a wide spectrum, from $\sim 10^{50}\,\text{GeV}$ for primordial black holes (PBHs) [61] down to $\sim 10^{-31}\,\text{GeV}$ for fuzzy dark matter [62].

- DM is preferably *cold*, i.e., non-relativistic at the time of structure formation. *Cold* dark matter (CDM) forms a central component of the ΛCDM model, successfully accounting for large-scale structure formation, dark matter halos, and the accelerated expansion history of the Universe. In contrast, *hot* dark matter (HDM), being relativistic, suppresses structure formation and is therefore disfavored. *Warm* dark matter (WDM) represents an intermediate scenario, though constructing consistent models with them remains challenging.

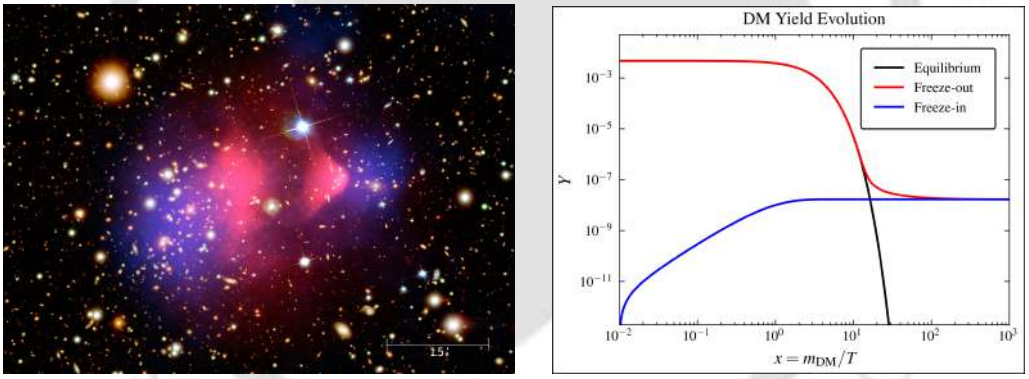

FIGURE 1.3: *Left*: X-ray image (in pink) superimposed over visible light image (in galaxies), with the matter distribution calculated from gravitational lensing (in blue) of the *Bullet Cluster*, adapted from *Chandra X-ray Observatory Photo Album*. *Right*: DM yield evolution pattern for freezing-out and freezing-in production modes, along with the equilibrium yield.

DM Production CDM can produce the correct relic density primarily through two different mechanisms: thermal freeze-out [30, 63], and non-thermal freeze-in [64]. This classification is also closely tied to its detectability. However, current observations do not reveal its fundamental properties, such as its nature, nor whether it consists of single or multiple components, leaving a wide scope for model building. We now elaborate on the two major production mechanisms.

- **Thermal Freeze-out:** In this scenario, DM particles are in thermal and chemical equilibrium with the SM particles in the early universe. As the temperature falls and the Universe expands, when the interaction rates of the processes that populates the DM (Γ) become smaller than the expansion rate of the Universe, i.e. the Hubble rate ($\mathcal{H}$), the DM particles freeze-out (FO) from the thermal bath and stays as relics. Primarily, weakly interacting massive particles (WIMPs) fall in this category. The evolution of the number density ($n_{\rm DM}$) of such a candidate is governed by the Boltzmann equation (BEQ):

$$\dot{n}_{\rm DM} + 3\mathcal{H} n_{\rm DM} = -\langle \sigma v \rangle_{2\leftrightarrow 2} \left[(n_{\rm DM})^2 - (n^{\rm eq}_{\rm DM})^2 \right] , \tag{1.15}$$

where, $\dot{n}_{\rm DM}$ is the time (t) derivative of $n_{\rm DM}$, and $\langle \sigma v \rangle_{2\leftrightarrow 2}$ is the thermal averaged cross section of the processes that keeps the DM in thermal equilibrium[2]. $n^{\rm eq}_{\rm DM}$ is the equilibrium number density of the DM defined as

$$n^{\rm eq}_{\rm DM} = \left(\frac{g_i}{2\pi^2} \right) m^2_{\rm DM} T K_2 \left(\frac{m_{\rm DM}}{T} \right) , \tag{1.16}$$

where, g_i, $m_{\rm DM}$ and T are the intrinsic DOFs, mass of the DM, and temperature of the Universe, respectively. $K_2(x)$ is the $2^{\rm nd}$ order modified Bessel function of second kind. Usually the evolution is quantified by a dimensionless quantity called yield, defined as $Y_{\rm DM} = (n_{\rm DM}/s)$, which remains unaffected by the expansion of the Universe in the radiation-dominated era, where $s = \left(2\pi^2/45\right) g_{*s} T^3$. Time and temperature are connected by the relation, $t = (1/2\mathcal{H})$, where $\mathcal{H} = 1.67\sqrt{g_{*\rho}}\left(T^2/M_P\right)$, $M_P \sim 10^{18}$ GeV, is the reduced Planck mass. g_{*s} and $g_{*\rho}$ are the entropy and matter DOFs, respectively. The relic density is defined in terms of the yield after freeze-out as

$$\Omega_{\rm DM} h^2 = 2.744 \times 10^8 \, m_{\rm DM} \, Y_{\rm DM}(x_0) , \tag{1.17}$$

where, $x_0 = (m_{\rm DM}/T_0)$, with $T_0 \sim 10^{-13}$ GeV is the present day CMB temperature.

- **Non-thermal Freeze-in:** In this case, DM particles never reach equilibrium with the SM bath particles due to its suppressed interactions, and are produced from decay or scattering of thermal bath particles out of equilibrium and freeze-in (FI). Feebly interacting massive particles (FIMPs) fall in this category. Depending on

[2]The thermal average of an observable $\mathcal{Q}$ is defined as $\dfrac{\int \prod_i d^3 p_i \; \mathcal{Q} \; \exp\left[\left(-\sum_i E_i\right)/T\right]}{\int \prod_i d^3 p_i \; \exp\left[\left(-\sum_i E_i\right)/T\right]}$ [65].

the temperature at which DM is predominantly produced, there are two types of FI scenarios: Infrared (IR) FI [64], and Ultraviolet (UV) FI [66]. In IR FI, DM is produced at low energies through feeble interactions with light mediators or thermal particles, with the relic density primarily determined by IR processes. In contrast, in UV FI, DM production occurs at high energies through processes mediated by higher dimensional operators or very heavy particles with masses close to the UV scale. The BEQ governing FIMP evolution is same as that of WIMPs, expect for the fact that the DM annihilation to SM is omitted, and additionally the decay of bath particles to DM is included, given as

$$\begin{aligned}\dot{n}_{\rm DM} + 3\mathcal{H} n_{\rm DM} = \; & \langle\Gamma\rangle_{1\to 2}\left[n^{\rm eq} - n_{\rm DM}\left(\frac{n^{\rm eq}}{n^{\rm eq}_{\rm DM}}\right)\right]^{0} \\ & + \langle\sigma v\rangle_{2\to 2}\left[(n^{\rm eq})^2 - n^2_{\rm DM}\left(\frac{n^{\rm eq}}{n^{\rm eq}_{\rm DM}}\right)^2\right]^{0},\end{aligned} \tag{1.18}$$

where $\langle\Gamma\rangle_{1\to 2}$ denotes the thermally averaged decay rate of SM particles into DM, and $\langle\sigma v\rangle_{2\to 2}$ represents the thermally averaged scattering rate of SM particles producing DM. The main characteristic of the FIMP BEQ is the tiny initial DM number density ($n_{\rm DM}$). Also, in case of FIMP, $\Gamma \ll \mathcal{H}$, so $\left(n_{\rm DM}/n^{\rm eq}_{\rm DM}\right) \ll 1$, and hence, terms proportional to it can be neglected. The DM yield evolution for freeze-out and freeze-in production modes, is shown in Fig. 1.3 (*right*).

DM Detection The detection of DM relies on its non-gravitational interactions with the visible sector, with WIMPs being particularly promising candidates, as FIMPs interaction with the SM is suppressed. Detection strategies include indirect detection (ID) via annihilation signals, collider searches through missing energy signatures, and direct detection (DD) via scattering off atomic nuclei or electrons. These possibilities are illustrated in the graphic, Fig. 1.4 and will be discussed in detail.

- **Direct Detection:** DD [67–69] aims to measure the tiny energy deposits, typically $\mathcal{O}$(KeV) to $\mathcal{O}$(eV), generated when galactic DM particles traverse the Earth and scatter off sensitive, underground detector materials. When scattering with atomic nuclei, the expected event rate relies on the DM's local density, its relative velocity, and the detector's target mass. Nuclear scattering is classified into two (non-relativistic) categories: *spin-independent* (SI) and *spin-dependent* (SD)

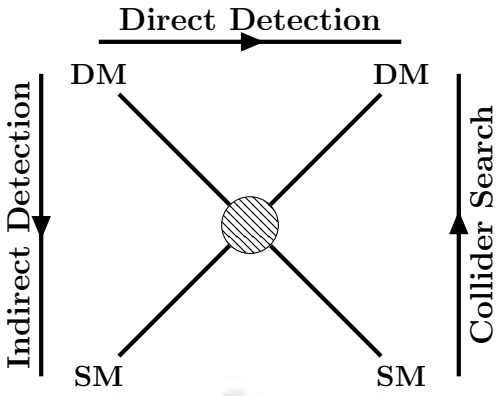

FIGURE 1.4: DM interaction with the SM via $2 \to 2$ process leads to different DM detection strategies: DM annihilation to SM produces indirect detection (ID), scattering of DM with SM provides direct detection (DD), and production of DM at collider experiments provide collider search.

interactions. SI scattering is independent of nuclear spin and features a coherent enhancement proportional to the square of the target's atomic mass number (A^2). Conversely, SD scattering rely entirely on the nuclear spin and lack this coherent enhancement factor, leading to much weaker experimental limits compared to SI interactions. Currently, the most stringent limits on SI interaction arise from the LUX-ZEPLIN experiment [70], which achieves a sensitivity of $\mathcal{O}(10^{-48})\,\mathrm{cm}^2$ for DM masses above ~ 5 GeV. In addition to nuclear interactions, DM also undergo scattering with electrons bound within atomic or molecular systems. Since electrons are significantly lighter than nuclei, the energy-momentum transferred during such a collision are much smaller. Hence, electron scattering is particularly crucial for detecting lighter DM particles that wouldn't deposit enough energy to trigger a nuclear recoil. In Fig. 1.5, we provide the SI DD limits for nucleon (*left*) and electron (*right*) scattering for various experiments.

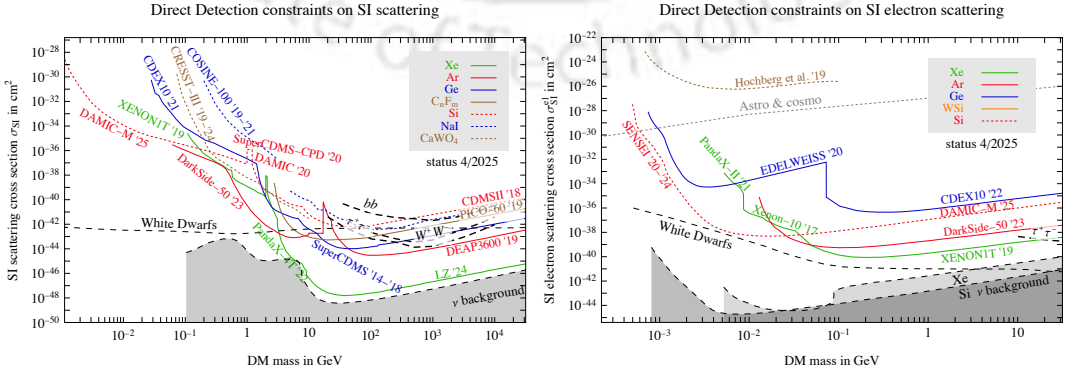

FIGURE 1.5: SI DD limits for nucleon (*left*) and electron (*right*) scattering from various experiments, adapted from [1].

- **Indirect Detection:** The goal of ID [71] is to observe SM particles generated by the annihilation or decay of dark matter (DM) particles within the galactic halo or beyond. This detection method relies on identifying anomalous excesses in cosmic ray fluxes near the Earth that cannot be explained by known astrophysical backgrounds. The production rate of these detectable signals depends on the DM annihilation or decay rate, the local DM density in the target region, and the final state multiplicity per event. The primary observable excesses we search for include high-energy gamma rays, neutrinos, and antimatter particles like positrons, antiprotons, etc. Because no statistically significant DM signal has been conclusively confirmed yet, these searches establish stringent upper bounds on the DM annihilation cross-section and decay lifetimes. The Fermi-LAT experiment [72, 73] places stringent constraints on DM annihilation, resulting in gamma ray production.

- **Collider Search:** DM search at colliders aim to produce DM particles directly in high energy particle collisions, such as those at the ongoing Large Hadron Collider (LHC) [74–76] or future lepton colliders [77]. Since DM particles have minimal interaction with ordinary matter, they escape detectors completely unnoticed, resulting in their production be inferred through a noticeable imbalance in the event's energy, known as missing energy (ME), $\not{E}$, or transverse momentum, known as missing transverse momentum (MET), $\not{E}_T$. The most prominent signature of this production is ME/MET accompanied by a single radiated SM particle, such as γ, jet, W, Z, or h, often referred to as a mono-X search. Additionally, experiments actively search for more complex features, like long-lived particles (LLPs) that leave tracks or produce displaced vertices, as well as rare processes like the invisible decays of Z or h. Despite rigorous investigations across vast model parameter spaces evaluating various masses, couplings, and spin states, no statistically significant DM signal has yet been confirmed at colliders.

1.2.2 Neutrino and Flavor Sector

The SM has a very non-trivial flavor structure, encoded in the hierarchy of masses of the fermions, flavor mixing angles, and a CP violating phase, the high scale origin of which still remains unexplained. Therefore, the fermion sector comprising of neutrinos, charged lepton, and quarks of different flavor, provide a rich ground for stress test of the SM as

well as search for BSM physics. The observation of neutrino oscillations provides clear evidence for non-zero masses of neutrino, which cannot be accommodated with the SM framework. This opens up avenues to search for high scale physics through mechanisms such as the Seesaw models [78–82]. Charged lepton flavor violation (cLFV) processes such as $\mu \to e\gamma$ [83, 84], are highly suppressed in the SM, making them extremely sensitive NP probes. Similarly, precision measurements of anomalous magnetic moments and electric dipole moments of charged leptons [85–90] offer complementary constraints. In the flavor sector, rare meson decays, meson mixing, and CP violation [91, 92] provide stringent tests of the SM and are sensitive to virtual NP effects. The interplay between these observables allows for a comprehensive survey of wide range of BSM scenarios across different energy scales.

Neutrino Masses and Mixing Neutrinos were postulated by Pauli in 1930 to account for the apparent non-conservation of energy and spin in β-decay, and were later incorporated into the theory of weak interactions. Within the SM framework, neutrino mass terms of both Dirac ($\overline{\nu_L}\nu_R$) and Majorana ($\overline{\nu_L^c}\nu_L$) types are not permitted by the field content and symmetries of the theory. While the SM assumes neutrinos to be massless, early anomalies in solar neutrino flux [93] hinted at physics beyond this picture. Neutrino oscillations, first proposed by B. Pontecorvo [94–96] and later formalized by Maki, Nakagawa, and Sakata [97], imply that neutrinos are massive and that flavor and mass eigenstates are misaligned, similar to the quark sector. This phenomenon was conclusively established by the Super-Kamiokande [35, 36], SNO [37], and KamLAND [38] experiments. In this framework, the flavor eigenstates ν_p ($p = e, \mu, \tau$) are related to the mass eigenstates ν_i ($i = 1, 2, 3$) via the unitary PMNS matrix, $|\nu_\alpha\rangle = U_{\text{PMNS}}|\nu_i\rangle$. The PMNS matrix is a 3×3 matrix with three rotation angles ($\theta_{12}, \theta_{13}, \theta_{23}$) and a CP violating Dirac phase (δ_{CP}). In addition, the PMNS matrix allows for the possibility of Majorana phases, which do not affect neutrino oscillation but have implications for lepton number violating processes. We now discuss some aspects of neutrinos in detail.

- **Neutrino Oscillation:** The mass eigenstates of the neutrinos, ν_i are the eigenstates of the free Hamiltonian (in vacuum), i.e. $H_0|\nu_i\rangle = E_i|\nu_i\rangle$ and they evolve with time to $e^{-iE_it}|\nu_i\rangle$. Hence, the flavor eigenstates at time t are superposition of flavor eigenstates at time $t = 0$, and therefore the probability of a flavor p

oscillating into a flavor r at time t is given by

$$P_{pr} = |\langle \nu_r(t)|\nu_p(t)\rangle|^2 = U_{pi}U^*_{ri}U_{rj}U^*_{pj}\, \exp\left[-i(E_i - E_j)t\right] . \tag{1.19}$$

Assuming that the neutrinos have same energy, $E_i \approx E + \left(m_i^2/2E\right)$, while traveling distance $\mathcal{D}$ the oscillation probability at time t is

$$P_{pr} = |\langle \nu_r(t)|\nu_p(t)\rangle|^2 = U_{pi}U^*_{ri}U_{rj}U^*_{pj}\, \exp\left(\frac{\Delta m^2_{ij}}{2E}\mathcal{D}\right) , \tag{1.20}$$

where, $\Delta m^2_{ij} = m^2_i - m^2_j$. The oscillation probability depends on the three angle and the Dirac phase, contained in the PMNS elements, as well as the mass square splittings, Δm^2_{ij}. However, only $|\Delta m^2_{31}|$ can be determined experimentally, and based on this two mass hierarchies arise, Normal Ordering (NO) and Inverted Ordering (IO), depending on which is the lightest neutrino mass eigenstate ν_1 or ν_3. Cosmological observation puts most stringent limits on the sum of the neutrino masses, i.e. $\sum_i m_{\nu_i} < 0.12$ (0.15) eV for NO (IO) [34]. Also, KATRIN [98] puts bounds on the effective electron neutrino mass, $m_{\nu_e} < 0.45$ eV. The globally fitted neutrino oscillation parameters [10] are tabulated in Tab 1.3. It should be noted neutrino oscillation cannot distinguish between Dirac or Majorana nature of neutrinos, which still is an open question.

Parameters	**Normal Ordering (NO)**	**Inverted Ordering (IO)**
Δm^2_{21} (10^{-5} eV^2)	$7.50^{+0.22}_{-0.20}$	
Δm^2_{31} (10^{-5} eV^2)	$2.55^{+0.02}_{-0.03}$	$2.45^{+0.02}_{-0.03}$
$\sin^2\theta_{12}/10^{-1}$	3.18 ± 0.16	
$\sin^2\theta_{23}/10^{-1}$	5.74 ± 0.14	$5.78^{+0.10}_{-0.17}$
$\sin^2\theta_{13}/10^{-1}$	$2.200^{+0.069}_{-0.062}$	$2.225^{+0.064}_{-0.070}$
$\delta_{\rm CP}/\pi$	$1.08^{+0.13}_{-0.12}$	$1.58^{+0.15}_{-0.16}$

TABLE 1.3: Best-fit $\pm$ 1σ limits on neutrino oscillation parameters from global fit presented in [10].

- **Weinberg Operator:** The simplest realization of neutrino mass generation arises at dimension 5 through the Weinberg operator [78, 99],

$$\frac{\lambda^{pr}\mathcal{O}_{\mathcal{W}}^{(5)}}{\Lambda_{\mathcal{W}}^{(5)}}, \qquad \text{where,} \qquad \mathcal{O}_{\mathcal{W}}^{(5)} = \left(\overline{\ell_p^c} H\right)\left(\widetilde{H}^\dagger \ell_r\right) + \text{h.c.} \tag{1.21}$$

where, $\Lambda_{\mathcal{W}}^{(5)}$ is the effective NP scale, and λ^{pr} is a dimensionless constant. This operator violates lepton number by two units ($\Delta L = 2$), and, after EWSB generated Majorana mass for neutrinos, which is given by $m_\nu^{pr} = \left(\lambda^{pr} v^2/\Lambda_{\mathcal{W}}^{(5)}\right)$. For sub-GeV neutrino masses with $\lambda^{pr} \sim \mathcal{O}(1)$, the NP scale, $\Lambda_{\mathcal{W}}^{(5)} \sim \mathcal{O}(10^{13})$ GeV, beyond the reach of any current or future experiment. It is worth noting that the inclusion of higher dimensional operators can significantly lower the corresponding NP scale. For instance, a simple generalization of the Weinberg operator to dimension d can be written as

$$\mathcal{O}_{\mathcal{W}}^{(d)} = \mathcal{O}_{\mathcal{W}}^{(5)} (H^\dagger H)^k, \tag{1.22}$$

where $k = (d-5)/2$, with d odd and $d > 5$. Correspondingly, the NP scale is reduced, yielding estimates such as $\Lambda_{\mathcal{W}}^{(7)} \sim \mathcal{O}(10^6)$ GeV and $\Lambda_{\mathcal{W}}^{(9)} \sim \mathcal{O}(10^4)$ GeV, and so on. These operators can also generate neutrino masses at one or more loops. The neutrino mass generated for d dimensional operator at n loop level can approximately be given by [100]

$$m_\nu^{pr} \sim \frac{v^2 \lambda^{pr}}{\Lambda_{\mathcal{W}}^{(d)} (16\pi^2)^n} \left(\frac{v}{\Lambda_{\mathcal{W}}^{(d)}}\right)^{d-5}. \tag{1.23}$$

The sensitivity of Weinberg operator has been extensively studied in context of colliders [101, 102]. Although the flavor diagonal couplings are strongly restricted from absolute neutrino mass measurements [103–105], the off-diagonal couplings are still accessible at energy scales of future colliders [101].

- **Neutrino Mass Models:** The Weinberg operator can be generated in a plethora of BSM scenarios. A tree-level UV completion requires a mediator that contracts $SU(2)_L$ indices between a doublet and an antidoublet, i.e. $2 \otimes \overline{2} = 1 \oplus 3$, thereby restricting the possibilities to a fermion singlet, scalar triplet, or fermion triplet. A doublet mediator is not allowed, and a scalar singlet cannot generate the operator at tree level. Among the most well-established realizations are the three types of Seesaw models. In these frameworks, the Weinberg operator is generated at

the tree level, thereby inducing non-zero neutrino masses. In the **Type-I** Seesaw

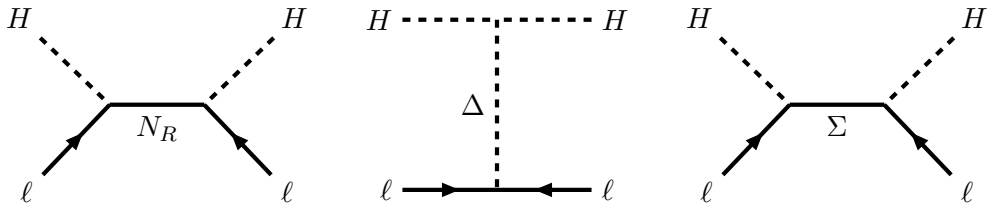

FIGURE 1.6: Seesaw mechanisms of type-I (*left*), type-II (*center*), and type-III (*right*), for neutrino mass generation via Weinberg operator at the tree level.

model, the SM is extended by a Majorana right handed neutrino (RHN), N_R. The relevant Lagrangian concerning the RHN is

$$\mathcal{L}_{N_R} \supset -Y_N \left(\overline{\ell}\widetilde{H}N_R\right) - \frac{1}{2}M_N \left(\overline{N_R^c}N_R\right) + \text{h.c.}\,, \tag{1.24}$$

where, Y_N and M_N are the neutrino Yukawa coupling, and the RHN mass, respectively. Integrating out the RHN generates the Weinberg operator, as shown in Fig. 1.6 (*left* panel). The **Type-II** Seesaw is characterized by the addition of a scalar triplet (Δ) with hypercharge, $Y = 2$, which couples with SM Higgs and lepton doublets as follows

$$\mathcal{L}_\Delta \supset -\frac{1}{2}Y_\Delta \left(\overline{\ell}\Delta i\sigma_2\ell^c\right) + \lambda_\Delta M_\Delta \left(H^T i\sigma_2 \Delta H\right) + \text{h.c.}\,, \tag{1.25}$$

where, the $SU(2)_L$ bi-doublet representation of the scalar triplet is

$$\Delta = \frac{1}{\sqrt{2}}\begin{pmatrix} \Delta^+ & \sqrt{2}\Delta^{++} \\ \sqrt{2}\Delta^0 & -\Delta^+ \end{pmatrix}. \tag{1.26}$$

The Weinberg operator is generated by integrating out the t-channel mediator, Δ, as shown in Fig. 1.4 (*center* panel). A hybrid of the first two types, in the **Type-III** Seesaw model, the SM is extended by a Majorana triplet fermion, Σ, and the relevant Lagrangian is

$$\mathcal{L}_\Sigma \supset -Y_\Sigma \left(\overline{\ell}\widetilde{H}\Sigma^c\right) - \frac{1}{2}M_\Sigma \text{Tr}\left(\overline{\Sigma}\Sigma^c\right) + \text{h.c.}\,, \tag{1.27}$$

where, the $SU(2)_L$ bi-doublet representation of the fermion triplet is

$$\Sigma = \frac{1}{\sqrt{2}} \begin{pmatrix} \Sigma^0 & \sqrt{2}\Sigma^+ \\ \sqrt{2}\Sigma^- & -\Sigma^0 \end{pmatrix} . \tag{1.28}$$

The Weinberg operator is generated by integrating out the s-channel mediator, Σ, as shown in Fig. 1.4 (*right* panel). Integrating out the heavy fields and post EWSB the generated Majorana neutrino mass of the three scenarios are shown below.

$$m_\nu = \begin{cases} \frac{v^2 Y_N}{2M_N} & \text{(Type-I)}\,, \\ \frac{v^2 \lambda_\Delta Y_\Delta}{M_\Delta} & \text{(Type-II)}\,, \\ \frac{v^2 Y_\Sigma}{2M_\Sigma} & \text{(Type-III)}\,. \end{cases} \tag{1.29}$$

Also, the Weinberg operator can be generated by NP at loop level and such possibilities are called radiative models. Popular models in this respect are the Zee model [106], the Scotogenic model [107], etc. These models are characterized by the fact that neutrino masses arise at loop level, allowing the masses of the heavy mediators to be lowered to experimentally accessible scales.

Charged Lepton Flavor Violation In the previous section, we saw how the observation of neutrino oscillations indicates flavor violation in the neutral lepton sector. For consistency, one may therefore expect analogous flavor mixing in the charged lepton sector as well. In this context, dedicated experimental searches have been pursued for a long time. Searches have targeted processes such as radiative decays ($\mu \to e\gamma$ [84], $\tau \to l\gamma$, with $l = e, \mu$ [108, 109]), three body decays ($\mu \to 3e$ [110], $\tau \to 3l$ [111]), and coherent $\mu \to e$ conversion in nuclei [112–115]. In the minimally extended SM which includes neutrino masses and mixing, contributions to cLFV processes are extremely suppressed, with radiative decay branching ratios as low as $\sim 10^{-54}$ [116], indicating large room for possible BSM physics. The limits on cLFV processes from several experimental searches are tabulated in Tab. 1.4.

Flavor Changing Neutral Currents In Sec. 1.2, we saw that the CKM mixing allows flavor changing charged currents (FCCC) in the quark sector. However, the Lagrangian provides no flavor changing neutral currents (FCNC), rendering such processes absent

Radiative Decays		$\mathcal{B}(\tau^- \to \mu^- e^+ e^-)$	$< 1.8 \times 10^{-8}$ [111]
$\mathcal{B}(\mu^- \to e^- \gamma)$	$< 3.1 \times 10^{-13}$ [84]	$\mathcal{B}(\tau^- \to \mu^+ e^- e^-)$	$< 1.5 \times 10^{-8}$ [111]
$\mathcal{B}(\tau^- \to e^- \gamma)$	$< 3.3 \times 10^{-8}$ [108]	$\mathcal{B}(\tau^- \to \mu^- \mu^+ \mu^-)$	$< 1.9 \times 10^{-8}$ [111]
$\mathcal{B}(\tau^- \to \mu^- \gamma)$	$< 4.2 \times 10^{-8}$ [109]	**Low Energy Colliders**	
Rare Z Decays		$\sigma(e^\pm \tau^\mp)/\sigma(\mu^+ \mu^-)$	$< 8.9 \times 10^{-6}$ [117]
$\mathcal{B}(Z \to e^\pm \mu^\mp)$	$< 2.6 \times 10^{-7}$ [118]	$\sigma(\mu^\pm \tau^\mp)/\sigma(\mu^+ \mu^-)$	$< 4.0 \times 10^{-6}$ [117]
$\mathcal{B}(Z \to e^\pm \tau^\mp)$	$< 5.0 \times 10^{-7}$ [119]	**Mesonic Radiations**	
$\mathcal{B}(Z \to \mu^\pm \tau^\mp)$	$< 6.5 \times 10^{-7}$ [119]	$\mathcal{B}(\tau^- \to e^- \pi^0)$	$< 8.0 \times 10^{-8}$ [120]
Three Body Decays		$\mathcal{B}(\tau^- \to \mu^- \pi^0)$	$< 1.1 \times 10^{-7}$ [121]
$\mathcal{B}(\mu^- \to e^- e^+ e^-)$	$< 1.0 \times 10^{-12}$ [110]	$\mathcal{B}(\tau^- \to e^- \rho^0)$	$< 2.2 \times 10^{-8}$ [122]
$\mathcal{B}(\tau^- \to e^- e^+ e^-)$	$< 2.7 \times 10^{-8}$ [111]	$\mathcal{B}(\tau^- \to \mu^- \rho^0)$	$< 1.7 \times 10^{-8}$ [122]
$\mathcal{B}(\tau^- \to e^+ \mu^- \mu^-)$	$< 1.7 \times 10^{-8}$ [111]	$\mathcal{B}(\tau^- \to e^- \phi)$	$< 2.0 \times 10^{-8}$ [122]
$\mathcal{B}(\tau^- \to e^+ \mu^- \mu^-)$	$< 1.7 \times 10^{-8}$ [111]	$\mathcal{B}(\tau^- \to \mu^- \phi)$	$< 2.3 \times 10^{-8}$ [122]

TABLE 1.4: The limits on branching ratios and cross sections of cLFV processes from different experimental searches.

at tree level. Although FCNC processes arise at loop level in the SM, they are highly suppressed. Consequently, searches for FCNC serve as stress tests for the SM and as sensitive probes of possible NP. Colliders and B-factories have searched for a wide range of FCNC processes, which include radiative decays such as $b \to s\gamma$ ($B \to X_s\gamma$ [123–125], $B \to K^*\gamma$ [126, 127]), semileptonic decays $b \to s\ell^+\ell^-$ ($B \to Kl^+l^-$ [128, 129], $B \to K^*l^+l^-$ [129, 130], $B_s \to \phi l^+l^-$ [131]), neutral meson mixing ($B^0 - \overline{B}^0$ [132], $B_s^0 - \overline{B}_s^0$ [133], $D^0 - \overline{D}^0$ [134]), and rare kaon decays ($K^+ \to \pi^+ \nu\overline{\nu}$ [135]), among others. Although these precision observables provide sensitive probes of potential NP, in most cases, the current measurements are largely consistent with the SM within experimental and theoretical uncertainties, and the flavor sector continues to offer strong constraints complementary to direct collider searches. Similar FCNC searches have also been conducted in the context of top quark production and decay [15, 136–140]. However, no significant deviations from the SM predictions have been observed so far, primarily due to limited precision in current top quark measurements. As the heaviest particle in the SM, the top quark offers a promising window into potential new physics. Consequently, FCNC studies involving the top quark are crucial for probing physics beyond the SM at current and future experimental frontiers. The limits on top quark FCNC processes from LHC searches are tabulated in Tab. 1.5.

Two Body Decays			Three Body Decays		
$\mathcal{B}(t \to Zq)$	$< 1.2 \times 10^{-4}$	[139]	$\mathcal{B}(t \to \mu^{\pm}\tau^{\mp}q)$	$< 8.7 \times 10^{-7}$	[140]
$\mathcal{B}(t \to hu)$	$< 1.9 \times 10^{-4}$	[141]	$\mathcal{B}(t \to e^{\pm}\mu^{\mp}u)$	$< 7.0 \times 10^{-8}$	[15]
$\mathcal{B}(t \to hc)$	$< 3.4 \times 10^{-4}$	[142]	$\mathcal{B}(t \to e^{\pm}\mu^{\mp}c)$	$< 8.9 \times 10^{-7}$	[15]

TABLE 1.5: The limits on FCNC decays of top quark from different LHC searches.

Purpose and Objective of the Thesis

Despite extensive searches at the LHC and other experiments, no conclusive evidence of BSM physics has been observed so far. In particular, the absence of new resonant states at the TeV scale has placed strong constraints on a wide class of fundamental theories that predict new particles within the accessible energy range. At the same time, several fundamental questions, such as the origin of DM, the structure of the flavor sector, etc., remain unanswered, rendering the SM to be an incomplete description of nature. In this context, where no significant increase in the LHC energy is anticipated in the immediate future, and upcoming lepton colliders are expected to operate at relatively lower energies, the strategy for probing NP may rely on indirect effects of seeing deviations from the Standard Model prediction. Effective Field Theories (EFTs) provide a systematic way to capture such effects arising from heavy DOFs that remain kinematically inaccessible and manifest only virtually.

The primary objective of this thesis is to explore the application of EFT frameworks in probing BSM physics, primarily focused at future collider experiments. In particular, the works considered in this thesis focus on the Standard Model Effective Field Theory (SMEFT) framework, within which we study several applications to different areas of High Energy Physics of current relevance. We consider modifications to Higgs Boson couplings with gauge bosons and fermions, and investigate flavor violating interactions that are highly suppressed in the SM. The aim is to quantify the sensitivity of collider observables to such effects and to develop analysis strategies for their estimation. In addition, this thesis employs the Dark Matter Effective Field Theory (DMEFT) framework, wherein the SM is extended by a DM candidate interacting with SM particles via higher dimensional effective operators. The objective is to examine whether such operators can account for the observed relic abundance of DM and other cosmological constraints, and

if they can warrant a discovery at the collider; then to explore if they encode information about early Universe dynamics, such as reheating, which may be indirectly probed through collider signatures.

The thesis is organized as follows. Chap. 2 develops the formalism of EFTs, including SMEFT and DMEFT. Chap. 3 provides an overview of collider phenomenology and analysis techniques. Chap. 4 and 5 present detailed applications of SMEFT to Higgs Physics and Flavor Physics, respectively. Chap. 6 focuses on the application of DMEFT to DM and its connection to early Universe dynamics. Finally, Chap. 7 summarizes the main results and outlines future prospects.

Chapter 2

Effective Field Theories

"Tell all the truth but tell it slant–"
Emily Dickinson

Contents

EFFECTIVE theories reproduce the observable behavior of a physical system within specified validity conditions, without relying on a complete description of the underlying fundamental dynamics. In the absence of a fundamental description valid across all energy scales, effective theories allow us to parameterize and quantify observables in terms of the DOFs relevant at that given energy. Effective descriptions are applicable at every energy scale, and a simple illustration can be drawn from atomic and molecular systems. In principle, *Quantum Mechanics* provides a complete description of the dynamics of atoms and molecules through the Schrodinger Equation. For interacting systems, this leads to a set of coupled equations whose complexity grows rapidly with the number of particles, making even systems of $\mathcal{O}(10)$ particles computationally demanding. Consequently, predicting macroscopic properties, such as the color of a solution formed by mixing compounds containing $\mathcal{O}(10^{23})$ molecules, becomes impossible from first principles. In this regime, an effective description emerges in the form of *Chemistry*, which replaces the underlying microscopic dynamics with simplified reaction rules and

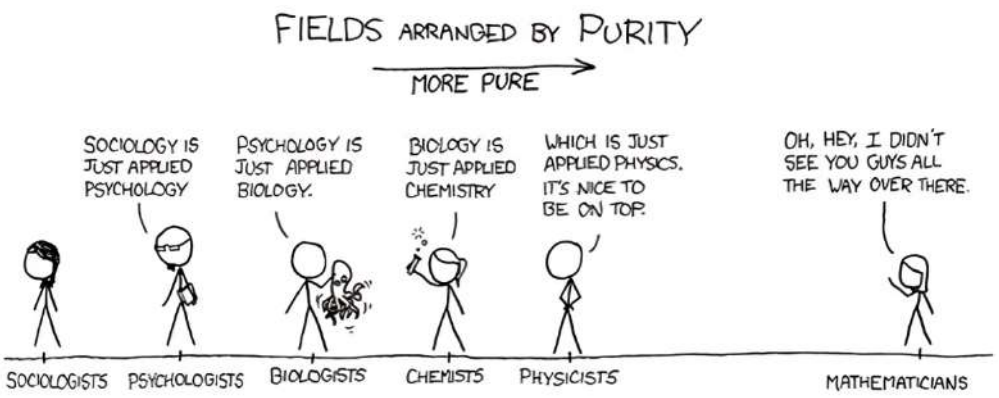

FIGURE 2.1: A graphic depicting how different fields are ordered based on *purity*, adapted from *xkcd*. Although mathematical constructs provide the most pure description of nature, the need for quantification necessitates approximate descriptions tailored to specific scenarios.

empirical laws, providing a sufficiently accurate account of the relevant observables. In Fig. 2.1, different fields are arranged according to their *purity*. While a single underlying fundamental theory may govern all physical phenomena, the need for quantification and applicability necessitates the use of different effective descriptions across distinct regimes. These working theories provide approximate yet sufficiently accurate frameworks that are well-suited to the problem at hand. So, in principle, effective theories make science *practical*. EFTs are effective theories that are formulated within the framework of quantum field theory, where the relevant DOFs are fundamental fields. They describe phenomena at a particular energy scale using the most general Lagrangian consistent with the symmetries, while systematically encoding the effects of NP present at different energy scales through incorporation of higher dimensional operators. In the following sections, we formally build EFT descriptions relevant for our studies.

2.1 Constructing Effective Field Theories

In order to design an appropriate EFT, on both a technical and a physical level, three key ingredients are required: **(I)** identification of the light fields, or relevant DOFs, at the scale of interest; **(II)** construction of all operators consistent with the symmetries of the system; and **(III)** a power counting scheme that governs the perturbative expansion and controls the estimate of the uncertainties. We now elaborate on each of these ingredients in detail.

Light Fields The light DOFs correspond to those fields that remain *active* at the scale of interest. Identifying them is the primary step in construction of an EFT, as the effects of NP manifest through their interactions, thereby governing the extent to which such effects can be probed in experiments. The choice of light fields can be illustrated in several well-known examples. In Chiral Perturbation Theory (ChPT) [143, 144], the relevant DOFs are the light (pseudo) Nambu-Goldstone bosons (pNGBs), whose interactions encode the non-perturbative QCD effects that dominate at low energies. In the Euler–Heisenberg theory [145, 146], which is valid at energies well below the electron mass (m_e), the electron field is integrated out, and the entire theory is expressed purely in terms of photon fields, which are the relevant DOFs in this case.

Symmetries In constructing EFT operators, one must ensure that they remain invariant under all symmetries that are operative at the energy scale of relevance, as they fundamentally restrict the allowed interactions in the theory. Construction of EFT operators usually follow two approaches: *top down*, and *bottom up*. In the *top down* approach, one starts from a preferred UV theory, whose low energy effects are captured by a restricted set of operators obtained by integrating out the heavy DOFs. In contrast, the *bottom up* approach proceeds without assuming a particular UV completion. Instead, one constructs the most general set of operators organized by a systematic expansion. In both approaches, the operators must abide by the symmetries of the low energy theory. Some examples in this context are as follows. In ChPT, the underlying symmetry is the approximate chiral symmetry $SU(N_f)_L \times SU(N_f)_R \to SU(N_f)_V$, where N_f denotes the number of light quark flavors. Similarly, in the Euler-Heisenberg Lagrangian, the relevant symmetries are Lorentz invariance and the $U(1)_{\rm EM}$ gauge symmetry.

Power Counting In an EFT, power counting is a very fundamental component, and it is just as important as something like gauge symmetry in UV theories. The power counting scheme provides a systematic way to handle the theoretical uncertainty. At each order, there is a finite number of operators, and the accuracy can be improved by working to higher order in the expansion parameter. In ChPT, the operator expansion is performed in powers of external momenta (p) and light quark masses (m_q) over the chiral symmetry breaking scale ($\Lambda_\chi = 4\pi F$), where, F is the chiral limit decay constant. Similarly, in the Euler-Heisenberg Lagrangian, the expansion is organized in inverse

powers of the electron mass, with higher dimensional operators suppressed by powers of $(1/m_e)$. This corresponds to an expansion of the amplitudes in the ratio of the electromagnetic field strength (α) or photon energy (p_γ) to the electron mass, such that higher order terms encode increasingly suppressed nonlinear photon interactions.

EFT	**ChPT ($N_f = 2$)**	**Euler-Heisenberg**
Light Fields	$\pi = \{\pi^\pm, \pi^0\} \to U = \exp\left(i\frac{\tau^I \pi^I}{F}\right)$	$A_\mu \to F_{\mu\nu}$
Symmetries	$SU(2)_L \times SU(2)_R \to SU(2)_V$	Lorentz, $U(1)_{\rm EM}$
Power Counting	$\sim \left(\frac{p^2}{\Lambda_\chi^2}\right), \left(\frac{m_q}{\Lambda_\chi}\right)$	$\sim \left(\frac{\alpha}{m_e}\right), \left(\frac{p_\gamma}{m_e}\right)$
Operators	$\frac{F^2}{4}\left(D_\mu U D^\mu U^\dagger\right), \frac{F^2}{4}\left(\chi U^\dagger + U\chi^\dagger\right)$	$(F_{\mu\nu}F^{\mu\nu})^2, \left(\widetilde{F}_{\mu\nu}F^{\mu\nu}\right)^2$

TABLE 2.1: EFT construction components and examples of operators for ChPT ($N_f = 2$) and Euler-Heisenberg Lagrangian. For ChPT, χ is defined as $2BM$, where, B is a constant and M is the light quark mass matrix. For EH theory, $\widetilde{F}_{\mu\nu}$ is the dual of $F_{\mu\nu}$.

2.1.1 Some Features of EFT Frameworks

While this thesis primarily focuses on the phenomenological applications of EFTs at colliders, the robustness of these predictions is deeply rooted in formal QFT. Constructing a mathematically consistent EFT, whether through *top-down* or *bottom-up* approach, requires careful investigation of several theoretical subtleties. In this section, we briefly outline three such aspects: (**I**) the emergence of local effective operators from inherently non-local actions, (**II**) the role of the covariant derivative expansion in preserving manifest gauge invariance, and (**III**) the order-by-order renormalizability of EFTs.

Preserving Locality of EFTs A fundamental requirement of any QFT is locality, which dictates that interactions occur at a single spacetime point. However, when heavy DOFs are formally integrated out of a UV-complete theory, the resulting effective action is inherently non-local. EFTs restore locality order-by-order via a systematic low-energy expansion [147]. This can be demonstrated for a simple scenario containing a light scalar field ϕ (with mass, m) and a heavy scalar field Φ (with mass, $M \gg m$), with an interaction term governed by a dimensionful coupling κ. The action for the UV model

is given by

$$S_{\rm UV} = \int \mathcal{L}_{\rm UV}\, d^4x = \int \left(\frac{1}{2}(\partial_\mu \phi)^2 - \frac{1}{2} m^2 \phi^2 + \frac{1}{2}(\partial_\mu \Phi)^2 - \frac{1}{2} M^2 \Phi^2 - \kappa\, \Phi \phi^2 \right) d^4x\,. \tag{2.1}$$

The generating functional of the theory is given by the path integral over both fields:

$$Z = \int [\mathcal{D}\phi][\mathcal{D}\Phi]\, e^{iS_{\rm UV}[\phi,\Phi]}\,. \tag{2.2}$$

To construct the effective action using ϕ, we integrate out the heavy field Φ. Integrating by parts, $(\partial_\mu \Phi)^2 \to -\,(\Phi \Box \Phi)$, allows us to write the Φ-dependent part of the action as a Gaussian integral with the differential operator $\left(\Box + M^2\right)$ and a background source $J(x) = -\kappa\, \phi^2(x)$. Executing this exact Gaussian integral yields the effective action, $S_{\rm EFT}[\phi] = S_{\rm light}[\phi] + \Delta S_{\rm EFT}$, where,

$$\Delta S_{\rm EFT} = \frac{\kappa^2}{2} \int \phi^2(x)\, G(x-y)\, \phi^2(y)\, d^4x\, d^4y\,. \tag{2.3}$$

Here, $G(x-y)$ is the Green's function of the heavy field, satisfying

$$(\Box_x + M^2)\, G(x-y) = -i\delta^{(4)}(x-y)\,. \tag{2.4}$$

The double integral over distinct coordinates x and y formally defines a non-local action. The ϕ field at point x interacts continuously with the ϕ field at point y via the exchange of the heavy mediator. To bridge this non-local action to a local EFT, we invoke the low-energy limit. In this regime where the momentum transfer is much smaller than the mass of Φ i.e. $p^2 \ll M^2$, or equivalently as an operator, $\Box \ll M^2$, the inverse differential operator can be Taylor expanded as a local derivative series:

$$\frac{1}{\Box + M^2} = \frac{1}{M^2}\left(1 - \frac{\Box}{M^2} + \frac{\Box^2}{M^4} - \cdots\right). \tag{2.5}$$

This expansion transforms the non-local Green's function into a Dirac delta function, $\delta^{(4)}(x-y)$ and its derivatives, which enforces $x = y$ and forces the double integral to collapse into a single spacetime point. Substituting this expansion back into the effective action generates the local EFT Lagrangian:

$$\Delta \mathcal{L}_{\rm EFT}(x) = \frac{\kappa^2}{2M^2}\phi^4(x) - \frac{\kappa^2}{2M^4}\phi^2(x)\Box\phi^2(x) + \frac{\kappa^2}{2M^6}\phi^2(x)\Box^2\phi^2(x) - \cdots\,. \tag{2.6}$$

The non-local heavy field exchange has been reduced to an infinite series of localized contact interactions, organized by strictly increasing mass dimension. This establishes the connection that the EFT is a local theory, given that one truncates the series expansion at a finite order appropriate for the energy scale of interest.

Covariant Derivative Expansion In the presence of gauge symmetries, expanding the functional determinant in terms of partial derivatives (∂_μ) and bare gauge fields (say, X_μ) breaks manifest gauge invariance at intermediate steps. To ensure the effective Lagrangian remains explicitly gauge invariant and covariant throughout the matching procedure, one must employ the Covariant Derivative Expansion (CDE) [148–150]. The one-loop effective action is given by

$$S_{\rm EFT} = \int \mathcal{L}_{\rm EFT}\, d^4x = i{\rm Tr}\ln(-D^2 - M^2 - U)\,, \tag{2.7}$$

where, U encapsulates any local interaction. CDE evaluates the functional trace[1] in the momentum basis. Extracting the plane-wave states i.e.

$$S_{\rm EFT} = i\int d^4x \int \frac{d^4q}{(2\pi)^4}\langle x|e^{-iq\cdot x}\ln(-D^2 - M^2 - U)e^{iq\cdot x}|x\rangle\,, \tag{2.8}$$

shifts the covariant derivative to $D_\mu \to D_\mu + iq_\mu$. The effective Lagrangian density then takes the local form

$$\mathcal{L}_{\rm EFT} = i\int \frac{d^4q}{(2\pi)^4}{\rm tr}\ln\left[(q^2 - M^2) - (2iq\cdot D + D^2 + U)\right]\,, \tag{2.9}$$

To establish a systematic local operator expansion, the free heavy propagator $(q^2 - M^2)$ is factored out:

$$\mathcal{L}_{\rm EFT} = i\int \frac{d^4q}{(2\pi)^4}{\rm tr}\left\{\ln(q^2 - M^2) + \ln\left[1 - \frac{2iq\cdot D + D^2 + U}{q^2 - M^2}\right]\right\}\,. \tag{2.10}$$

The first term is irrelevant and discarded. The second term is evaluated via the Taylor expansion where the expansion parameter is defined as

$$\frac{2iq\cdot D + D^2 + U}{q^2 - M^2}\,. \tag{2.11}$$

[1] Tr refers to functional trace, whereas tr indicates matrix trace.

Following symmetric loop integration over the momenta d^4q, the remaining covariant derivatives are algebraically rearranged using their commutator, $[D_\mu, D_\nu] = -ig_X X_{\mu\nu}$, where, g_X is the characteristic gauge coupling. The physical field strength tensor $X_{\mu\nu}$ emerges naturally, guaranteeing manifest gauge invariance at every perturbative order. Crucially, for this operator expansion to be well-defined, the series must strictly converge. This requires the covariant operators in the numerator to be significantly smaller than the heavy mass squared in the denominator. Because the EFT operators are generated by both the covariant derivative D_μ and its commutators, it is not sufficient to merely assume that the momentum transfer of the propagating DOFs is small i.e. $p^2 \ll M^2$. It also strictly demands that the ambient background gauge field strength residing inside the covariant derivative must also be fundamentally bounded by the heavy scale $g_X X_{\mu\nu} \ll M^2$.

Renormalization Scheme Dependence A common historical misconception is that EFTs, by virtue of containing an infinite tower of higher-dimensional operators, are strictly "non-renormalizable" and thus lack predictive quantum structure. In reality, EFTs are systematically renormalizable *order-by-order* in the $1/\Lambda$ expansion. When the theory is truncated at a fixed mass dimension, all UV divergences generated can be entirely absorbed into a finite set of counter-terms corresponding to the effective coefficients and SM parameters present at or below that dimension. To systematically compute this renormalization and track the running of effective operators, the choice of renormalization scheme is critical [150]. In EFTs, the low-energy DOFs are often massless or treated as effectively massless relative to the heavy scale Λ. This scheme dependence can be explicitly demonstrated using a toy model as follows:

$$S_{\rm UV} = \int \mathcal{L}_{\rm UV}\, d^4x = \int \left(\frac{1}{2}(\partial_\mu \phi)^2 + \frac{1}{2}(\partial_\mu \Phi)^2 - \frac{1}{2} M^2 \Phi^2 - \widetilde{\kappa}\, \Phi^2 \phi \right) d^4x \,, \tag{2.12}$$

where, ϕ is massless and Φ is the heavy field. Integrating out the Φ field at one-loop yields trilinear (ϕ^3) and quartic (ϕ^4) self couplings. To simplify, we focus on the trilinear coupling given by

$$\mathcal{L}_{\rm EFT} \supset -\frac{C}{3!}\phi^3 \,. \tag{2.13}$$

We evaluate the one-loop self-energy for the light field, ϕ (shown in Fig. 2.2) induced by the trilinear coupling. Using dimensional regularization ($d = 4 - 2\epsilon$) and a renormalization scale μ, the amplitude is given by

$$\Sigma(p^2) = \frac{C^2\mu^{2\epsilon}}{2} \int \frac{d^dk}{(2\pi)^d} \frac{1}{k^2(k-p)^2} \,. \tag{2.14}$$

Evaluating this integral at a finite external momentum ($p^2 \neq 0$) isolates the short-

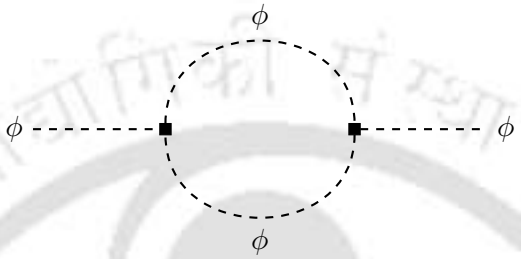

FIGURE 2.2: One-loop self energy correction of the light field, ϕ via trilinear ϕ^3 coupling.

distance physics, revealing a purely Ultraviolet (UV) divergence ($1/\epsilon_{\rm UV}$) alongside a momentum-dependent logarithm:

$$\Sigma(p^2) = \frac{C^2}{32\pi^2} \left[\frac{1}{\epsilon_{\rm UV}} + \ln\left(\frac{\mu^2}{-p^2}\right) + \text{finite} \right] . \tag{2.15}$$

If one attempts to use the traditional on-shell (OS) scheme, the mass counter-term $\delta m^2_{\rm OS}$ must be evaluated at the physical mass pole, which for this strictly massless field is $p^2 = 0$. However, taking the $p^2 \to 0$ limit forces the logarithm to undergo a severe infrared (IR) divergence:

$$\delta m^2_{\rm OS} = \lim_{p^2 \to 0} \Sigma(p^2) \to \infty \,. \tag{2.16}$$

The OS counterterm formulation mathematically breaks down because it forces the absorption of this unshielded IR singularity. Absorbing deep IR physics into a local UV counter-term destroys the scale separation upon which the EFT relies. Consequently, the OS scheme is structurally incompatible with massless EFT DOFs. Conversely, the mass-independent $\overline{\rm MS}$ scheme uniquely resolves this by isolating and subtracting only the short-distance UV divergence:

$$\delta m^2_{\overline{\rm MS}} = -\frac{C^2}{32\pi^2} \frac{1}{\epsilon_{\rm UV}} \,. \tag{2.17}$$

By strictly isolating the UV behavior, the $\overline{\text{MS}}$ scheme enforces the scale separation inherent to EFTs. The IR singularities correctly remain untouched in the renormalized amplitude, eventually canceling against real emission processes in physical cross-sections using the KLN theorem.

2.2 Standard Model Effective Field Theory

Although the discovery of the Higgs boson completed the SM, no significant evidence of NP has been observed since. Consequently, experimental search strategies for BSM scenarios have evolved from fundamental theories such as supersymmetry [151] to more model-independent approaches based on effective operators and simplified models. In this scenario, SMEFT [11, 14, 150, 152] is the most preferred framework. The SMEFT framework extends the SM by systematically incorporating NP effects through higher dimensional operators constructed from SM fields. A complementary framework to the SMEFT is the κ framework [153], where the NP effects are parametrized through rescalings of the Higgs couplings to SM particles by multiplicative factors. More details on this in App. 2.A. In the following sections, we discuss the construction and features of SMEFT in details.

2.2.1 SMEFT Operator Construction

Since the SMEFT framework is constructed upon the SM, its DOFs correspond to the SM fields, and the constructed operators of this theory are required to respect Lorentz invariance as well as the SM gauge symmetry, $SU(3)_C \times SU(2)_L \times U(1)_Y$. Two popular variations in this context are the Higgs Effective Field Theory (HEFT) [154] and the Weak Effective Field Theory (WEFT) [155]. Both frameworks assume $SU(3)_C \times U(1)_{\text{EM}}$ symmetry, but differ in their field content and the realization of the electroweak symmetry. We discuss these frameworks in App. 2.B. The power counting in SMEFT is realized through a hierarchical expansion of operators in inverse powers of the effective scale, Λ. This effective scale Λ roughly characterizes the mass of the heavy NP resonance that has been integrated out, assuming couplings of $\mathcal{O}(1)$. More generally, however, Λ may also encode additional factors such as loop suppressions or combinations of masses of multiple

heavy states. Further details are discussed in Sec. 2.2.1. The SMEFT Lagrangian is

$$\mathcal{L}_{\text{SMEFT}} = \mathcal{L}_{\text{SM}} + \sum_{i,d} \frac{C_i^{(d)} \mathcal{O}_i^{(d)}}{\Lambda^{d-4}} = \mathcal{L}_{\text{SM}} + \frac{C_{\mathcal{W}}^{(5)} \mathcal{O}_{\mathcal{W}}^{(5)}}{\Lambda} + \sum_i \frac{C_i^{(6)} \mathcal{O}_i^{(6)}}{\Lambda^2} + \cdots , \tag{2.18}$$

where, $\mathcal{O}_i^{(d)}$ correspond to the i^{th} operator of dimension d, and $C_i^{(d)}$ is the corresponding dimensionless Wilson's coefficient (WC). In the following paragraphs, we discuss SMEFT operators of different dimensions and categories in detail.

Operators of Dimension ≤ 6 SMEFT operators first appear at dimension 5, where the Weinberg operator is the only operator at this order. A detailed discussion of this operator has already been done in Sec. 1.2.2. Although the first higher dimensional contribution appears at dimension 5, the dominant phenomenological effects of NP at leading order (LO) are typically governed by dimension 6 operators. These operators can be expressed in different bases, depending on the underlying motivation, such as the Warsaw [11] and SILH [152] bases. In the Warsaw basis, there are 59 independent dimension 6 operators, classified according to their field content and listed in Tab. 2.2. We now proceed to discuss each of these operator classes in detail.

- $\boldsymbol{X^3}$ **Operators:** These operators modify both triple and quartic gauge couplings, and further induce interactions involving five and six gauge bosons, which are absent in the SM. In particular, the operators $\mathcal{O}_W$ and $\mathcal{O}_{\widetilde{W}}$ generate anomalous Lorentz structures that affect charged triple gauge couplings (TGC), leading to distinctive phenomenological signatures that have been extensively studied at the LHC [156, 157].

- $\boldsymbol{H^6/H^4D^2}$ **Operators:** This class of operators modifies the Higgs potential and induces modifications to the triple and quartic Higgs self-couplings. In addition, they are phenomenologically linked to scenarios with an electroweak first-order phase transition, as studied in [158, 159]. However, some of these effects can be partially absorbed through appropriate field redefinitions of the Higgs field. Further, the operator $\mathcal{O}_{HD}$ shifts the Z boson mass after EWSB and is therefore strongly constrained by electroweak precision observables (EWPO) [160].

- $\boldsymbol{\Psi^2 H^3}$ **Operators:** These operators induce rescalings of the SM Yukawa couplings. In context of the leptonic operator $\mathcal{O}_{eH}$, non-zero flavor off-diagonal WCs can

Dimension 6 SMEFT Operators					
$\boldsymbol{X^3}$		$\boldsymbol{H^6}$ / $\boldsymbol{H^4D^2}$		$\boldsymbol{\Psi^2H^3}$	
$\mathcal{O}_G$	$f^{ABC}G_\mu^{A\nu}G_\nu^{B\rho}G_\rho^{C\mu}$	$\mathcal{O}_H$	$(H^\dagger H)^3$	$\mathcal{O}_{eH}$	$(H^\dagger H)(\overline{\ell}_p e_r H)$
$\mathcal{O}_{\widetilde{G}}$	$f^{ABC}\widetilde{G}_\mu^{A\nu}G_\nu^{B\rho}G_\rho^{C\mu}$	$\mathcal{O}_{H\Box}$	$(H^\dagger H)\Box(H^\dagger H)$	$\mathcal{O}_{uH}$	$(H^\dagger H)(\overline{q}_p u_r \widetilde{H})$
$\mathcal{O}_W$	$\epsilon^{IJK}W_\mu^{I\nu}W_\nu^{J\rho}W_\rho^{K\mu}$	$\mathcal{O}_{HD}$	$\left(H^\dagger D^\mu H\right)^*\left(H^\dagger D_\mu H\right)$	$\mathcal{O}_{dH}$	$(H^\dagger H)(\overline{q}_p d_r H)$
$\mathcal{O}_{\widetilde{W}}$	$\epsilon^{IJK}\widetilde{W}_\mu^{I\nu}W_\nu^{J\rho}W_\rho^{K\mu}$				
$\boldsymbol{X^2H^2}$		$\boldsymbol{\Psi^2XH}$		$\boldsymbol{\Psi^2H^2D}$	
$\mathcal{O}_{HG}$	$H^\dagger H\, G^A_{\mu\nu}G^{A\mu\nu}$	$\mathcal{O}_{eW}$	$(\overline{\ell}_p\sigma^{\mu\nu}e_r)\tau^I H W^I_{\mu\nu}$	$\mathcal{O}_{H\ell}^{(1)}$	$(H^\dagger i\overleftrightarrow{D_\mu}H)(\overline{\ell}_p\gamma^\mu\ell_r)$
$\mathcal{O}_{H\widetilde{G}}$	$H^\dagger H\, \widetilde{G}^A_{\mu\nu}G^{A\mu\nu}$	$\mathcal{O}_{eB}$	$(\overline{\ell}_p\sigma^{\mu\nu}e_r)H B_{\mu\nu}$	$\mathcal{O}_{H\ell}^{(3)}$	$(H^\dagger i\overleftrightarrow{D_\mu^I}H)(\overline{\ell}_p\tau^I\gamma^\mu\ell_r)$
$\mathcal{O}_{HW}$	$H^\dagger H\, W^I_{\mu\nu}W^{I\mu\nu}$	$\mathcal{O}_{uG}$	$(\overline{q}_p\sigma^{\mu\nu}T^A u_r)\widetilde{H}\, G^A_{\mu\nu}$	$\mathcal{O}_{He}$	$(H^\dagger i\overleftrightarrow{D_\mu}H)(\overline{e}_p\gamma^\mu e_r)$
$\mathcal{O}_{H\widetilde{W}}$	$H^\dagger H\, \widetilde{W}^I_{\mu\nu}W^{I\mu\nu}$	$\mathcal{O}_{uW}$	$(\overline{q}_p\sigma^{\mu\nu}u_r)\tau^I\widetilde{H}\, W^I_{\mu\nu}$	$\mathcal{O}_{Hq}^{(1)}$	$(H^\dagger i\overleftrightarrow{D_\mu}H)(\overline{q}_p\gamma^\mu q_r)$
$\mathcal{O}_{HB}$	$H^\dagger H\, B_{\mu\nu}B^{\mu\nu}$	$\mathcal{O}_{uB}$	$(\overline{q}_p\sigma^{\mu\nu}u_r)\widetilde{H}\, B_{\mu\nu}$	$\mathcal{O}_{Hq}^{(3)}$	$(H^\dagger i\overleftrightarrow{D_\mu^I}H)(\overline{q}_p\tau^I\gamma^\mu q_r)$
$\mathcal{O}_{H\widetilde{B}}$	$H^\dagger H\, \widetilde{B}_{\mu\nu}B^{\mu\nu}$	$\mathcal{O}_{dG}$	$(\overline{q}_p\sigma^{\mu\nu}T^A d_r)H\, G^A_{\mu\nu}$	$\mathcal{O}_{Hu}$	$(H^\dagger i\overleftrightarrow{D_\mu}H)(\overline{u}_p\gamma^\mu u_r)$
$\mathcal{O}_{HWB}$	$H^\dagger\tau^I H\, W^I_{\mu\nu}B^{\mu\nu}$	$\mathcal{O}_{dW}$	$(\overline{q}_p\sigma^{\mu\nu}d_r)\tau^I H\, W^I_{\mu\nu}$	$\mathcal{O}_{Hd}$	$(H^\dagger i\overleftrightarrow{D_\mu}H)(\overline{d}_p\gamma^\mu d_r)$
$\mathcal{O}_{H\widetilde{W}B}$	$H^\dagger\tau^I H\, \widetilde{W}^I_{\mu\nu}B^{\mu\nu}$	$\mathcal{O}_{dB}$	$(\overline{q}_p\sigma^{\mu\nu}d_r)H\, B_{\mu\nu}$	$\mathcal{O}_{Hud}$	$(\widetilde{H}^\dagger i D_\mu H)(\overline{u}_p\gamma^\mu d_r)$
$\boldsymbol{\Psi^4:(LL)(LL)}$		$\boldsymbol{\Psi^4:(RR)(RR)}$		$\boldsymbol{\Psi^4:(LL)(RR)}$	
$\mathcal{O}_{\ell\ell}$	$(\overline{\ell}_p\gamma_\mu\ell_r)(\overline{\ell}_s\gamma^\mu\ell_t)$	$\mathcal{O}_{ee}$	$(\overline{e}_p\gamma_\mu e_r)(\overline{e}_s\gamma^\mu e_t)$	$\mathcal{O}_{\ell e}$	$(\overline{\ell}_p\gamma_\mu\ell_r)(\overline{e}_s\gamma^\mu e_t)$
$\mathcal{O}_{qq}^{(1)}$	$(\overline{q}_p\gamma_\mu q_r)(\overline{q}_s\gamma^\mu q_t)$	$\mathcal{O}_{uu}$	$(\overline{u}_p\gamma_\mu u_r)(\overline{u}_s\gamma^\mu u_t)$	$\mathcal{O}_{\ell u}$	$(\overline{\ell}_p\gamma_\mu\ell_r)(\overline{u}_s\gamma^\mu u_t)$
$\mathcal{O}_{qq}^{(3)}$	$(\overline{q}_p\gamma_\mu\tau^I q_r)(\overline{q}_s\gamma^\mu\tau^I q_t)$	$\mathcal{O}_{dd}$	$(\overline{d}_p\gamma_\mu d_r)(\overline{d}_s\gamma^\mu d_t)$	$\mathcal{O}_{\ell d}$	$(\overline{\ell}_p\gamma_\mu\ell_r)(\overline{d}_s\gamma^\mu d_t)$
$\mathcal{O}_{\ell q}^{(1)}$	$(\overline{\ell}_p\gamma_\mu\ell_r)(\overline{q}_s\gamma^\mu q_t)$	$\mathcal{O}_{eu}$	$(\overline{e}_p\gamma_\mu e_r)(\overline{u}_s\gamma^\mu u_t)$	$\mathcal{O}_{qe}$	$(\overline{q}_p\gamma_\mu q_r)(\overline{e}_s\gamma^\mu e_t)$
$\mathcal{O}_{\ell q}^{(3)}$	$(\overline{\ell}_p\gamma_\mu\tau^I\ell_r)(\overline{q}_s\gamma^\mu\tau^I q_t)$	$\mathcal{O}_{ed}$	$(\overline{e}_p\gamma_\mu e_r)(\overline{d}_s\gamma^\mu d_t)$	$\mathcal{O}_{qu}^{(1)}$	$(\overline{q}_p\gamma_\mu q_r)(\overline{u}_s\gamma^\mu u_t)$
		$\mathcal{O}_{ud}^{(1)}$	$(\overline{u}_p\gamma_\mu u_r)(\overline{d}_s\gamma^\mu d_t)$	$\mathcal{O}_{qu}^{(8)}$	$(\overline{q}_p\gamma_\mu T^A q_r)(\overline{u}_s\gamma^\mu T^A u_t)$
		$\mathcal{O}_{ud}^{(8)}$	$(\overline{u}_p\gamma_\mu T^A u_r)(\overline{d}_s\gamma^\mu T^A d_t)$	$\mathcal{O}_{qd}^{(1)}$	$(\overline{q}_p\gamma_\mu q_r)(\overline{d}_s\gamma^\mu d_t)$
				$\mathcal{O}_{qd}^{(8)}$	$(\overline{q}_p\gamma_\mu T^A q_r)(\overline{d}_s\gamma^\mu T^A d_t)$
$\boldsymbol{\Psi^4:(LR)(LR)}$		$\boldsymbol{\Psi^4:\Delta B=\Delta L=1}$			
$\mathcal{O}_{\ell edq}$	$(\overline{\ell}_p^I e_r)(\overline{d}_s q_t^I)$	$\mathcal{O}_{duq}$	$\epsilon^{ABC}\epsilon_{JK}\left[(d_p^A)^T C u_r^B\right]\left[(q_s^{CJ})^T C\ell_t^K\right]$		
$\mathcal{O}_{quqd}^{(1)}$	$(\overline{q}_p^J u_r)\epsilon_{JK}(\overline{q}_s^K d_t)$	$\mathcal{O}_{qqu}$	$\epsilon^{ABC}\epsilon_{JK}\left[(q_p^{AJ})^T C q_r^{BK}\right]\left[(u_s^C)^T C e_t\right]$		
$\mathcal{O}_{quqd}^{(8)}$	$(\overline{q}_p^J T^A u_r)\epsilon_{JK}(\overline{q}_s^K T^A d_t)$	$\mathcal{O}_{qqq}$	$\epsilon^{ABC}\epsilon_{JN}\epsilon_{KM}\left[(q_p^{AJ})^T C q_r^{BK}\right]\left[(q_s^{CM})^T C\ell_t^N\right]$		
$\mathcal{O}_{\ell equ}^{(1)}$	$(\overline{\ell}_p^J e_r)\epsilon_{JK}(\overline{q}_s^K u_t)$	$\mathcal{O}_{duu}$	$\epsilon^{ABC}\left[(d_p^A)^T C u_r^B\right]\left[(u_s^C)^T C e_t\right]$		
$\mathcal{O}_{\ell equ}^{(3)}$	$(\overline{\ell}_p^J\sigma_{\mu\nu}e_r)\epsilon_{JK}(\overline{q}_s^K\sigma^{\mu\nu}u_t)$				

TABLE 2.2: The full set of dimension 6 operators in Warsaw basis [11]. The bold headings classify the different sets of operators. Here, X, H, D, and Ψ denote the field strength tensor, Higgs doublet, covariant derivative, and fermion field, respectively. In the context of Ψ^4 operators, the notation $(LL)(LL)$ denotes that both the first and the second bilinear each contain two LH fermions. Similarly, for $(LL)(RR)$, the first bilinear consists of two LH fermions, while the second contains two RH fermions, and so on. $\Delta B = \Delta L = 1$ refers to as baryon and lepton number violation by one unit each.

generate lepton flavor violating Higgs decays, which have been extensively searched for at the LHC [161–163].

- $\boldsymbol{X^2H^2}$ **Operators:** These operators underpin a wide range of BSM scenarios and constitute some of the most relevant interactions in SMEFT. They contribute to charged TGCs, modify Higgs-gauge interactions, shift the Z mass, and can induce $Z-\gamma$ mixing. This class of operators will be studied in detail in Chap. 4.

- $\boldsymbol{\Psi^2XH}$ **Operators:** This class of operators is referred to as *dipole* operators, as they mediate magnetic dipole moments (MDMs) and electric dipole moments (EDMs) of fermions after EWSB. The MDM contributions arise from the real parts of the WCs, while the EDM contributions originate from their imaginary parts, and are therefore strongly constrained by EDM/MDM measurements [164]. In addition, these operators also induce $\psi\overline{\psi}Z/\psi\overline{\psi}Zh$ interactions, which will be studied in Sec. 4.1.

- $\boldsymbol{\Psi^2H^2D}$ **Operators:** These operators are referred to as *Higgs-current* operators and provide leading modifications to $\psi\overline{\psi}Z/\psi\overline{\psi}Zh$ vertices. They are strongly constrained by EWPO [165], as they modify the $\psi\overline{\psi}Z$ couplings with the same Lorentz structure as in the SM. In addition, depending on their flavor structure, they can induce quark and lepton flavor violating processes.

- $\boldsymbol{\Psi^4}$ **Operators:** *Four-fermion* operators are one of the most important classes of dimension 6 operators in SMEFT and form the cornerstone of flavor physics observables. Owing to their contact interaction nature, without propagator suppression, they are subject to stringent experimental constraints. These operators also typically arise from tree level UV completions [166], and are therefore associated with popular BSM scenarios such as Z' models, leptoquarks, and other BSM scalar extensions. In addition, there exist four $\Delta B = \Delta L = 1$ *four-fermion* operators at dimension 6, which are severely constrained by proton decay searches [167].

Operators of Dimension >6 Operators beyond dimension 6 are typically suppressed by higher powers of Λ, and are therefore often subleading. Nevertheless, there exist scenarios where their contributions become phenomenologically relevant and must be taken into account. At dimension 7, there are 18 independent operators (listed in Tab. 2.3) [12, 168, 169], all of which violate lepton number. Among these, 12 correspond to $\Delta L = 2$ operators, while the remaining 6 satisfy $\Delta B = \Delta L = 1$ condition. The Weinberg operator is already tightly constrained by neutrino mass measurements,

rendering its experimental probes challenging. In such scenario, dimension 7 operators provide alternative avenues to generate neutrino masses, with potential implications for collider phenomenology [102, 170]. However, the non-observation of neutrinoless double beta decay imposes tight constraints on such possibilities [170]. At dimension 8, there

Dimension 7 SMEFT Operators			
$\mathcal{O}^{pr}_{\ell H}$	$\epsilon_{JK}\epsilon_{MN}(\overline{\ell_p^{Jc}}\ell_r^M)H^K H^N (H^\dagger H)$	$\mathcal{O}^{pr}_{\ell eHD}$	$\epsilon_{JK}\epsilon_{MN}(\overline{\ell_p^{Jc}}\gamma_\mu e_r)H^K H^M iD^\mu H^N$
$\mathcal{O}^{pr}_{\ell HD1}$	$\epsilon_{JK}\epsilon_{MN}(\overline{\ell_p^{Jc}}D^\mu \ell_r^K)H^M D_\mu H^N$	$\mathcal{O}^{pr}_{\ell HD2}$	$\epsilon_{JM}\epsilon_{KN}(\overline{\ell_p^{Jc}}D^\mu \ell_r^K)H^M D_\mu H^N$
$\mathcal{O}^{pr}_{\ell HB}$	$\epsilon_{JK}\epsilon_{MN}(\overline{\ell_p^{Jc}}\sigma_{\mu\nu}\ell_r^M)H^K H^N B^{\mu\nu}$	$\mathcal{O}^{pr}_{\ell HW}$	$\epsilon_{JK}(\epsilon\tau^I)_{MN}(\overline{\ell_p^{Jc}}\sigma_{\mu\nu}\ell_r^M)H^K H^N W^{I\mu\nu}$
$\mathcal{O}^{prst}_{\overline{e}\ell\ell\ell H}$	$\epsilon_{JK}\epsilon_{MN}(\overline{e_p}\ell_r^J)(\overline{\ell_s^{Kc}}\ell_t^M)H^N$	$\mathcal{O}^{prst}_{\overline{d}\ell Q\ell H1}$	$\epsilon_{JK}\epsilon_{MN}(\overline{d_p}\ell_r^J)(\overline{Q_s^{Kc}}\ell_t^M)H^N$
$\mathcal{O}^{prst}_{\overline{d}\ell Q\ell H2}$	$\epsilon_{JM}\epsilon_{KN}(\overline{d_p}\ell_r^J)(\overline{Q_s^{Kc}}\ell_t^M)H^N$	$\mathcal{O}^{prst}_{\overline{d}\ell ueH}$	$\epsilon_{JK}(\overline{d_p}\ell_r^J)(\overline{u_s^c}e_t)H^K$
$\mathcal{O}^{prst}_{\overline{Q}u\ell\ell H}$	$\epsilon_{JK}(\overline{Q_p}u_r)(\overline{\ell_s^c}\ell_t^J)H^K$	$\mathcal{O}^{prst}_{\overline{d}u\ell\ell D}$	$\epsilon_{JK}(\overline{d_p}\gamma_\mu u_r)(\overline{\ell_s^{Jc}}iD^\mu \ell_t^K)$
$\mathcal{O}^{prst}_{\overline{\ell}dud\widetilde{H}}$	$\epsilon^{ABC}(\overline{\ell_p}d_r^A)(\overline{u_s^{Bc}}d_t^C)\widetilde{H}$	$\mathcal{O}^{prst}_{\overline{\ell}dddH}$	$\epsilon^{ABC}(\overline{\ell_p}d_r^A)(\overline{d_s^{Bc}}d_t^C)H$
$\mathcal{O}^{prst}_{\overline{e}Qdd\widetilde{H}}$	$\epsilon_{JK}\epsilon^{ABC}(\overline{e_p}Q_r^{JA})(\overline{d_s^{Bc}}d_t^C)\widetilde{H}^K$	$\mathcal{O}^{prst}_{\overline{\ell}dQQ\widetilde{H}}$	$\epsilon_{JK}\epsilon^{ABC}(\overline{\ell_p}d_r^A)(\overline{Q_s^{Bc}}Q_t^{JC})\widetilde{H}^K$
$\mathcal{O}^{prst}_{\overline{e}dddD}$	$\epsilon^{ABC}(\overline{e_p}\gamma_\mu d_r^A)(\overline{d_s^{Bc}}iD^\mu d_t^C)$	$\mathcal{O}^{prst}_{\overline{\ell}QddD}$	$\epsilon^{ABC}(\overline{\ell_p}\gamma_\mu Q_r^A)(\overline{d_s^{Bc}}iD^\mu d_t^C)$

TABLE 2.3: List of independent dimension 7 SMEFT operators, adapted from [12]. The top 12 (above the divider) correspond to $\Delta L = 2$ operators, while the bottom 6 correspond to $\Delta B = \Delta L = 1$ operators.

are 44,807 independent operators [171, 172]. Their effects become particularly relevant when quadratic dimension 6 contributions are included, as these enter at $\mathcal{O}(\Lambda^{-4})$, the same order as the interference between the SM and dimension 8 operators. Moreover, dimension 8 operators can give rise to exclusive NP effects, such as neutral TGCs, which are absent in the SM, and first appear at this order. Such effects have been studied at the LHC [173, 174].

Matching EFT to UV Completions

The connection between an EFT and its underlying UV complete theory is established through a matching procedure, wherein the heavy DOFs are integrated out and the effects systematically encoded into higher dimensional operators. This allows us to relate measurable low energy observables to the structure of the underlying theory. Depending on the structure of the UV completion, the operators may arise either at tree level or through loop generated processes involving heavy fields. For loop generated scenarios, naive dimensional analysis implies the WC scales as $C \sim (4\pi)^{-2L}$, where L is the

lowest loop order at which the operator is generated. This hierarchy has important phenomenological implications, as tree generated operators typically possess larger WCs and therefore induce the leading deviations from the SM, in comparison to loop generated operators which are suppressed by at least an additional factor of $(4\pi)^{-2}$. It is therefore useful to classify operators into two categories: (**I**) Potentially Tree Generated (PTG) operators [175] can be generated at tree level in at least one class of UV completions. Within the SMEFT framework, the operators of classes: H^6, H^4D^2, Ψ^2H^3, Ψ^2H^2D and Ψ^4 are PTG operators. (**II**) Loop Generated (LG) operators [175] cannot be generated at tree level in any weakly coupled, renormalizable UV completion, and therefore necessarily arise from loop diagrams. Within the SMEFT framework, the operators of classes: X^3, X^2H^2, and Ψ^2XH are LG operators. In the following, we illustrate this classification through explicit examples of matching to NP models, demonstrating how representative PTG and LG operators arise from integrating out heavy fields.

Matching at Tree Level For demonstrating tree level matching, we consider a simple NP scenario containing a heavy vector boson Z'_μ of mass $M_{Z'}$, coupled to both RH electron current and the Higgs current. The relevant terms of the Lagrangian are given below

$$\mathcal{L}_{\rm UV} \supset \frac{1}{2}M^2_{Z'}Z'_\mu Z'^\mu + g_e^{pr}\, Z'_\mu(\overline{e_p}\gamma^\mu e_r) + g_H Z'_\mu(H^\dagger i\overleftrightarrow{D^\mu}H)\,. \tag{2.19}$$

Here, we implicitly assume that the kinetic mixing between the heavy Z' and the SM hypercharge boson, B i.e. $\epsilon\, Z'_{\mu\nu}B^{\mu\nu}$ is sufficiently small, safely setting the mixing parameter $\epsilon \to 0$ to simplify the scenario. Furthermore, the mass $M_{Z'}$ is assumed to be generated dynamically via the spontaneous symmetry breaking of the extended $U(1)_{Z'}$ gauge symmetry by the VEV of a complex scalar field, which preserves the underlying gauge invariance of the theory. Before integrating out the heavy field, it is crucial to verify the conservation of the current to which the Z' couples, $J^\mu = g_e^{pr}(\overline{e_p}\gamma^\mu e_r) + g_H(H^\dagger i\overleftrightarrow{D^\mu}H)$. Using the Dirac equation, $i\gamma^\alpha\partial_\alpha e_r\,(i\partial_\alpha\overline{e_r}\gamma^\alpha) = m_r e_r\,(-m_r\overline{e_r})$. The divergence of the leptonic vector current is explicitly evaluated as

$$\partial_\mu J^\mu_e = \partial_\mu(\overline{e_p}\gamma^\mu e_r) = (\partial_\mu\overline{e_p})\gamma^\mu e_r + \overline{e_p}\gamma^\mu(\partial_\mu e_r) = i(m_p - m_r)\overline{e_p}e_r = 0\,, \tag{2.20}$$

where, we assumed $m_p \approx m_r \approx 0$ in the high energy regime. Similarly, we evaluate the divergence of the Higgs current, $J^\mu_H = i[H^\dagger(\partial^\mu H) - (\partial^\mu H^\dagger)H]$. Applying the product

rule yields $\partial_\mu J^\mu_H = i[H^\dagger(\Box H) - (\Box H^\dagger)H]$. The classical equations of motion for the Higgs field yields $\Box H = -\mu^2 H - 2\lambda|H|^2 H$ and its adjoint $\Box H^\dagger = -\mu^2 H^\dagger - 2\lambda|H|^2 H^\dagger$. Substituting these expressions,

$$\partial_\mu J^\mu_H = i[H^\dagger(\Box H) - (\Box H^\dagger)H] = i[(-\mu^2|H|^2 - 2\lambda|H|^4) - (-\mu^2|H|^2 - 2\lambda|H|^4)] = 0 \quad (2.21)$$

Therefore, the total current is strictly conserved i.e. $\partial_\mu J^\mu = \partial_\mu J^\mu_e + \partial_\mu J^\mu_H = 0$. The classical equation of motion for the massive Z' field is given by:

$$\partial_\nu Z'^{\nu\mu} + M^2_{Z'} Z'^\mu = J^\mu \quad \longrightarrow \quad \partial_\mu \partial_\nu Z'^{\nu\mu} + M^2_{Z'} \partial_\mu Z'^\mu = \partial_\mu J^\mu \,. \quad (2.22)$$

Since the field strength tensor $Z'^{\nu\mu}$ is antisymmetric, the term $\partial_\mu \partial_\nu Z'^{\nu\mu}$ identically vanishes. Combined with the current conservation condition ($\partial_\mu J^\mu = 0$), this algebraically enforces the transversality condition: $\partial_\mu Z'^\mu = 0$. This condition removes the unphysical scalar mode, ensuring the vector field accurately propagates only 3 physical DOFs. With transversality enforced, the equation of motion elegantly simplifies to $\left(\Box + M^2_{Z'}\right) Z'^\mu = J^\mu$. At energies much below the mass of Z', $E \ll M_{Z'}$, the heavy field can be integrated out using its classical equation of motion,

$$Z'_\mu \simeq \frac{1}{M^2_{Z'}} \left[g_e^{pr} Z'_\mu (\overline{e_p} \gamma^\mu e_r) + g_H (H^\dagger i \overleftrightarrow{D_\mu} H) \right] . \quad (2.23)$$

Substituting this back into the mass term of in the Lagrangian generates an effective interaction,

$$\mathcal{L}_{\text{EFT}} \supset \frac{1}{2M^2_{Z'}} \left[g_e^{pr} Z'_\mu (\overline{e_p} \gamma^\mu e_r) + g_H (H^\dagger i \overleftrightarrow{D^\mu} H) \right]^2 . \quad (2.24)$$

Expanding, the cross-term yields

$$\mathcal{L}_{\text{EFT}} \supset \frac{g_e^{pr} g_H}{M^2_{Z'}} (\overline{e_p} \gamma^\mu e_r)(H^\dagger i \overleftrightarrow{D_\mu} H) \,. \quad (2.25)$$

This operator belongs to the $\Psi^2 H^2 D$ class and arises directly from the tree-level exchange of the heavy vector mediator. Consequently, the corresponding WC is unsuppressed by loop factors and scales as $\left[C_{He}/\Lambda^2\right]_{pr} \sim \left(g_e^{pr} g_H / M^2_{Z'}\right)$, characteristic of a PTG operator. The Feynman diagrams corresponding to the tree level matching schematic is shown in Fig. 2.3.

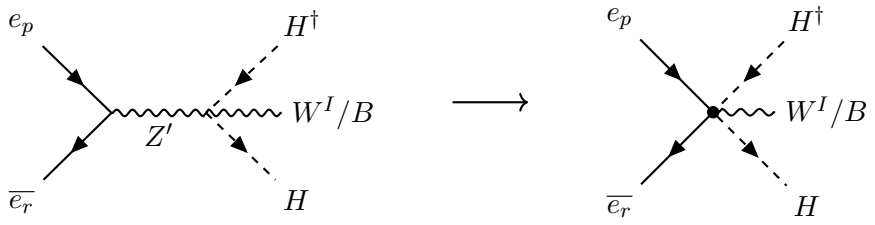

FIGURE 2.3: Feynman diagrams showing a tree level matching between a Z' model and SMEFT operator $\mathcal{O}_{He}$.

Matching at Loop Level To demonstrate loop level matching, we now consider another NP scenario involving a heavy complex scalar S of mass M_S, charged under the hypercharge gauge group with field strength tensor $B_{\mu\nu}$, and coupled to the Higgs doublet via a portal interaction. The relevant terms of the Lagrangian are given below

$$\mathcal{L}_{\text{UV}} \supset |D_\mu S|^2 - M_S^2|S|^2 - \lambda'|S|^2(H^\dagger H)\,, \tag{2.26}$$

where $D_\mu = \partial_\mu - ig'B_\mu$. We note that the quartic self-interaction, $-\lambda_S|S|^4$, is omitted from our UV Lagrangian. Since S is charged under $U(1)_Y$, gauge invariance strictly forbids terms linear in S. As a result, the classical equation of motion yields $S = 0$. As the classical field configuration is zero, there is no tree-level exchange. In the functional formalism, quantum fluctuations are integrated around this $S = 0$ vacuum. The $\lambda_S|S|^4$ term represents a 4-point vertex of these fluctuations. Around a zero background, a 4-point vertex does not contribute to the one-loop functional determinant. It only generates 8-shaped diagram topologies that contribute at the two-loop order. Restricting our matching to strictly truncate at leading-log one-loop accuracy i.e. $\mathcal{O}(1/16\pi^2)$, this term decouples and is systematically neglected. The effective theory is obtained by integrating out S at one-loop, which can be systematically performed using the functional determinant [176]. We start with the generating functional

$$Z = \int [\mathcal{D}S^\dagger][\mathcal{D}S]\, e^{i\int \mathcal{L}_{\text{UV}}\, d^4x} \tag{2.27}$$

By integrating the derivative term by parts, the quadratic part of the heavy scalar action can be written as

$$i\int \mathcal{L}_{\text{UV}}\, d^4x = i\int S^\dagger \left(-D^2 - M_S^2 - \lambda' H^\dagger H\right) S\, d^4x \tag{2.28}$$

Performing the exact Gaussian integral over the complex scalar fields mathematically yields the inverse functional determinant of the quadratic operator:

$$Z \propto \left[\mathrm{Det}\left(-D^2 - M_S^2 - \lambda' H^\dagger H\right)\right]^{-1} , \tag{2.29}$$

Equating this to the formal definition of the effective action, we obtain

$$Z \equiv e^{i\int \mathcal{L}_{\mathrm{EFT}}\, d^4x} \quad \Longrightarrow \quad i\int \mathcal{L}_{\mathrm{EFT}}\, d^4x = -\ln \mathrm{Det}\left(-D^2 - M_S^2 - \lambda' H^\dagger H\right) . \tag{2.30}$$

Utilizing the trace-log operator identity, we can write the effective action compactly as

$$S_{\mathrm{EFT}} = i\,\mathrm{Tr}\ln\left(-D^2 - M_S^2 - \lambda' H^\dagger H\right) . \tag{2.31}$$

To ensure manifest gauge invariance at intermediate steps, we evaluate this functional trace using CDE. Extracting the plane-wave states $e^{\pm iq\cdot x}$ shifts the covariant derivative as $D_\mu \to D_\mu + iq_\mu$. Factoring out the free heavy propagator $(q^2 - M_S^2)$ and neglecting the first term allows us to extract the local effective Lagrangian density:

$$\begin{aligned}\Delta\mathcal{L}_{\mathrm{EFT}} &= i\int \frac{d^4q}{(2\pi)^4}\mathrm{tr}\ln\left[1 - \frac{2iq\cdot D + D^2 + \lambda' H^\dagger H}{q^2 - M_S^2}\right] , \\ &= i\int \frac{d^4q}{(2\pi)^4}\mathrm{tr}\left[-\frac{2iq\cdot D + D^2 + \lambda' H^\dagger H}{q^2 - M_S^2} - \frac{(2iq\cdot D + D^2 + \lambda' H^\dagger H)^2}{2\left(q^2 - M_S^2\right)^2} - \cdots\right] ,\end{aligned} \tag{2.32}$$

The operator $(H^\dagger H)B_{\mu\nu}B^{\mu\nu}$ arises from the higher-order terms in this expansion, specifically involving one insertion of the Higgs portal interaction $\lambda' H^\dagger H$ and multiple insertions of the covariant derivative. Following symmetric loop integration over the momenta d^4q, the remaining covariant derivatives are algebraically rearranged using their commutator, $[D_\mu, D_\nu] = -ig' B_{\mu\nu}$. Because D_μ is never explicitly separated into partial derivatives and bare fields, the physical field strength tensor $B_{\mu\nu}$ emerges naturally, guaranteeing manifest gauge invariance. Performing the full integration and trace evaluation yields the effective operator

$$\mathcal{L}_{\mathrm{EFT}} \supset \frac{\lambda' g'^2}{96\pi^2 M_S^2}(H^\dagger H)\, B_{\mu\nu}B^{\mu\nu} . \tag{2.33}$$

This operator belongs to the X^2H^2 class and is generated only at the loop level, as no tree-level diagram can connect two Higgs fields and two gauge bosons through a renormalizable interaction. The WC is therefore suppressed by a loop factor, $(C_{HB}/\Lambda^2) \sim (\lambda' g'^2/16\pi^2 M_S^2)$, characteristic of LG operators. The Feynman diagrams corresponding to the loop level matching is shown in Fig. 2.4.

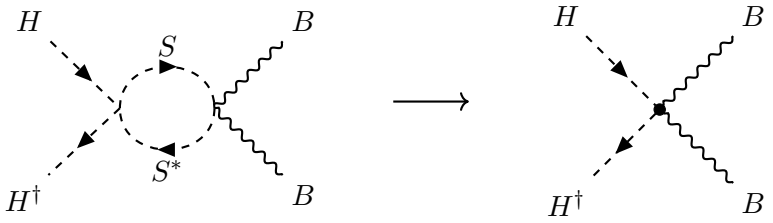

FIGURE 2.4: Feynman diagrams showing a loop level matching between a complex scalar model and SMEFT operator $\mathcal{O}_{HB}$.

2.3 Dark Matter Effective Field Theory

As discussed in Sec. 1.2.1, the evidence for dark matter (DM) is compelling, and a plethora of particle physics models have been proposed to accommodate viable DM candidates. However, the absence of any confirmed non-gravitational detection implies that no particular model is currently favored. In this context, DMEFT provides a model-independent and systematic framework to incorporate DM interactions with the SM. The DMEFT framework extends the SM by introducing one or more DM candidates that interacts with SM fields through effective operators constructed from both SM and DM DOFs. This framework has been extensively developed and studied in the literature [16, 176–183].

2.3.1 DMEFT Operator Construction

The DMEFT Lagrangian is given as follows

$$\mathcal{L}_{\text{DMEFT}} = \mathcal{L}_{\text{SM}} + \mathcal{L}_{\text{DM}} + \sum_{i,d} \frac{C_i^{(d)} \mathcal{O}_i^{(d)}}{\Lambda^{d-4}} \,, \tag{2.34}$$

where the operator $\mathcal{O}_i^{(d)}$ can be decomposed as $\mathcal{O}_i^{(d)} \sim \mathcal{O}_i^{\text{SM}} \mathcal{O}_i^{\text{DM}}$. Here, $\mathcal{O}_i^{\text{SM}}$ is constructed from SM fields, while $\mathcal{O}_i^{\text{DM}}$ is composed of DM fields. This factorization reflects the requirement that the operators be invariant under the SM gauge symmetries as well as any symmetry that stabilizes the dark matter candidate, with SM and DM fields taken to be singlets under each other's symmetry groups. In addition, the operators must respect Lorentz invariance. It should be noted that DMEFT operators can also be constructed without imposing an explicit DM symmetry [184]. In such scenarios, the stability of the DM can be ensured kinematically, by requiring its mass to be lower than that of its potential decay products, or dynamically, by suppressing the interaction rates

sufficiently so that its lifetime exceeds that of the Universe. In this thesis, however, we restrict ourselves to operators that respect an inherent $\mathcal{Z}_2$ symmetry, which guarantees the stability of the DM candidate.

Possible $\mathcal{O}^{\mathrm{SM}}$ Structures The simplest SM scalar singlet structure is $H^\dagger H$, which gives rise to the Higgs-portal DM models. Other scalar structures include $(H^\dagger H)^2$, $\overline{\ell_L} H e_R$, $\overline{q_L}\widetilde{H} u_R$, $\overline{q_L} H d_R$, $B_{\mu\nu}B^{\mu\nu}$, $W^I_{\mu\nu}W^{I\mu\nu}$, and $G^A_{\mu\nu}G^{A\mu\nu}$. In addition, vector and tensor structures can also be constructed. Some examples include fermion current operators such as $\overline{\ell_L}\gamma_\mu \ell_L$, $\overline{q_L}\gamma_\mu q_L$, $\overline{e_R}\gamma_\mu e_R$, $\overline{u_R}\gamma_\mu u_R$, and $\overline{d_R}\gamma_\mu d_R$, as well as the structure $H^\dagger i\overleftrightarrow{D}_\mu H$, which mediates Z-portal DM interactions. Similarly, simple tensor structures such as $B_{\mu\nu}$ lead to DM *dipole* interactions. Fermionic tensor structures, including $\overline{\ell_L} H \sigma_{\mu\nu} e_R$, $\overline{q_L}\widetilde{H}\sigma_{\mu\nu} u_R$, and $\overline{q_L} H \sigma_{\mu\nu} d_R$, can also be constructed. All these structures are invariant under the SM gauge symmetries. The vector and tensor structures must be contracted with the corresponding $\mathcal{O}^{\mathrm{DM}}$ components in order to be Lorentz invariant.

Possible $\mathcal{O}^{\mathrm{DM}}$ Structures The possible structures of $\mathcal{O}^{\mathrm{DM}}$ depend on the nature of the DM field, which may be a real scalar (Φ), complex scalar (Φ, $\Phi^\dagger$), Dirac fermion (χ, $\overline{\chi}$), Majorana fermion (N), real vector boson (X_μ), or complex vector boson (X_μ, $X_\mu^\dagger$). In this work, we restrict ourselves to real scalar and vector fields for bosonic dark matter, and to Dirac fermions in the fermionic case. Scalar DM generates simple structures such as Φ^2, Φ^4, and $\partial_\mu\Phi\,\partial^\mu\Phi$. For vector DM, depending on whether the field is Abelian or non-Abelian, the leading structures are $X_{\mu\nu}X^{\mu\nu}$ and $X_\mu X^\mu$, respectively. In the non-Abelian case, additional self-interaction terms such as $X_\mu X^\mu X_\nu X^\nu$ can also arise. For Dirac DM, all Lorentz structures are in principle allowed, including scalar, vector, and tensor bilinears, namely $\overline{\chi}\chi$, $\overline{\chi}\gamma_\mu\chi$, and $\overline{\chi}\sigma_{\mu\nu}\chi$.

Relevant DMEFT Operators Combining the SM and DM building blocks discussed above, one can systematically construct the DMEFT operators by forming Lorentz invariant combinations. The complete set of DMEFT operators up to dimension 7, for real scalar and vector DM as well as Dirac fermionic DM, is presented in Tab. 2.4, while assuming that the DM transforms under a $\mathcal{Z}_2$ symmetry. A few representative examples of such operators are discussed below.

- **Higgs-portal Operators:** These operators connect to the SM via Higgs boson mediator [185, 186]. These operators are strongly constrained by DD and Higgs invisible branching ratio measurements [187].

$$\begin{cases} (H^\dagger H)\Phi^2 \\ (H^\dagger H)(\partial_\mu \Phi \partial^\mu \Phi) \end{cases} , \quad (H^\dagger H)\overline{\chi}\chi \ , \quad \begin{cases} (H^\dagger H)X_\mu X^\mu \\ (H^\dagger H)X_{\mu\nu}X^{\mu\nu} \end{cases} . \tag{2.35}$$

- **Leptophilic Operators:** These operators correspond to interactions where the DM couples exclusively to leptonic currents of the SM [188–190]. Such operators are interesting as they evade strong constraints from hadronic processes and direct detection experiments. They lead to characteristic signatures at colliders and in precision measurements involving leptons.

$$(\overline{\ell_L} H e_R)\Phi^2 \ , \quad \begin{cases} (\overline{\ell_L}\gamma_\mu \ell_L)(\overline{\chi}\gamma^\mu \chi) \\ (\overline{e_R}\gamma_\mu e_R)(\overline{\chi}\gamma^\mu \chi) \end{cases} , \quad (\overline{\ell_L} H e_R) X_\mu X^\mu \, . \tag{2.36}$$

- **Photophilic Operators:** These operators describe interactions where DM couples predominantly to the SM electroweak field strength tensors [57, 58]. Such couplings give rise to distinctive signatures in processes involving photons, including mono-γ signals at colliders and ID via gamma rays.

$$(B_{\mu\nu}B^{\mu\nu})\Phi^2 \ , \quad \begin{cases} B_{\mu\nu}(\overline{\chi}\sigma^{\mu\nu}\chi) \\ (B_{\mu\nu}B^{\mu\nu})\overline{\chi}\chi \end{cases} , \quad (B_{\mu\nu}B^{\mu\nu})X_\mu X^\mu \, . \tag{2.37}$$

Appendix: Effective Field Theories

2.A The κ Modifier Framework

The κ framework provides a model-independent parametrization of potential deviations from the SM predictions in Higgs boson interactions. In this approach, the couplings of the Higgs boson to the SM fields are rescaled by multiplicative factors κ_i, defined such that

$$g_{hXX} = \kappa_X \, g^{\rm SM}_{hXX} \, , \tag{2.38}$$

DMEFT Operators upto Dimension 7		
Scalar (Φ)	**Dimension 4**	$(\overline{\ell_L} H e_R)\Phi^2$
	$(H^\dagger H)\Phi^2$	$(G^A_{\mu\nu} G^{A\mu\nu})\Phi^2$
	Dimension 6	$(W^I_{\mu\nu} W^{I\mu\nu})\Phi^2$
	$(H^\dagger H)(\partial_\mu \Phi \partial^\mu \Phi)$	$(B_{\mu\nu} B^{\mu\nu})\Phi^2$
	$(\overline{q_L}\widetilde{H} u_R)\Phi^2$	**Dimension 7**
	$(\overline{q_L} H d_R)\Phi^2$	$(\overline{\ell^c} H)(\widetilde{H}^\dagger \ell)\Phi^2$
Fermion (χ)	**Dimension 5**	**Dimension 7**
	$(H^\dagger H)\overline{\chi}\chi$	$(\overline{q_L}\widetilde{H} u_R)(\overline{\chi}\chi)$
	$B_{\mu\nu}(\overline{\chi}\sigma^{\mu\nu}\chi)$	$(\overline{q_L} H d_R)(\overline{\chi}\chi)$
	Dimension 6	$(\overline{\ell_L} H e_R)(\overline{\chi}\chi)$
	$(\overline{q_L}\gamma_\mu q_L)(\overline{\chi}\gamma^\mu\chi)$	$(\overline{q_L}\widetilde{H}\sigma_{\mu\nu} u_R)(\overline{\chi}\sigma^{\mu\nu}\chi)$
	$(\overline{\ell_L}\gamma_\mu \ell_L)(\overline{\chi}\gamma^\mu\chi)$	$(\overline{q_L} H \sigma_{\mu\nu} d_R)(\overline{\chi}\sigma^{\mu\nu}\chi)$
	$(\overline{u_R}\gamma_\mu u_R)(\overline{\chi}\gamma^\mu\chi)$	$(\overline{\ell_L} H \sigma_{\mu\nu} e_R)(\overline{\chi}\sigma^{\mu\nu}\chi)$
	$(\overline{d_R}\gamma_\mu d_R)(\overline{\chi}\gamma^\mu\chi)$	$(G^A_{\mu\nu} G^{A\mu\nu})(\overline{\chi}\chi)$
	$(\overline{e_R}\gamma_\mu e_R)(\overline{\chi}\gamma^\mu\chi)$	$(W^I_{\mu\nu} W^{I\mu\nu})(\overline{\chi}\chi)$
	$(H^\dagger i\overleftrightarrow{D_\mu} H)(\overline{\chi}\gamma^\mu\chi)$	$(B_{\mu\nu} B^{\mu\nu})(\overline{\chi}\chi)$
Vector (X_μ)	**Dimension 4**	$(\overline{\ell_L} H e_R) X_\mu X^\mu$
	$(H^\dagger H) X_\mu X^\mu$	$(G^A_{\mu\nu} G^{A\mu\nu}) X_\mu X^\mu$
	Dimension 6	$(W^I_{\mu\nu} W^{I\mu\nu}) X_\mu X^\mu$
	$(H^\dagger H)(X_{\mu\nu} X^{\mu\nu})$	$(B_{\mu\nu} B^{\mu\nu}) X_\mu X^\mu$
	$(\overline{q_L}\widetilde{H} u_R) X_\mu X^\mu$	**Dimension 7**
	$(\overline{q_L} H d_R) X_\mu X^\mu$	$(\overline{\ell^c} H)(\widetilde{H}^\dagger \ell) X_\mu X^\mu$

TABLE 2.4: Complete set of DMEFT operators up to dimension 7, for real scalar (Φ) and vector (X_μ) DM as well as Dirac fermionic DM (χ), assuming they transform under a $\mathcal{Z}_2$ symmetry.

where X denotes a given particle species, and $g^{\rm SM}_{hXX}$ is the corresponding SM coupling value. This modification propagates directly to production cross sections and decay widths. For a given production mode i and decay channel j, the signal strength modifier is defined as

$$\mu_i^f = \frac{\sigma_i}{\sigma_i^{\rm SM}} \times \frac{\mathcal{B}_j}{\mathcal{B}_j^{\rm SM}} = \frac{\kappa_i^2\,\kappa_j^2}{\kappa_H^2}\,, \tag{2.39}$$

where, $\mathcal{B}$ is the branching ratio, and κ_H^2 rescales the total Higgs width, defined as

$$\kappa_H^2 = \sum_j \kappa_j^2 \, \mathcal{B}_j^{\rm SM} \, . \tag{2.40}$$

Loop-induced vertices, such as $h \to \gamma\gamma$ and $h \to gg$, are either expressed in terms of effective modifiers κ_γ, κ_g, or resolved in terms of underlying modifiers like κ_t, κ_W, etc. The former parameterization is more general, and allows including possible new particle contributions in loops. The κ framework is particularly useful for capturing effects of heavy NP that modifies Higgs couplings without introducing new light DOFs or altering the Lorentz structure of interactions. However, it does not account for momentum-dependent structures, which are more naturally described within an EFT framework. Global fits to Higgs data by the ATLAS [6] and CMS [7] provide stringent constraints on the κ parameters, summarized in These results indicate no significant deviation from

$\boldsymbol{\kappa}$	**Vertex**	**95% C.L. limits ATLAS** [6]	**95% C.L. limits CMS** [7]
κ_W	hWW	1.05 ± 0.06	1.02 ± 0.08
κ_Z	hZZ	0.99 ± 0.06	1.04 ± 0.07
κ_T	$ht\bar{t}$	0.94 ± 0.11	$1.01^{+0.11}_{-0.10}$
κ_B	$hb\bar{b}$	0.89 ± 0.11	$0.99^{+0.17}_{-0.16}$
κ_τ	$h\tau\tau$	0.93 ± 0.07	0.92 ± 0.08
κ_G	hgg	0.95 ± 0.07	0.92 ± 0.08
κ_γ	$h\gamma\gamma$	1.01 ± 0.06	1.10 ± 0.08

TABLE 2.5: Constraints on κ parameters from global fits of Higgs data by the ATLAS and CMS collaborations.

SM expectations within experimental uncertainties, thereby placing strong constraints on NP scenarios that modify Higgs interactions.

2.B Other EFTs: HEFT and WEFT

EFTs beyond the SMEFT provide complementary descriptions of low-energy physics under different assumptions about the underlying dynamics. In particular, both HEFT and WEFT are constructed to respect the same low-energy gauge symmetries as the SM after EWSB, i.e. $SU(3)_C \times U(1)_{\rm EM}$. However, they differ significantly in how the electroweak symmetry is realized and in their field content and power counting schemes.

Higgs Effective Field Theory (HEFT) HEFT provides a framework to describe EWSB without assuming that the Higgs boson belongs to an exact $SU(2)_L$ doublet. Instead, the Higgs field is treated as a singlet under the electroweak symmetry, while the Goldstone bosons (π) associated with EWSB are described nonlinearly through a unitary matrix

$$U(x) = \exp\left(i\frac{\tau^I \pi^I(x)}{v}\right) . \tag{2.41}$$

similar to ChPT discussed in Sec. 2.1. In contrast to SMEFT, where the Higgs is embedded in a doublet, HEFT allows for more general interactions between the Higgs and gauge bosons, say, hVV and $hhVV$ interactions are decoupled. The field content consists of the SM gauge fields, fermions, the physical Higgs scalar h, and the Goldstone bosons encoded in $U(x)$. The power counting in HEFT is organized as a derivative expansion rather than a strict canonical dimension expansion, similar to ChPT.

Weak Effective Field Theory (WEFT) WEFT is constructed as a low energy EFT below the electroweak scale, where the heavy DOFs such as the W, Z, Higgs boson, and top quark have been integrated out. The relevant symmetry is therefore the unbroken $SU(3)_C \times U(1)_{\rm EM}$, and electroweak symmetry is no longer manifest. The field content of WEFT consists only of light fermions (quarks and leptons) and gauge fields corresponding to QCD (g) and QED (γ). As a result, the effective operators are typically constructed from fermion bilinears and four-fermion interactions, which mediate low-energy processes such as FCNCs, weak decays, and EWPOs. The power counting in WEFT follows a canonical dimension expansion, similar to the SMEFT framework.

Chapter 3

Collider Phenomenology

"When the facts change, I change my mind. What do you do, Sir?"
John Maynard Keynes

Contents

PARTICLE colliders provide powerful experimental setups to probe fundamental interactions in controlled environments. By colliding accelerated initial state particles, such as protons or electrons, at very high energies, one can probe short distance interactions that are otherwise inaccessible. With the control over the initial state energies, and in some cases initial state spin configurations, colliders provide unique opportunities to probe resonances expected at a specific energy range, as well as, NP with particular chiral structures. In addition to discovery of NP, collider experiments also provide ground for precision measurement of SM parameters, thereby indirectly constraining NP models. One such example can be provided by the Large Electron Positron (LEP) collider measurements of electroweak precision observables (EWPO), which placed stringent constraints on NP by testing the SM at the loop level with very high accuracy. The complementarity between collider experiments and observation based searches, as well as, between different types of colliders, further enhances the overall sensitivity to a wide range of NP scenarios. In Fig. 6.19, we show the LHC tunnel at CERN (*left*) alongside a

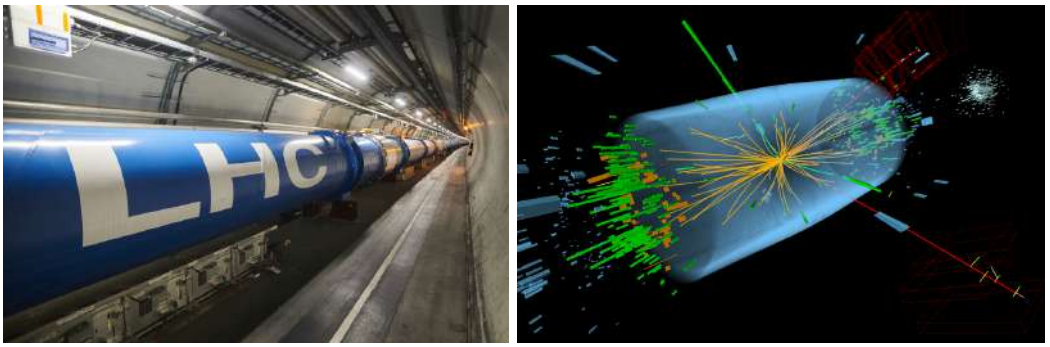

FIGURE 3.1: A section of the 27 km LHC tunnel at CERN (*left*). A candidate event in the search for the Higgs boson at the CMS detector, showing two electrons and two muons (*right*). Both adapted from CERN image gallery.

candidate event displaying Higgs boson production at the LHC (*right*). In the following sections, we discuss several aspects of particle colliders in detail.

3.1 Physics at High Energy Particle Colliders

At high energy particle colliders, accelerated particle beams are brought into collision at a defined center-of-mass (CM) energy, where this available energy is converted into a spectrum of final state particles. The probability of a given process is determined by the corresponding scattering amplitude ($\mathcal{M}$), with measurable quantities expressed through total (σ) or differential ($d\sigma$) cross sections. By varying the collision energy and luminosity, colliders can probe different kinematic regimes and enhance its search prospects. At hadron colliders like the Large Hadron Collider (LHC), collsion occurs between protons and their composite nature implies that interactions occur between constituent partons, resulting in a complex collision system. This necessitates the use of parton distribution functions (PDFs) and careful treatment of QCD effects. In contrast, lepton colliders offer well-defined initial states with minimal substructure, allowing for a less complex collision dynamics and more precise reconstruction ability. The sensitivity of collider searches is governed by the interplay of energy reach, luminosity, and detector performance. In the following sections, we discuss the distinct features of hadron and lepton collider environments along with the features relevant for phenomenology, and outline how the particles produced in such collisions are detected.

3.1.1 Physics at Hadron Colliders

At hadron colliders like the LHC, protons are grouped into bunches. With approximately ~ 3000 bunches circulating in each beam, each bunch containing about 10^{11} protons, and the bunches cross at intervals of 25 ns, corresponding to a crossing frequency of 40 MHz. The microscopic beam parameters are connected to the observable event rates through the concept of luminosity. The instantaneous luminosity $\mathfrak{L}$ quantifies the flux of incoming particles and can be expressed schematically as

$$\mathfrak{L} \sim \frac{N_b\, n_p^2\, f}{A}\,, \tag{3.1}$$

where, N_b is the number of bunches, n_p is the number of protons per bunch, f is the bunch crossing frequency, and A is the effective transverse overlap area of the beams. The number of events for a given process is directly related to the luminosity through

$$N_{\text{events}} = \sigma \int \mathfrak{L}\, dt \equiv \sigma\, \mathfrak{L}_{\text{int}}\,, \tag{3.2}$$

where, σ is the production cross section and $\mathfrak{L}_{\text{int}}$ is the integrated luminosity. This expression provides a direct bridge between machine parameters and the statistical reach of colliders. For a production process $pp \to X$ at hadron colliders, the total cross section can be factorized into long and short distance contributions as

$$\sigma_X = \sum_{a,b} \int_0^1 dx_1\, dx_2\; f_a(x_1, \mu_F^2)\, f_b(x_2, \mu_F^2)\; \hat{\sigma}_{ab\to X}\left(x_1, x_2, c\left(\mu_R^2\right), \frac{Q^2}{\mu_R^2}, \frac{Q^2}{\mu_F^2}\right). \tag{3.3}$$

Here, $\hat{\sigma}_{ab\to X}$ denotes the partonic cross section, which provides the short distance dynamics of the underlying hard scattering process. The coupling $c(\mu_R^2)$ incorporates the interaction strength and the renormalization scale μ_R is introduced to regulate ultraviolet divergences arising in quantum corrections. The variables x_1 and x_2 are the momentum fractions of the incoming particles that are carried by the partons a and b, respectively, while the parton distribution functions f_a and f_b gives the probability distribution for finding these partons inside the proton. The factorization scale μ_F separates the long distance physics encoded in the PDFs from the perturbatively short distance cross section, and absorbs collinear divergences into the scale dependence of the PDFs. Due to the variable partonic energies, hadron colliders can effectively scan a wide range of CM

energies and search for NP resonances over a large mass range, and are therefore often referred to as *discovery* machines.

Parton Distribution Functions Although we collide protons at hadron colliders, at the short range interactions happen between the constituent quarks and gluons, referred to as partons. The distribution of partons in a proton is encoded in the PDFs, denoted as $f_i(x, \mu_F^2)$, which describe the probability density of finding a parton of type i carrying the proton's momentum fraction x at a given factorization scale μ_F. The scale dependence arises due to QCD radiation and is governed by the Dokshitzer–Gribov–Lipatov–Altarelli–Parisi (DGLAP) evolution equations, which resum logarithms of the form $\ln(\mu_F^2)$ [191]. With the increase in energy, gluon splitting processes increase, leading to large number of low x parton constituents. Since, the composite quark-gluon systems that govern the PDFs are non-perturbative in nature, they cannot be calculated from first principles of perturbative QCD. Rather, they are extracted from global fits to experimental data from deep inelastic scattering (DIS), Drell–Yan (DY) processes, and collider measurements. Some examples of PDF sets are CT [192], MMHT [193], and NNPDF [194]. They provide the PDF inputs along with associated uncertainties, which play an important role in precise prediction of collider cross sections.

Collider Kinematics and Observables The basic kinematics at the LHC, operating at a CM energy $\sqrt{s} = 13$ TeV, is characterized by the collision of two protons with 4-momenta $P_1^\mu = (0, 0, +6.5, 6.5)$ TeV and $P_2^\mu = (0, 0, -6.5, 6.5)$ TeV, where the components are given as (p_x, p_y, p_z, E). Consequently, the 4-momenta of the colliding partons are given by $p_1^\mu = x_1 P_1^\mu$ and $p_2^\mu = x_2 P_2^\mu$, and the corresponding partonic CM energy is given by $\hat{s} = x_1 x_2 s$. Following the collision, the energy of the incoming partons is converted into new particles, which subsequently decay into stable, detectable final states, e.g., $pp \to Z \to e^+e^-$. The produced particles propagate through the detector, where their kinematic properties are reconstructed from measurables quantities. Based on the geometry of collider detectors, it is convenient to describe particle momenta in terms of cylindrical coordinates with respect to the beam axis, as shown in Fig. 3.2. Three key kinematic variables are: the transverse momentum p_T, the polar angle θ, and the

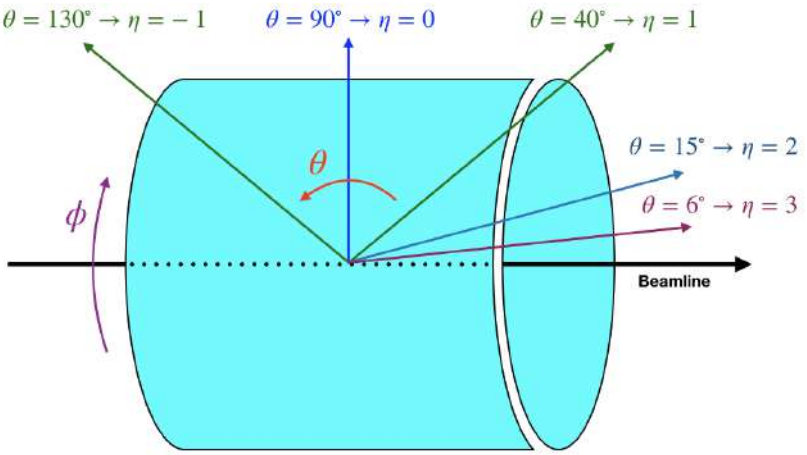

FIGURE 3.2: The geometric representation of cylindrical co-ordinates at a detector, adapted from [2]. Pseudorapidity (η) is a function of the polar angle θ goes from $-\pi$ to $+\pi$. The azimuthal angle ϕ goes around the beam.

azimuthal angle ϕ. The definitions are as follows:

$$p_T = \sqrt{p_x^2 + p_y^2}\,, \quad \theta = \cos^{-1}\left(\frac{p_z}{\sqrt{p_x^2 + p_y^2 + p_z^2}}\right), \quad \phi = \tan^{-1}\left(\frac{p_y}{p_x}\right). \tag{3.4}$$

The angles θ and ϕ describe the direction of the particle trajectory, where θ is measured with respect to the beam axis and ϕ is in the plane transverse to it. Since, the initial state momentum is directed along the p_z direction, under boosts, p_x and p_y are invariant, whereas p_z and E transform as

$$\begin{aligned} p_z &\longrightarrow p_z \cosh\beta + E \sinh\beta\,, \\ E &\longrightarrow p_z \sinh\beta + E \cosh\beta\,. \end{aligned} \tag{3.5}$$

The variables p_T and ϕ are independent of p_z and E, hence, boost invariant, whereas, θ is frame-dependent. For collider studies, a more preferred quantity is rapidity, which is defined as

$$y = \frac{1}{2}\ln\left(\frac{E + p_z}{E - p_z}\right). \tag{3.6}$$

Under boost, rapidity itself isn't invariant, but differences in rapidities between particles, which is usually measured, is invariant.

$$y \longrightarrow y + \ln\left(\cosh\beta + \sinh\beta\right) \quad \Longrightarrow \quad \Delta y \longrightarrow \Delta y\,. \tag{3.7}$$

In the massless limit, $p_z = E\cos\theta$ rapidity reduces to the pseudorapidity, denoted by η, defined as

$$\eta = \frac{1}{2}\ln\left(\frac{E+p_z}{E-p_z}\right) = \frac{1}{2}\ln\left(\frac{1+\cos\theta}{1-\cos\theta}\right) = \ln\cot\left(\frac{\theta}{2}\right). \tag{3.8}$$

In Fig. 3.2, we visually illustrate the relation between θ and η. If the detector surface is unwrapped onto a flat sheet, the x-y coordinates correspond to the η-ϕ variables. The distance between two detected particles is given by ΔR, defined as

$$\Delta R = \sqrt{(\Delta\eta)^2 + (\Delta\phi)^2}, \tag{3.9}$$

where, $\Delta\eta$ and $\Delta\phi$ are the η and ϕ separation between the particles, respectively. Another important observable is the invariant mass (of i particles), M_i, defined as

$$M_i = \sqrt{\left(\sum_i p_i\right)^2}. \tag{3.10}$$

where, p_i is the 4-momentum of the i^{th} particle. For on-shell decay of particle X to i particles, 4-momentum conservation requires the invariant mass to peak at X mass.

$$\sum_i p_i = p_X \quad \Longrightarrow \quad M_i = \sqrt{p_X^2} = M_X\,. \tag{3.11}$$

Concerning DM searches, there are two important observables that rely on the energy imbalance of visible particles, namely missing transverse energy (MET), $\not{E}_T$, and missing energy, $\not{E}$. These are defined as

$$\not{E}_T = \sqrt{\left(\sum_{\text{visible}} p_x\right)^2 + \left(\sum_{\text{visible}} p_y\right)^2}, \quad \not{E} = \sqrt{s} - \sum_{\text{visible}} E\,, \tag{3.12}$$

where the summations run over all detected objects. Since the definition of $\not{E}$ relies on the knowledge of the CM energy of the process, this observable is primarily applicable to lepton colliders, where $\sqrt{s}$ is well-defined. These observables exhibit distinctive signatures for DM, however, they also receive irreducible contributions from SM processes involving neutrinos in the final state. Consequently, efficient signal-background discrimination strategies are required, which will be discussed in detail in Chap. 6.

3.1.2 Physics at Lepton Colliders

Lepton colliders provide a clean and well-controlled environment for studying particle interactions. Leptons are elementary particles and do not possess any substructure, resulting in precisely known initial states with fixed CM energy, an advantage over hadron colliders. This allows for accurate reconstruction of events and access to kinematics not possible in hadronic collisions, thereby, enabling high precision study of the SM. The absence of PDF uncertainties in measurements simplifies theoretical predictions, making estimations more reliable. However, at higher CM energies, initial state radiation (ISR) effects are significant [195], though measurements remain more precise than at hadron colliders. As a result, lepton colliders are particularly well-suited for precision measurements of particle properties such as masses, couplings, and decay widths, and hence often referred to as *precision* machines. Another important advantage is the possibility of polarization of the initial state beams, which provides additional sensitivity to the certain chiral structure of interactions and enhances the ability to disentangle NP effects. Furthermore, the clean experimental environment, characterized by low QCD contamination and reduced pile-up, significantly improves signal identification and reduces systematics. However, unlike hadron colliders, which can access very high energies, lepton colliders are typically limited in their achievable CM energy, especially in the case of e^+e^- machines, due to significant synchrotron radiation losses, which scale as $\sim (E/m)^4$. In this context, muon colliders provide a promising alternative, as the much larger mass of the muon substantially suppresses such radiation losses. However, the realization of a muon collider remains an active area of research and is not yet an established project. Hence, the complementarity between hadron and lepton colliders provides an ideal setting for particle physics, combining discovery potential with precision measurements. In Tab. 3.1, we provide a comparison between hadron and lepton colliders, highlighting their respective advantages and differences. In the following section, we discuss beam polarization in detail, which will be a central theme in the subsequent chapters.

Initial State Beam Polarization Beam polarizability of initial states at a collider refers to the control over the spin orientation of the incoming lepton beams, which can be aligned either parallel or anti-parallel to their direction of motion, referred to as *longitudinal* polarization, or oriented perpendicular to it, referred to as *transverse* polarization. Beam polarization is a unique advantage of lepton colliders, as leptons are elementary

Feature	Hadron Colliders	Lepton Colliders
Beam particles	Protons (composite)	$e^{\pm}/\mu^{\pm}$ (elementary)
Initial state	Partonic (q/g with PDFs)	Well-defined, no substructure
Energy reach	Very high (up to 100 TeV)	Limited (especially for e^+e^-)
Environment	Messy (QCD, pile-up)	Clean (low background)
Precision	Moderate	Very precise
Reconstruction	Relatively difficult	Easier and more accurate
Discovery	Excellent for new resonances	Limited by energy
Radiation	Negligible	Significant for electrons
Polarization	Final state	Initial and final state

TABLE 3.1: Feature comparison between hadron colliders and lepton colliders.

particles and their spin states can be prepared and controlled with high precision. In contrast, while polarization of hadron beams is in principle possible, the composite nature of hadrons makes it significantly more challenging to achieve, maintain, and interpret in a clean manner. In practice, polarization is achieved at the source [196]. For electron beams, polarized electrons are produced using photoemission from specially prepared photocathodes illuminated by circularly polarized laser light, which transfers its helicity to the emitted electrons. These polarized beams are then accelerated while preserving their spin orientation using spin rotators and damping rings. For positrons, polarization can be generated through pair production using polarized photons. Muon beam polarization is more challenging compared to electrons due to the low retainability of polarization in case of muons. Typically, polarized muons are obtained from the decay of pions ($\pi^{\pm} \to \mu^{\pm}\nu$), where the weak interaction naturally produces highly polarized muons. However, preserving this polarization during acceleration and storage is non-trivial due to spin precession in magnetic fields and depolarization effects. Maintaining polarization of the beam during acceleration requires careful control of depolarizing effects such as synchrotron radiation and spin precession in presence of magnetic fields. The degree of polarizability is quantified by

$$P = \frac{N_R - N_L}{N_R + N_L}\,, \tag{3.13}$$

where, $N_{R,L}$ denote the number of RH and LH particles, respectively. From the physics perspective, beam polarization plays an important role in enhancing sensitivity to specific interactions. Since weak interactions are chiral in nature, adjusting the polarization allows selective enhancement or suppression of background processes. This significantly improves the extraction of NP parameters, helps disentangle different operator structures, and increases the overall precision. In addition, spin-polarization based asymmetries provide clean observables that are less sensitive to systematic uncertainties, making them powerful tools in precision extraction of NP effects in collider studies.

- **Longitudinal Polarization:** Such polarization is characterized by the alignment of the spins of the beam particles along or opposite to the direction of propagation. Longitudinal polarization enables the disentanglement of chiral structures by weighting the contributions from different chiral components of the interaction. The cross section in presence of longitudinal polarization is given as

$$\sigma\left(P_{e^+}, P_{e^-}\right) = \sum_{A=L,R} \sum_{B=L,R} \left(1 + \lambda_A P_{e^+}\right)\left(1 + \lambda_B P_{e^-}\right) \sigma_{AB}\,, \tag{3.14}$$

  where, $\lambda_R(\lambda_L) = +1(-1)$ are the helicities of the initial states, σ_{AB} are the cross sections corresponding to those helicities. By tuning P_{e^+} and P_{e^-}, certain chiral structures, particularly those arising from SMEFT operators, can be specifically enhanced. The implications of this will be discussed in detail in Chap. 5. The SM is predominantly a left-chiral theory, therefore, longitudinal polarization provides an additional advantage by enabling the possibility of suppression of SM backgrounds. This, in turn, enhances the sensitivity to NP scenarios that exhibit chiral structures different from those of the SM. One such example is the SM neutrino background, which constitutes a major background in DM searches via mono-X signatures. The neutrino pair production process, $e^+e^- \to \nu\overline{\nu}$, happens through two channels: an s-channel mediated by the Z boson and a t-channel mediated by the W boson. At high energies, the t-channel W-mediated contribution dominates and is purely left-chiral in nature. Consequently, an appropriate choice of beam polarization can significantly suppress this background. This effect is illustrated in Fig. 3.3. In the *left* panel, we show the variation of the ratio $(\sigma_{\text{polarized}}/\sigma_{\text{unpolarized}})$ as a function of the electron and positron beam polarizations. The suppression is maximized when the electron beam is predominantly right-handed (RH) and the

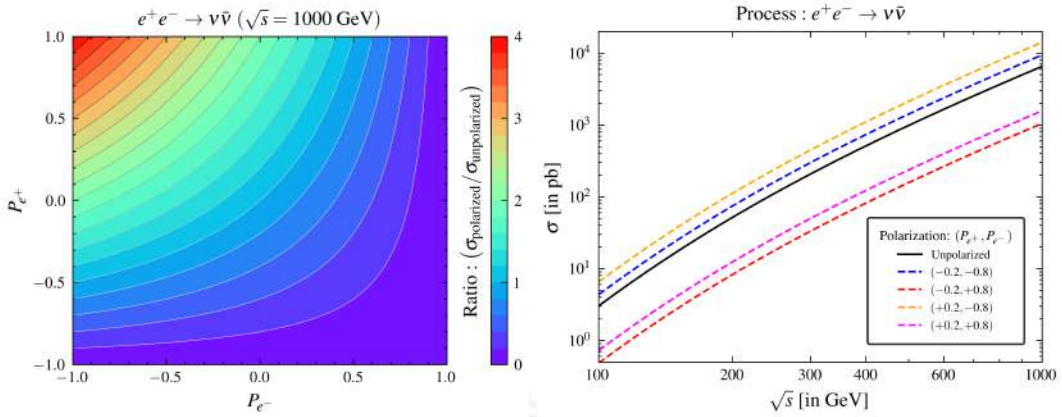

FIGURE 3.3: *Left*: Polarization dependence of $(\sigma_{\text{polarized}}/\sigma_{\text{unpolarized}})$ for $e^+e^- \to \nu\overline{\nu}$ production at the ILC $\sqrt{s}$ =1 TeV. *Right*: Cross section of $e^+e^- \to \nu\overline{\nu}$ as a function of CM energy for different polarization settings.

positron beam is predominantly left-handed (LH), while the opposite configuration enhances the cross section. Since complete polarization is not experimentally achievable, the *right* panel of Fig. 3.3 shows the variation of the total cross section for $e^+e^- \to \nu\overline{\nu}$ as a function of the CM energy for realistic polarization configurations projected for the International Linear Collider (ILC) [197]. As expected, due to the dominance of the t-channel contribution, the cross section increases with increasing CM energy, and the polarization combination $(P_{e^+}, P_{e^-}) = (-0.2, +0.8)$, yields maximum suppression.

- **Transverse Polarization:** Transverse polarization refers to the setup in which the spins of the beam particles are aligned perpendicular to the direction of the beam. Due to its transverse alignment, it introduces an additional directional degree of freedom in the transverse plane. In practice, transverse polarization is obtained by first producing longitudinally polarized beams, followed by using spin rotators to orient the spins into the perpendicular plane before collision. However, achieving and maintaining transverse polarization is experimentally challenging. In circular colliders, spin precession in magnetic fields, governed by the Thomas-BMT equation [198, 199], leads to continuous rotation of the spin direction, resulting in depolarization over time, rendering stable transverse polarization significantly more difficult to realize compared to longitudinal polarization. From a physics perspective, transverse polarization provides access to observables that are otherwise inaccessible, particularly those involving asymmetries in azimuthal plane. The presence of transverse polarization induces a dependence of the differential cross

section on the azimuthal angle (ϕ), which in context of an e^+e^- can be written in a general form as

$$\frac{d\sigma}{d\phi} = \frac{\sigma_0}{2\pi}\left[1 + P^T_{e^-}P^T_{e^+}\left(A\cos 2\phi + B\sin 2\phi\right)\right], \tag{3.15}$$

where, σ_0 is the unpolarized cross section. A, B encode the underlying dynamics of the interaction, and $P^T_{e^-}$, $P^T_{e^+}$ are the degree of transverse polarization of the electron and positron beams, respectively. The azimuthal dependence arises only in the presence of transverse polarization and vanishes otherwise. However, extracting the interaction dynamics requires a more refined treatment, as a full integration over ϕ eliminates the A and B dependent terms. Therefore, aptly defined angular integrations or weighted asymmetries must be employed to isolate these contributions. An asymmetry observable can then be constructed as

$$A_\phi = \frac{\int_0^\pi \frac{d\sigma}{d\phi}d\phi - \int_\pi^{2\pi}\frac{d\sigma}{d\phi}d\phi}{\int_0^{2\pi}\frac{d\sigma}{d\phi}d\phi} = \frac{2}{\pi}P^T_{e^-}P^T_{e^+}B\,. \tag{3.16}$$

This shows that the asymmetry is directly proportional to the product of transverse polarizations and isolates the $\sin 2\phi$ term. Such observables provide a clean probe of CP-violating effects as well as interference structures in context of both the SM and NP scenarios. More implications of this will be discussed in Sec. 4.3.

3.1.3 Particle Detection at Colliders

Particle detection at colliders has undergone remarkable evolution, closely following advances in both accelerator technology and improvement in our understanding of particle interactions. Early particle detectors date back to cloud chambers and bubble chambers, which provided visual evidences of charged particle trajectories, and enabled discoveries such as the positron [200]. However, their relatively slow data accumulation rates made them unsuitable for large luminosities. The transition to electronic detectors began with spark chambers and multi-wire proportional chambers (MWPCs), which enabled faster and more efficient event data recording. With the advent of colliders like the Super Proton Synchrotron (SPS) [201] and later the Tevatron [202], detector designs became more sophisticated. Experiments such as UA1 and UA2 at the SPS introduced the concept of large detectors, with nearly complete coverage of the detector solid angle, enabling full

event reconstruction and leading to the discovery of the W and Z bosons. The development of silicon-based tracking detectors marked a major milestone during the Large Electron Positron (LEP) collider [203] and Tevatron runs. Silicon trackers provided improved spatial resolution, allowing for the identification of secondary vertices from heavy flavor decays, which played essential role for top quark and B-physics studies. Similarly, calorimeters improved significantly, with the use of dense materials and fine segmentation enabling better energy measurements and particle identification. Modern detectors, such as ATLAS and CMS at the LHC, represent the culmination of these developments. They are designed with nearly 4π coverage, combining multiple subsystems to achieve precise tracking, calorimetry, and muon detection. Advanced trigger and data processing systems allow these detectors to handle the large event rates produced at the LHC. Fig. 3.4

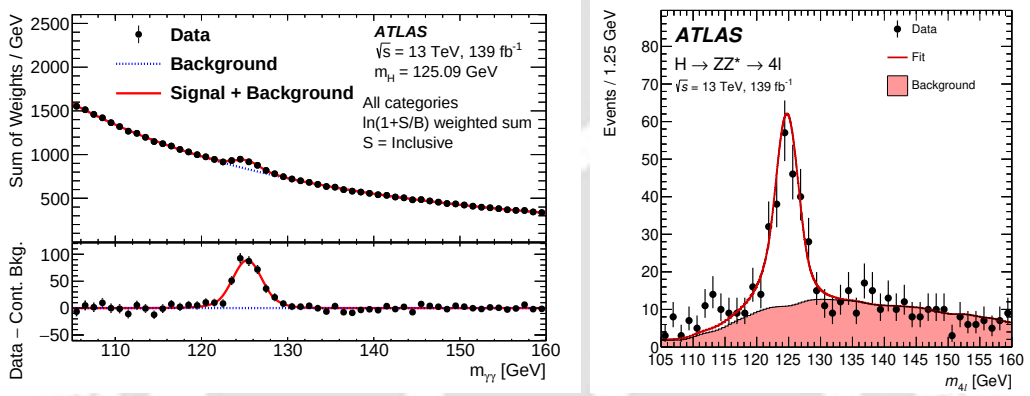

FIGURE 3.4: Higgs reconstruction from invariant mass of di-photon (*left*) and 4 lepton (*right*) events at the LHC 13 TeV 139 fb^{-1}

shows Higgs reconstruction from invariant mass of di-photon (*left*) [204] and 4 lepton (*right*) [205] events at the LHC 13 TeV 139 fb^{-1}. In the following sections, we discuss the physics at detectors, its architecture and strategy of reconstruction of objects.

Detector Physics and Design Particle detectors rely, primarily, on the interaction of particles with matter. Charged particles lose energy through ionization and excitation of detector material, and their trajectories can be tracked. Photons and electrons initiate electromagnetic showers in materials, while hadrons produce hadronic showers via strong interactions. Neutrinos escape detection, leading to energy imbalance in overall event, unraveled via missing energy signatures. By combining information from different subsectors of the detector, one can reconstruct the identity, and 4-momenta of the produced particles. A modern detector like the CMS is composed of several concentric layers, as

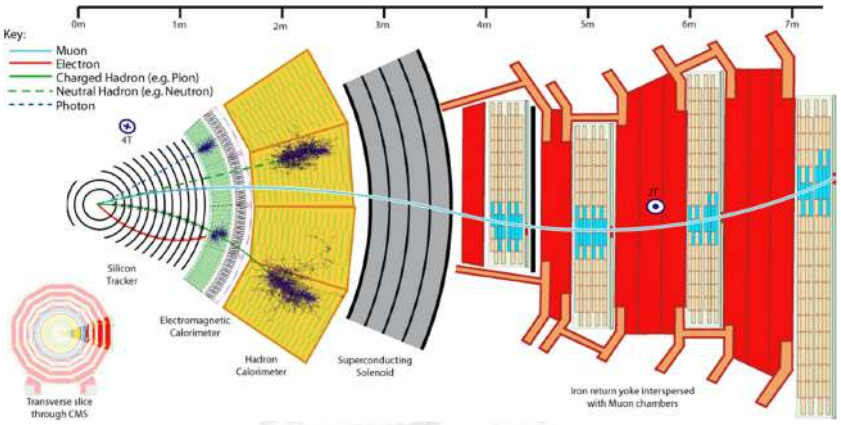

FIGURE 3.5: Transverse slice of the CMS detector displaying different layers, adapted from [3].

illustrated in Fig. 3.5, each optimized for specific measurements:

- **Silicon Tracker:** The innermost component of the detector system consists of silicon pixels and strip detectors, designed to precisely measure the trajectories of charged particles. It operates within a strong magnetic field, allowing momentum reconstruction by measuring the curvature of tracks. It also provides excellent vertex resolution, crucial for identifying displaced and secondary vertices.

- **Electromagnetic Calorimeter (ECAL):** Surrounding the silicon tracker, the ECAL measures the energy of electrons and photons. It is typically made of dense materials, such as lead tungstate crystals in case of CMS, where these particles initiate electromagnetic showers. Incident particle energy is reconstructed using the total deposited energy in the ECAL.

- **Hadronic Calorimeter (HCAL):** Located outside the ECAL, the HCAL measures the energy of hadrons such as pions and protons. It consists of alternating layers of absorber and active material, aimed to capture hadronic showers. Together with the ECAL, it provides a complete measurement of visible energy.

- **Superconducting Solenoid:** Beyond the HCAL, CMS features a large solenoidal magnet that generates a strong magnetic field ($\sim$ 3.8 T), strongly bending the trajectories of charged particles. This enables momentum determination and charge identification with enhanced precision.

- **Muon Chamber:** The outermost layer of the CMS detector consists of gas-ionization detectors embedded in the iron return yoke. Since muons are highly

penetrating, they traverse the inner detector and calorimeters with minimal energy loss, making them identifiable, primarily, in this outer system.

The combination of these subsystems allows for efficient particle identification. Future upgrades of collider detectors aim to cope with higher luminosities and increased event complexities. For instance, future upgrades of the LHC [206] as well as future colliders [207, 208], will feature upgraded tracking systems with improved granularity, enhanced calorimetry for better energy resolution, and improved trigger and data acquisition systems. Further, precision timing detectors are also being introduced to mitigate beam remanent pile-up. These advancements will significantly improve the sensitivity to both SM as well as NP effects.

Detection of Objects In this section, we focus on the reconstruction of the key visible objects at colliders, detailing on trigger strategies, energy resolution, and identification efficiencies. We emphasize how these objects are defined and utilized in analyses.

- **Detection of Photons:** Photons are reconstructed as localized energy deposits in the ECAL without any associated charged tracks. Trigger strategies usually rely on high transverse momentum (p_T) photon candidates, often combined with isolation requirements to suppress backgrounds from neutral hadron decays. In modern detectors, the energy resolution of photons is typically at the level of $\sim$ 1-2% at high energies, while identification efficiencies are usually $> 80\%$, varying from detector-to-detector. Isolation of photon is usually done based on the absence of significant additional energy in a cone around the photon, significantly reducing QCD backgrounds.

- **Detection of Electrons:** Electrons are identified through a combination of charged particle tracks in the inner detector and corresponding energy deposits in the electromagnetic calorimeter. An important feature of this reconstruction is the matching between the track momentum and calorimetric energy deposit. Electron triggers are based on p_T thresholds along with identification and isolation requirements. The energy resolution is comparable to that of photons, while the average identification efficiencies are typically in the range of 70-90%. Bremsstrahlung effects in the tracker can affect the energy measurement of electrons and are taken into account in reconstruction algorithms.

- **Detection of Muons:** Muons are reconstructed using tracks in both the inner detector and the outer muon chamber. Muon triggers are very robust, with relatively low background contamination, and are typically based on p_T thresholds. As muons penetrate without depositing much energy in calorimeters, only momentum resolution is relevant, and depends on the combined performance of the tracker and muon chambers. It is typically at the percent level for a wide momentum range. Identification efficiencies for muons are generally high i.e. $> 90\%$, making them extremely clean probes in collider analyses.

- **Detection of Jets:** Jets arise from the hadronization of quarks and gluons produced in the final states. Since partons cannot be observed directly due to QCD confinement, they manifest as collimated sprays of hadrons. Jets are reconstructed using clustering algorithms, which group nearby energy deposits and tracks into a single object characterized by a jet radius parameter R. One such algorithm is the anti-k_T algorithm [209], which is a sequential recombination clustering algorithm defined through the following distance measures (between objects α and β):

$$d_{\alpha\beta} = \left[\min\left(\frac{1}{p_{T,\alpha}^2}, \frac{1}{p_{T,\beta}^2}\right)\frac{\Delta R_{\alpha\beta}^2}{R^2}\right], \qquad d_{\alpha B} = \left[\frac{1}{p_{T,\alpha}^2}\right], \tag{3.17}$$

  where $\Delta R_{\alpha\beta}^2 = (\eta_\alpha - \eta_\beta)^2 + (\phi_\alpha - \phi_\beta)^2$ and R is the jet radius parameter. The algorithm proceeds iteratively throught the following steps: (**I**) Compute all $d_{\alpha\beta}$ and $d_{\alpha B}$. (**II**) Find $\min\{d_{\alpha\beta}, d_{\alpha B}\}$. (**III**) If $\min = d_{\alpha\beta}$, recombine $\alpha, \beta \to k$ with $p_k^\mu = p_\alpha^\mu + p_\beta^\mu$. (**IV**) If $\min = d_{\alpha B}$, declare object α a jet and remove it from the list. This procedure is repeated until no particles remain. In addition, algorithms are also constructed for tagging heavy quark jets i.e. c and b jets [210], primarily based on the multiplicities of constituents of jets. The energy resolution of jets is generally poorer than that of leptons or photons, typically $\sim 10\%$ at high energies, and is dependent on detector calibration and pile-up conditions.

The summary of object reconstruction and detector performance is shown as a schematic diagram in Fig. 3.6.

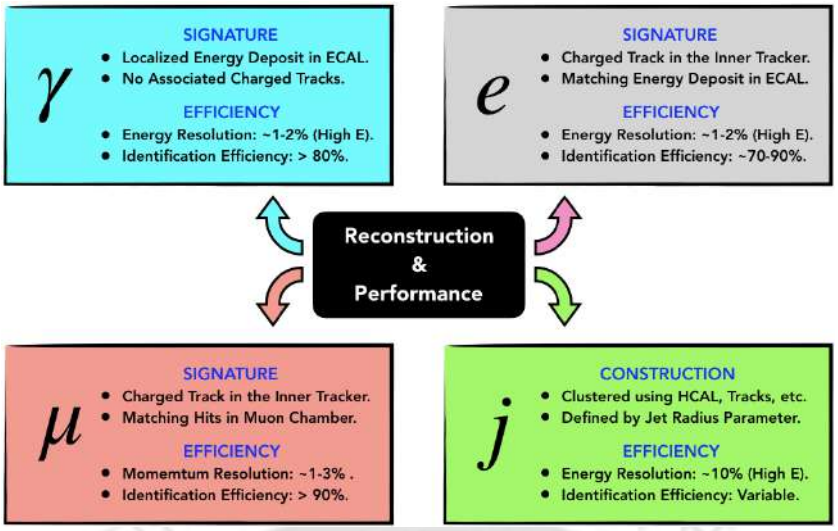

FIGURE 3.6: Schematic diagram showing object reconstruction and detector performance information for photons, electrons, muons, and jets.

3.2 Future Hadron and Lepton Colliders

Collider experiments has played a central role in shaping our understanding of fundamental physics. Early hadron colliders, such as the Super Proton Synchrotron (SPS) [201] at CERN, marked a significant milestone by enabling $p\bar{p}$ collisions at high energies, leading to the discovery of the W and Z bosons. This was followed by the Tevatron at Fermilab, which operated at CM energy of upto 1 TeV and facilitated the discovery of the top quark [24]. In parallel, lepton colliders provided a complementary avenue for precision measurements. The Large Electron Positron (LEP) [203] collider at CERN enabled precision studies of the electroweak sector, including measurements of the Z pole properties and constraints on the Higgs boson mass prior to its discovery. The LHC, operating at CM energies of up to 13.6 TeV, represents the current frontier of high-energy colliders, with the discovery of the Higgs boson, being its most notable achievement. Despite its successes, the absence of direct evidence of NP at the LHC motivates the need for future collider experiments with improved capabilities. In this context, several proposals for next-generation collider experiments are under active consideration. These include upgrades to existing facilities, such as the HL-LHC, as well as future hadron and lepton colliders. Each of these aim to explore specific regions of parameter space, reflecting the complementarity between energy frontier and precision frontier approaches. In addition to experimental developments, collider studies relies heavily on realistic simulations to model signal and background processes, as well as detector effects. These tools enable

precise predictions and are essential for interpreting experimental data in the context of theoretical models. A detailed description of the simulation framework used in this work is provided in the App. 3.A. In the following sections, we briefly outline the key features of these future collider projects.

Future Hadron Colliders Due to the stability of protons, they can be densely bunched, and their large mass leads to negligible synchrotron radiation losses. As a result, hadron colliders can achieve very high CM energies and accumulate large luminosities, which constitute the primary objectives of future hadron collider programs. Such high energies provide access to potential multi-TeV resonances predicted in many extensions of the SM. We discuss some of the proposed hadron colliders below.

- **High Luminosity LHC (HL-LHC):** The HL-LHC [206] is a future upgrade of the LHC, designed to operate at a CM energy of $\sqrt{s} = 14$ TeV, aiming for a total integrated luminosity of $\sim 3\,\text{ab}^{-1}$. It will utilize the existing $\sim$ 27 km tunnel at CERN, with operations expected to begin around 2030. The primary goal is precision measurements of the Higgs boson couplings [211], in particular the Higgs self-coupling [212], which remains poorly constrained at current LHC runs. In addition, the HL-LHC aims to study several rare SM processes, and perform indirect searches for NP. Key upgrades include improved inner tracking systems, enhanced trigger capabilities, and precision timing detectors to mitigate high pile-up conditions.

- **Super Proton-Proton Collider (SppC):** The SppC [213] is a proposed hadron collider in China, designed to reach CM energies of $\sqrt{s} \sim$ 70-100 TeV. Projection studies for the SppC have considered an integrated luminosity reach of $\sim$ 3–30 ab^{-1}. It is planned to be housed in a $\sim$ 100 km circular tunnel. The project is expected to succeed to the e^+e^- run at the CEPC, whose possible operation expected in the 2040s. Its physics goals include direct searches for heavy NP states at the multi-TeV scale as well as precision SM measurements.

- **Future Circular Collider (FCC-hh):** The FCC-hh [214] is a proposed pp collider at CERN with a planned CM energy of $\sqrt{s} = 100$ TeV and a target integrated luminosity reach of $\sim 30\,\text{ab}^{-1}$. It is expected to be preceeded by an e^+e^- collider (FCC-ee) running in the same tunnel. It would be constructed in a new $\sim$ 100 km

tunnel around the Geneva region, with a expected start of operation in the 2040s for the e^+e^- stage. The FCC-hh aims to significantly extend the discovery reach for multi-TeV NP, probe Higgs self-coupling with high precision, and explore rare SM processes.

Future e^+e^- Colliders (Linear) Electron-positron colliders provide a clean experimental environment, enabling precision measurements of SM and NP parameters. Linear e^+e^- colliders, in particular, offer superior control over the initial state, with reduced ISR effects and improved preservation of polarized beams compared to circular machines. However, their linear configuration limits the achievable CM energy due to practical constraints on accelerator length. We discuss some of the proposed linear colliders below.

- **International Linear Collider (ILC):** The ILC [77, 197, 215–219] is a proposed linear e^+e^- collider based on superconducting radio-frequency (SCRF) cavity technology. It is proposed to operate at a CM energy of $\sqrt{s} = 250$ GeV, with upgrade options to 500 GeV, and finally, 1 TeV. The ILC projects a integrated luminosity reach of $\sim$ 2-8 ab^{-1}, over different stages. The accelerator would extend over a length of $\sim$ 20 km at the 250 GeV stage, increasing to $\sim$ 31 km for 500 GeV. The timeline for operation depends on approval, with optimistic projections suggesting early-to-mid 2040s. The ILC primarily aims to serve as a Higgs factory, enabling extremely precise measurements of Higgs couplings, as well as detailed studies of the top and electroweak sector. A key advantage of the ILC is the use of polarized beams, achieving beam polarization of $\sim \pm 80\%$ for electron beam, and $\sim \pm 20$-$\pm 30\%$ for positron beam, depending on the CM energy.

- **Compact Linear Collider (CLiC):** The CLiC [77, 220, 221] is a proposed multi-TeV linear e^+e^- collider under development at CERN. In contrast to the ILC, CLIC employs a novel two-beam acceleration scheme using normal-conducting radio-frequency structures, achieving very high accelerating gradients. This enables a more compact design while reaching significantly higher energies. CLiC is planned to be implemented in stages, with CM energies of 380 GeV, 1.5 TeV, and 3 TeV, with a target integrated luminosity reach of $\sim$ 1-5 ab^{-1}. The corresponding machine lengths are approximately 11 km, 29 km, and 50 km, respectively, for the

three different stages, with expected operation around 2040s. The CLiC would allow both precision measurements and direct searches for NP at the energy frontier. The initial stage focuses on top pair threshold physics, while the higher energy stages extend sensitivity to BSM phenomena. Furthermore, CLIC is designed to provide electron beam polarization of approximately ±80%, whereas positron beam polarization is not currently envisaged. The high energy reach and staged approach make CLIC complementary to the ILC, albeit with more challenging beam conditions due to ISR and other beam-induced backgrounds (BIBs).

Future Lepton Colliders (Circular) Circular electron-positron colliders offer advantages in terms of high luminosity operation and the potential for future upgrades within the same infrastructure, such as transitions to electron-proton or proton-proton collision modes. However, they face limitations in achieving and maintaining high beam polarization and are more significantly affected by radiative effects, particularly synchrotron radiation, limiting the CM energy reach for electrons. In the following, we briefly discuss some of the proposed circular e^+e^- collider facilities.

- **Future Circular Collider (FCC-ee):** The FCC-ee [222] is a proposed high luminosity circular e^+e^- collider at CERN, designed as the first stage of the broader FCC program. It plans to operate at multiple CM energies, viz. the Z pole ($\sqrt{s} \approx 91$ GeV, with integrated luminosity up to ~ 150 ab^{-1}), WW threshold (~ 160 GeV, ~ 10 ab^{-1}), Higgs factory stage ($\sim$ 240-250 GeV, $\sim$ 5–10 ab^{-1}), and top-pair threshold (~ 365 GeV, ~ 1.5 ab^{-1}). The primary physics goals include ultra-precise measurements of the Z pole observables, along with threshold W, Higgs and top production cross section measurements, with sensitivities reaching unprecedented levels.

- **Circular Electron Positron Collider (CEPC):** The CEPC [213] is a proposed circular e^+e^- collider in China, primarily designed as a Higgs factory. It is expected to operate at $\sqrt{s} \sim 240$ GeV with an integrated luminosity of $\sim$ 5-6 ab^{-1}, along with a Z-pole run at $\sqrt{s} \sim 90$ GeV, with up to $\sim$ 10–20 ab^{-1}. The CEPC will preceed the SppC in the same ring. The physics program focuses primarily on precision Higgs measurements, and electroweak observables at the Z pole. A key feature of CEPC is its role as a cost-optimized Higgs factory with upgrade potential

to a hadron collider in the same infrastructure, a model which is also followed by the FCC program.

Future Muon Colliders Future muon colliders [223–225] represent a novel class of lepton colliders, exploiting the large muon mass to suppress synchrotron radiation and enable circular or compact configurations than can access very high energies. Proposed designs span CM energies from ~ 3 TeV up to $\sim$ 10-14 TeV or beyond, with projected integrated luminosities ranging from ~ 1 to 10 ab^{-1} depending on the stage. In addition, novel proposals such as the μTRISTAN [226] project envisage both asymmetric μ^+e^- and symmetric $\mu^+\mu^+$ collision stages, with CM energy reaches of approximately 346 GeV and 2 TeV, respectively, in their initial runs. Owing to the exotic nature of the initial states, these configurations benefit from significantly reduced SM contamination, thereby offering enhanced sensitivity to specific new physics scenarios. Further details on the μ^+e^- stage are discussed in Sec. 5.2. The collider rings of muon colliders are expected to be significantly smaller than electron machines at comparable energies, with typical radii of a few kilometers. The physics goals include both Higgs studies, including direct s-channel Higgs production at lower energies, and exploration of the energy frontier at multi-TeV scales, with strong sensitivity to heavy NP resonances. A unique feature of muon colliders is their ability to combine the clean environment of a lepton collider with energy reach ike hadron colliders. However, they face significant technological challenges, particularly in muon production, cooling, and handling of BIBs from muon decays. All proposed future collider scenarios are summarized in Tab. 3.2.

3.3 Statistical Inference in Collider Physics

The interpretation of data of nature is inherently statistical in nature, with collider data being no exception. Experiments are subject to finite resolution of detectability, limited statistic, and unfolding effects, making it impossible to directly infer underlying physical laws from raw measurements alone. As a result, statistical methods play a central role in both discoveries and precision studies at colliders. In a strict sense, any observed feature that is not statistically significant cannot be reliably associated with an underlying physical phenomenon. Historically, several signals of new resonances or deviations from the SM predictions have emerged at colliders, only to diminish with the accumulation of

Collider	CM Energy, $\sqrt{s}$	Luminosity, $\mathfrak{L}_{\text{int}}$
Future Hadron Colliders		
HL-LHC	14 TeV	3 ab^{-1}
SppC	70-100 TeV	3-30 ab^{-1}
FCC-hh	100 TeV	30 ab^{-1}
Future e^+e^- Colliders (Linear)		
ILC	250, 500 GeV, 1 TeV	2-8 ab^{-1}
CLiC	380 GeV, 1.5, 3 TeV	1-5 ab^{-1}
Future e^+e^- Colliders (Circular)		
CEPC	240 GeV	5-6 ab^{-1}
FCC-ee	91, 160, 240, 365 GeV	1.5-150 ab^{-1}
Future Muon Colliders		
$\mu^+\mu^-$	3-10 TeV	1-10 ab^{-1}
μ^+e^-	$\sim 346, 775$ GeV	1 ab^{-1}
$\mu^+\mu^+$	$\sim 2, 6$ TeV	1 ab^{-1}

TABLE 3.2: Summary of future collider experiments with representative center-of-mass energies and projected integrated luminosities.

more data. A notable example is the transient excess around 750 GeV in the diphoton channel reported at the early Run-II of the LHC, which initially generated significant interest in the community, but was later understood to be a statistical fluctuation [227–229]. Similarly, a number of long-standing anomalies in flavor physics, such as deviations in B-meson decay observables [50], have persisted over time but have not yet reached a statistical significance sufficient enough to be established as a direct implication of BSM physics. These illustrate that statistical significance is the criterion that elevates an observation from a mere fluctuation to an evidence of NP. In collider physics, this is typically quantified in the context of signal (S) and background (B) event counts. In context NP searches, a signal hypothesis corresponds to the presence of NP contributions, while the background generally represents known SM processes that can mimic the same final state. A commonly used measure are the ratios Z_1 and Z_2, referred to as

Signal Significance [9], as defined as

$$Z_1 = \frac{S}{\sqrt{B}}\,, \qquad Z_2 = \frac{S}{\sqrt{S+B}}\,. \tag{3.18}$$

Z_1 provides an estimate of how the signal count overrides above statistical uncertainty of the background count under the assumption of Poisson statistics. Z_2 is a more refined version which account for both signal and background uncertainties. A furthermore refined version is

$$Z_3 = \sqrt{2\left[(S+B)\ln\left(1+\frac{S}{B}\right) - S\right]}\,. \tag{3.19}$$

In the regime of large B, the definitions are equivalent, i.e. $Z \approx Z_1 \approx Z_2 \approx Z_3$. In practice, a significance of $Z \approx 5$, referred to a 5σ deviation, is required to claim a discovery, while $Z \approx$ 2-3 may indicate tension with the SM. However, precise constraints on NP scenarios at collider experiments, as well as in phenomenological studies, require more sophisticated statistical techniques. In the following sections, we discuss some statistical techniques employed in studies to estimate limits on NP and extract BSM parameters from collider data.

Method of Maximum Likelihood The method of maximum likelihood or the log-likelihood method [9] provides a framework for parameter estimation based on the probability of observing events given a model. Let $\{x_i\}$ denote a set of independent observations drawn from a probability density function (pdf) $f(x;\boldsymbol{\theta})$, where $\boldsymbol{\theta}$ represents the set of model parameters. The likelihood function is defined as

$$\mathscr{L}(\boldsymbol{\theta}) = \prod_{i=1}^{N} f(x_i;\boldsymbol{\theta})\,. \tag{3.20}$$

It is often convenient to work with the log-likelihood,

$$\ln\mathscr{L}(\boldsymbol{\theta}) = \sum_{i=1}^{N} \ln f(x_i;\boldsymbol{\theta})\,. \tag{3.21}$$

The maximum likelihood estimator (MLE), $\hat{\boldsymbol{\theta}}$, is obtained by maximizing $\ln\mathscr{L}(\boldsymbol{\theta})$,

$$\left.\frac{\partial \ln\mathcal{L}}{\partial\boldsymbol{\theta}}\right|_{\boldsymbol{\theta}=\hat{\boldsymbol{\theta}}} = 0\,. \tag{3.22}$$

For counting experiments, where the number of observed events n follows a Poisson distribution with the expected count being $\mu(\boldsymbol{\theta}) = S(\boldsymbol{\theta}) + B$, the likelihood takes the form

$$\mathscr{L}(\boldsymbol{\theta}) = \frac{\mu(\boldsymbol{\theta})^n e^{-\mu(\boldsymbol{\theta})}}{n!} \,. \tag{3.23}$$

In practice, inference is often performed using the profile likelihood ratio,

$$\lambda(\boldsymbol{\theta}) = \frac{\mathscr{L}(\boldsymbol{\theta})}{\mathscr{L}(\hat{\boldsymbol{\theta}})} \,. \tag{3.24}$$

The test statistic is defined as

$$q(\boldsymbol{\theta}) = -2 \ln \lambda(\boldsymbol{\theta}) \,, \tag{3.25}$$

is asymptotically distributed as a χ^2 distribution under Wilks' theorem [230], providing a connection to confidence intervals and hypothesis testing.

Method of Least Squares The method of least squares or the χ^2 method [9] is another widely used technique for parameter estimation when measurements are approximately Gaussian distributed. Consider a set of N measurements $\{y_i\}$ with corresponding theoretical predictions $\{\mu_i(\boldsymbol{\theta})\}$ and uncertainties (standard deviations) $\{\sigma_i\}$. The goodness of fit is quantified through the χ^2 function,

$$\chi^2(\boldsymbol{\theta}) = \sum_{i=1}^{N} \frac{(y_i - \mu_i(\boldsymbol{\theta}))^2}{\sigma_i^2} \,, \tag{3.26}$$

and, the best-fit parameters $\hat{\boldsymbol{\theta}}$ are obtained by minimizing χ^2 with respect to the model parameters,

$$\left. \frac{\partial \chi^2}{\partial \boldsymbol{\theta}} \right|_{\boldsymbol{\theta}=\hat{\boldsymbol{\theta}}} = 0 \,. \tag{3.27}$$

In the presence of correlated uncertainties, the χ^2 function generalizes to

$$\chi^2(\boldsymbol{\theta}) = \sum_{i,j=1}^{N} (y_i - \mu_i(\boldsymbol{\theta}))\, (V^{-1})_{ij}\, (y_j - \mu_j(\boldsymbol{\theta})) \,, \tag{3.28}$$

where, V is the covariance matrix. The covariance matrix V encodes both the variances and correlations among the measured observables, and is defined as

$$V_{ij} = \mathrm{Cov}(y_i, y_j) = \langle (y_i - \langle y_i \rangle)(y_j - \langle y_j \rangle) \rangle \,. \tag{3.29}$$

In particular, the diagonal elements correspond to the variances, $V_{ii} = \sigma_i^2$, while the off-diagonal elements describe correlations between different observables. It is often convenient to express the covariance matrix in terms of the correlation matrix ρ_{ij}, $V_{ij} = \rho_{ij}\,\sigma_i\sigma_j$, where $\rho_{ij} \in [-1, 1]$ and $\rho_{ii} = 1$. Under the Gaussian assumption, the least-squares method is equivalent to the maximum likelihood method. The minimum value χ^2_{min} provides a measure of goodness of fit, and for a correct model, it follows a χ^2 distribution with $(N - M)$ DOFs, where N is the number of independent measurements, say bins of a distribution and M is the number of fitted parameters. Confidence intervals on $\boldsymbol{\theta}$ can be obtained from contours of constant $\Delta\chi^2 = \chi^2 - \chi^2_{\mathrm{min}}$.

Optimal Observable Technique The Optimal Observable Technique (OOT) [231, 232] provides a statistically optimal model to estimate parameters from differential observables, and is particularly useful in scenarios probing small deviations from the SM. We consider a general scenario in which the SM is extended by NP contributions, such that the theoretical differential cross section can be expressed as

$$\mathcal{O}(\phi) \equiv \frac{d\sigma_{\mathrm{T}}}{d\phi} = \sum_i c_i f_i(\phi) \,, \tag{3.30}$$

where, ϕ denotes the relevant phase space variables, $f_i(\phi)$ are linearly independent functions dependent on ϕ, and the coefficients c_i encode the underlying NP parameters, say WCs. Our objective is to determine the coefficients c_i with maximal statistical precision. Assuming a constant event rate over a period of collider run, the total number of events N is

$$N = \sigma_{\mathrm{T}}\, \mathfrak{L}_{\mathrm{int}}, \qquad \text{where,} \qquad \sigma_{\mathrm{T}} = \int \mathcal{O}(\phi)\, d\phi \,, \tag{3.31}$$

The optimal covariance matrix for the parameters c_i is given by

$$V_{ij} = \frac{1}{\mathcal{L}_{\mathrm{int}}} (M^{-1})_{ij} \,, \qquad \text{where,} \qquad M_{ij} = \int \frac{f_i(\phi)\, f_j(\phi)}{\mathcal{O}(\phi)}\, d\phi \,. \tag{3.32}$$

This demonstrates that the achievable precision is governed by the integrated luminosity and the functional dependence of the differential cross section. The covariance matrix V_{ij} determines the correlations among the coefficients c_i. Considering, "seed" values c_i^0 around which the deviations are studied, one can construct the χ^2 function,

$$\chi^2 = \epsilon \sum_{i,j} (c_i - c_i^0)\,(V_0^{-1})_{ij}\,(c_j - c_j^0)\,, \tag{3.33}$$

where, V_0 denotes the covariance matrix evaluated at $c_i = c_i^0$, and ϵ represents an overall efficiency factor accounting for detector and selection effects. The OOT is optimal in the sense that it saturates the Cramer-Rao bound [9], providing the smallest possible statistical uncertainties for unbiased estimators of the parameters c_i. It is therefore widely used in precision studies and in constraining EFT coefficients at collider experiments.

Appendix: Collider Phenomenology

3.A Collider Simulation Framework

Collider simulations play a crucial role in the study of NP. Since analytical cross section based estimates are often insufficient to capture the full complexity of collider environments, simulation tools are employed to model the entire chain of processes from the underlying model all the way upto experimental observables. These frameworks enable the generation of realistic-like event samples, incorporating both field theory inputs as well as detector effects, and are indispensable for estimating sensitivities of NP scenarios. A typical collider analysis proceeds through several well-defined stages:

- **Model Implementation:** The first step involves implementing the model, which is primarily generating the Feynman rules associated with all the interaction vertices. Useful tools in this respect is `FeynRules` [233], which extracts Feynman rules from user-defined Lagrangian and field contents, and outputs as Universal FeynRules Output (`UFO`) [234] model files.

- **Matrix Element Generators:** Matrix element generators calculate parton-level cross sections and generate Monte Carlo events based on the imported `UFO` model. These simulations provide the kinematic distributions of final state particles before

radiative and hadronization effects are included. One popular software in this respect is `MG5_aMC` [235].

- **Parton Shower:** The outgoing partons from the hard process undergo QCD radiation, modeled through parton shower algorithms. This stage simulates the emission of soft and collinear radiations, effectively resumming large logarithmic corrections and producing realistic jet structures. This is primarily done using `Pythia8` [236].

- **Detector Effects:** The particles produced after shower are passed through a detector simulation, which models the response of a real detector. This includes effects such as finite resolution, object reconstruction, particle identification, and acceptance cuts, thereby bridging the gap between theory and experiment. `Delphes3` [237] handles detector simulation, with `FastJet3` [238] dedicatedly performing jet constructions.

- **Statistical Analysis:** Finally, simulated signal and background events are analyzed using statistical methods to extract physical information. This includes constructing observables, applying selection criteria, and placing constraints on model parameters. The `ROOT` [239] framework provides an integrated environment for such analysis.

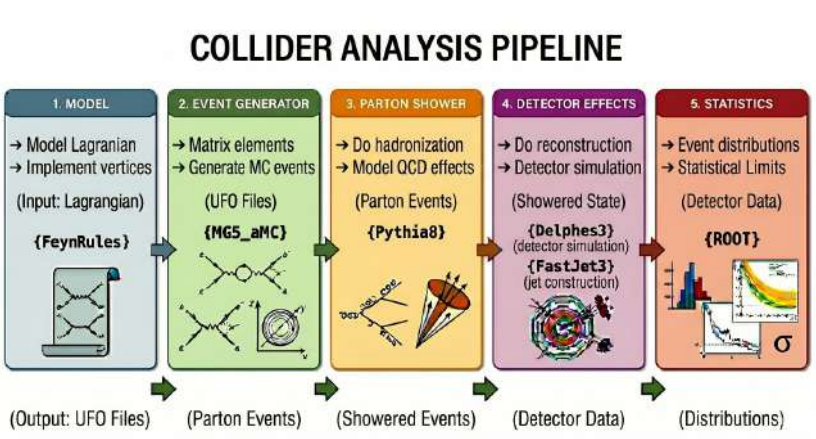

FIGURE 3.7: Schematic diagram showing the entire collider analysis pipeline, from model implementation to statistical analysis.

The schematic diagram of the pipeline is shown in Fig. 3.7. This extended pipeline ensures that theoretical predictions can be robustly compared with data, allowing for reliable interpretation of potential deviations from the SM.

Chapter 4

Application to Higgs Physics

"There is another world, but it is in this one."
Paul Éluard

Contents

Since the discovery of the Higgs boson, particle physicists have devoted significant effort to the precise scrutiny of its properties. While current measurements show remarkable agreement with SM predictions, the Higgs sector remains one of the most promising portals for uncovering BSM physics. In particular, precise measurements of the Higgs interactions with electroweak gauge bosons, W and Z, as well as the photon, are of paramount importance. Any deviation from SM expectations could indicate the presence of higher scale physics, potentially shedding light on fundamental open questions such as the naturalness of the electroweak scale, the origin of CP violation, and the structure of the Higgs vacuum.

Among the various Higgs production mechanisms, although gluon-gluon fusion (ggF) yields the largest cross section at the LHC, sub-leading processes such as vector boson fusion (VBF) and associated production (Higgs-strahlung) offer enhanced sensitivity to NP in the electroweak sector, owing to their direct dependence on Higgs-gauge couplings. An additional advantage of these channels is their relevance at both hadron and lepton

colliders. At lepton colliders, Higgs-strahlung dominates at lower CM energies, while VBF becomes increasingly important at higher energies. This complementarity across different collider environments enables a more comprehensive and robust probe of possible deviations from the SM.

This chapter comprehensively investigates the application of the SMEFT framework to anomalous Higgs-gauge boson couplings across future hadron and lepton collider environments. Sec. 4.1 begins by exploring these couplings at the HL-LHC, utilizing the Zh associated production mode to constrain Higgs-gauge coupling modifiers while highlighting the distinct impacts of Higgs-current and dipole contact operators. Transitioning to the precision-oriented environment of future lepton colliders, Sec. 4.2 evaluates the optimal extraction of the hVV couplings at an e^+e^- Higgs factory, demonstrating how the use of polarized beams can maximize the statistical sensitivity of the EFT parameters. Finally, Sec. 4.3 delves into the CP-violating structures of the Higgs-gauge interactions, employing spin correlation asymmetries across multiple Higgs decay channels to effectively isolate and constrain CP-odd SMEFT interactions that otherwise remain elusive in standard total cross section based approaches.

4.1 Higgs-Gauge Boson Couplings at the HL-LHC

Higgs couplings in SMEFT via Zh production at the HL-LHC.
S. Bhattacharya, S. Biswas, A. Sarkar.
Phys.Rev.D 111 (2025) 11, 11 (e-Print: 2403.03001 [hep-ph])..

While many of the Higgs boson's properties closely mimic that of a SM-like isodoublet [240], precision measurements allow for robust NP studies via the Higgs sector. One standard way of parametrizing the Higgs couplings beyond the SM is to use the κ framework [241], where any deviation from the SM is taken into consideration by variation of the κ parameter, where $\kappa = 1$ depicts SM. For example, concerning the hZZ coupling, the corresponding $\kappa_Z = \left(g_{hZZ}/g_{hZZ}^{SM}\right)$. Most of the Higgs studies at the LHC uses such parametrisation and so do we. However, one needs to be vigilant about the possible sources of NP that generates such contributions and need to be consistent with null observation of NP searches while scanning the possible values that κ can acquire[1].

[1]We will address this issue later in a specific context.

Over the last two runs, LHC experiments, ATLAS [6] and CMS [7] have almost pinned down the Higgs couplings to less than 10% uncertainty, however, the HL-LHC run will prove to be significant for establishing a clearer picture of Higgs characteristics. The Higgs couplings associated with gauge bosons have been studied extensively in the existing literature from various point of views. They include bounds on the anomalous couplings [242–246], Higgs CP properties [247–251], etc. The procedure involves dedicated signal observables as well as in the EFT framework [252–266] in variety of production and decay channels in context of the current and future colliders.

In this analysis, we study the NP effects in hZZ and qqZ couplings as well as the fully NP induced $qqZh$ coupling in the Zh associated production mode at the HL-LHC frontier. We adhere to the κ framework to depict NP contribution coming to hZZ coupling, whereas the NP contributions to qqZ and $qqZh$ are studied within the realm of SMEFT [150]. We would also like to note here, that while the contributions to $\kappa_Z \neq 1$ may very well appear from the SMEFT operators, however, there are restrictions like Z mass corrections, which may constrain such contributions. Therefore, parametrising the hZZ coupling via κ_Z makes us explore possibilities even beyond SMEFT. In short, by using both κ framework and SMEFT, we are basically taking the leading contributions to the relevant couplings that affect the chosen process.

Out of the different channels of Higgs production, the Vh ($V = W, Z$) production cross-section turn out to be more sensitive to the variation of effective operators concerned in the modification of the aforementioned couplings. In this analysis, we study the Zh channel. There have been a number of analysis concerning the Wh/Zh production modes [253–259]. However, the effect of dipole contact operators in context of the $qqZ/qqZh$ couplings have been neglected. The effect of dipole operators have been studied in [267], but concerning the Wh mode only. We show that the presence of both Higgs-current as well as dipole contact operators appreciably alter the existing bounds on the concerned couplings at the present and projected LHC sensitivities.

The organization of the section is as follows: we discuss SMEFT operators relevant for our analysis and their sensitivities in Sec. 4.1.1, constraints on the coupling modifiers as well as SMEFT coefficients from current data in Sec. 4.1.2, detailed collider analysis in Sec. 4.1.3 and concluding remarks in Sec. 4.1.4.

4.1.1 EFT Framework and Relevant Operators

The couplings of primary interest for this chapter are the $qqZ/qqZh$ and hZZ vertices which appear in both VBF as well as Zh production modes of the Higgs boson. The set of interaction terms involve those connecting to the gauge fields, field strength tensor (or the dual of it) along with the Higgs field and quark bilinear with all possible Lorentz structure, adhering to $U(1)_{\rm EM}$ gauge symmetry after EWSB, as furnished below.

$$\mathcal{L}_{\rm SM} = g_{uL}^{\rm SM}\, Z_\mu \overline{u_L}\gamma^\mu u_L + g_{uR}^{\rm SM}\, Z_\mu \overline{u_R}\gamma^\mu u_R + g_{dL}^{\rm SM}\, Z_\mu \overline{d_L}\gamma^\mu d_L + g_{dR}^{\rm SM}\, Z_\mu \overline{d_R}\gamma^\mu d_R\,; \tag{4.1}$$

$$\mathcal{L}_\kappa = \kappa_Z \frac{m_Z^2}{v}\, Z_\mu Z^\mu h\,; \tag{4.2}$$

$$\begin{aligned}
\mathcal{L}_{\rm NP} = {} & g_{ZZ}\,\frac{h}{v} Z^{\mu\nu} Z_{\mu\nu} + g_{Z\widetilde{Z}}\,\frac{h}{v} Z^{\mu\nu}\widetilde{Z}_{\mu\nu} + g_{\gamma Z}\,\frac{h}{v} A^{\mu\nu} Z_{\mu\nu} + g_{\gamma\widetilde{Z}}\,\frac{h}{v} A^{\mu\nu}\widetilde{Z}_{\mu\nu} \\
& + g_u^L\, Z_\mu \overline{u_L}\gamma^\mu u_L + g_u^R\, Z_\mu \overline{u_R}\gamma^\mu u_R + g_d^L\, Z_\mu \overline{d_L}\gamma^\mu d_L + g_d^R\, Z_\mu \overline{d_R}\gamma^\mu d_R \\
& + \delta_u^L\,\frac{h}{v} Z_\mu \overline{u_L}\gamma^\mu u_L + \delta_u^R\,\frac{h}{v} Z_\mu \overline{u_R}\gamma^\mu u_R + \delta_d^L\,\frac{h}{v} Z_\mu \overline{d_L}\gamma^\mu d_L + \delta_d^R\,\frac{h}{v} Z_\mu \overline{d_R}\gamma^\mu d_R \\
& + g_u\,\frac{1}{v}(\overline{u_L}\sigma^{\mu\nu} u_R + \overline{u_R}\sigma^{\mu\nu} u_L) Z_{\mu\nu} + g_d\,\frac{1}{v}(\overline{d_L}\sigma^{\mu\nu} d_R + \overline{d_R}\sigma^{\mu\nu} d_L) Z_{\mu\nu} \\
& + \delta_u\,\frac{h}{v^2}(\overline{u_L}\sigma^{\mu\nu} u_R + \overline{u_R}\sigma^{\mu\nu} u_L) Z_{\mu\nu} + \delta_d\,\frac{h}{v^2}(\overline{d_L}\sigma^{\mu\nu} d_R + \overline{d_R}\sigma^{\mu\nu} d_L) Z_{\mu\nu}\,.
\end{aligned} \tag{4.3}$$

Here, κ_Z is the SM hZZ coupling modifier. The advantage of the κ framework in addition to heavy integrable NP scenarios is that it enables us to consider undetected light degrees of freedom without explicitly introducing an NP scale. In the above equations, the notations have their usual meanings, particularly note $Z_{\mu\nu} = \partial_\mu Z_\nu - \partial_\nu Z_\mu$, $\widetilde{Z}_{\mu\nu} = \epsilon_{\mu\nu\alpha\beta} Z^{\alpha\beta}$ where Z_μ denotes the physical Z boson, $\epsilon_{\mu\nu\alpha\beta}$ is a completely antisymmetric tensor and $\sigma^{\mu\nu} = \frac{i}{2}[\gamma^\mu, \gamma^\nu]$.

In the absence of direct observational evidence of NP signals at current experiments, one of the best possible ways to gauge the effects of NP is through higher dimensional effective operators constructed out of the SM fields respecting the SM gauge symmetry. They are popularly referred to as SMEFT operators. Note here that SMEFT operators also include the Higgs field as an isodoublet under the SM gauge group; while there are efforts to keep it beyond (for example, in HEFT [268]), given the Higgs properties closely mimic that of a SM doublet, we choose the SMEFT framework to explore the limit of NP[2].

[2]Operators with two Higgs doublets [269, 270], or a right handed neutrino [169, 271–273] have also been found out.

These operators are suppressed by an appropriate power of a heavy NP mass scale (Λ) integrated out, depending on the mass-scale of the operator. Understandably, the effects of such operators diminish with higher mass dimensions of the operators, hence we will constrict ourselves to the lowest dimension operators that contribute to the processes studied in this chapter, which appear in dimension 6[3]; operators of dimension 8 [171, 172] may also contribute, but we have not considered them in our analysis. We provide a detailed matching of Eq. (4.3) with the standard SMEFT framework in the Warsaw basis [11] later in this section.

SMEFT Operators Associated with Zh Production As discussed in Sec. 2.2, the SMEFT Lagrangian can be written as:

$$\mathcal{L} = \mathcal{L}_{SM} + \sum_{i,\,d} \frac{C_i\,\mathcal{O}_i^{(d)}}{\Lambda^{(d-4)}}\,, \tag{4.4}$$

where $\mathcal{O}_i^{(d)}$ represents operators of dimension d and C_i represents the WCs. Throughout this chapter, the effective scale is set to $\Lambda = 1$ TeV, while the resulting bound or sensitivity is obtained for the corresponding WCs, C_i. It is simple to understand that the limit on C_i can be rescaled easily for different choices of Λ, following $\left(C_i/\Lambda^2\right) = \left(C_i'/\Lambda'^2\right)$. Although the validity of the effective limit depends on the choice of Λ, strictly speaking, the CM energy of the reaction should abide by $\sqrt{s} < \Lambda$. At hadron colliders, it is difficult to ensure such a condition; we elaborate upon the possibility later.

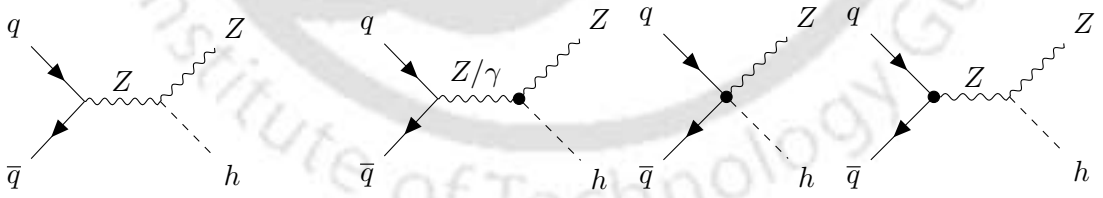

FIGURE 4.1: SM and EFT contributions to the Zh associated production mode at the LHC. Dotted vertices refer to the presence of EFT operators.

There is no unique basis for the choice of these operators and all the different bases are equivalent. We choose the Warsaw basis for our representation. The SMEFT operators relevant to Zh associated production, and applied throughout the subsequent collider

[3]It is well known that the only SMEFT operator in dimension 5 is the Weinberg operator $\overline{N}N^c$; $N = H^\dagger \epsilon \ell$, which generates Majorana neutrino mass.

analyses in this section, are tabulated in Tab. 4.1, and the corresponding Feynman diagrams are shown in Fig. 4.1. The vertices with a blob represent effective operator contributions, which modify hZZ, qqZ vertices, and additional contributions are obtained via γZh and $qqZh$ vertices.

Before moving forward, as mentioned in Sec. 2.2, the operators are classified majorly into two categories i.e. LG operators or PTG operators for NPs which are weakly coupled and decoupling [176]. The LG operators are suppressed additionally by a factor of $(4\pi)^2$ coming from the loops, and hence their contributions are expected to be suppressed in comparison to the PTG operators if the underlying NP scale is the same. However, this additional suppression factor for the LG operators is not intrinsically incorporated in most SMEFT studies; to maintain uniformity of nomenclature, we will use the operator classification as in [11].

CP-even hZZ modifiers
$\mathcal{O}_{H\Box} = (H^\dagger H)\Box(H^\dagger H)$
$\mathcal{O}_{HD} = (H^\dagger D_\mu H)(H^\dagger D^\mu H)$
$\mathcal{O}_{HW} = (H^\dagger H)W^I_{\mu\nu}W^{I\mu\nu}$
$\mathcal{O}_{HB} = (H^\dagger H)B_{\mu\nu}B^{\mu\nu}$
$\mathcal{O}_{HWB} = (H^\dagger \tau^I H)W^I_{\mu\nu}B^{\mu\nu}$
CP-odd hZZ modifiers
$\mathcal{O}_{H\widetilde{W}} = (H^\dagger H)\widetilde{W}^I_{\mu\nu}W^{I\mu\nu}$
$\mathcal{O}_{H\widetilde{B}} = (H^\dagger H)\widetilde{B}_{\mu\nu}B^{\mu\nu}$
$\mathcal{O}_{H\widetilde{W}B} = (H^\dagger \tau^I H)\widetilde{W}^I_{\mu\nu}B^{\mu\nu}$

Higgs-current operators
$\mathcal{O}^{(1)}_{Hq} = (H^\dagger i\overleftrightarrow{D_\mu} H)(\bar{q}_p\gamma^\mu q_r)$
$\mathcal{O}^{(3)}_{Hq} = (H^\dagger i\overleftrightarrow{D^i_\mu} H)(\bar{q}_p\tau^i\gamma^\mu q_r)$
$\mathcal{O}_{Hu} = (H^\dagger i\overleftrightarrow{D_\mu} H)(\bar{u}_p\gamma^\mu u_r)$
$\mathcal{O}_{Hd} = (H^\dagger i\overleftrightarrow{D_\mu} H)(\bar{d}_p\gamma^\mu d_r)$
Dipole operators
$\mathcal{O}_{uW} = (\bar{q}_p\sigma^{\mu\nu}u_r)\tau^I\widetilde{H}W^I_{\mu\nu}$
$\mathcal{O}_{uB} = (\bar{q}_p\sigma^{\mu\nu}u_r)\widetilde{H}B_{\mu\nu}$
$\mathcal{O}_{dW} = (\bar{q}_p\sigma^{\mu\nu}d_r)\tau^I HW^I_{\mu\nu}$
$\mathcal{O}_{dB} = (\bar{q}_p\sigma^{\mu\nu}d_r)HB_{\mu\nu}$

TABLE 4.1: Dimension 6 SMEFT operators: *Left:* hZZ vertex modifiers, *Right:* $qqZ/qqZh$ contact vertices (Higgs-current and dipole types), relevant to Vh associated production. Here, p and r are quark family indices. For complex operators, the presence of respective hermitian conjugates is assumed. For relevance: $D_\mu = \partial_\mu + ig\,\tau^I W^I_\mu + ig'YB_\mu$, $W^i_{\mu\nu} = \partial_\mu W^I_\nu - \partial_\nu W^I_\mu + g\epsilon^{IJK}W^J_\mu W^K_\nu$, $B_{\mu\nu} = \partial_\mu B_\nu - \partial_\nu B_\mu$, $H^\dagger i\overleftrightarrow{D_\mu}H = iH^\dagger D_\mu H - i(D_\mu H)^\dagger H$, $H^\dagger i\overleftrightarrow{D^I_\mu}H = iH^\dagger\tau^I D_\mu H - i(D_\mu H)^\dagger\tau^I H$, $\widetilde{V}_{\mu\nu} = \epsilon_{\mu\nu\rho\sigma}V^{\rho\sigma}$ $(V = W^I, B)$.

A few observations related to the operators as mentioned in Tab. 4.1 are as follows: The operators $\mathcal{O}_{H\Box}$ and $\mathcal{O}_{HD}$ modify the Higgs gauge boson coupling by a multiplicative factor without introducing any new Lorentz structure, amounting to a renormalization of the Higgs field. As such the contribution can be absorbed in the coupling modifier.

The operators $\mathcal{O}_{HW}$, $\mathcal{O}_{HB}$ and $\mathcal{O}_{HWB}$ contribute in the modification of the hZZ vertex. These amount to the CP-conserving anomalous Higgs gauge boson coupling. The operators $\mathcal{O}_{H\widetilde{W}}$, $\mathcal{O}_{H\widetilde{B}}$ and $\mathcal{O}_{H\widetilde{W}B}$ contribute in the modification of the hZZ vertex. These amount to the CP-violating anomalous Higgs gauge boson coupling. The operators $\mathcal{O}_{Hq}^{(1)}$, $\mathcal{O}_{Hq}^{(3)}$, $\mathcal{O}_{Hu}$ and $\mathcal{O}_{Hd}$ contribute to the 4-point interaction $qqZh$. These operators also contribute to the qqZ vertex and are referred to as Higgs-current operators since their form is analogous to current, $j^\mu = \overline{\psi}\gamma^\mu\psi$. The operators $\mathcal{O}_{uW}$, $\mathcal{O}_{uB}$, $\mathcal{O}_{dW}$ and $\mathcal{O}_{dB}$ contribute to the 4-point interaction $qqZh$. These operators also contribute to the qqZ vertex, contribute to the dipole moments of quarks, and hence can be referred to as dipole operators. A complete matching between the coefficients of $\mathcal{L}_{NP}$ in Eq. (4.1) and the SMEFT coefficients as in Tab. 4.1 are shown in Tab. 4.2.

Coefficient	**Warsaw equivalent**
g_{ZZ}	$2\left(c_w^2 C_{HW} + s_w^2 C_{HB} + s_w c_w C_{HWB}\right) v^2/\Lambda^2$
$g_{\gamma Z}$	$\left(2 s_w c_w^2 (C_{HW} - C_{HB}) + (s_w^2 - c_w^2) C_{HWB}\right) v^2/\Lambda^2$
$g_{Z\widetilde{Z}}$	$2\left(c_w^2 C_{H\widetilde{W}} + s_w^2 C_{H\widetilde{B}} + s_w c_w C_{H\widetilde{W}B}\right) v^2/\Lambda^2$
$g_{\gamma\widetilde{Z}}$	$\left(2 s_w c_w^2 (C_{H\widetilde{W}} - C_{H\widetilde{B}}) + (s_w^2 - c_w^2) C_{H\widetilde{W}B}\right) v^2/\Lambda^2$
g_u^L	$-\left(C_{Hq}^{(1)} + C_{Hq}^{(3)}\right) ev^2/\left(2\Lambda^2 s_w c_w\right)$
g_d^L	$-\left(C_{Hq}^{(1)} - C_{Hq}^{(3)}\right) ev^2/\left(2\Lambda^2 s_w c_w\right)$
g_u^R	$-C_{Hu} ev^2/\left(2\Lambda^2 s_w c_w\right)$
g_d^R	$-C_{Hd} ev^2/\left(2\Lambda^2 s_w c_w\right)$
δ_u^L	$-\left(C_{Hq}^{(1)} + C_{Hq}^{(3)}\right) ev^2/\left(\Lambda^2 s_w c_w\right)$
δ_d^L	$-\left(C_{Hq}^{(1)} - C_{Hq}^{(3)}\right) ev^2/\left(\Lambda^2 s_w c_w\right)$
δ_u^R	$-C_{Hu} ev^2/\left(\Lambda^2 s_w c_w\right)$
δ_d^R	$-C_{Hd} ev^2/\left(\Lambda^2 s_w c_w\right)$
g_u	$\left(s_w C_{uB} - c_w C_{uW}\right) ev^2/\sqrt{2}\Lambda^2$
g_d	$\left(s_w C_{dB} + c_w C_{dW}\right) ev^2/\sqrt{2}\Lambda^2$
δ_u	$\sqrt{2}\left(s_w C_{uB} - c_w C_{uW}\right) ev^2/\Lambda^2$
δ_d	$\sqrt{2}\left(s_w C_{dB} + c_w C_{dW}\right) ev^2/\Lambda^2$

TABLE 4.2: Matching between coefficients in Eq. (4.3) and the SMEFT coefficients. s_w and c_w are the sine and cosine of the Weinberg angle.

Parametrization of Production Cross Sections When SMEFT effects are included, the cross section consists of three types of terms viz. the pure SM contribution,

the SM plus EFT interference ($\propto \Lambda^{-2}$ from dimension six operators) and the pure EFT contribution ($\propto \Lambda^{-4}$). Inclusion of dimension 8 operators would result in SM plus EFT interference contribution $\propto \Lambda^{-4}$ which is comparable to the pure EFT contribution from dimension 6 terms, however, we do not consider them in this analysis. The production cross section in presence of SMEFT operators takes the form:

$$\sigma = \sigma^{(SM)} + \sum_{i=1}^{n_L} C_i \sigma_i^{(L)} + \sum_{i\leq j}^{n_Q} C_i C_j \sigma_{ij}^{(Q)} \,, \tag{4.5}$$

where n_L and n_Q refers to the number of linear and quadratic SMEFT contributions. The effective scales Λ^{-2} and Λ^{-4} are absorbed in the cross sections $\sigma_i^{(L)}$ and $\sigma_{ij}^{(Q)}$ respectively. In the presence of coupling modifiers κ, the cross section in equation (4.5) takes the form as below,

$$\begin{aligned}
\sigma &= \kappa^2\, \sigma^{(SM)} + \sum_{i=1}^{n_L} (\alpha_i^{(L)}\kappa + \beta_i^{(L)}\kappa^2)\, C_i\, \sigma_i^{(L)} + \sum_{i\leq j}^{n_Q} (1 + \alpha_{ij}^{(Q)}\kappa + \beta_{ij}^{(Q)}\kappa^2)\, C_i C_j\, \sigma_{ij}^{(Q)} \,, \\
\mu &= \kappa^2 + \sum_{i=1}^{n_L} (\alpha_i^{(L)}\kappa + \beta_i^{(L)}\kappa^2)\, C_i\, \mu_i^{(L)} + \sum_{i\leq j}^{n_Q} (1 + \alpha_{ij}^{(Q)}\kappa + \beta_{ij}^{(Q)}\kappa^2)\, C_i C_j\, \mu_{ij}^{(Q)} \,,
\end{aligned} \tag{4.6}$$

where μ is the signal strength, i.e. $\mu = \sigma/\sigma_{SM}$. Differential cross sections can be parametrized in a similar manner. At the hadron collider, an analytical form of the cross section is difficult to write due to the uncertainty of the incoming momenta of the partons. However, we can numerically fit the production cross section as a function of the parameters and this turns out to be equally useful for gauging the effects of NP. In the following, we fit the operator coefficients following (4.6) at 14 TeV LHC for the Zh associated production process considering one operator at a time. The variation of the total production cross section are shown in Fig. 4.2 (for CP-even hZZ modifiers and Higgs-current operators) and 4.3 (for CP-odd hZZ modifiers and dipole operators). The ratio of the total production cross section for moving from 13 TeV to 14 TeV are also shown. We adopt the following methodology, the effective Lagrangian is implemented in `FeynRules` [233] to generate the `UFO` model [274] file. The model file is validated with standard UFOs like `SMEFTsim` [275] and `SMEFTatNLO` [276]. This model file is then fed into the event generator `MG5_aMC` [235] to obtain the above cross sections at LO. The cross sections are generated at production level without decaying Z or h to any specific decay mode without any kinematic cuts. The PDF set and flavor scheme choice are

`NN23LO1` [277] PDF set and $U(2)_q \times U(2)_u \times U(2)_d$, respectively.

A few key points observed are as follows: The Higgs-current operators have significant linear as well as quadratic contributions indicating large pure EFT contribution. The enhancement of the EFT terms result from the absence of propagator suppression in the production process. The dipole operators have no linear contribution. This is because they bind fermions with different chiralities and hence do not interfere with the SM process. Due to the absence of linear dependence, they cause variation in the cross section only in the positive direction. All the operators except $\mathcal{O}_{Hq}^{(3)}$ shows near symmetric behaviour along the positive and negative side. The operator $\mathcal{O}_{Hq}^{(3)}$ dips around $C_{Hq}^{(3)} = -0.2$ and then continues to rise as we go further in the negative direction. This is due to strong linear as well as quadratic dependence and the trade off between them happens away from $C_{Hq}^{(3)} = 0$ towards the negative axis. When moving from 13 TeV to 14 TeV LHC, the contact operators i.e. operators associated with $qqZ/qqZh$ vertices, significantly boost the production cross sections. The other operators are less sensitive.

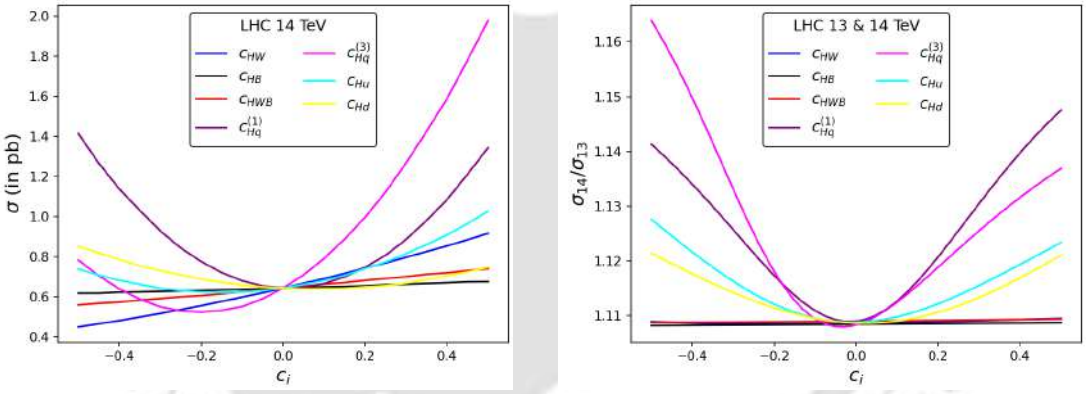

FIGURE 4.2: *Left:* Variation of Zh associated production cross section with variation in CP-even hZZ modifiers and Higgs-current effective operator coefficients at the 14 TeV LHC. *Right:* Variation in the ratio of production cross section of the 14 TeV LHC to the 13 TeV LHC with variation in the effective operator coefficients. See figure inset for the colour codes.

For our analysis, we consider the two operators $\mathcal{O}_{Hq}^{(3)}$ and $\mathcal{O}_{uW}$ as a representative of the Higgs-current and dipole class respectively. It should be noted that the choice is based on their sensitivity to the production cross section, however other operators from the respective classes maybe more sensitive to particular observables or be less bounded from experiments. Our consideration is based on proof of concept and any other operator can be chosen in lieu of these. Along with the coupling modifier κ_Z (which approximately estimates the EFT effect to the hZZ vertex), this forms our EFT parameter space: $\{\kappa_Z, C_{uW}, C_{Hq}^{(3)}\}$. The parametrized coefficients for signal strength associated with Zh

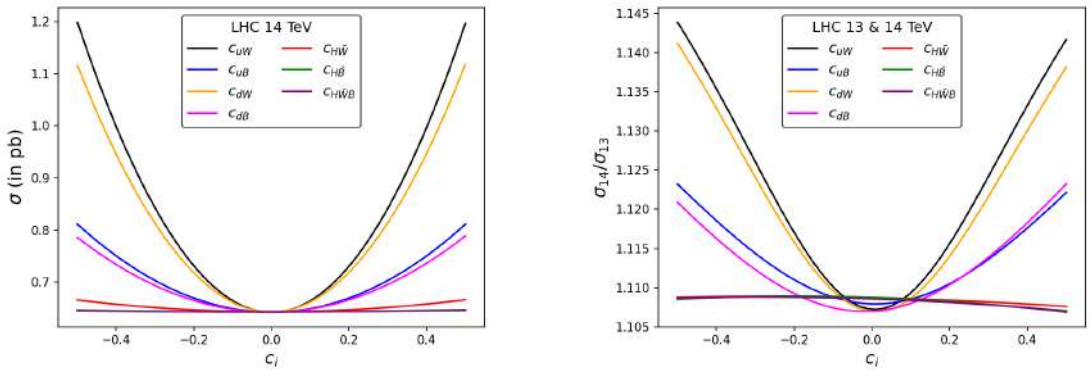

FIGURE 4.3: *Left:* Variation of Zh associated production cross section with change in CP-odd hZZ modifiers and dipole effective operator coefficients at the 14 TeV LHC. *Right:* Variation in the ratio of production cross section of the 14 TeV LHC to the 13 TeV LHC with change in effective operator coefficients. See figure inset for the colour codes.

production with these operators following Eq. (4.6), derived via a multidimensional numerical fit, are tabulated in Tab. 4.3. This parametrization gives an overview of the EFT effects on the inclusive cross section. Coefficients of linear terms in 1, κ_Z, C_{uW} and $C_{Hq}^{(3)}$ are not present in our parametrization as it is evident from Eq. (4.6) that the interference between SM and SMEFT vertices appear as coefficient of $\kappa_Z\, C_{Hq}^{(3)}$. Further, the coefficients of $\kappa_Z\, C_{uW}$, $\kappa_Z^2\, C_{uW}$, $C_{uW}\, C_{Hq}^{(3)}$, $\kappa_Z\, C_{uW}\, C_{Hq}^{(3)}$ and $\kappa_Z^2\, C_{uW}\, C_{Hq}^{(3)}$ vanish because of no interference between the SM and $\mathcal{O}_{Hq}^{(3)}$ operators with diagrams with $\mathcal{O}_{uW}$ operator as the dipole operator mixes quarks of different chiralities ($\overline{q}_L\sigma_{\mu\nu}q_R$ / $\overline{q}_R\sigma_{\mu\nu}q_L$) in contrary to the SM or Higgs-current operators which mixes quarks of same chirality ($\overline{q}_L\gamma_\mu q_L$ / $\overline{q}_R\gamma_\mu q_R$).

We shall also note that the variation of the cross-section presented here with EFT operator coefficients, have been done without considering the constraints on these operators. We shall do it in the next section. We get the dominant physics contribution to the process under consideration and the resultant parametrization, which remains intact with the modified range of the operator coefficients that will be used for scanning the parameter space.

It should be further noted that due to the presence of momentum dependence in EFT vertices or absence of propagators, effect of EFT operators are evident mostly at the tails of differential distribution. Hence, presence of EFT, if any, can be best interpreted from

Coefficients	1	C_{uW}	$C_{Hq}^{(3)}$	$(C_{uW})^2$	$\left(C_{Hq}^{(3)}\right)^2$	$C_{uW}\ C_{Hq}^{(3)}$
1	–	–	–	3.0277	4.2429	–
κ_Z	–	–	1.7060	0.2106	0.3880	–
$(\kappa_Z)^2$	1.0000	–	0.1439	0.2000	−0.0472	–

TABLE 4.3: The parametrized coefficients (μ_i, μ_{ij}) for operators $\mathcal{O}_{Hq}^{(3)}$, $\mathcal{O}_{uW}$ and κ_Z contributing to Zh production at 14 TeV LHC, following Eq. (4.6).

changes to the differential distributions. Fig. 4.4 shows the ratio of the invariant mass distribution, $M_{Zh} = \sqrt{(p_Z + p_h)^2}$ for Zh production in the presence of EFT operators to the corresponding SM prediction at the 14 TeV LHC.

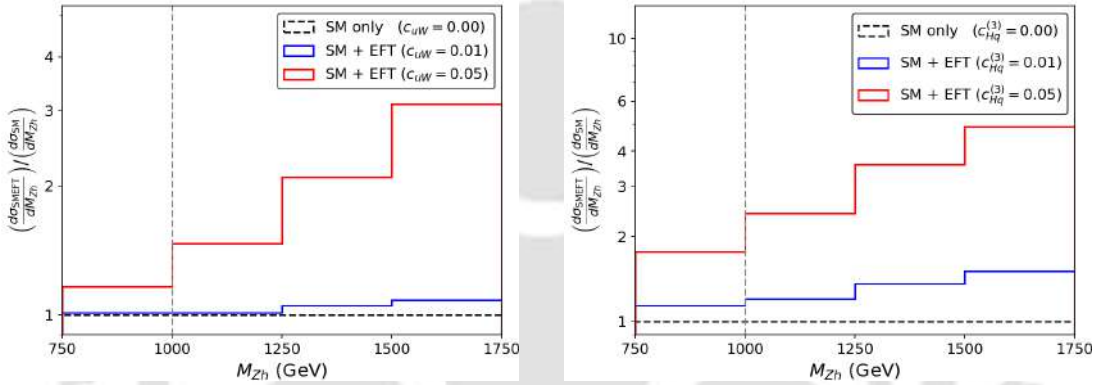

FIGURE 4.4: *Left:* Ratio of the invariant mass distribution, M_{Zh} for Zh production in presence of $\mathcal{O}_{uW}$ operator to the corresponding SM prediction at the LHC 14 TeV. *Right:* Same for $\mathcal{O}_{Hq}^{(3)}$ operator. The grey vertical line refers to the EFT scale, $\Lambda = 1$ TeV.

Comparison with Other Higgs Production Modes The operators $\mathcal{O}_{uW}$ and $\mathcal{O}_{Hq}^{(3)}$ are not unique to the Vh ($V = W, Z$) associated production mode. It appears in the vector boson fusion (VBF) and single top production in association with Higgs (thj) as well. The thj process has a comparatively smaller cross section and it is not ideal for the study of these operators, but the VBF mode has a larger cross section compared to Vh associated production mode, as considered here. These operators are also associated with the diboson production ($VV = WW, WZ, ZZ$) processes. However, the ratio of the signal production cross-section including EFT and that of the SM contribution is more sensitive to the changes in the WCs in Vh mode compared to that of VBF and VV channels. This has been illustrated in Fig. 4.5 for the operators $\mathcal{O}_{Hq}^{(3)}$ (left) and

$\mathcal{O}_{uW}$ (right) [4]. Also, for both VV and VBF modes, pure contact interaction diagrams are absent, so EFT contributions always come in presence of one or more propagators. Hence, for the study of $qqZ/qqZh$ vertices, Zh production is considered in our analysis.

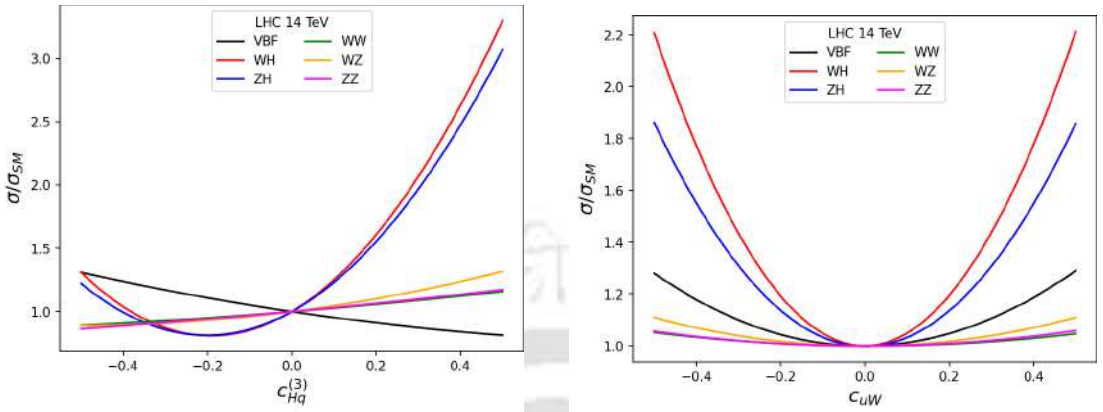

FIGURE 4.5: *Left:* Variation in the ratio of production cross section to the SM cross section in VBF, Vh and VV processes at the 14 TeV LHC with variation in effective coefficient $C_{Hq}^{(3)}$. *Right:* Same for C_{uW}.

4.1.2 Constraints on hZZ Couplings

As established, the current uncorrelated bounds from ATLAS (139 fb^{-1}) and CMS (138 fb^{-1}) are based on Run II data and involve a global fit over the main five production and decay channels. Since we intend to study Zh associated production with h subsequently decaying to a bottom pair, the bottom Higgs coupling modifier, κ_B, is also important for this analysis. Higgs decay to a bottom pair has been studied intensely at the LHC across several channels, and the bounds are given in terms of signal strength (μ), i.e. the ratio of the observed signal to the SM predicted value. In Tab. 4.4 we list out the uncorrelated bounds on the coupling modifiers as well as the signal strengths of the Higgs decay to bottom pair in the Zh production channel.

Considering the bounds on the signal strength, we can limit the coupling modifiers using the measured signal strengths as shown in Eq. (4.7).

$$\mu_{hbb}^{Zh} = \frac{(\sigma^{Zh} \times (B.R.)_{hbb})}{(\sigma^{Zh} \times (B.R.)_{hbb})_{SM}} = \frac{\kappa_Z^2 \kappa_B^2}{0.1775 + 0.5809\kappa_B^2 + 0.2416\kappa_Z^2}\,. \tag{4.7}$$

[4] One should however note here that the sensitivity of a specific channel not only depends on the signal cross-section, but also relies on the background contribution and the efficiency in extracting the signal.

Measurable	Bound	Source
κ_Z	[0.97, 1.11]	CMS ($pp \to h$) [7]
	[0.94, 1.05]	ATLAS ($pp \to h$) [6]
κ_B	[0.85, 1.11]	CMS ($pp \to h$) [7]
	[0.79, 1.01]	ATLAS ($pp \to h$) [6]
μ_{hbb}^{Zh}	[0.59, 1.17]	CMS ($pp \to Zh, h \to b\bar{b}$) [5]
	[0.85, 1.33]	ATLAS ($pp \to Zh, h \to b\bar{b}$) [4]

TABLE 4.4: Constraints on κ_Z, κ_B and μ_{Hbb}^{Zh} (at 95% C.L.) from ATLAS and CMS experiments.

In evaluating Eq. (4.7), both the Higgs couplings with the bottom quark as well as with Z bosons have been modified keeping coupling with other fermions unchanged. κ_Z appears from the production cross-section, while κ_B appears from the decay branching fraction, pertaining to the fact that Higgs production and decay modes are those predicted in the SM, the NP effects only enters via rescaling of the Higgs coupling strength. The denominator comes from the modification of the Higgs decay width, which is easily adjusted within the observed total Higgs decay width at LHC for moderate values of κ parameters. We can see that for $\kappa_Z = \kappa_B = 1$, the signal strength turns one. We further invoke the custodial symmetry requirement $\kappa_W = \kappa_Z$. This assumption reduces the number of free parameters in the model and is consistent with the LHC bounds reported in [6, 7]. However, this assumption can be relaxed, and the impact of doing so in our analysis is discussed in App. 4.E. The bounded region is shown in Fig. 4.6. Additionally, superimposing the current correlated bound on the $\kappa_V - \kappa_F$ space from the combined Higgs measurement gives the status of the most accurate constraint from the current data. The uncertainties are less than 10% from the SM prediction.

Constraints on the Effective Coupling Coefficients In context of the study of Higgs couplings in effective framework, several collaborations [278–282] has attempted to provide global bounds based on Higgs, Top and Diboson data from Tevatron, LHC and LEP. Similar fits have been done including B-Physics data with LHC top and bottom quark studies [283, 284]. Similarly, global fits have also been performed based on Electroweak Precision data as well as Δ_{CKM} measurement [165]. Customarily, both ATLAS and CMS have done a number of studies on constraining the EFT operators across

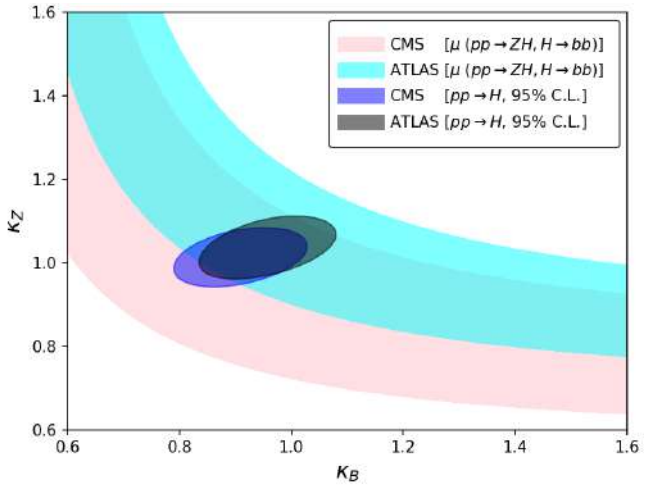

FIGURE 4.6: Constraints on coupling modifiers κ_Z and κ_B based on combined limit on $pp \to Zh$, $h \to b\bar{b}$ production signal strength (bands) [4, 5] as well as the combined experimental best fit from all Higgs production and decay processes (ellipses) [6, 7] at ATLAS and CMS experiments.

various channels using latest data. While ATLAS uses SMEFT, CMS uses Higgs Effective Lagrangian parametrization, we will consider bounds from ATLAS [4, 285–287] only. Also, there have been numerous studies concerning SMEFT, projecting constraints for future collider experiments [288–290]. We tabulate the constraints on the coefficients C_{uW} and $C_{Hq}^{(3)}$ from current data in Tab. 4.16 and 4.6. The contraints on other dipole and Higgs-current operators are listed in App. 4.A.

Coefficient	Bound	C.L.	Flavor Scheme [Source]
C_{uW}	[-0.375, 0.375]	95%	$U(3)_q \times U(3)_u \times U(3)_d$ [291]
	[-0.290, 0.290]	95%	$U(2)_q \times U(2)_u \times U(2)_d$ [292]
	[-0.084, 0.029]	95%	$U(1)_Q \times U(1)_t$ [278]
	[-0.012, 0.048]	90%	$U(3)_q \times U(3)_u \times U(3)_d$ [284]
	[-0.079, 0.109]	95%	$U(1)_Q \times U(1)_t$ [282]
	[-0.120, 0.510]	95%	$U(1)_Q \times U(1)_t$ [279]

TABLE 4.5: Constraints on dipole operator coefficient C_{uW} from existing studies, see the references for details. q, u and d are the SM LH quark doublet, RH up and down-type quark singlets, respectivey. Q and t refers to the third generation LH quark doublet and RH Top quark singlet, respectively.

A few comments and clarifications on the existing bounds: The bounds in Tab. 4.4 and 4.6 are individual bounds for the operator coefficients, where all other operator coefficient values are set to zero. The bounds for some of the studies in Tab. 4.4 and 4.6 are provided for $\left(C_i/\Lambda^2\right)$ or $\left(C_i v^2/\Lambda^2\right)$. The values provided on the tables are normalized to $\Lambda = 1$

Coefficient	Bound	C.L.	Flavor Scheme [Source]
$C_{Hq}^{(3)}$	[-0.432, 0.062]	95%	$U(2)_q \times U(2)_u \times U(3)_d$ [278]
	[-0.375, 0.344]	95%	$U(1)_Q \times U(1)_t$ [278]
	[-0.702, 0.104]	68%	$U(3)_q \times U(3)_u \times U(3)_d$ [165]
	[-0.080, 0.100]	95%	$U(3)_q \times U(3)_u \times U(3)_d$ [286]
	[-0.018, 0.026]	68%	$U(3)_q \times U(3)_u \times U(3)_d$ [4]
	[-0.150, 0.520]	95%	$U(3)_q \times U(3)_u \times U(3)_d$ [285]
	[-0.023, 0.053]	90%	$U(3)_q \times U(3)_u \times U(3)_d$ [284]
	[-0.017, 0.012]	95%	$U(2)_q \times U(2)_u \times U(3)_d$ [279]
	[-0.032, 0.048]	95%	$U(1)_Q \times U(1)_t$ [279]
	[-0.008, 0.016]	95%	$U(2)_q \times U(2)_u \times U(3)_d$ [281]

TABLE 4.6: Constraints on Higgs-current operator coefficient $C_{Hq}^{(3)}$ from existing studies, see the references for details.

TeV. The flavor schemes associated with different analyses are tabulated as well in the tables. The bounds significantly change as per flavor assumptions. In this analysis, we will assume a $U(2)_q \times U(2)_u \times U(2)_d$, stating that the third generation is completely decoupled from the first two generations. This assumption is guided by the fact that the collisions at LHC contributing to Zh production are evidently light quarks (b quark collisions are suppressed by PDFs). The bounds are from different analyses at difference confidence levels (C.L.). For our analysis in suceeding sections, we consider the EFT benchmarks: $C_{uW} = 0.01, 0.05$ and $C_{Hq}^{(3)} = \pm 0.01, \pm 0.05$. Since, only the flavor scheme of [292] match with our flavor scheme, we only adhere to their bounds for C_{uW}. For $C_{Hq}^{(3)}$, none of the flavor scheme matches with our choice and we need not adhere to any of them. Still numerically, for C_{uW}, the benchmark 0.01 is consistent with all the bounds in Tab. 4.4, while the benchmark 0.05 is consistent with [279, 282, 291, 292] only. Similarly, for $C_{Hq}^{(3)}$, the benchmark 0.01 is consistent with all the bounds in Tab. 4.6, while -0.01 is not consistent with [281]. The benchmarks 0.05 and -0.05 are more wishful, and is incompatible with [4, 279, 281] and [4, 279, 281, 284], respectively, caveat to the flavor assumptions. The CP-violating gauge-Higgs operators listed in Tab. 4.1 are constrained by the fermion dipole moment observables, such as electron and neutron dipole moments, as they contribute at one loop to dipole operators. The current limits on the electron and neutron dipole moments are 1.1×10^{-29} and 3.0×10^{-26} (in units of e

cm), respectively [293]. These operators are also constrained by the measurements of the triple gauge-interactions of the form $WW\gamma$ and WWZ at LEP and the CP asymmetry measured in the $B \to X_s\gamma$ decay. The CP asymmetry measured in $B \to X_s\gamma$ decay is $A_{B\to X_s\gamma} = 0.015(20)$. Bound on the imaginary part of dipole operator C_{uW} from neutron EDM [164] (assuming $U(2)_q \times U(2)_u \times U(2)_d$ flavor scheme) is shown below:

$$\mathfrak{Im}(C_{uW}) < 0.000672 \tag{4.8}$$

The bound on other dipole operators are listed in App. 4.A. The bounds are extremely stringent, hence difficult to probe at collider experiments. For our case, we restrict ourselves to the real dipole coefficients, hence evading these bounds. The bounds on light quark dipole operators from electron EDM appear at two loop involving a Yukawa interaction in the loop and hence are insignificant in comparison to other constraints [294].

4.1.3 Collider Analysis: LHC and HL-LHC

In this section, we will discuss the event generation and analysis in the context of the current and future HL-LHC data. We have simulated $pp \to Zh \to (l^+l^-)(b\bar{b})$ process at the LHC 13 TeV and 14 TeV CM energies. The PDF set used is `NN23LO1` and the renormalization and factorization scales are set at the default dynamical scale choice of `MG5_aMC`. The signal and background informations will be detailed in Sec. 4.1.3.

As noted in Sec. 4.1.1, before proceeding with the collider analysis in the presence of EFT operators, it is important to check the validity of the effective approximation for the collider setup. The validity condition is $\sqrt{\hat{s}} < \Lambda$, where $\sqrt{\hat{s}}$ is the partonic CM energy. Because ensuring this criterion is difficult in hadron colliders like the LHC, where collisions between partons happen at variable centre of mass energies, one way to deal with this is to construct the invariant mass of the final state particles, M_{Zh}, to guess the energy scale at which the partonic collisions take place. This is depicted in Fig. 4.7 for the production process at a particular EFT benchmark point, and we observe that almost all the events obey the effective validation criteria when $\Lambda = 1$ TeV. Now, the generated signal and background events are fed in `Pythia8` [295] for parton showering. The showered events are fed in `Fastjet3` [238] for jet clustering using the `anti` k_t algorithm [209] with jet radius 0.5 and jet $p_T \geq 20$ GeV. Finally, the events are

processed through `Delphes3`, using the card `delphes_card_cms`, to take into account finite detector resolution effects, as well as particle identification, reconstruction and jet tagging. The processed events are analyzed using `MadAnalysis5` [296].

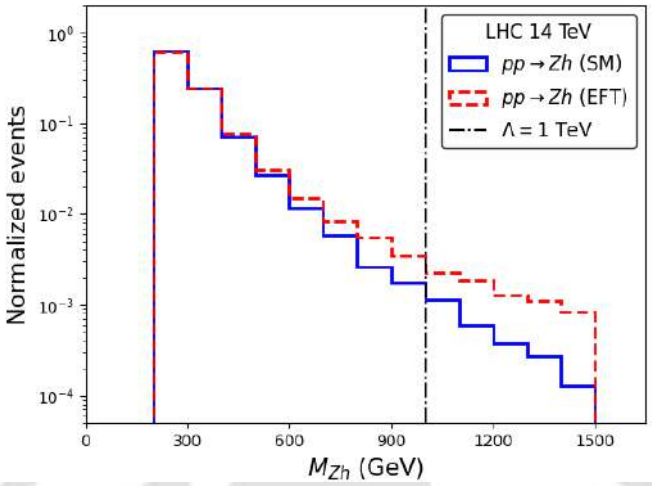

FIGURE 4.7: Invariant mass of Zh for the parton level processes in absence as well as presence of EFT operators at $\Lambda = 1$ TeV.. Here we consider the EFT benchmark point corresponding to $\{\kappa_Z, C_{uW}, C_{Hq}^{(3)}\} = \{1.00, 0.05, 0.05\}$.

Cut-based Analysis We consider the signal to be $pp \to Z(l^+l^-)h(b\bar{b})$ i.e. a dilepton di-bjet signal. This signal is comparatively clean due to the presence of charged leptons with invariant mass of the dilepton system peaking around Z mass. The possible SM backgrounds for this signal process are $pp \to t\bar{t}$, $pp \to ZZ$, $gg \to Zh$ and $pp \to Zb\bar{b}$. NLO corrections to both signal and background processes are taken into account by multiplying the production cross sections for each process by its NLO K factor, where $K = \sigma_{\rm NLO}/\sigma_{\rm LO}$. The LO and NLO cross sections are calculated using `MG5_aMC@NLO` at LHC 13 TeV and the K factors for different processes are: Zh: 1.288 (for $pp \to Zh$), 2.000 (for $gg \to Zh$), $Zb\bar{b}$: 1.230, $t\bar{t}$: 1.338 and ZZ: 1.461 [297–299].

We perform the analysis for two different setups viz. LHC 13 TeV 139 fb^{-1} (equivalent to Run II) and LHC 14 TeV 3000 fb^{-1} (future HL-LHC projection). We introduce some basic cuts common for all the analysis. These can be detailed as: $P_T^j > 20.0$ GeV, $P_T^l > 10.0$ GeV, $-5.0 < \eta_j < 5.0$, $-2.5 < \eta_l < 2.5$, $\Delta R_{jj} > 0.4$, $\Delta R_{lj} > 0.4$, $\Delta R_{ll} > 0.4$, where, subscripts j and l refer to jets and leptons respectively, and the kinematic variables have their usual definitions as in collider literature [2]. Apart from these, to ensure exclusive $l^+l^-b\bar{b}$ signal we select events with $N_b = 2$ and $N_l = 2$. The relevant distributions of kinematic variables and observables are plotted in Fig. 4.8 for 13 TeV and 14 TeV LHC.

Choosing $N_j < 5$ for Zh considerably reduces the pure hadronic backgrounds at LHC. We further choose a wide M_{bb} cut around the Higgs mass to make sure that we retain most of the signal while eliminating the backgrounds. The presence of dileptons enables us to use some additional cuts. Owing to the better detectability of leptons, a narrow cut on M_{ll} around the Z mass significantly reduces the $t\bar{t}$ background. Finally due to the absence of invisible particles in the final state (apart from neutrinos possibly coming from b-decay) rejecting events with large missing transverse energy, MET (MET > 30 GeV) removes backgrounds with neutrinos in final state like leptonic $t\bar{t}$ mode. The entire cut flow for SM Zh process (in absence of EFT contributions) is tabulated in Tab. 4.7.

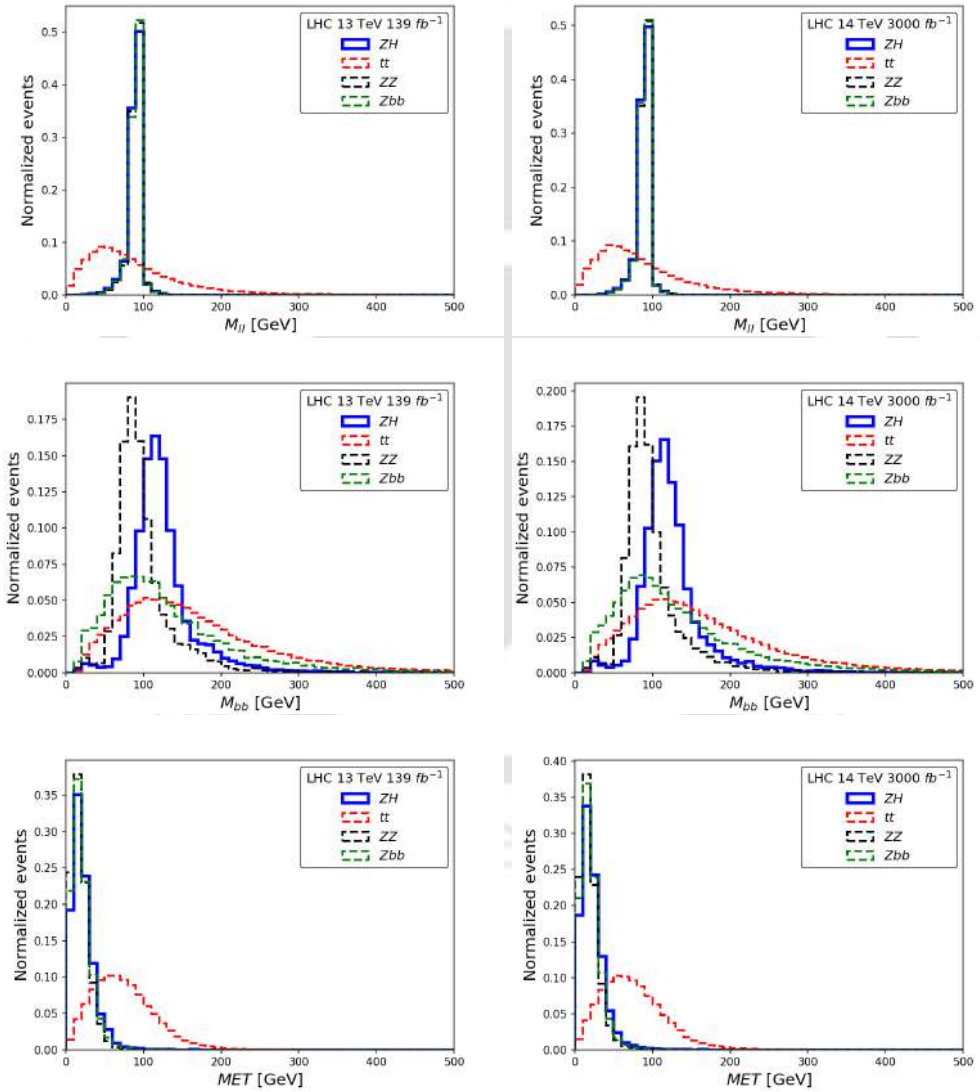

FIGURE 4.8: *Top Left:* Invariant mass of dilepton at the LHC 13 TeV corresponding to the SM signal and backgrounds. *Top Right:* Same for LHC 14 TeV. *Middle Left:* Invariant mass of di-bjet at the LHC 13 TeV. *Bottom Right:* Same for LHC 14 TeV. *Bottom Left:* Missing transverse energy at the LHC 13 TeV. *Bottom Right:* Same for LHC 14 TeV.

Cuts	LHC 13 TeV 139 fb^{-1}				LHC 14 TeV 3000 fb^{-1}			
	S	B	S/B	z	S	B	S/B	z
Basic Cuts	569	1016890	0.0006	0.56	13327	25581580	0.0005	2.63
$N_j < 5$	309	369549	0.0008	0.51	7054	9079825	0.0008	2.34
$M_{bb} \in$ (110.0, 140.0) GeV	126	56059	0.0022	0.53	2858	1382411	0.0021	2.43
$M_{ll} \in$ (80.0, 100.0) GeV	107	11674	0.0092	0.99	2456	285269	0.0086	4.59
MET < 30 GeV	91	5472	0.0166	1.23	2026	129095	0.0156	5.62

TABLE 4.7: Cut flow and signal significance (z) for the SM $Z(l^+l^-)h(b\bar{b})$ associated production signal with the SM background processes at LHC with $\sqrt{s}$ =13 TeV and luminosity of 139 fb^{-1} and at LHC with $\sqrt{s}$ = 14 TeV and integrated luminosity of 3000 fb^{-1}. Apart, we use the following notations, S: Signal events, B: Background events, S/B: Signal to background ratio.

BPs $\left(\kappa_Z, C_{uW}, C_{Hq}^{(3)}\right)$	S	B	S/B	z	ϵ_s	ϵ_b
SM (1.00, 0.00, 0.00)	2026	129095	0.0156	5.62	2.09×10^{-2}	8.72×10^{-4}
BP1 (1.00, 0.05, 0.00)	2142		0.0166	5.94	2.19×10^{-2}	
BP2 (1.00, 0.00, 0.05)	2238		0.0173	6.21	2.10×10^{-2}	
BP3 (1.00, 0.00, -0.05)	1869		0.0145	5.19	2.09×10^{-2}	

TABLE 4.8: Signal significance of the $Z(l^+l^-)h(b\bar{b})$ production process (at LHC with $\sqrt{s}$ =14 TeV and luminosity 3000 fb^{-1}) after the final selection cuts listed in Tab. 4.7 for different benchmark points (BPs) in presence of effective operators, along with signal (ϵ_s) and background (ϵ_b) efficiencies.

For signal significance, we use the Asimov definition [300]:

$$z = \sqrt{2\left((S+B)\ln\left(1+\frac{S}{B}\right) - S\right)}, \tag{4.9}$$

where S is the number of signal events and B is the number of background events. The Asimov significance is derived from the likelihood ratio, which takes into account the full statistical model, including the Poisson nature of signal and background events. Hence it is more statistically rigorous, not only for small event counts or comparable signal-background scenarios, but also in the general case. On Taylor expansion in the limit $S \ll B$, the Asimov significance approximates to $S/\sqrt{B}$, which is the more common definition. The number of signal and background events can further be parametrized in terms of the coupling modifiers and the effective operator coefficients as shown in

Eq. 4.10.

$$\begin{aligned} S &= \mathcal{L} \times \sigma^{S}_{\text{SM+EFT}}(\kappa_V, C_i) \times B.R.^{S}(\kappa_B, C_i) \times \epsilon_s \,, \\ B &= \mathcal{L} \times \sigma^{B}_{\text{SM}} \times B.R.^{B} \times \epsilon_b \,; \end{aligned} \tag{4.10}$$

where, $\mathcal{L}$ is the integrated luminosity, ϵ_s and ϵ_b are the signal and background cut efficiencies respectively. The EFT effects on Z branching to leptons is parametrized in App. 4.D. From Tab. 4.7, it is clear that the signal significance improves significantly as we move to the high luminosity frontier.

The second part of the analysis features the inclusion of EFT operators. In the presence of EFT operators, there is a significant change in the signal significance. This has been illustrated in Tab. 4.8 in the presence of SMEFT operators at some benchmark values. The relevant kinematic variables and observables for the different benchmark points are shown in Fig. 4.21 of App. 4.C. The deviation from the SM signal is minuscule. The benchmarks are chosen at some standard values to gauge the effect on the overall parameter space.

BDT-based Analysis With the advent of modern machine learning tools, multivariate analysis has become a norm in collider analysis [301, 302]. Among the machine learning techniques, boosted decision tree (BDT) based algorithms are extremely popular due to their stability as well as accuracy even for smaller datasets. With an aim to improve the signal background separation with more accuracy, we perform an analysis using the `XGBoost` classifier [303]. The core setup of the analysis is kept similar to the cut-based counterpart. Since we observed higher significance at 14 TeV, 3000 fb^{-1} LHC, we will perform the BDT based analysis exclusively for the HL-LHC run. The training sets for signal ($pp \to Z(l^+l^-)h(b\bar{b})$) and backgrounds ($pp \to t\bar{t}$, $pp \to ZZ$, $gg \to Zh$ and $pp \to Zb\bar{b}$) are prepared and weighted according to its number strength at 3000 fb^{-1}. This weighted data is subjected to the same basic cuts as used in the cut-based analysis. The feature selection is done in a similar line with the Vh, $h \to b\bar{b}$ analysis at ATLAS [4]. The features are detailed below:

- Transverse momentum of the leading lepton: p_T^l
- Transverse momentum of the leading b-jet: p_T^b
- Number of jets (inclusive of b-jets): N_j

- Missing transverse energy: MET
- Transverse momentum of the dilepton system: p_T^{ll}
- Transverse momentum of the di-b-jet system: p_T^{bb}
- Invariant mass of the dilepton system: M_{ll}
- Invariant mass of the di-b-jet system: M_{bb}
- Separation in (η, ϕ) space between the leptons: ΔR^{ll}
- Separation in (η, ϕ) space between the b-jets: ΔR^{bb}
- Difference in η between the dilepton and di-b-jet system: $\Delta\eta^{ll,bb}$
- Difference in ϕ between the dilepton and di-b-jet system: $\Delta\phi^{ll,bb}$

The detailed correlation heatmap between the features for signal and backgrounds is shown in App. 4.B. To prevent features with large magnitudes (like p_T, MET, etc.) from dominating over small valued features (like $\Delta\eta$, ΔR, etc.), all the features are scaled about their mean value ($\overline{x}$) by their standard deviation (SD) i.e. $(x - \overline{x})/SD$. This ensures all features are more or less at equal footing at the beginning of the training process. The signal and background events are divided in a 1:1 ratio for training and testing each process. For training, the overall signal weight is equated with the overall background weight, ensuring an equal number of signal and background events entering the training process. The BDT model is constructed using `XGBClassifier` and the hyperparameter tuning is done using `GridSearchCV` [304]. The details of the optimal hyperparameters are listed in Tab. 4.17 in App. 4.B. The model is 3-fold cross-validated using `StratifiedKFold` [304]. Since the distributions for the SM plus EFT benchmarks vary very little from the SM distributions, we train only the SM signal and backgrounds and test on the SM as well as on SM plus EFT benchmarks.

The highlights of the BDT analysis are shown in Fig.4.9. As a metric for evaluation of our model, we use the Receiver Operating Curve (ROC) Area Under the Curve (AUC). The AUC value for the training set is 0.9777. For the test sets, the AUC obtained are 0.9740, 0.9743 and 0.9744 respectively for SM, BP1 and BP2. This indicates that there was very little overfitting and the BPs fared very well on the model trained with SM inputs. To enhance the signal significance, we have set the threshold classifier score at 0.95. This means we will only keep events with a BDT classifier score greater than or equal to 0.95. By doing this, we maintain a roughly similar background efficiency as in

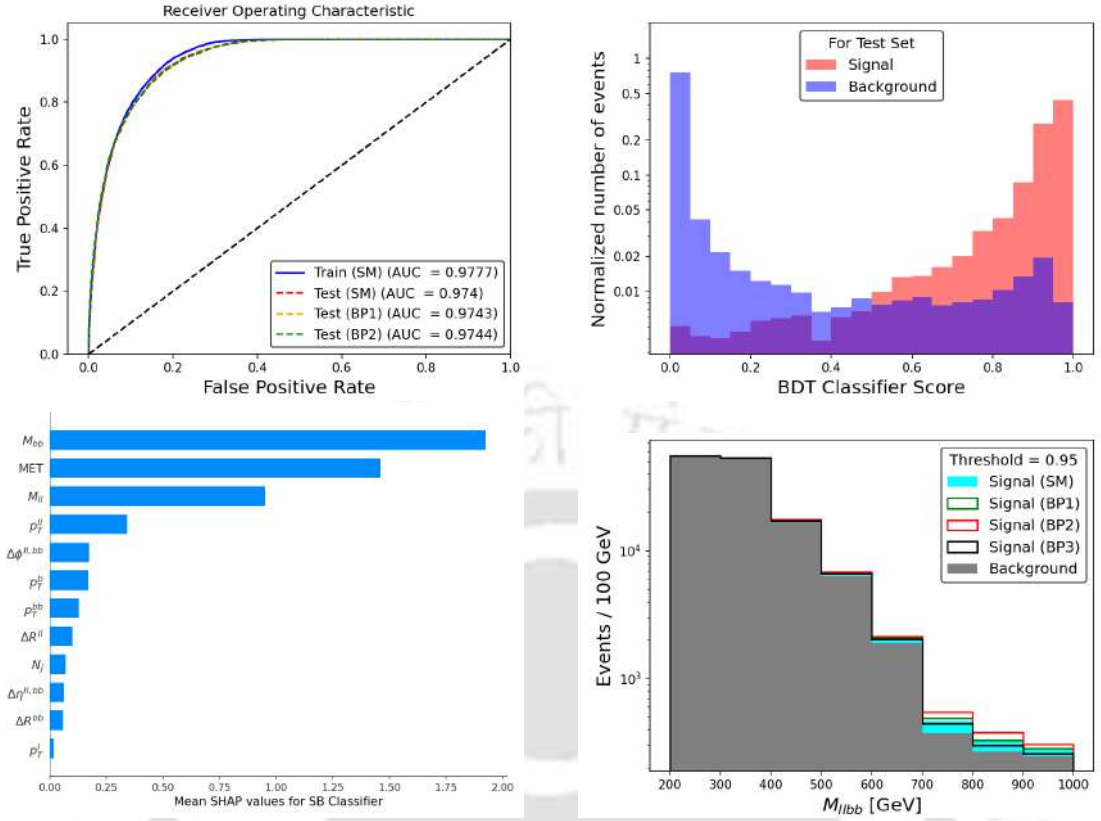

FIGURE 4.9: *Top Left:* The ROC curve for the training and testing (SM as well as BPs) data. *Top Right:* The distribution of the BDT classifier score for the SM signal and backgrounds. *Bottom Left:* The mean absolute SHAP values for the features used for training the BDT model. *Bottom Right:* M_{llbb} distribution of signal and background processes post threshold selection of 0.95.

the cut-based analysis, making it easier to compare signal efficiencies between the two methods. The feature importance of a machine learning model can be realized using SHapley Additive exPlanations (SHAP) [305] values for the features. SHAP values show how each feature affects each final prediction, the significance of each feature compared to others, and the model's reliance on the interaction between features. The SHAP values for the model are plotted in Fig. 4.9 using the `shap` module. It is distinctly observed that M_{bb} turns out to be the best discriminating feature. MET, M_{ll} and p_T^{ll} turn out to be the other important features which were also taken into account in the cut-based analysis. Corresponding to the threshold value of 0.95, the significance and cut efficiencies of the signal and background processes for the BDT analysis are detailed in Tab. 4.9. It is observed that for similar background numbers, there is a significant boost in the signal numbers for both SM and other EFT benchmark points, compared to the cut-based analysis.

BPs (κ_Z, C_{uW}, $C_{Hq}^{(3)}$)	S	B	S/B	z	ϵ_s	ϵ_b
SM (1.00, 0.00, 0.00)	4048	129397	0.0313	11.20	4.17×10^{-2}	8.74×10^{-4}
BP1 (1.00, 0.05, 0.00)	4217		0.0326	11.66	4.33×10^{-2}	
BP2 (1.00, 0.00, 0.05)	4762		0.0368	13.16	4.47×10^{-2}	
BP3 (1.00, 0.00, -0.05)	3484		0.0269	9.64	3.89×10^{-2}	

TABLE 4.9: Signal significance of the $Z(l^+l^-)h(b\bar{b})$ production process (at LHC 14 TeV 3000 fb^{-1}) from BDT based analysis (with threshold: 0.95) at different benchmark points (BPs) in presence of effective operators, along with signal (ϵ_s) and background (ϵ_b) efficiencies.

Two Parameter χ^2 Analysis The χ^2 test [241] serves as a statistical measure to evaluate the degree of conformity between empirical observations and theoretical expectations within the framework of a contingency table. In statistical literature, there exist a number of definitions for the χ^2 function. These definitions are more or less equivalent and can be used interchangeably. For our case, we shall use Pearson's definition where the χ^2 is defined as follows:

$$\chi^2 = \sum_j^{bins} \left(\frac{\mathscr{O}^j(\kappa_i, C_i) - \mathscr{O}^j_{\rm SM}}{\Delta N^j(\kappa_i, C_i)} \right)^2 = \sum_j^{bins} \left(\frac{\Delta\mathscr{O}^j(\kappa_i, C_i)}{\Delta N^j(\kappa_i, C_i)} \right)^2 . \tag{4.11}$$

Here, $\mathscr{O}$ is a differential distribution. For our analysis, $\mathscr{O} = (d\sigma/dM_{llbb})$, which is the invariant mass of all the visible final state particles following relevant cut/BDT analysis. We define $\Delta\mathscr{O}^j(\kappa_i, C_i) = \mathscr{O}^j(\kappa_i, C_i) - \mathscr{O}^j_{\rm SM}$, where $\mathscr{O}^j(\kappa_i, C_i)$ corresponds to events in the j^{th} bin of the M_{llbb} distribution, in presence of effective operators and coupling modifiers and $\mathscr{O}^j_{\rm SM}$ corresponds to signal events in the same bin under the SM process. $\Delta N^j(\kappa_i, C_i) = \sqrt{\mathscr{O}^j(\kappa_i, C_i) + \mathscr{O}^j_{\rm SM}}$ is the statistical uncertainty in the number of events for that bin.

Considering the better performance of the BDT analysis over the cut based analysis, we use the signal and background efficiencies based on the BDT analysis. The χ^2 analysis is performed corresponding to the binned M_{llbb} distribution. The dataset post the threshold cut is divided into 8 bins from 200-1000 GeV in intervals of 100 GeV. The events with higher values of M_{llbb} are removed in order to adhere to the EFT limit. The BDT analysis is repeated for several benchmarks on the parameter space and the distributions corresponding to some of the benchmarks are shown in App. 4.C. For a Poisson distributed binned data, the number of DOFs is given by $D = (N - M)$, where N is the

number of bins and M is the number of fitted parameters. In this case, $D = 8 - 2 = 6$. Usually the constraints on the parameter space of physical parameters are reported in terms of C.L. The C.L. can be interpreted from the χ^2 values. The 68% and 95% C.L. for $D = 6$ corresponds to $\chi^2 \approx 7.01$ and $\chi^2 \approx 12.59$ respectively. The χ^2 for different parameter benchmarks in $\kappa_Z - \kappa_B$ plane are shown in Fig. 4.10.

Fig. 4.10 shows that the 68% C.L. bounds are moderately sensitive to the parameter $C_{Hq}^{(3)}$ corresponding to the Higgs-current interaction. This is because $\sigma/\sigma_{\rm SM}$ changes significantly under the variation of $C_{Hq}^{(3)}$ in the Vh channel (see Fig. 4.5 left). However, it requires higher values of C_{uW} to show similar effect in the χ^2 plots. This is mostly due to the fact that the dipole operators contribute at $(1/\Lambda^4)$ order. Further, it should also be noted that the EFT effects can negate each other as evident from the benchmark $\{C_{uW}, C_{Hq}^{(3)}\} = \{0.05, -0.01\}$ (see Fig. 4.10 bottom right) where the positive contribution on the cross section from C_{uW} is cancelled by the negative contribution from $C_{Hq}^{(3)}$ showing negligible deviation from the SM contribution even for non-zero EFT contributions.

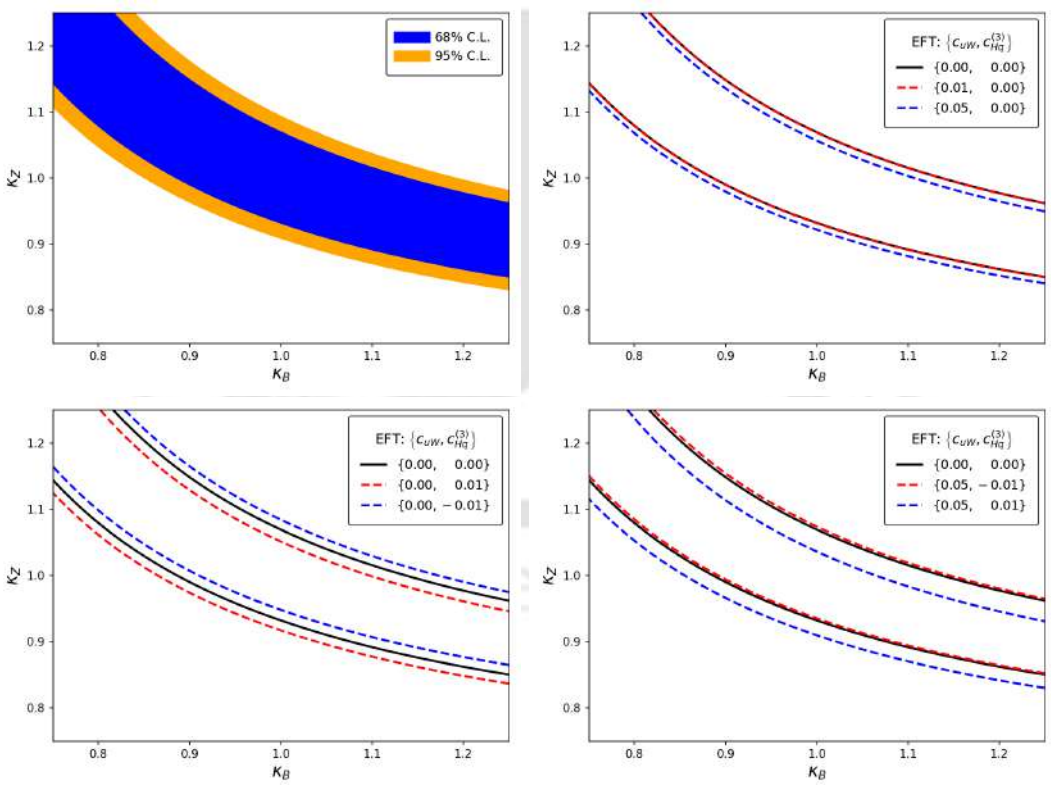

FIGURE 4.10: *Top Left:* χ^2 plots showing 68% C.L. and 95% bounds in the $\kappa_Z - \kappa_B$ space at LHC 14 TeV 3000 fb^{-1}. *Top Right, Bottom Left* and *Bottom Right:* Shift in 68% C.L. bounds for different values of effective coefficients.

The 68% and 95% C.L. bounds on the EFT couplings are shown in Fig. 4.11, which shows

similar sensitivities of the EFT operators and modifiers as in Fig. 4.10. The effects of EFT contributions to Z decay branching and the assumption of custodial symmetry on these bounds are discussed in App. 4.D and App. 4.E, respectively. Vh production has been studied in literature like [253, 259] focusing on the boosted regime. However, both these analyses do not consider the light quark dipole operators which we include in our analysis. Considering the boosted regime is interesting as EFT effects are strongly evident there and hence the bounds on $C_{Hq}^{(3)}$ are slightly more stringent in both studies compared to our case. However, as we emphasized in our paper, the boosted regime may invalidate the EFT assumption, necessitating careful consideration. Studies like [255, 260] focus on double differential observables with combination of multiple channels which results in further improvement in bound.

Similar to the M_{llbb} distribution, other sensitive observables like H_T (scalar sum of p_T of visible particles) can also be used to perform this analysis. Another popular method is to train a ML based algorithm that separates the SM and SM+EFT contribution based on a set of discriminating observables. However, such model requires better segregation between the observables of the two classes which is evidently difficult even at HL-LHC once we abide by the EFT limit.

Other Future *pp* Colliders As observed in Fig. 4.2 and 4.3, the Zh production cross section enhances for both the Higgs-current and dipole interactions, with increase in CM energy. This motivates the possibility of better extraction of these NP contributions at higher CM energy possible at future collider runs like the HE-LHC (expected to run at $\sqrt{s} = 27$ TeV), FCC-hh (expected to run at $\sqrt{s} = 100$ TeV), etc. $\sigma/\sigma_{\rm SM}$ is plotted in Fig. 4.12 (left) for different CM energies ($\sqrt{s}$) at some of the benchmarks $\{C_{uW}, C_{Hq}^{(3)}\}$: BP1 $\{0.05, 0.00\}$, BP2 $\{0.00, 0.05\}$ and BP3 $\{0.05, 0.05\}$. All the benchmarks show enhancement in EFT effects, however we observe stronger enhancement for the Higgs-current interaction (BP2) in comparison to the dipole interaction (BP1). The combined presence of both the operators (BP3) shows the highest enhancement in cross-section. While these results show promise to better estimate the dipole operator in particular, the prospect of accelerating protons to such high energies remains a distant possibility. Fig. 4.12 (right) shows the validity of EFT limit, having the invariant mass peak well below $\Lambda = 1$ TeV even in context of future pp colliders with higher CM energies.

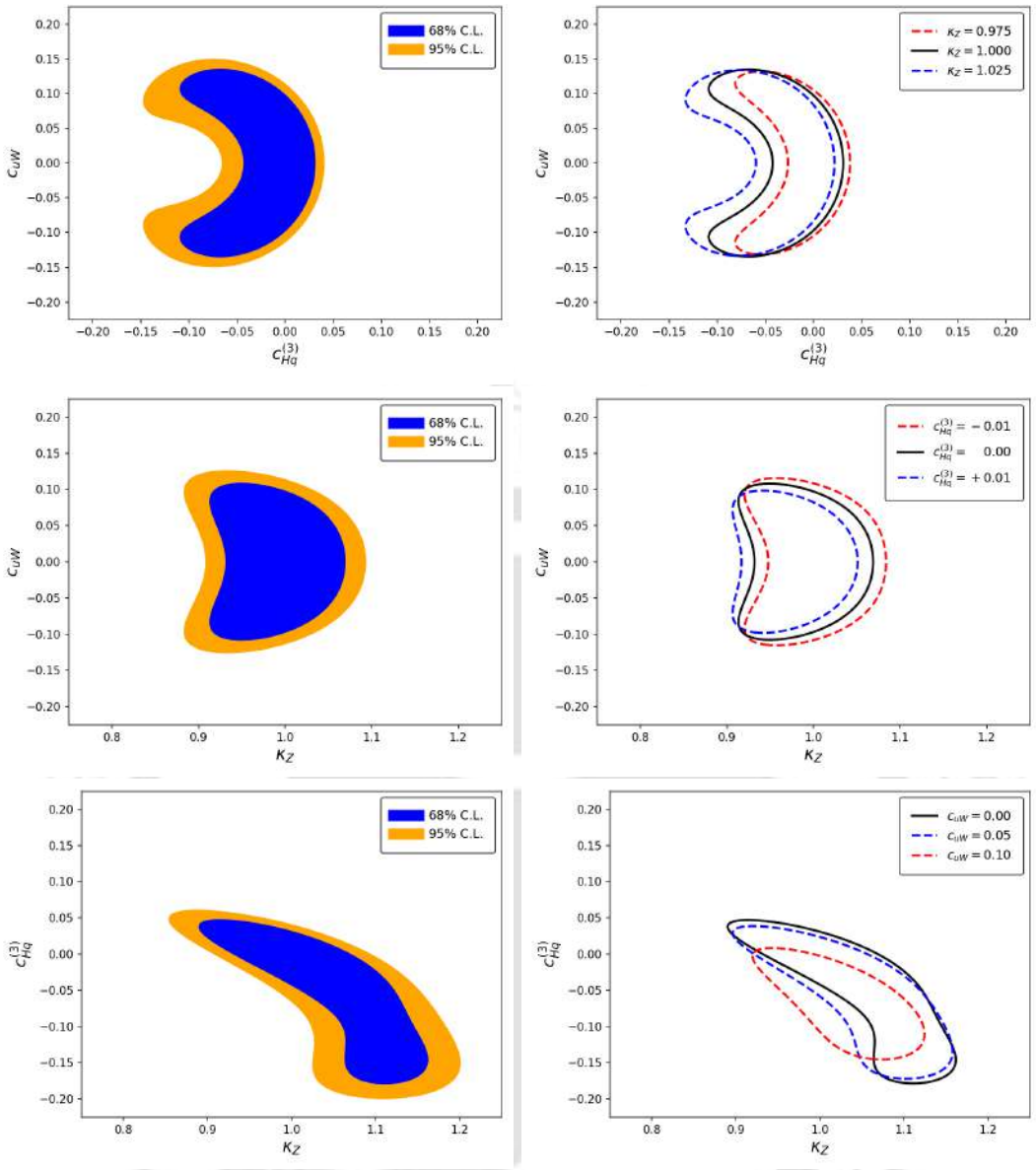

FIGURE 4.11: *Top Left, Middle Left* and *Bottom Left:* 68% and 95% C.L. bounds on effective coefficients at the 14 TeV 3000 fb^{-1} LHC. *Top Right, Middle Right* and *Bottom Right:* Shift in 68% C.L. in presence of different modifiers or EFT coefficients.

This happens due to the dominance of SM process, while larger WC would flatten the distribution having more events with higher invariant mass.

4.1.4 Summary and Conclusion

We have presented an analysis of Zh associated production at the LHC in the presence of dimension 6 SMEFT operators and coupling modifiers. We chose a simple parametrisation to match the coupling modifiers that stem from dimension 6 SMEFT operators

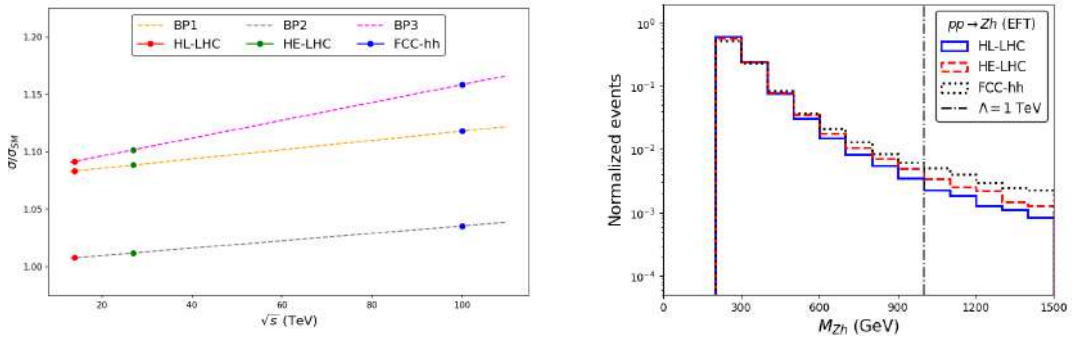

FIGURE 4.12: *Left:* Variation in the ratio of Zh production cross section to the SM cross section at different CM energies for benchmarks $\{C_{uW}, C_{Hq}^{(3)}\}$: BP1 $\{0.05, 0.00\}$, BP2 $\{0.00, 0.05\}$ and BP3 $\{0.05, 0.05\}$. *Right:* Invariant mass of Zh for the parton level processes in presence of EFT operators at BP3 for different future pp collider runs.

in the Warsaw basis. We analysed the signal and background contributions at various benchmark points, which allows maximum cross-section within the allowed values of the EFT parameters and coupling modifiers adhering to the constraints appearing from existing collider and flavour constraints. We performed both cut-based and BDT analyses using kinematic variables relevant to the process. The NP scale is safely chosen at $\Lambda = 1$ TeV, which abides by the effective limit having the invariant mass distribution peak appearing well below Λ.

A comparison of Tab. 4.8 and 4.9 shows that the BDT analysis performs better than the cut-based analysis presented in the previous section, as expected. One obtains almost a factor of 2 enhancement in the estimation of the significances for the various BPs considered in our analysis. This is due to the fact that the BDT comes with better efficiency for the signal events even though the background efficiency remains almost the same. We have obtained more than 9σ (5σ) significance using BDT (cut-based) analysis for all our chosen benchmark points. We further note that corresponding to our flavor scheme choice, $U(2)_q \times U(2)_u \times U(2)_d$, the corresponding background contributions have limited sensitivity to the EFT operators introduced here, hence we do not include them in our analysis.

A χ^2 analysis is performed in the two-dimensional parameter space of the EFT operator coefficients as well as in the coupling modifiers. The bounds on the $C_{uW} - C_{Hq}^{(3)}$ plane are more constrained than those on the $\kappa_Z - \kappa_B$ plane, owing to the fact that the differential distribution M_{llbb} is extremely sensitive to EFT effects especially at the tail. Based on the plots in Fig. 4.10, it is evident that the EFT contributions significantly alter the

bounds on the $\kappa_Z - \kappa_B$ plane. Similarly, coupling modifiers can also impact the bounds in the EFT coefficient planes as evident from Fig. 4.11. It is observed that even with the tight constraints on the operators, the presence of the Higgs-current operator $\mathcal{O}_{Hq}^{(3)}$ results in visible changes on the bounds in the $\kappa_Z - \kappa_B$ plane. The individual impact of the dipole operator $\mathcal{O}_{uW}$ is relatively small and does not show any significant deviation from the SM predictions. This is mainly because they do not interfere with the SM process and the contributions are obtained only at $(1/\Lambda^4)$ order. However, as discussed in Sec. 4.1.3, a significant increase in sensitivity is expected with an increase in the CM energy, possible at future high-energy collider runs. Even then, the contributions from $\mathcal{O}_{Hq}^{(3)}$ will still dominate.

In this analysis, we have omitted CP-odd contributions to the dipole operators, primarily because they are strongly bounded from EDM measurements. Therefore, it is difficult to detect their effects via signal cross-section. Dedicated CP-violating observables are required to decipher a disentanglement from that of a CP-even case. While addressing this challenge via inclusive cross-sections at hadron colliders is inherently limiting, we will directly tackle the isolation of these elusive CP-odd structures using spin-correlation asymmetries at lepton colliders in Sec. 4.3.

4.2 Optimal Extraction of Higgs-Gauge Couplings

Optimal estimation of Higgs-gauge boson couplings at the future e^+e^- colliders.
S. Bhattacharya, A. Subba, A. Sarkar.
Phys.Rev.D 112 (2025) 11, 11 (e-Print: 2508.08893 [hep-ph]).

A multitude of experimental investigations at the LHC [205, 242, 306–318] have imposed stringent constraints on the spin-parity quantum numbers of the Higgs boson, as well as its interactions with gluons and electroweak gauge bosons. Current measurements are in agreement with the SM prediction of a scalar boson with quantum numbers $J^{PC} = 0^{++}$. Nonetheless, the presence of small deviations from the SM in the form of anomalous couplings remains experimentally permissible. In BSM theories, interactions with the Higgs boson may occur through several anomalous couplings, which lead to new tensor structures in the interaction terms that can be both CP-even or CP-odd.

As noted in the previous section, the hadronic environment of the LHC imposes limitations on measurement precision due to QCD backgrounds, pile-up, and uncertainties associated with PDFs. This has motivated the proposal of high-luminosity and high-precision lepton colliders, such as the ILC [216, 218, 319–321], FCC-ee [322], CEPC [323–325] and CLiC [326–329], which offer a complementary environment for Higgs boson studies. Projected experimental uncertainties on Higgs couplings at future e^+e^- colliders are expected to reach the per-mille level [77, 216, 330–332], significantly surpassing the capabilities of the LHC.

A particularly clean setting for precision Higgs physics is provided by an e^+e^- collider operating at a center-of-mass energy of $\sqrt{s} = 250$ GeV, which is the focus of current work. In this energy regime, the dominant Higgs production channel is the Higgs-strahlung process, $e^+e^- \to Zh$, which proceeds via s-channel exchange of a Z boson. The Higgs-strahlung production mechanism allows for model-independent measurements of Higgs boson properties by reconstructing the Higgs mass from the recoil mass spectrum of the Z boson, independent of the Higgs decay mode. Moreover, the ability to polarize the initial e^- and e^+ beams in the linear collider provides an additional handle to disentangle helicity structures of electroweak interactions and enhance sensitivity to specific interaction channels.

In this section, we study the potential of the ILC to probe these anomalous Higgs-gauge couplings in the Zh production process. Building on the framework established in Sec. 4.1.1, we utilize SMEFT to parameterize deviations from the SM predictions. Our aim is to obtain the optimal limit on the operator coefficients contributing to the hZZ vertex and Zh production at the ILC.

This section is organized as follows: In Sec. 4.2.1, we briefly review the specific subset of SMEFT operators and bounds relevant to this lepton collider analysis. In Sec. 4.2.2, we discuss the event selection using the dilepton recoil mass observable. We focus on the $l^+l^-b\bar{b}$ final state owing to the large Higgs branching fraction to the $b\bar{b}$ channel. In Sec. 4.2.3, we discuss in brief the OOT methodology. In Sec. 4.2.4, we discuss the one parameter limits on WCs obtained for unpolarized and polarized beams scenario. We conclude in Sec. 4.2.5.

4.2.1 Operators Relevant to hVV Coupling

Building upon the SMEFT framework and the Warsaw basis operators established in Sec. 4.1.1, we focus on the three CP-even ($\mathcal{O}_{HW}$, $\mathcal{O}_{HB}$, $\mathcal{O}_{HWB}$) and their dual CP-odd ($\mathcal{O}_{H\widetilde{W}}$, $\mathcal{O}_{H\widetilde{B}}$, $\mathcal{O}_{H\widetilde{W}B}$) operators that induce anomalous contributions to the Zh production process. Upon EWSB, these operators induce anomalous contributions to the hZZ coupling of the form

$$\delta\,\Gamma_{hZZ} = \kappa_{hZZ}\left(\frac{h}{v}Z_{\mu\nu}Z^{\mu\nu}\right) + \kappa_{h\widetilde{Z}Z}\left(\frac{h}{v}\widetilde{Z}_{\mu\nu}Z^{\mu\nu}\right), \tag{4.12}$$

where

$$\begin{aligned}
\kappa_{hZZ} &= \frac{2v^2}{\Lambda^2}\left[\cos^2\theta_W\, C_{HW} + \cos\theta_W \sin\theta_W\, C_{HWB} + \sin^2\theta_W\, C_{HB}\right], \\
\kappa_{h\widetilde{Z}Z} &= \frac{2v^2}{\Lambda^2}\left[\cos^2\theta_W\, C_{H\widetilde{W}} + \cos\theta_W \sin\theta_W\, C_{H\widetilde{W}B} + \sin^2\theta_W\, C_{H\widetilde{B}}\right].
\end{aligned} \tag{4.13}$$

Apart from anomalous hZZ coupling, the operators allow for tree level s-channel Zh production mediated by a massless photon, which otherwise is a loop process in the SM. The anomalous $hZ\gamma$ coupling is obtained as,

$$\delta\,\Gamma_{hZ\gamma} = \kappa_{hZ\gamma}\left(\frac{h}{v}Z_{\mu\nu}A^{\mu\nu}\right) + \kappa_{h\widetilde{Z}\gamma}\left(\frac{h}{v}\widetilde{Z}_{\mu\nu}A^{\mu\nu}\right), \tag{4.14}$$

where

$$\begin{aligned}
\kappa_{hZ\gamma} &= \frac{v^2}{\Lambda^2}\left[2\cos\theta_W \sin\theta_W\,(C_{HW} - C_{HB}) + (\sin^2\theta_W - \cos^2\theta_W)\,C_{HWB}\right], \\
\kappa_{h\widetilde{Z}\gamma} &= \frac{v^2}{\Lambda^2}\left[2\cos\theta_W \sin\theta_W\,(C_{H\widetilde{W}} - C_{H\widetilde{B}}) + (\sin^2\theta_W - \cos^2\theta_W)\,C_{H\widetilde{W}B}\right].
\end{aligned} \tag{4.15}$$

We do not consider operators affecting $f\bar{f}V$ or $f\bar{f}VH$ couplings as they are tightly constrained from LEP data. Various studies [243, 254, 264–266, 333–360] have been done to probe the structure of anomalous Higgs-gauge couplings using the kinematic and angular distribution at LHC and e^+e^- colliders. Quantum tomography [361–365] has also been used to constrain anomalous $hVV, V \in \{Z, W\}$ coupling. On the experimental side, the current limits at 68% C.L. on the WCs of the above operators are provided by

CMS [366] (assuming $\Lambda = 1$ TeV):

$$\begin{aligned} C_{HW} &= [-0.79, +0.51], \quad & C_{H\widetilde{W}} &= [-0.76, +0.41], \\ C_{HWB} &= [-1.62, +1.50], \quad & C_{H\widetilde{W}B} &= [-1.57, +0.83], \\ C_{HB} &= [-0.23, +0.16], \quad & C_{H\widetilde{B}} &= [-0.23, +0.12]. \end{aligned} \tag{4.16}$$

As stated before, in this work we explore the extent to which optimal observable analysis of production cross-sections can constrain modifications to the Higgs-gauge couplings, and highlight the complementarity of this program with current LHC studies. Our analysis underscores the central role that an e^+e^- Higgs factory can play in elucidating the nature of electroweak symmetry breaking and probing the structure of BSM physics.

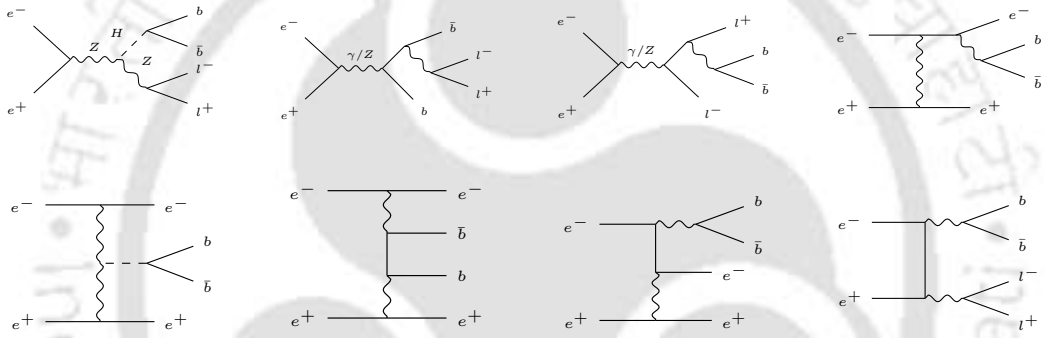

FIGURE 4.13: Representative Feynman diagrams denoting the production of two leptons and two b quarks at the leading order in the SM.

4.2.2 Collider Analysis: ILC 250 GeV

The signal process considered here is the Higgs-strahlung process followed by the leptonic decay of the Z boson and the Higgs boson decay to a pair of b-quarks at the ILC, i.e., $e^+e^- \to Z(l^+l^-)h(b\bar{b})$ for the SM as well as the dimension 6 effective operators listed in Tab. 4.1 that contribute to it. The dominant background to the $l^+l^-b\bar{b}$ final state arises from $e^+e^- \to Z(l^+l^-)Z(b\bar{b})$. A subdominant background from Z-boson fusion Higgs production, $e^+e^- \to e^+e^-h(b\bar{b})$, contributes negligibly at $\sqrt{s} = 250$ GeV and is therefore neglected. The $ZZ\gamma$ process could also dilute the analysis; however, the p_T cut on final photons reduces such contribution significantly. We also consider the effect of ISR on the overall selection kinematics of the processes. The schematic Feynman

diagrams representing signal and some of the background processes are illustrated in Fig. 4.13.

Operationally, the dimension 6 operators listed in Tab. 4.1 are implemented in `FeynRules` [233] to obtain a UFO model file. The corresponding UFO model [234] is exported to `MG5_aMC` [235] for Monte Carlo event generation. The matrix level events are then passed through `Pythia8` [236] for showering of partons and hadronization of final state particles. Finally, the detector simulations are implemented using `Delphes3` [237] with the ILC parameters [219]. For b-tagging of final jets, we employ the loose working point, corresponding to an average tagging efficiency of 80%. Event selection requires exactly two oppositely charged leptons and two b-tagged jets, with the additional condition that the final state contains no hard ($p_T > 10$ GeV) photons.

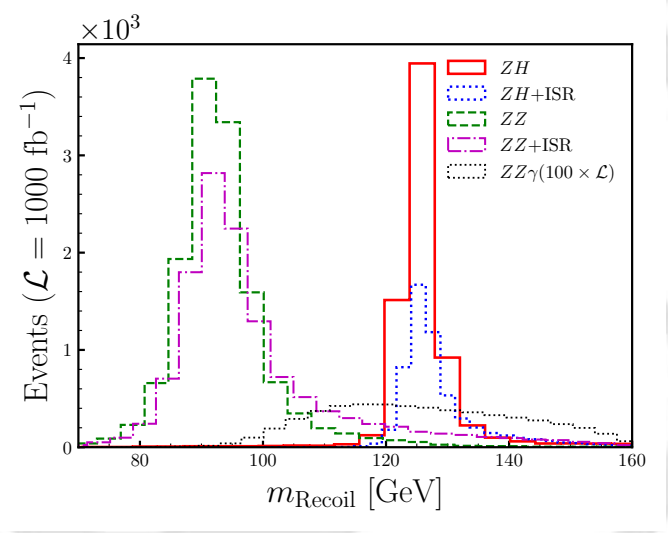

FIGURE 4.14: Recoil mass distribution normalized to $\mathfrak{L}_{\rm int} = 1000$ fb^{-1} for signal and two background processes viz. ZZ and $ZZ\gamma$. The kinematic effect of ISR are highlighted for Zh and ZZ processes.

In order to select the phase space which maximizes the significance, a number of kinematic variables are constructed using the four momenta of final four objects. We train `LightGBM` BDT models separately for the unpolarized and polarized beam configurations: $(P_{e^+}, P_{e^-}) = (+30\%, -80\%)$ and $(-30\%, +80\%)$, respectively. The input features for the BDTs consist of several kinematic observables, whose details are provided in App. 4.F. Among these variables, the recoil mass of the dilepton system, $m_{\rm Recoil}$, emerges as the most effective discriminator between signal and background. The distribution normalized to $\mathfrak{L}_{\rm int} = 1000$ fb^{-1} representing $m_{\rm Recoil}$ for signal and two major background processes (ZZ and $ZZ\gamma$) with and without ISR are shown in Fig. 4.14. The p_T cut on the final

photons removes the $ZZ\gamma$ background significantly, and the corresponding distributions are rescaled by a factor of 100 in integrated luminosity for visualization. The number of events for the case of the signal (Zh) reduces due to ISR as the interaction energy lowers below 250 GeV, leading to a lower cross-section. However, no significant change in shape and count is observed for the ZZ process. Nevertheless, the recoil mass stands out to nullify the effect of ISR on segregating the signal phase space from that of the background. We apply the following selection cut on the recoil mass:

$$|m_{\text{Recoil}} - m_h| < 2 \text{ GeV}\,, \tag{4.17}$$

Events and signal significance before and after the m_{Recoil} cut are furnished in Tab. 4.10 for both polarized and unpolarized beams. After applying the recoil mass cut, we find that the background becomes nearly negligible compared to the signal.

(P_{e^+}, P_{e^-})	Process	Before m_{Recoil} cut		After m_{Recoil} cut	
		Events	$\mathcal{Z} = S/B$	Events	$\mathcal{Z} = S/B$
Unpolarized	Signal (S)	1879	0.11	1610	36.9
	Background (B)	16652		44	
$(+30\%, -80\%)$	Signal (S)	2580	0.12	2189	31.2
	Background (B)	21252		70	
$(-30\%, +80\%)$	Signal (S)	2045	0.13	1746	61.0
	Background (B)	15722		29	

TABLE 4.10: Cutflow table for signal and backgrounds, at the ILC $\sqrt{s} = 250$ GeV and an integrated luminosity of 1000 fb^{-1}.

4.2.3 Optimal Statistical Significance

The OOT [232, 367–370] is a powerful method to estimate model parameters or couplings from experimental data with maximum statistical sensitivity. By constructing observables that are analytically derived from the dependence of the differential cross-section on the parameters of interest, this approach ensures the most efficient use of the available kinematic information by minimizing the covariance matrix. It is particularly useful in precision measurements, where small deviations from the SM predictions are expected to be estimated. The differential cross section for any given collider process can be written

in the form

$$\mathcal{O}(\phi) = \frac{d\sigma}{d\phi}\bigg|_{\texttt{observed}} = \epsilon_{\texttt{S}} \, \frac{d\sigma}{d\phi}\bigg|_{\texttt{S,theory}} + \epsilon_{\texttt{B}} \, \frac{d\sigma}{d\phi}\bigg|_{\texttt{B,theory}} = \sum_i \, g_i f_i(\phi) \,, \tag{4.18}$$

where ϕ is a phase-space variable, g_i are the functions containing the NP couplings, and f_i are the functions of the phase-space variable, ϕ. The subscripts $\texttt{S}$ and $\texttt{B}$ refer to signal and background, respectively. $\epsilon_{\texttt{S}}$ and $\epsilon_{\texttt{B}}$ are the signal and background detection efficiencies, following all the cuts and final state signal identification. The optimal covariance matrix upon minimization ($\partial V_{ij}/\partial g_j = 0$) is obtained as,

$$V_{ij} = \frac{M_{ij}^{-1}}{\mathfrak{L}_{\text{int}}} = \frac{1}{\mathfrak{L}_{\text{int}}} \int \frac{f_i(\phi) f_j(\phi)}{\mathcal{O}(\phi)} d\phi \,. \tag{4.19}$$

Correspondingly, the optimal χ^2 is given by

$$\chi^2 = \sum_{i,j} \, (g_i - g_i^0) \; V_{ij}^{-1} \; (g_j - g_j^0) \, \Big|_{g=g^0} \,, \tag{4.20}$$

where g^0 corresponds to the seed values of the coefficients g. The input seed values can come from different sources like available measurements, predictions from a different experiment, etc. In the case of sensitivity prediction of an unobserved NP scenario, the seed value is usually determined by setting the seed values of the NP couplings to zero.

For $e^+e^- \to Zh$ production at the ILC, we map the accessible phase space using the variable $\cos\theta$, which is the emerging angle of the Z boson. The differential observable can be written in terms of polarization degrees as

$$\begin{aligned}
\mathcal{O}(\cos\theta) \; &= \epsilon_{\texttt{S}} \, \frac{d\sigma}{d\cos\theta}\bigg|_{\texttt{S,theory}} \\
&= \epsilon_{\texttt{S}} \; \left\{ g_0^L \, (1 - \overline{P_{e^+}})(1 - P_{e^-}) + g_0^R \, (1 + \overline{P_{e^+}})(1 + P_{e^-}) \right\} f_0 \\
&+ \; \epsilon_{\texttt{S}} \; \left\{ g_1^L \, (1 - \overline{P_{e^+}})(1 - P_{e^-}) + g_1^R \, (1 + \overline{P_{e^+}})(1 + P_{e^-}) \right\} f_1 \\
&+ \; \epsilon_{\texttt{S}} \; \left\{ g_2^L \, (1 - \overline{P_{e^+}})(1 - P_{e^-}) + g_2^R \, (1 + \overline{P_{e^+}})(1 + P_{e^-}) \right\} f_2 \,.
\end{aligned} \tag{4.21}$$

The background contribution is small after the signal selection cuts are applied, as seen from Sec. 4.2.2, and this has been neglected to estimate optimal sensitivity. The linearly independent phase-space functions f_i are defined as follows:

$$f_0 = \beta \,, \qquad f_1 = \beta \cos\theta \,, \qquad f_2 = \beta \cos^2\theta \,, \tag{4.22}$$

where,

$$\beta = \frac{\sqrt{\lambda(s, m_Z^2, m_h^2)}}{32\pi s^2}\,. \tag{4.23}$$

Here, λ is the Källén function defined as $\lambda(x, y, z) = x^2 + y^2 + z^2 - 2xy - 2yz - 2zx$. With $\sqrt{s} = 250$ GeV, $m_Z = 91$ GeV and $m_h = 125$ GeV, we obtain: $\beta \approx 31$ pb. With all the SM constants replaced by their respective values, the dimensionless g_i as in Eq. (4.21) turn out to be functions of the WCs only. We list the expressions for g_i in App. 4.G. Given that there is no hint of BSM, we choose the seed values of all the WCs to be zero to find an optimal range in which they can be extracted.

4.2.4 Sensitivity of EFT Operators

In this section, we present projected sensitivities to the dimension 6 operators (listed in Tab. 4.1) derived using the OOT. Constraints on the corresponding WCs are obtained following the optimized signal selection strategy described earlier. We perform the analysis for various beam polarization configurations, highlighting the improvement in sensitivity enabled by polarized e^+e^- collisions. For benchmarking, we also compare our projections with existing limits from the LHC and provide estimates relevant to future collider runs. Tab. 4.11 summarizes the optimal 68% CL limits (corresponding to $\chi^2 = 1$) on the WCs at the ILC with $\sqrt{s} = 250$ GeV, in comparison with current CMS constraints at 13 TeV with $\mathfrak{L}_{\text{int}} = 138$ fb^{-1}. Two ILC scenarios are considered: (**I**) unpolarized beams with $\mathfrak{L}_{\text{int}} = 138$ fb^{-1}, and (**II**) a polarized setup combining $(+30\%, -80\%)$ and $(-30\%, +80\%)$ beam configurations, each contributing 69 fb^{-1}, summing to the same total integrated luminosity.

The sensitivity to the CP-even operator C_{HW} improves by approximately a factor of 6 in the unpolarized ILC scenario compared to the current LHC constraints, with beam polarization providing an additional enhancement to about a factor of 7. For C_{HWB}, the improvement is even more pronounced, reaching nearly a factor of 7 in the unpolarized case and exceeding a factor of 10 when polarized beams are employed. In the case of C_{HB}, the unpolarized ILC limit is slightly weaker than the LHC bound; however, the introduction of beam polarization yields an improvement of roughly 1.5 times. These results highlight the critical role of beam polarization in maximizing the precision reach of future lepton colliders.

WCs	LHC (13 TeV 138 fb^{-1})	ILC (250 GeV 138 fb^{-1})	
		Unpolarized	Polarized ($\pm 30\%, \mp 80\%$)
C_{HW}	$[-0.79, +0.51]$	$[-0.11, +0.11]$	$[-0.09, +0.08]$
C_{HWB}	$[-1.62, +1.50]$	$[-0.24, +0.22]$	$[-0.16, +0.15]$
C_{HB}	$[-0.23, +0.16]$	$[-0.69, +0.41]$	$[-0.14, +0.14]$
$C_{H\widetilde{W}}$	$[-0.76, +0.41]$	$[-1.36, +1.36]$	$[-1.16, +1.16]$
$C_{H\widetilde{W}B}$	$[-1.57, +0.83]$	$[-2.50, +2.50]$	$[-1.98, +1.98]$
$C_{H\widetilde{B}}$	$[-0.23, +0.12]$	$[-2.16, +2.16]$	$[-1.84, +1.84]$

TABLE 4.11: 68% CL bounds on CP-even (*top half*) and CP-odd (*bottom half*) operator coefficients at the LHC vs. from Zh production at the ILC 250 GeV. For the polarized case, we choose $\mathfrak{L}_{\text{int}} = 69$ fb^{-1} for polarization setups $(+30\%, -80\%)$ and $(-30\%, +80\%)$ each.

For the CP-odd operators, the current LHC limits generally demonstrate stronger sensitivity compared to the ILC projections obtained via the optimal observable technique. This reduced sensitivity at the ILC arises because the optimal observable method probes CP-odd effects predominantly at the quadratic level in the differential cross section, which inherently suppresses the constraints. As reflected in Tab. 4.11, the allowed parameter ranges for these operators remain significantly wider at the ILC, even with beam polarization. To enhance sensitivity to CP-odd operators, alternative strategies, such as leveraging spin-polarization asymmetries or dedicated CP-odd observables, could provide more powerful and direct probes, thus offering complementary avenues to tighten these bounds at future lepton colliders. A detailed study exploiting these specific observables to robustly constrain CP-odd operators is presented in Section 4.3.

We further study the projected sensitivities of the relevant SMEFT operator coefficients at the ILC with an integrated luminosity of 1000 fb^{-1} per polarization configuration, and a combined dataset yielding 2000 fb^{-1} luminosity. The one-parameter sensitivity projections are shown in Fig. 4.15 for graphical representation. The gray dashed lines indicate the 68% C.L. i.e., $\chi^2 = 1$ and 95% CL ($\chi^2 = 3.84$) thresholds. The corresponding numerical limits are listed in Tab. 4.12. For the CP-even operators, the results demonstrate notable variations in sensitivity across the different configurations. The C_{HW} operator benefits significantly from beam polarization; the $(+30\%, -80\%)$ setup yields the most stringent bounds at both 68% and 95% C.L., improving roughly by a factor of two compared to the unpolarized case. The $(-30\%, +80\%)$ configuration shows weaker

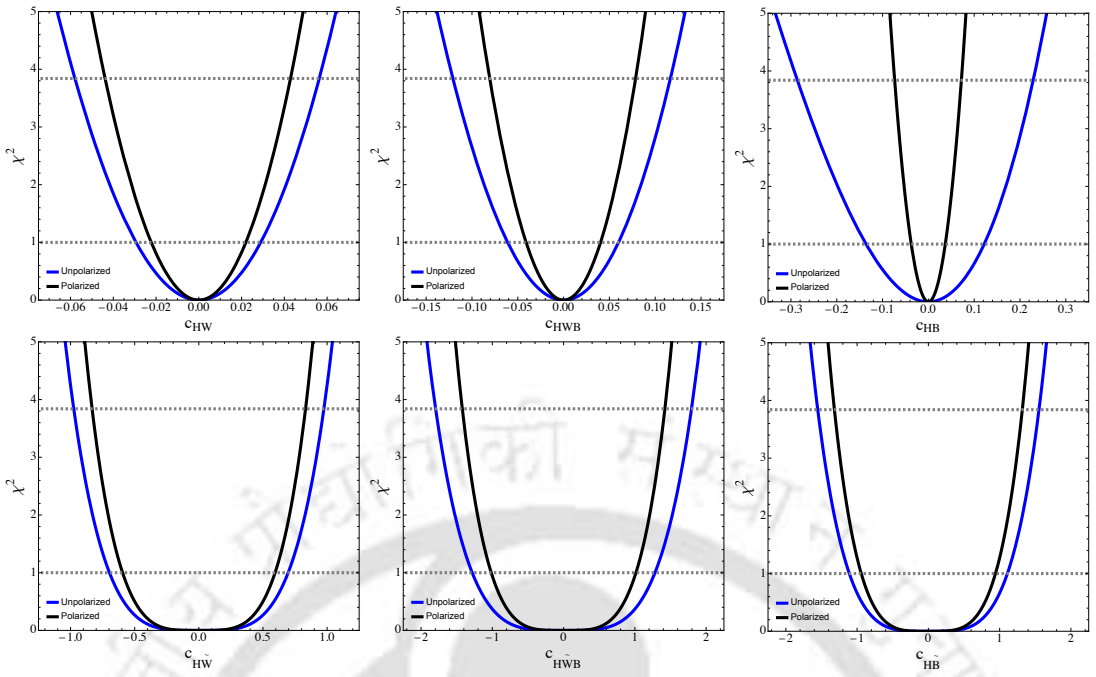

FIGURE 4.15: One parameter optimal sensitivity plots from Zh production at the ILC 250 GeV for unpolarized and polarized setups. For the unpolarized case, $\mathfrak{L}_{\text{int}} = 2000$ fb^{-1}, and for the polarized case each polarization setup i.e. $(+30\%, -80\%)$ and $(-30\%, +80\%)$ corresponds to $\mathfrak{L}_{\text{int}} = 1000$ fb^{-1}, hence giving a combined luminosity, $\mathfrak{L}_{\text{int}} = 2000$ fb^{-1}.

WCs	**C.L.**	**Projected sensitivities**				
		Unpolarized		**(+30%, −80%)**	**(−30%, +80%)**	**Polarized**
		$\mathfrak{L}_{\text{int}} = 1000$ fb^{-1}	$\mathfrak{L}_{\text{int}} = 2000$ fb^{-1}	$\mathfrak{L}_{\text{int}} = 1000$ fb^{-1}	$\mathfrak{L}_{\text{int}} = 1000$ fb^{-1}	$\mathfrak{L}_{\text{int}} = 2000$ fb^{-1}
C_{HW}	68%	$[-0.04, +0.04]$	$[-0.03, +0.03]$	$[-0.02, +0.02]$	$[-0.17, +0.16]$	$[-0.02, +0.02]$
	95%	$[-0.08, +0.08]$	$[-0.06, +0.06]$	$[-0.04, +0.04]$	$[-0.34, +0.31]$	$[-0.04, +0.04]$
C_{HWB}	68%	$[-0.09, +0.08]$	$[-0.06, +0.06]$	$[-0.33, +0.31]$	$[-0.04, +0.04]$	$[-0.04, +0.04]$
	95%	$[-0.17, +0.16]$	$[-0.12, +0.12]$	$[-0.66, +0.60]$	$[-0.08, +0.08]$	$[-0.08, +0.08]$
C_{HB}	68%	$[-0.20, +0.17]$	$[-0.14, +0.12]$	$[-0.10, +0.10]$	$[-0.04, +0.04]$	$[-0.04, +0.04]$
	95%	$[-0.44, +0.31]$	$[-0.28, +0.23]$	$[-0.19, +0.20]$	$[-0.08, +0.08]$	$[-0.07, +0.07]$
$C_{H\widetilde{W}}$	68%	$[-0.83, +0.83]$	$[-0.70, +0.70]$	$[-0.60, +0.60]$	$[-2.18, +2.18]$	$[-0.59, +0.59]$
	95%	$[-1.16, +1.16]$	$[-0.98, +0.98]$	$[-0.83, +0.83]$	$[-3.05, +3.05]$	$[-0.83, +0.83]$
$C_{H\widetilde{W}B}$	68%	$[-1.52, +1.52]$	$[-1.28, +1.28]$	$[-4.28, +4.28]$	$[-1.02, +1.02]$	$[-1.02, +1.02]$
	95%	$[-2.14, +2.14]$	$[-1.80, +1.80]$	$[-5.99, +5.99]$	$[-1.42, +1.42]$	$[-1.42, +1.42]$
$C_{H\widetilde{B}}$	68%	$[-1.32, +1.32]$	$[-1.11, +1.11]$	$[-2.04, +2.04]$	$[-0.95, +0.95]$	$[-0.94, +0.94]$
	95%	$[-1.85, +1.85]$	$[-1.55, +1.55]$	$[-2.86, +2.86]$	$[-1.33, +1.33]$	$[-1.32, +1.32]$

TABLE 4.12: Projected sensitivities of CP-even (*top half*) and CP-odd (*bottom half*) SMEFT operator coefficients from Zh production at the ILC 250 GeV. For the polarized setup, we combine polarization setups: $(+30\%, -80\%)$ and $(-30\%, +80\%)$, each with luminosities, $\mathfrak{L}_{\text{int}} = 1000$ fb^{-1}, hence the combined setup of $\mathfrak{L}_{\text{int}} = 2000$ fb^{-1}.

sensitivity for this operator, illustrating the asymmetric impact of polarization states. In the case of C_{HWB}, the situation is reversed with the $(-30\%, +80\%)$ polarization providing the strongest limits, surpassing both the unpolarized and the $(+30\%, -80\%)$ runs by

a considerable margin. This complementarity between polarized states underscores the importance of running both configurations for a comprehensive probe. The combined analysis again improves the bounds further, achieving nearly a factor of two improvement over single configurations. For C_{HB}, the $(-30\%, +80\%)$ polarization scenario delivers the best sensitivity, with bounds tighter by roughly a factor of four compared to the unpolarized run.

Turning to the CP-odd operators, the sensitivities exhibit a more varied pattern. For $C_{H\widetilde{W}}$, the $(+30\%, -80\%)$ polarization setup outperforms the others, improving constraints by approximately 30% relative to unpolarized collisions. The flipped polarization configuration is less sensitive. For $C_{H\widetilde{W}B}$ and $C_{H\widetilde{B}}$, the $(-30\%, +80\%)$ run provides stronger bounds than either unpolarized or flipped configuration individually. However, combining all data still leads to a modest but meaningful improvement, demonstrating the statistical benefit of aggregating diverse polarization states. Overall, these projections emphasize the critical role of beam polarization in enhancing sensitivity to dimension 6 operators at the ILC, with different operators responding distinctly to polarization choices. The combined dataset invariably delivers the most stringent bounds, leveraging the complementarity and statistical gains across all configurations.

We further compare our results with [358], which analyzed $e^+e^- \to Zh$ at $\sqrt{s} = 250$ GeV under identical beam polarizations and an integrated luminosity of 2000 fb^{-1}. That study parameterized the anomalous hZZ vertex in terms of three real couplings, a_Z, b_Z, and $\widetilde{b}_Z$, extracted from angular and cross-section observables. In the SMEFT framework, our dimension 6 operators contribute only to b_Z and $\widetilde{b}_Z$. Inverting the couplings, we obtain $b_Z \in [-0.0079, +0.0079]$ and $\bar{b}_Z \in [-1.517, +1.517]$. The bound on the CP-even parameter b_Z agrees well with [358], while the much weaker limit on the CP-odd parameter $\bar{b}_Z$, about two orders of magnitude larger, reflects the limited CP sensitivity of total cross-section observables and underscores the need for the dedicated CP-odd and spin-correlation analyses discussed in the next section. In addition, the two parameter sensitivity contours are illustrated in Fig. 4.16, providing a complementary view of the correlations and degeneracies between operator coefficients that are not captured in the one parameter analysis. Additional sensitivity contours are presented in App. 4.I.

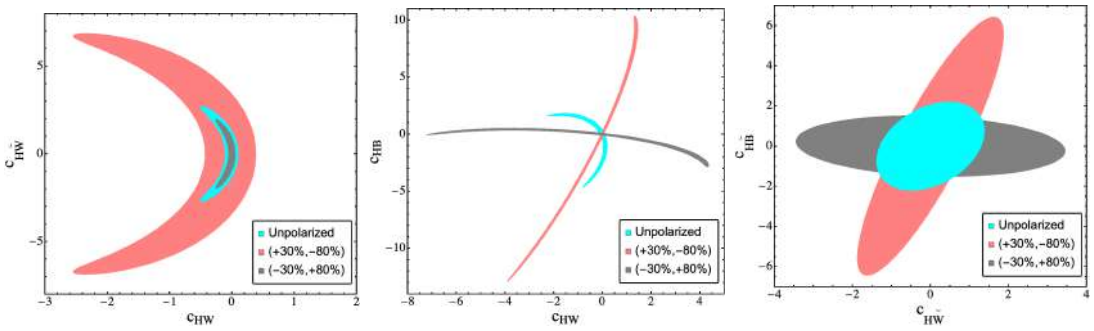

FIGURE 4.16: Two parameter 95% CL optimal sensitivity plots from Zh production at the ILC 250 GeV for unpolarized and different polarization setups. For each setup, $\mathfrak{L}_{\text{int}} = 1000$ fb^{-1}.

4.2.5 Summary and Conclusion

The associated production of a single Higgs boson with a Z boson, commonly referred to as the Higgs-strahlung process, offers a clean and model-independent channel to probe Higgs-gauge couplings with high precision. In this study, we focused on the final state consisting of two oppositely charged, same-flavor leptons and two b-tagged jets in e^+e^- collisions at a CM energy of $\sqrt{s} = 250$ GeV, incorporating scenarios with polarized initial beams. The deviations from the SM expectations are parameterized by the SMEFT framework, allowing us to constrain the coefficients of higher-dimensional operators that modify the hZZ and $hZ\gamma$ interactions. Event selection is performed via the recoil mass technique, targeting the Higgs boson through the invariant mass spectrum of the Z-tagged dilepton system.

The statistical extraction of the sensitivity to the WCs is carried out using the OOT, which maximizes information from kinematic distributions by exploiting interference patterns between SM and SMEFT amplitudes. Our analysis demonstrates that beam polarization plays a crucial role in enhancing sensitivity to various operators. When comparing our results with current bounds from the CMS experiment at $\sqrt{s} = 13$ TeV and $\mathfrak{L}_{\text{int}} = 138$ fb^{-1}, we find that the ILC setup, with polarized beams, yields significantly tighter constraints, improving the bounds on CP-even operators by factors ranging from 1.5 to 10. This improvement stems from the linear interference term between the SM and the CP-even SMEFT contributions, which scales as $1/\Lambda^2$ and benefits strongly from the clean environment and polarization of the e^+e^- collider.

On the other hand, the sensitivity to CP-odd operators is comparatively weaker than that of CMS. This is attributed to the fact that CP-odd operators contribute dominantly

at quadratic order in $1/\Lambda^2$, resulting in suppressed effects at the amplitude level. Consequently, our observable, being inclusive in nature, lacks sensitivity to CP-odd interference effects. This highlights the need for a more targeted analysis involving CP-sensitive observables such as angular asymmetries, triple-product correlations, or differential distributions optimized for CP violation, a task we undertake directly in Sec. 4.3.

Finally, we present projections at higher integrated luminosity of $\mathfrak{L}_{\text{int}} = 2000$ fb^{-1} for two different ILC running scenarios: an unpolarized beam and a combination of two complementary polarized beam configurations $(+30\%, -80\%)$ and $(-30\%, +80\%)$, with integrated luminosity of $\mathfrak{L}_{\text{int}} = 2000$ fb^{-1} each. We observe that different polarization choices enhance sensitivity to different subsets of operators due to their distinct helicity structures. The combination of the two polarization configurations, with $\mathfrak{L}_{\text{int}} = 2000$ fb^{-1}, yields the strongest bounds across the operator basis, effectively exploiting the polarization-enhanced interference terms. These results reinforce the power of polarized e^+e^- collisions at the ILC in probing new physics in the Higgs sector with high precision.

4.3 Spin Asymmetries for Higgs-Gauge Couplings

Probing CP-violating Higgs-gauge couplings with Higgsstrahlung at e^-e^+ colliders.
A. Subba, S. Bhattacharya, A. Sarkar.
Phys.Rev.D 113 (2026) 5, 055018 (e-Print: 2511.18541 [hep-ph]).

In Sec. 4.2, we explored anomalous hZZ and $hZ\gamma$ couplings at the e^+e^- collider setup using the OOT, which determines the maximal sensitivity achievable from cross section-based observables. While that approach demonstrated significant improvement in constraining the CP-even operators beyond current LHC bounds, the sensitivity to CP-odd operators remained limited. This is primarily because such operators do not interfere with the SM amplitudes in total cross section-based measurements, making their effects harder to detect through traditional observables. Polarization and spin-correlation observables provide a more incisive probe of CP-odd operators, as they are sensitive to interference effects that remain inaccessible in inclusive cross-section measurements.

In this section, we extend our investigation of the $e^+e^- \to Zh$ production process at the ILC ($\sqrt{s} = 250$ GeV) by simultaneously analyzing the Z boson polarization and

the spin correlations among multiple vector bosons originating from the Higgs decays. This enables a comprehensive assessment of the sensitivity to both CP-even and CP-odd anomalous hVV interactions. Specifically, we consider three dominant Higgs decay channels: $h \to b\bar{b}$, $h \to WW^*$, and $h \to ZZ^*$. While the $b\bar{b}$ mode provides the highest event statistics, the WW^* and ZZ^* channels offer complementary advantages by introducing anomalous contributions at both the production and decay vertices. The resulting spin-correlated observables constitute a rich set of kinematic handles, whose combined effects substantially enhance the overall sensitivity to both CP-even and CP-odd operators.

Building upon the SMEFT framework and the Warsaw basis operators established in Sec. 4.1.1, the anomalous contributions introduced modify the production and decay of the Higgs boson, particularly in processes involving neutral and charged electroweak gauge bosons. The modifications to the hZZ and $hZ\gamma$ vertices follow the exact parametrizations detailed previously in Sec. 4.2.1. Furthermore, the inclusion of the $h \to WW^*$ decay channel requires the consideration of anomalous hWW couplings. The EFT operators contribute to the hWW vertex via the following modifications:

$$\delta\,\Gamma_{hWW} = \kappa_{hWW}\left(\frac{h}{v}\,W^{+}_{\mu\nu}W^{-\mu\nu}\right) + \kappa_{h\widetilde{W}W}\left(\frac{h}{v}\,\widetilde{W}^{+}_{\mu\nu}W^{-\mu\nu}\right), \tag{4.24}$$

where

$$\kappa_{hWW} = \frac{2v^2}{\Lambda^2}C_{HW}\,, \qquad \kappa_{h\widetilde{W}W} = \frac{2v^2}{\Lambda^2}C_{H\widetilde{W}}\,. \tag{4.25}$$

As noted, the CP-even terms interfere with SM amplitudes, allowing their effects to appear at $\mathcal{O}(1/\Lambda^2)$ in observables like cross sections and decay rates. In contrast, the CP-odd contributions remain suppressed to $\mathcal{O}(1/\Lambda^4)$ in such observables, making their detectability far more challenging. The next section describes the construction of spin-related observables used in this study and the specific asymmetries employed to isolate the $\mathcal{O}(1/\Lambda^2)$ interference effects of the various CP-violating SMEFT operators.

The remainder of this section is organized as follows: The reconstruction methodology of spin-related observables is detailed in Sec. 4.3.1. The results of the sensitivity analysis across the three principal Higgs decay channels are presented in Sec. 4.3.2. A global interpretation combining information from all decay modes is provided in Sec. 4.3.3. Finally, the main conclusions of this spin asymmetry study are summarized in Sec. 4.3.4.

4.3.1 CP-even and CP-odd Observables

In the presence of both a CP-even operator ($\mathcal{O}_E$) and a CP-odd operator ($\mathcal{O}_O$) at dimension 6, the structure of any observable can be understood from the squared matrix element,

$$\begin{aligned}|\mathcal{M}|^2 &= |\mathcal{M}_{\rm SM} + \mathcal{M}_E + \mathcal{M}_O|^2 \\ &= |\mathcal{M}_{\rm SM}|^2 + 2\ {\rm Re}\,(\mathcal{M}^\star_{\rm SM}\mathcal{M}_E + \mathcal{M}^\star_{\rm SM}\mathcal{M}_O + \mathcal{M}^*_E\mathcal{M}_O) + |\mathcal{M}_E|^2 + |\mathcal{M}_O|^2. \quad (4.26)\end{aligned}$$

This expansion is completely general, and the contribution of each term depends on the CP properties of the observable under consideration. For CP-even observables, such as the total or differential cross section, the interference terms that are odd under a CP transformation vanish after phase-space integration. In particular, the terms

$$2\ {\rm Re}\,(\mathcal{M}^\star_{\rm SM}\mathcal{M}_O + \mathcal{M}^\star_E\mathcal{M}_O) \quad (4.27)$$

do not contribute, as they are CP-odd by construction. Consequently, the leading NP contribution to CP-even quantities arises from the interference between the SM amplitude and the CP-even operator, scaling as $\mathcal{O}(\Lambda^{-2})$, followed by pure dimension 6 squared contributions of order $\mathcal{O}(\Lambda^{-4})$.

In contrast, CP-odd observables are specifically designed to be odd under CP transformations. For such quantities, the interference between the SM and the CP-odd operator, ${\rm Re}(\mathcal{M}^\star_{\rm SM}\mathcal{M}_O)$, provides the leading non-vanishing term, contributing at $\mathcal{O}(\Lambda^{-2})$. Additional effects from the interference between two dimension 6 operators, ${\rm Re}(\mathcal{M}^\star_E\mathcal{M}_O)$, appear at $\mathcal{O}(\Lambda^{-4})$. Hence, the construction of observables sensitive to CP-odd effects is essential, as they retain the interference terms that vanish in inclusive or CP-even measurements, thereby providing enhanced sensitivity to CP-violating NP already at the interference level.

The polarization and spin correlation parameters of the massive spin-1 boson provide a large set of observables which have an $\mathcal{O}(\Lambda^{-2})$ dependence with CP-violating higher dimensional operators. In general, for a system of N particles with spin $s \in \{s_1, s_2, \cdots, s_n\}$, there will be a total of $4s_1(s_1+1) \times 4s_2(s_2+1)\cdots 4s_n(s_n+1)$ spin observables. Considering $e^-e^+ \to Zh$ production, our three chosen decay channels of the Higgs boson

($h \to b\bar{b}/WW^\star/ZZ^\star$) give a total of 8/729/729 different spin observables in each respective decay channel. For the $h \to b\bar{b}$ decay, we do not consider the reconstruction of b-jet polarization in the current work. The Z boson polarizations were used in previous literature [341, 352, 371, 372] to probe CP violation in the Higgs sector. We study the sensitivity of each decay channel along with the combination of multiple channels.

These spin parameters are reconstructed from the joint angular distribution of the final state charged fermions. We discuss in brief the methodology of obtaining these spin observables in terms of the asymmetries in angular functions of final fermions (for detailed discussion, we refer the reader to [373, 374]). For a massive spin-1 boson, the production dynamics are represented in terms of a density matrix as

$$\rho(\lambda, \lambda') \propto \mathcal{M}(\lambda)\mathcal{M}^\star(\lambda'), \tag{4.28}$$

where $\mathcal{M}$ is the helicity amplitude and $\lambda \in [-1, 0, 1]$ are three possible helicity states of the massive spin-1 boson. The density matrix can be parameterized in terms of three vector $\overrightarrow{p} = \{p_x, p_y, p_z\}$ and five tensorial T_{ij} polarizations, given in cartesian form as

$$\rho(\lambda, \lambda') = \frac{1}{3}\left[\mathbb{I}_{3\times3} + \frac{3}{2}\overrightarrow{p}\cdot\overrightarrow{S} + \sqrt{\frac{3}{2}}T_{ij}\{S_i, S_j\}\right], \tag{4.29}$$

where $\{S_i, S_j\}$ represents the anti-commutation between the basis of the spin-1 particle $S_i \in \{S_x, S_y, S_z\}$. Given the spin-1 boson decay to a pair of fermions ($V \to f\overline{f}'$), the differential cross section would be given by [373]

$$\begin{aligned}\frac{1}{\sigma}\frac{d\sigma}{d\Omega_f} = \frac{3}{8\pi}\Bigg[&\left(\frac{2}{3} - (1-3\delta)\frac{T_{zz}}{\sqrt{6}}\right) + \alpha p_z\cos\theta_f + \sqrt{\frac{3}{2}}(1-3\delta)T_{zz}\cos^2\theta_f \\ &+ \left(\alpha p_x + 2\sqrt{\frac{2}{3}}(1-3\delta)T_{xz}\cos\theta_f\right)\sin\theta_f\cos\phi_f + (1-3\delta)\left(\frac{T_{xx}-T_{yy}}{\sqrt{6}}\right)\sin^2\theta_f\cos(2\phi_f) \\ &+ \left(\alpha p_y + 2\sqrt{\frac{2}{3}}(1-3\delta)T_{yz}\cos\theta_f\right)\sin\theta_f\sin\phi_f + \sqrt{\frac{2}{3}}(1-3\delta)T_{xy}\sin^2\theta_f\sin(2\phi_f)\Bigg],\end{aligned} \tag{4.30}$$

where $\sigma = \sigma_V \times \Gamma(V \to f\overline{f}')$ with σ_V the production cross section. Here, θ_f and ϕ_f are the polar and azimuth orientation of the fermion f, evaluated in the rest frame of the mother boson (V) with its would-be momentum along the z-axis. The initial beam direction and the mother boson momentum in the lab frame define the $x-z$ plane, i.e., $\phi = 0$ plane, in the rest frame of the boson as well. The expressions for spin analyzing

parameters α and δ are given in App. 4.J. For a spin-1 boson decaying to two fermions through the vertex structure $\overline{f}\gamma^\mu\left(f_L P_L + f_R P_R\right) f' V_\mu$, $P_{L/R} = (1 \mp \gamma_5)/2$ and in the high energy limit $\delta \to 0, \alpha_W = -1$ and $\alpha_Z = -0.219$ [374].

The parameters of the density matrix can be obtained by performing a partial integration of the differential rate with respect to the polar and azimuth angle of the final state fermions. For example, the asymmetry related to p_x is given by [374]

$$\begin{aligned}\mathcal{A}_x &= \left(\int_{\theta=0}^{\pi}\int_{\phi=0}^{\pi/2} - \int_{\theta=0}^{\pi}\int_{\phi=\pi/2}^{3\pi/2} + \int_{\theta=0}^{\pi}\int_{\phi=3\pi/2}^{2\pi}\right) d\Omega \left(\frac{1}{\sigma}\frac{d\sigma}{d\Omega}\right) , \\ &\equiv \frac{\sigma(\sin\theta\cos\phi > 0) - \sigma(\sin\theta\cos\phi < 0)}{\sigma(\sin\theta\cos\phi > 0) + \sigma(\sin\theta\cos\phi < 0)} = \frac{3}{4}\alpha_Z p_x \, . \end{aligned} \tag{4.31}$$

The other remaining five polarization parameters can be similarly obtained through partially integrating out the differential rate. Numerically, the elements of the density matrix are computed in the form of asymmetries given by

$$\begin{aligned}\mathcal{A}[p_i] &= \frac{\sigma(c_i > 0) - \sigma(c_i < 0)}{\sigma(c_i > 0) + \sigma(c_i < 0)} \propto p_i, \; i \in \{x, y, z\}, \\ \mathcal{A}[T_{ij}] &= \frac{\sigma(c_i c_j > 0) - \sigma(c_i c_j < 0)}{\sigma(c_i c_j > 0) + \sigma(c_i c_j < 0)} \end{aligned} \tag{4.32}$$

where $c_x = \sin\theta\cos\phi$, $c_y = \sin\theta\sin\phi$, and $c_z = \cos\theta$. These angular functions or correlators relate the differential rate to the polarization parameters. Similar to the one-particle case, the two- and three-particle spin correlation parameters can be obtained numerically in the form of asymmetries in the joint angular functions of the final fermions.

Further, these asymmetries behave differently under CP transformation. For example, the polarization asymmetries $\mathcal{A}_y$, $\mathcal{A}_{xy}$, and $\mathcal{A}_{yz}$ are odd under CP, while other one-particle polarization asymmetries are even under CP transformation. Similarly, the correlation observables are also divided into two classes of asymmetries depending upon their reaction to CP transformation (see ref. [375] for detailed classification). The availability of CP-odd asymmetries becomes very important to probe the CP-odd NP which otherwise would only appear in a quadratically suppressed form in CP-even observables. In the next section, we discuss the sensitivity of these observables to the WCs, particularly focusing on the CP-odd operators. We will begin with the dominant $b\bar{b}$ decay channel where we focus on one-particle polarization asymmetries and move on to the three-particle system.

4.3.2 Sensitivities of Spin Asymmetries

In this section, we present a detailed study of the sensitivity of various Higgs decay channels to the dimension 6 operators listed in Tab. 4.1, considering quadratic dependence on the corresponding WCs. The cross section for any observable process is parameterized as

$$\sigma(C_i) = \sigma_0 + \sum_{i=1}^{3} \sigma_i C_i + \sum_{i \geq j} \sigma_{ij} C_i C_j + \sum_{k=1}^{6} \sigma_{kk} C_k^2, \tag{4.33}$$

where σ_0 denotes the SM cross section, σ_i encodes the interference between the SM and the three CP-even dimension 6 operators, σ_{ij} represents the interference between two CP-even operators, and σ_{kk} captures the quadratic contributions from both CP-even and CP-odd operators. For asymmetry observables, we parameterize the cross-section weighted asymmetries ($\mathcal{A}\sigma/\sigma$) according to their transformation properties under CP. The CP-even asymmetries are fitted using Eq. (4.33) for their numerator $\Delta\sigma = \mathcal{A}\sigma$, while the CP-odd asymmetries are parameterized as

$$\Delta\sigma(C_i) = \sum_{i=1}^{3} \sigma_i C_i + \sum_{i \geq j} \sigma_{ij} C_i C_j, \tag{4.34}$$

where the linear term σ_i arises solely from the three CP-odd operators, and σ_{ij} corresponds to interference terms between CP-even and CP-odd contributions.

Higgs decay to $b\bar{b}$ pair We begin with the dominant decay mode of the Higgs boson, $h \to b\bar{b}$ (B.R. $\approx 58\%$), studied in the associated production channel $Zh \to l^+l^-b\bar{b}$. The event generation, detector simulation pipeline, background composition (ZZ, $ZZ\gamma$), and handling of initial-state radiation (ISR) follow the exact methodology established in Sec. 4.2.2. As previously demonstrated in Fig. 4.14, the recoil-mass observable (m_{Recoil}) retains strong discriminating power between the signal and background even in the presence of ISR. Events are selected by imposing $m_{\text{Recoil}} \geq 120$ GeV to effectively suppress the dominant ZZ background. The advantage of this recoil mass reconstruction is that it remains independent of the Higgs decay channel.

The anomalous interactions here arise from modifications to the hZZ and $hZ\gamma$ vertices (detailed previously in Sec. 4.2.1). Since the b-quark polarization is not reconstructed, only the Z boson spin parameters contribute to the angular structure. The angular observables are extracted from leptons in the rest frame of the decaying Z boson. To

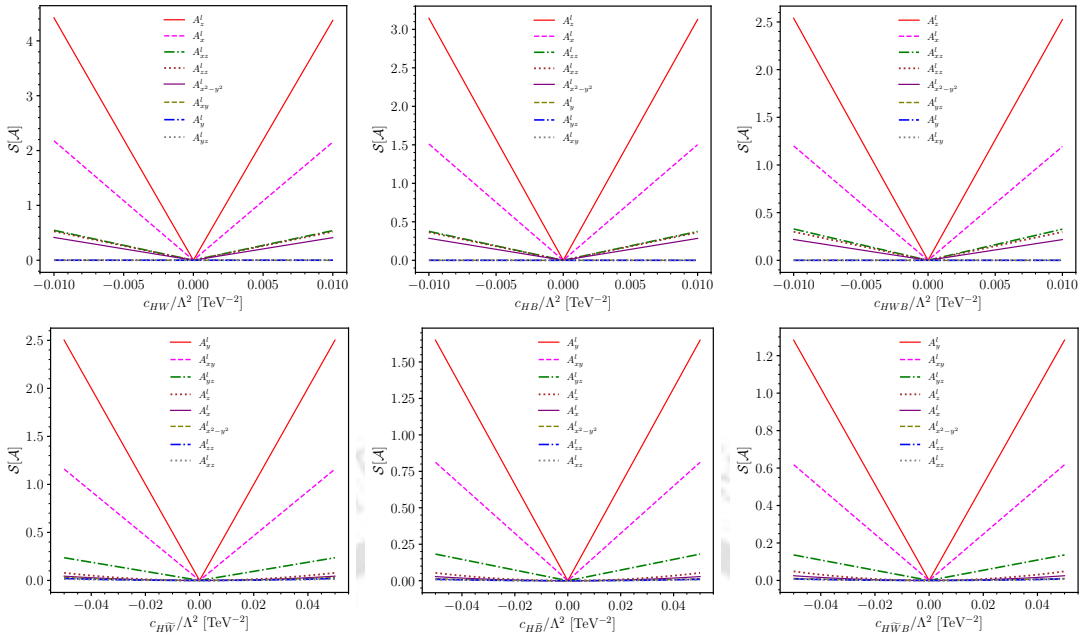

FIGURE 4.17: Sensitivity of asymmetries to the WCs of the dimension 6 operators affecting hZZ and $hZ\gamma$ coupling in Zh production process. The distribution are obtained for $e^+e^- \to Zh \to l^-l^+b\bar{b}$ process at $\sqrt{s} = 250$ GeV, $\Lambda = 1$ TeV with initial polarized beams, $(P_{e^+}, P_{e^-}) = (\pm 0.3, \mp 0.8)$ and an integrated luminosity of $\mathfrak{L}_{\text{int}} = 1$ ab^{-1} for each polarization setting. No systematic errors are considered.

enhance statistical sensitivity, events are categorized in bins of $\cos\theta_Z$, where θ_Z is the production angle of the Z boson in the lab frame as

$$B_n = -1 + \frac{(n-1)}{4} < \cos\theta_Z \leq -1 + \frac{n}{4}, \quad n = 1, \ldots, 8. \tag{4.35}$$

The sensitivity of a given observable $\mathscr{O}$ to a WC, C is defined as

$$\mathcal{S}[\mathscr{O}, C] = \frac{|\mathscr{O}(C) - \mathscr{O}(0)|}{\delta\mathscr{O}},$$

where $\delta\mathscr{O} = \sqrt{\delta\mathscr{O}^2_{\text{syst.}} + \delta\mathscr{O}^2_{\text{syst.}}}$ denotes the estimated uncertainty in the measurement of observable $\mathscr{O}$.

Fig. 4.17 shows the resulting sensitivity distributions at $\mathfrak{L} = 1$ ab^{-1} for each set of beam polarization $(P_{e^+}, P_{e^-}) = (\pm 0.3, \mp 0.8)$. For CP-even operators i.e., $\mathcal{O}_{HW}$, $\mathcal{O}_{HB}$, and $\mathcal{O}_{HWB}$, we observe that the most sensitive observables are the CP-even asymmetries $\mathscr{A}_z$ followed by $\mathscr{A}_x$. These asymmetries receive leading-order contributions at $\mathcal{O}(1/\Lambda^2)$ due to interference between the SM and the CP-even SMEFT amplitudes. In contrast, the CP-odd asymmetries, namely $\mathscr{A}_y$, $\mathscr{A}_{xy}$, and $\mathscr{A}_{yz}$, exhibit negligible sensitivity to

these operators. This behavior is expected, as contributions from CP-even operators to CP-odd observables only arise at second order in the SMEFT expansion, i.e., $\mathcal{O}(1/\Lambda^4)$, and are therefore strongly suppressed. On the other hand, when we consider CP-odd operators, we observe a complementary pattern. The asymmetry $\mathscr{A}_y$ emerges as the most sensitive observable across all three CP-odd operators studied. This is consistent with theoretical expectations, as $\mathscr{A}_y$ is explicitly CP-odd and can receive leading-order contributions at $\mathcal{O}(1/\Lambda^2)$. This highlights the unique role of CP-odd asymmetries in isolating contributions from CP-violating SMEFT operators, which would otherwise be challenging to probe using CP-even observables alone.

Higgs decay to $WW^\star$ ($h \to l\nu jj$) We now turn our attention to the decay mode of the Higgs boson into a pair of W bosons, specifically the semi-leptonic final state of the process $h \to W^\star W \to l\nu jj$. This channel constitutes the second most dominant Higgs decay mode (B.R. $\approx 21\%$) at the LHC after $h \to b\bar{b}$, and provides complementary sensitivity to anomalous couplings due to the spin-1 nature of the W bosons and their correlations. The simulation pipeline is similar to that of the $b\bar{b}$ channel, with the following parton level kinematic cuts:

$$p_T^j \geq 20 \text{ GeV}\,, \quad p_T^l \geq 10 \text{ GeV}\,, \quad |\eta_l| \leq 2.5\,, \quad \Delta R_{ab} \geq 0.4\,, \quad |\eta_j| \leq 5.0\,, \tag{4.36}$$

where $\Delta R_{ab} \equiv \sqrt{(\Delta\eta)^2 + (\Delta\phi)^2}$, $(a, b \in \{l, j\})$ denotes the angular separation between any pair of leptons or jets in the final state, and η represents the pseudorapidity. The event selection focuses on final states with exactly three isolated leptons, two jets, and missing transverse energy, corresponding to $Zh \to l^+l^- + h(W^{(*)}W \to l\nu jj)$. A Z boson candidate is reconstructed by requiring a pair of same-flavor, oppositely charged leptons with an invariant mass close to the nominal Z boson mass, specifically

$$|m_{l^+l^-} - m_Z| \leq 5 \text{ GeV}, \quad \text{with } m_Z = 91.19 \text{ GeV}.$$

In addition, to ensure that the selected events are consistent with the associated Zh production topology, we require the recoil mass against the identified dilepton system from the Z boson to satisfy $m_{\text{Recoil}} \geq 120$ GeV thereby suppressing background contributions from processes not associated with on-shell Higgs boson production. The dimension 6 operators listed in Tab. 4.1 modify both the production and decay dynamics of this channel.

On the production side, deviations arise through anomalous contributions to the hZZ and $hZ\gamma$ couplings, which affect the angular correlations and kinematic distributions of the Zh system. On the decay side, the Higgs coupling to W bosons, hWW, is altered by additional effective operators, explicitly shown in Eq. (4.25), which introduce new Lorentz structures and modify the spin correlation between the decay products. These modifications can manifest as distortions in the angular observables of the final-state particles.

The $h \to WW^\star$ decay channel would allow for two and three body spin correlations along with three spin-1 polarizations parameters. However, to reconstruct the vector polarization associated with the hadronic W decay and their correlations, one needs to know the identity of the final two jets. In the current work, we follow the tagging procedure developed in previous works [375, 376] using boosted decision trees (BDT) to tag the identity of the final two jets in an *up/down* type class.

The final two jets are reconstructed using the anti-k_T [209] clustering algorithm. For truth labeling of the two jets, we use the angular distance ΔR, between the two hardest jets and two parton level light quarks. In the case where both the jets are closer to one type of quark, we truth-tagged the hardest jet of that particular quark flavor. Further, we construct several continuous and discrete observables from the jets to be used as input features for our BDT model. The list of features is provided in Tab. 4.13. Continuous variables, such as particle momenta, are normalized by the jet energy. We also compute the number of mother particles that have traveled a distance $d > 0.3$ mm from the primary vertex. Such particles give rise to final displaced tracks (tracks originating from a secondary vertex). And in the case of a jet initiated by a c quark, we can have a significant number of short-lived kaons (K^0_S) leading to such displaced tracks. The p_T weighted jet-charge variables are also used as additional features.

The classification model is based on an `XGBoost` [303] binary classifier with the binary logistic objective and evaluated using the log-loss metric. A grid search over learning rate, number of boosting rounds, and tree depth identified the optimal configuration: learning rate of 0.05, 500 boosting rounds, and a maximum depth of 10. Column and row sub-sampling (0.7) and regularization terms (L1 = 1.0, L2 = 1.0) were used to control over-fitting. The model was trained using 3-fold cross-validation to ensure generalizability. Model performance was evaluated via iterative sub-sampling of test data, achieving $\approx$

Feature	Description
N_γ, N_l, $N_{\pi^\pm}$, $N_{k^\pm}$	Number of γ, $l^\pm$, $\pi^\pm$, and $k^\pm$
$p_\gamma, p_l, p_\pi, p_k$	Four-momentum of γ, $l^\pm$, $\pi^\pm$, and $k^\pm$
$p_T^\gamma, p_T^l, p_T^{\pi^\pm}, p_T^{k^\pm}$	Scalar sum p_T of respective particles
Q_J^k	Jet charge ($k \in \{0, 1\}$)
N_d	Count of mother with lifetime $d > 0.3$ mm.

TABLE 4.13: List of observables used as input features for BDT in order to classify two leading jets as either *up/down* type jets. The features are derived for $e^+e^- \to Zh \to 3l\not{E}2j$ process at $\sqrt{s} = 250$ GeV at the detector (`Delphes`) level.

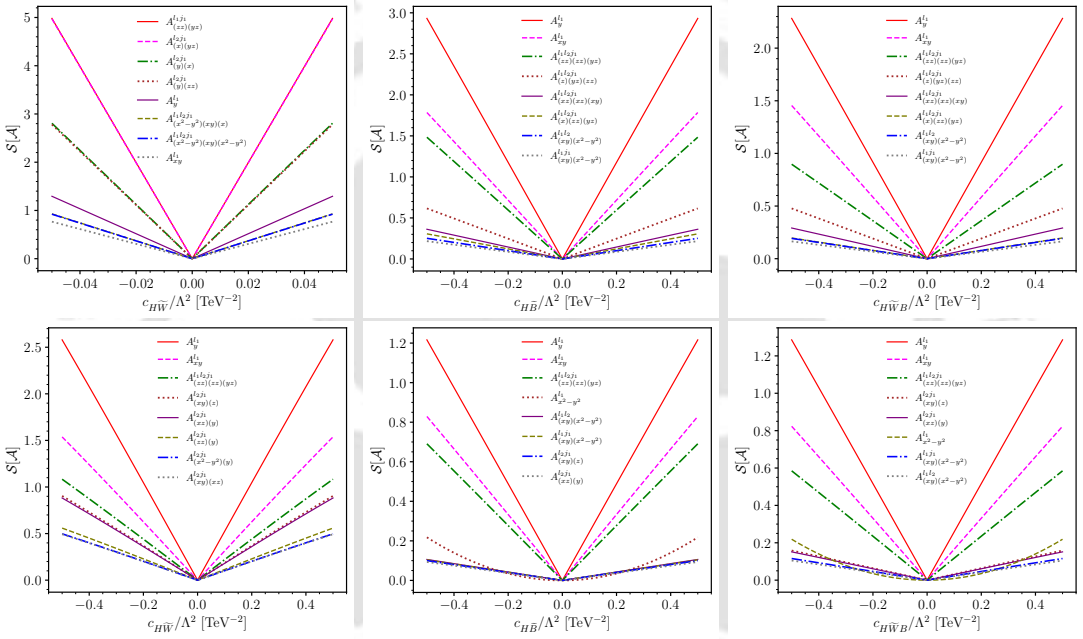

FIGURE 4.18: In the top row, we show the sensitivity for asymmetries as a function of one WC at a time obtained with $h \to WW^\star$ channel and in the bottom row, the sensitivity for $h \to ZZ^\star$ are shown. Only top eight sensitive asymmetries for each CP-odd WC are shown. The distribution are obtained at $\sqrt{s} = 250$ GeV, $\Lambda = 1$ TeV with beam polarization $(P_{e^+}, P_{e^-}) = (\pm 0.3, \mp 0.8)$ and an integrated luminosity $\mathfrak{L}_{\rm int} = 1$ ab^{-1}. No systematic errors are taken in this analysis.

78% classification accuracy with a variance of $\approx 0.01\%$. The trained model is further used to reconstruct the spin asymmetries of three spin-1 bosons.

The sensitivities of the $h \to WW^\star$ channel to the three CP-odd dimension 6 operators are shown in the top row of Fig. 4.18. The plots display the response of the most significant eight angular asymmetries to variations in $C_{H\widetilde{W}}$, $C_{H\widetilde{B}}$, and $C_{H\widetilde{W}B}$. For the $C_{H\widetilde{W}}$ coupling, the mixed asymmetry $\mathcal{A}^{l_1 j_1}_{(zz)(yz)}$, which correlates the $\sin(3\theta)$ mode of the lepton from the Z boson with the $\cos\theta \sin\phi$ mode of the leading jet from the

W boson, exhibits the highest sensitivity. A comparable enhancement is observed for $\mathcal{A}^{l_2 j_1}_{(yz)(x)}$, indicating strong correlations between angular structures in the leptonic and hadronic decay sectors. For the $C_{H\widetilde{B}}$ and $C_{H\widetilde{W}B}$ coefficients, the dominant sensitivity arises from the parity-odd lepton asymmetry $\mathcal{A}^{l}_{y}$. This is followed by $\mathcal{A}^{l}_{xy}$, which encodes azimuthal–polar correlations characteristic of CP-violating effects in the leptonic decay plane. Overall, the leading sensitivities are governed by single- and mixed-angular observables that transform odd under parity and CP, making them optimal probes of CP-odd interactions in the $WW^{\star}$ topology. It should be noted that, although quadratic contributions from SMEFT operators are included in the analysis, Figures 4.17 and 4.18 show that the resulting constraints are sufficiently stringent that these quadratic effects remain numerically insignificant.

Higgs decay to four leptons ($h \to e^{-}e^{+}\mu^{-}\mu^{+}$) We finally analyze the fully leptonic channel $h \to ZZ^{(*)} \to e^{+}e^{-}\mu^{+}\mu^{-}$, corresponding to the $Zh \to l^{+}l^{-} + h(ZZ^{\star} \to e^{+}e^{-}\mu^{+}\mu^{-})$ topology. Despite its smaller branching ratio ($\approx 3\%$), this process offers clean kinematics and negligible background, enabling full reconstruction of the intermediate Z polarizations. Moreover, due to the spin-1 nature of the Z bosons, this channel is highly sensitive to the tensor structure of the hZZ vertex, making it a powerful probe of anomalous Higgs couplings arising from higher-dimensional operators. At the parton level, basic kinematic acceptance cuts are applied to all leptons to ensure detector-level observability and to regulate soft and collinear divergences. These cuts are implemented in MG5 and are given by

$$p_T^{l} \geq 10 \text{ GeV}\,, \qquad \Delta R_{l_1 l_2} \geq 0.4\,, \qquad |\eta_l| \leq 2.5\,, \tag{4.37}$$

where $\Delta R_{l_1 l_2} = \sqrt{(\Delta\eta)^2 + (\Delta\phi)^2}$ is the angular separation between any pair of leptons, and η_l denotes the pseudorapidity. To ensure that the selected events originate from an on-shell Z boson and to suppress non-resonant background, the recoil mass against the dilepton system is required to lie within the Higgs mass window: 123 GeV $\leq m_{\text{Recoil}} \leq$ 127 GeV, where the recoil mass is computed as $m_{\text{Recoil}} = \sqrt{(p_{\text{initial}} - p_{l^+l^-})^2}$, with p_{initial} being the total incoming momentum and $p_{l^+l^-}$ the momentum of the tagged Z boson. The Higgs boson candidate is reconstructed from the remaining four-lepton final state consisting of two electrons and two muons. To ensure compatibility with the Higgs resonance, the invariant mass of the four-lepton system is required to satisfy 120 GeV $\leq$

$m_{4l} \leq 130$ GeV. This selection efficiently suppresses continuum ZZ backgrounds and enhances the signal purity of Higgs decays.

The sensitivity of the $h \to ZZ^\star$ channel to the CP-odd operators is shown in the bottom row of Fig. 4.18, where we highlight eight dominant asymmetries. The distributions are rescaled by a factor of ten for better visualization, as the deviations in this channel are statistically suppressed. For all three WCs $C_{H\widetilde{W}}$, $C_{H\widetilde{B}}$, and $C_{H\widetilde{W}B}$, the most sensitive observable is the parity-odd lepton asymmetry $\mathcal{A}_y^{l_Z}$, arising from the azimuthal modulation of the lepton associated with the on-shell Z boson. The next leading sensitivities are observed in mixed-angular asymmetries such as $\mathcal{A}_{xy}^{l_Z}$ and $\mathcal{A}_{(zz)(yz)}^{l_1 l_2}$, which encode correlations among the leptons emitted from the Higgs decay chain $h \to ZZ^\star$. Across all operators, the sensitivity pattern remains largely consistent, indicating that the dominant effects originate from parity-odd angular structures in the leptonic decay planes. The fully leptonic $h \to ZZ^\star$ topology thus provides a clean environment where angular asymmetries serve as sensitive probes of CP-violating interactions in the Higgs–gauge sector.

4.3.3 Combined Sensitivity of Operators

The projected 95% C.L. limits on the dimension 6 operators modifying the Higgs–vector boson interactions are summarized in Tab. 4.14. The results are derived from the analysis of three Higgs decay channels: $h \to b\bar{b}$, $h \to WW^\star$, and $h \to ZZ^\star$, based on spin asymmetries and total cross-section information in Zh production at $\sqrt{s} = 250$ GeV with an integrated luminosity of 1000 fb^{-1} per polarization configuration.

Among the operators considered, the $h \to WW^\star$ decay channel provides the most stringent constraints for those directly modifying the hWW vertex. Specifically, C_{HW} attains its strongest bound in the $h \to WW^\star$ mode with limits of $[-0.001, +0.001]$, which is about an order of magnitude tighter than the $h \to b\bar{b}$ result and nearly two orders better than the $h \to ZZ^\star$ channel. The CP-odd operator $C_{H\widetilde{W}}$ follows a similar trend, with the $h \to WW^\star$ channel giving $[-0.041, +0.041]$, compared to $[-0.190, +0.190]$ from $h \to b\bar{b}$ and $[-3.721, +3.721]$ from $h \to ZZ^\star$. This improvement reflects the strong spin-correlation sensitivity of the semi-leptonic $h \to WW^\star$ observables to both CP-even and CP-odd tensor structures in the hVV interaction. For all other operators, the $h \to b\bar{b}$ channel yields the dominant sensitivity due to its large branching ratio and

WCs	$l^-l^+b\bar{b}$	$l^-l^+WW^\star$	$l^-l^+ZZ^\star$	Combined
C_{HW}	$[-0.012, +0.012]$	$[-0.001, +0.001]$	$[-0.081, +0.050]$	$[-0.001, +0.001]$
$C_{H\widetilde{W}}$	$[-0.190, +0.190]$	$[-0.041, +0.041]$	$[-3.721, +3.721]$	$[-0.040, +0.040]$
C_{HB}	$[-0.020, +0.020]$	$[-0.101, +0.098]$	$[-0.775, +0.502]$	$[-0.020, +0.020]$
$C_{H\widetilde{B}}$	$[-0.325, +0.325]$	$[-1.032, +1.032]$	$[-6.670, +6.667]$	$[-0.322, +0.312]$
C_{HWB}	$[-0.015, +0.015]$	$[-0.111, +0.108]$	$[-0.508, +0.271]$	$[-0.014, +0.014]$
$C_{H\widetilde{W}B}$	$[-0.360, +0.360]$	$[-1.148, +1.148]$	$[-6.889, +6.889]$	$[-0.346, +0.346]$

TABLE 4.14: 95% C.L. one parameter limits of WCs obtained using cross section and asymmetries for three different decay channels of the Higgs boson and also their combinations for $e^+e^- \to Zh$ production. The limits are obtained at $\sqrt{s} = 250$ GeV, $\Lambda = 1$ TeV, $\mathfrak{L}_{\text{int}} = 1000$ fb^{-1} for each set of beam polarization with zero systematics.

well-reconstructed final state. The limits on C_{HB} and C_{HWB} are $[-0.020, +0.020]$ and $[-0.015, +0.015]$, respectively, which are approximately five times stronger than the corresponding bounds from $h \to WW^\star$ and over an order of magnitude better than those from $h \to ZZ^\star$. In the CP-odd sector, $C_{H\widetilde{B}}$ and $C_{H\widetilde{W}B}$ remain comparatively weakly constrained in individual channels due to their suppressed interference. The $ZZ^\star$ mode gives limits of $\mathcal{O}(6)$, while the $b\bar{b}$ channel improves these to around 0.3. The combined fit tightens the bounds further to $[-0.322, +0.312]$ and $[-0.346, +0.346]$, respectively, representing nearly a tenfold improvement over the $ZZ^\star$-only sensitivity. Overall, Tab. 4.14 demonstrates a clear complementarity among the decay channels: the $h \to WW^\star$ channel dominates for C_{HW} and $C_{H\widetilde{W}}$ due to polarization-enhanced sensitivity, the $h \to b\bar{b}$ channel leads for all remaining operators owing to statistical precision, and the $h \to ZZ^\star$ channel, while limited by event rates, provides valuable kinematic clarity supporting the combined SMEFT constraints.

At this stage, we compare the constraints on the CP-even WCs obtained in this work with the bounds previously derived using the OOT in the $h \to b\bar{b}$ channel in Sec. 4.2. Using only the differential cross section, the OOT analysis at an integrated luminosity of 2 ab^{-1} yields sensitivities of

$$\begin{aligned} C_{HW}/\Lambda^2 &\in [-0.04, +0.04]\ \text{TeV}^{-2}\,, \\ C_{HB}/\Lambda^2 &\in [-0.07, +0.07]\ \text{TeV}^{-2}\,, \\ C_{HWB}/\Lambda^2 &\in [-0.08, +0.08]\ \text{TeV}^{-2}\,. \end{aligned} \tag{4.38}$$

The incorporation of Z boson polarization asymmetries in the same framework substantially improves the discriminatory power, leading to the tightened bounds

$$\begin{aligned} C_{HW}/\Lambda^2 &\in [-0.01, +0.01]\ \text{TeV}^{-2}\,, \\ C_{HB}/\Lambda^2 &\in [-0.02, +0.02]\ \text{TeV}^{-2}\,, \\ C_{HWB}/\Lambda^2 &\in [-0.02, +0.02]\ \text{TeV}^{-2}\,. \end{aligned} \tag{4.39}$$

Hence, the inclusion of polarization asymmetries of the Z boson alone not only enhances the sensitivity to CP-odd operators, but also introduces an additional independent χ^2 contribution in the CP-even sector, resulting in an overall improvement of approximately a factor of four in the corresponding limits.

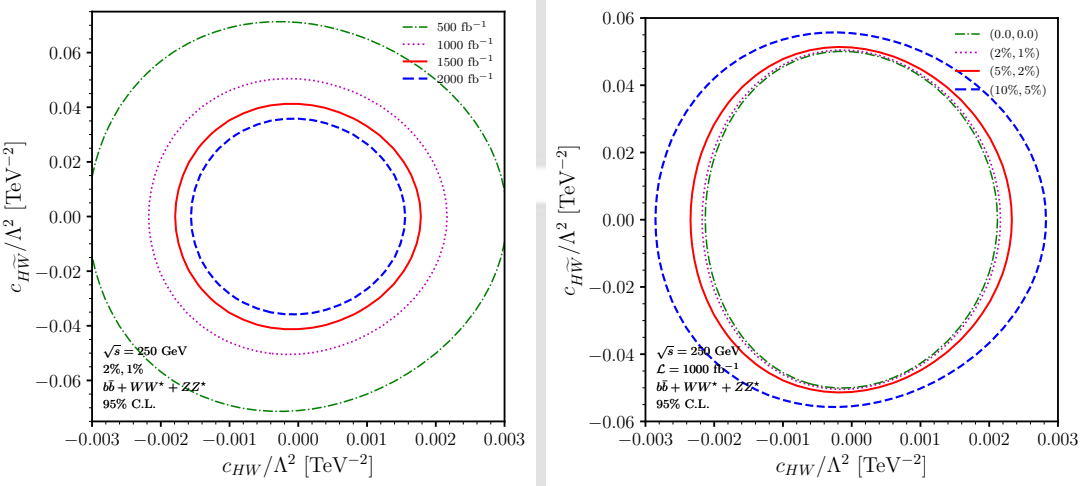

FIGURE 4.19: Impact of integrated luminosity (left panel) and systematic uncertainties (right panel) on two-dimensional 95% CL contours in the WC plane, using combined Higgs decay channels ($h \to b\bar{b}$, $h \to WW^\star$, $h \to ZZ^\star$) from Zh production at $\sqrt{s} =$ 250 GeV e^+e^- collider.

Next, we perform two-dimensional projections in the $(C_{HW}, C_{H\widetilde{W}})$ plane to study the impact of integrated luminosity and systematic uncertainties on the attainable limits of the WCs. The left panel of Fig. 4.19 illustrates the evolution of the allowed parameter space with increasing $\mathfrak{L}_{\text{int}}$, assuming systematic uncertainties of 2% on the total cross section and 1% on asymmetries. Contours are displayed for four benchmark luminosities: 500, 1000, 1500, and 2000 fb^{-1}, evaluated separately for each beam polarization configuration. A clear tightening of the contours is observed with increasing luminosity, reflecting the enhanced statistical power to resolve small deviations from the SM expectations. This behavior is particularly pronounced for operators whose interference terms scale linearly with event yields, demonstrating the importance of high-statistics datasets

in constraining dimension 6 effects. The right panel of Fig. 4.19 examines the role of experimental systematic uncertainties at a fixed integrated luminosity of 1000 fb^{-1}. Four representative uncertainty configurations are considered for the total cross section and asymmetry measurements: $(0, 0)$, $(2\%, 1\%)$, $(5\%, 2\%)$, and $(10\%, 5\%)$. As expected, increasing systematic uncertainties lead to a noticeable degradation in sensitivity, manifested as enlarged allowed regions in the $(C_{HW}, C_{H\widetilde{W}})$ plane. A significant tightening of the contours is observed when moving from the conservative $(10\%, 5\%)$ to the moderate $(5\%, 2\%)$ scenario, indicating a strong sensitivity improvement once systematics are reduced below a few percent. Beyond this point, however, the contour areas show minimal further shrinkage, signaling a saturation in the achievable precision limited by the remaining systematic floor. This suggests that to probe the anomalous hVV couplings in Higgs-strahlung processes, especially when incorporating spin-sensitive observables across multiple Higgs decay channels, both high-statistics datasets and tightly controlled systematics are indispensable. Future high-luminosity e^+e^- colliders thus offer an ideal environment, where reduced experimental systematics and large integrated luminosities can jointly maximize the reach of SMEFT analyses.

4.3.4 Summary and Conclusion

The precise determination of the Higgs-gauge couplings (hVV, with $V = Z, W, \gamma$) remains a central goal of future high-energy e^+e^- colliders, offering powerful tests of electroweak symmetry breaking and sensitivity to new physics. This study investigates anomalous hVV interactions through the process $e^+e^- \to Zh$ at $\sqrt{s} = 250$ GeV, employing spin-based asymmetries that access interference effects absent in total rate measurements. These observables enable direct discrimination between CP-even and CP-odd operator contributions and significantly extend the sensitivity beyond that of previous rate-based analyses.

By analyzing the three major Higgs decay channels: $h \to b\bar{b}$, $WW^{(*)}$, and $ZZ^{(*)}$, we observe a clear complementarity among them. The $h \to WW^\star$ channel provides the strongest constraints on both the CP-even and CP-odd operators $\mathcal{O}_{HW}$ and $\mathcal{O}_{H\widetilde{W}}$ that modify the hWW vertex directly, driven by its rich spin correlation structure. The $h \to b\bar{b}$ mode, with its large event yield and clean reconstruction, dominates the sensitivity to operators affecting the hZZ and $h\gamma Z$ interactions, while the $h \to ZZ^\star$ channel, though

statistically limited, offers a clean probe of parity-odd angular structures and serves as a consistency test. A combined analysis across all decay modes yields the most stringent overall bounds, substantially improving upon both current LHC limits and previous ILC projections, particularly in the CP-odd sector.

A comparison with the recent analysis of [377], where constraints on the CP-violating WCs were derived using the azimuthal angle observable $\Delta\Phi_{ll}$ in the $h \to b\bar{b}^*$ channel at $\mathfrak{L}_{\rm int} = 3$ ab^{-1}, is particularly instructive. Their study reports

$$\begin{aligned} C_{H\widetilde{W}}/\Lambda^2 &\in [-0.28, +0.28]\ \text{TeV}^{-2}\,, \\ C_{H\widetilde{B}}/\Lambda^2 &\in [-0.35, +0.35]\ \text{TeV}^{-2}\,, \\ C_{H\widetilde{W}B}/\Lambda^2 &\in [-0.38, +0.38]\ \text{TeV}^{-2}\,. \end{aligned} \tag{4.40}$$

In contrast, our analysis of the same $h \to b\bar{b}^*$ decay mode yields significantly stronger bounds,

$$\begin{aligned} C_{H\widetilde{W}}/\Lambda^2 &\in [-0.15, +0.15]\ \text{TeV}^{-2}\,, \\ C_{H\widetilde{B}}/\Lambda^2 &\in [-0.26, +0.26]\ \text{TeV}^{-2}\,, \\ C_{H\widetilde{W}B}/\Lambda^2 &\in [-0.29, +0.29]\ \text{TeV}^{-2}\,. \end{aligned} \tag{4.41}$$

Thus, for the $C_{H\widetilde{W}}$ operator in the $h \to b\bar{b}$ channel alone, our constraint is tighter by nearly a factor of three. Moreover, incorporating the $h \to WW^*$ decay mode substantially enhances the sensitivity: the $C_{H\widetilde{W}}/\Lambda^2$ coefficient is constrained to $\in [-0.03, +0.03]$, representing an improvement of $\mathcal{O}(1)$ compared to the $b\bar{b}$ channel. For the remaining operators, $C_{H\widetilde{B}}/\Lambda^2$ and $C_{H\widetilde{W}B}/\Lambda^2$, our limits improve upon [377] by approximate factors of 1.34 and 1.31, respectively. These bounds become even more stringent once the additional set of decay channels are included.

The impact of luminosity and systematic uncertainties has also been quantified. Increasing integrated luminosity leads to a progressive tightening of the allowed regions in the WCs planes, reflecting enhanced statistical precision. Conversely, systematic effects on total cross sections and asymmetry measurements become dominant once uncertainties exceed a few percent. Beyond this threshold, sensitivity improvements saturate, underscoring the need for both large datasets and sub-percent-level systematic control to fully exploit the precision potential of future colliders. Overall, this work demonstrates that

spin asymmetry observables substantially enhance the reach of SMEFT studies in Higgs-strahlung. They provide a clean and direct handle on CP-even and CP-odd effects, leveraging interference-driven sensitivities inaccessible to total rate analyses. When combined with multiple Higgs decay channels and polarized beams, these observables form a powerful framework for probing higher-dimensional operators with unprecedented precision. Future high-luminosity e^+e^- colliders thus present an ideal environment for advancing the precision frontier of Higgs physics and testing the SM at the sub-percent level.

Appendix: Application to Higgs Physics

4.A Constraints on $qqZ/qqZh$ Operators

The constraints on dipole (other than C_{uW}) and Higgs-current (other than $C_{Hq}^{(3)}$) operator coefficients from existing studies are listed in Tab. 4.15 and 4.16, respectively.

Coefficient	Bound	C.L.	Flavor Scheme [Source]
C_{uB}	[-0.602, 0.602]	95%	$U(3)_q \times U(3)_u \times U(3)_d$ [291]
	[-0.780, 0.780]	95%	$U(2)_q \times U(2)_u \times U(2)_d$ [292]
	[-0.199, 0.093]	95%	$U(1)_Q \times U(1)_t$ [278]
	[-0.036, 0.324]	90%	$U(3)_q \times U(3)_u \times U(3)_d$ [284]
	[-0.430, 0.284]	95%	$U(1)_Q \times U(1)_t$ [282]
	[-4.500, 1.200]	95%	$U(1)_Q \times U(1)_t$ [279]
C_{dW}	[-0.484, 0.484]	95%	$U(3)_q \times U(3)_u \times U(3)_d$ [291]
	[-0.360, 0.360]	95%	$U(2)_q \times U(2)_u \times U(2)_d$ [292]
C_{dB}	[-0.769, 0.769]	95%	$U(3)_q \times U(3)_u \times U(3)_d$ [291]
	[-0.960, 0.960]	95%	$U(2)_q \times U(2)_u \times U(2)_d$ [292]

TABLE 4.15: Constraints on dipole operator coefficients from existing studies; see the references for details.

Coefficient	Bound	C.L.	Flavor Scheme [Source]
$C_{Hq}^{(1)}$	[-2.659, 0.381]	95%	$U(2)_q \times U(2)_u \times U(3)_d$ [278]
	[-1.147, 1.585]	95%	$U(1)_Q \times U(1)_t$ [278]
	[-0.260, 0.115]	68%	$U(3)_q \times U(3)_u \times U(3)_d$ [165]
	[-1.600, 0.430]	95%	$U(3)_q \times U(3)_u \times U(3)_d$ [285]
	[-0.048, 0.021]	90%	$U(3)_q \times U(3)_u \times U(3)_d$ [284]
	[-0.100, 0.140]	95%	$U(2)_q \times U(2)_u \times U(3)_d$ [279]
	[-0.031, 0.049]	95%	$U(1)_Q \times U(1)_t$ [279]
	[-0.023, 0.047]	95%	$U(2)_q \times U(2)_u \times U(3)_d$ [281]
C_{Hu}	[-0.458, 0.375]	95%	$U(2)_q \times U(2)_u \times U(3)_d$ [278]
	[-1.038, 0.449]	68%	$U(3)_q \times U(3)_u \times U(3)_d$ [165]
	[-0.060, 0.036]	90%	$U(3)_q \times U(3)_u \times U(3)_d$ [284]
	[-0.190, 0.100]	68%	$U(3)_q \times U(3)_u \times U(3)_d$ [4]
	[-0.075, 0.073]	95%	$U(2)_q \times U(2)_u \times U(3)_d$ [279]
	[-1.200, 2.900]	95%	$U(1)_Q \times U(1)_t$ [279]
	[-0.056, 0.081]	95%	$U(2)_q \times U(2)_u \times U(3)_d$ [281]
C_{Hd}	[-0.187, 0.229]	95%	$U(2)_q \times U(2)_u \times U(3)_d$ [278]
	[-0.520, 0.267]	68%	$U(3)_q \times U(3)_u \times U(3)_d$ [165]
	[-2.600, 8.300]	95%	$U(3)_q \times U(3)_u \times U(3)_d$ [285]
	[-0.130, 0.071]	95%	$U(2)_q \times U(2)_u \times U(3)_d$ [279]
	[-0.150, 0.040]	95%	$U(2)_q \times U(2)_u \times U(3)_d$ [281]

TABLE 4.16: Constraints on Higgs-current operator coefficients from existing studies; see the references for details.

Bounds on the imaginary part of dipole operators from neutron EDM [164] (assuming a $U(2)_q \times U(2)_u \times U(2)_d$ flavor scheme) are shown below:

$$\begin{aligned} \mathfrak{Im}(C_{uB}) &< 0.000368 \\ \mathfrak{Im}(C_{dW}) &< 0.000002 \\ \mathfrak{Im}(C_{dB}) &< 0.000001 \end{aligned} \tag{4.42}$$

4.B Details of BDT Analysis

Feature selection is an integral and significant part of any machine learning analysis. The presence of too many redundant features causes a model to learn unnecessary characteristics; as such, we expect the features to have little dependence on one another. The correlation matrix captures the interdependence among the features very accurately. For our BDT model, the feature correlation heatmap is shown in Fig. 4.20. Darker patches refer to high correlation. Apart from features like p_T^l and p_T^{ll}, or p_T^b and p_T^{bb}, where correlation is naturally expected, most of the features show little to no correlation, enhancing the model's learnability against general data. Apart from feature selection, another important aspect of model tuning is hyperparameter optimization. Proper tuning prevents the model from overfitting, resulting in better performance on new data. The optimized hyperparameters for the model are detailed in Tab. 4.17.

Hyperparameters for the XGBClassifier model	**Optimal value**
Number of boosting rounds (`n_estimators`)	50
Maximum depth of a tree (`max_depth`)	5
Learning rate for the model (`learning_rate`)	0.15
Fraction of samples used each tree (`subsample`)	0.8
Fraction of features used for each tree (`colsample_bytree`)	1.0
Minimum sum of instance weight in a child (`min_child_weight`)	50
Minimum loss reduction for further partition (`gamma`)	0.75
L1 regularization term on weights (`reg_alpha`)	8
L2 regularization term on weights (`reg_lambda`)	60
Maximum step size for each iteration (`max_delta_step`)	2

TABLE 4.17: The optimal hyperparameter values for the model mined using `GridSearchCV`. The `objective` hyperparameter is fixed at `"binary:logistic"`.

4.C Additional Differential Distributions

Kinematic distributions for different EFT benchmark points are shown in Fig. 4.21. The M_{llbb} distribution post BDT score threshold choice of 0.95 are shown in Fig. 4.22. The benchmarks $\{c_{uW}, c_{Hq}^{(3)}\}$ are: *Left:* BC1 $\{0.00, -0.20\}$, BC2 $\{0.00, -0.10\}$, and BC3

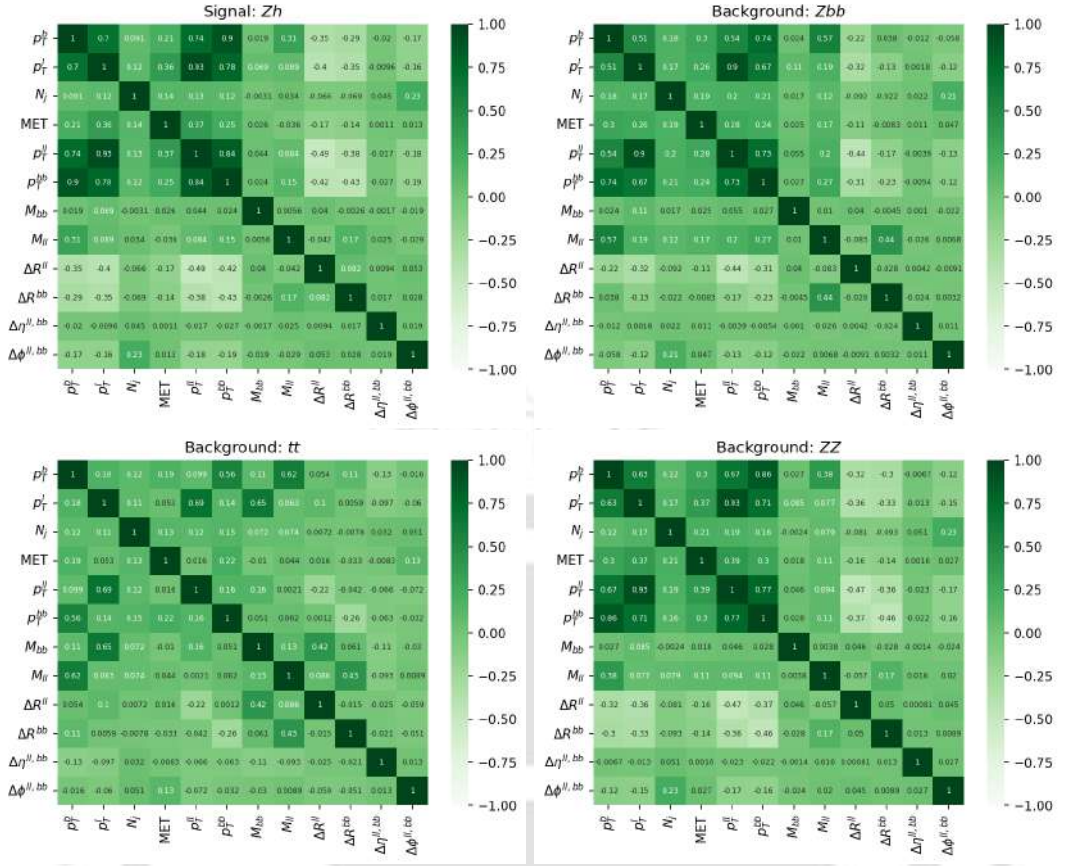

FIGURE 4.20: *Top Left:* Correlation matrix for the features used in training the XGBoost model for Zh process. *Top Right:* Zbb process. *Bottom Left:* $t\bar{t}$ process. *Bottom Right:* ZZ process.

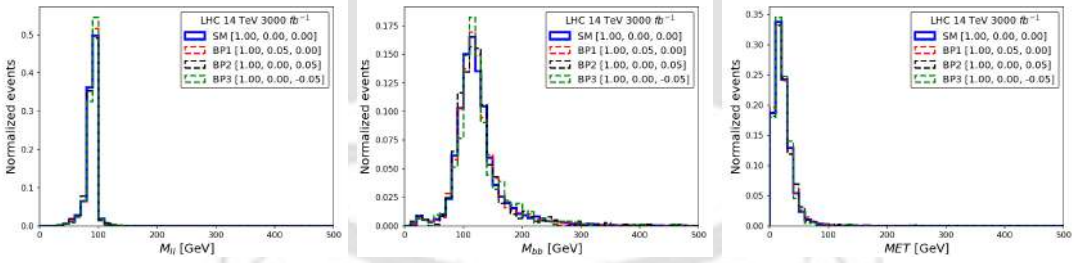

FIGURE 4.21: *Top Left:* Invariant mass of dilepton, *Top Right:* invariant mass of dibjet, and *Bottom:* missing transverse energy corresponding to $Z(l^+l^-)h(b\bar{b})$ at $\sqrt{s}$ =14 TeV at different EFT benchmark points shown in Table 4.8.

$\{0.00, -0.01\}$; *Center:* BC4 $\{0.00, 0.01\}$, BC5 $\{0.00, 0.10\}$, and BC6 $\{0.00, 0.20\}$; *Right:* BD1 $\{0.01, 0.00\}$, BD2 $\{0.10, 0.00\}$, and BD3 $\{0.20, 0.00\}$.

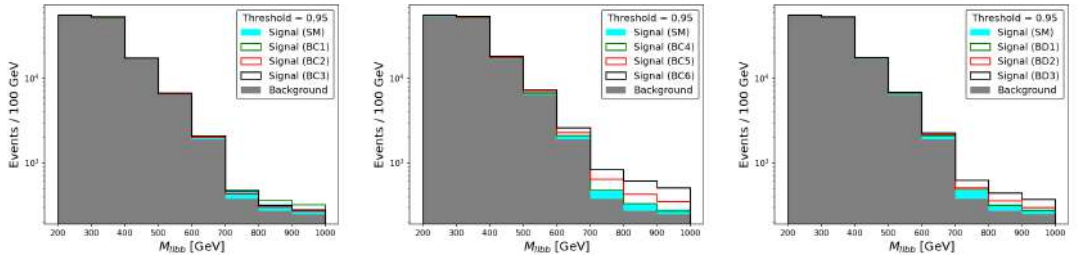

FIGURE 4.22: M_{llbb} distributions for different EFT benchmarks post threshold choice of 0.95.

4.D Z Branching Ratio Corrections

The correction to the Z decay width in the presence of $\mathcal{O}_{uW}$ and $\mathcal{O}_{Hq}^{(3)}$ can be parametrized as:

$$\Gamma_Z = \Gamma_Z^{SM}\left[1 + 0.0047\left(C_{uW}\right)^2 + 0.0099\left(C_{Hq}^{(3)}\right)^2 + 0.0976\left(C_{Hq}^{(3)}\right)\right] \tag{4.43}$$

The correction to $Z \to l^+l^-$ branching is parametrized as:

$$(B.R.)_{Zll} = \frac{\Gamma_{Zll}}{\Gamma_Z} = \frac{(B.R.)_{Zll}^{SM}}{\left[1 + 0.0047\left(C_{uW}\right)^2 + 0.0099\left(C_{Hq}^{(3)}\right)^2 + 0.0976\left(C_{Hq}^{(3)}\right)\right]} \tag{4.44}$$

Fig. 4.23 shows how the 68% C.L. limits change depending on whether EFT corrections to the Z branching are included or not. The effect is not very strong, but it is taken into account in our analysis.

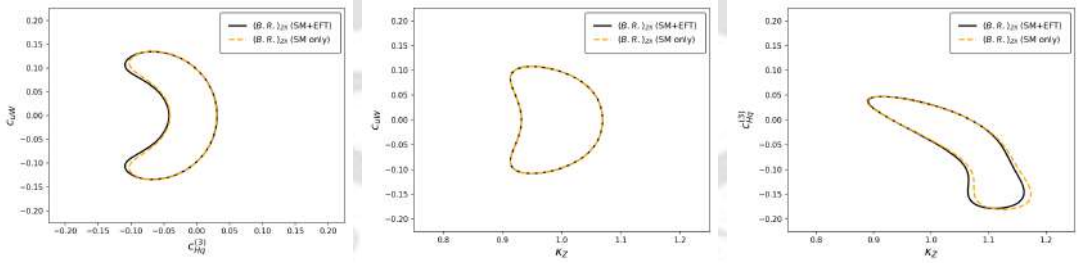

FIGURE 4.23: Shift in 68% C.L. limits depending on whether EFT corrections to the Z branching are included or not.

4.E Effect of Custodial Symmetry

In Sec. 4.1.2, we imposed the custodial symmetry condition $\kappa_W = \kappa_Z$. However, this assumption can be relaxed. In this section, we explore how the 68% C.L. limits change under two scenarios: (**I**) with custodial symmetry, where $\kappa_W = \kappa_Z$ (as discussed in

Sec. 4.1.2), and (**II**) without custodial symmetry, where $\kappa_W \neq \kappa_Z$ and $\kappa_W = 1$, assuming an SM-like coupling of the Higgs to the W boson while treating κ_Z as a free parameter. For the second scenario, the Higgs production signal strength via the Zh channel is given by:

$$\mu_{hbb}^{Zh} = \frac{(\sigma^{Zh} \times (B.R.)_{hbb})}{(\sigma^{Zh} \times (B.R.)_{hbb})_{SM}} = \frac{\kappa_Z^2 \kappa_B^2}{0.3929 + 0.5809\kappa_B^2 + 0.0262\kappa_Z^2}. \tag{4.45}$$

Fig. 4.24 illustrates how the 68% C.L. limits are affected by the assumption of custodial symmetry. The assumption significantly impacts our bounds, particularly when κ_Z deviates from 1.

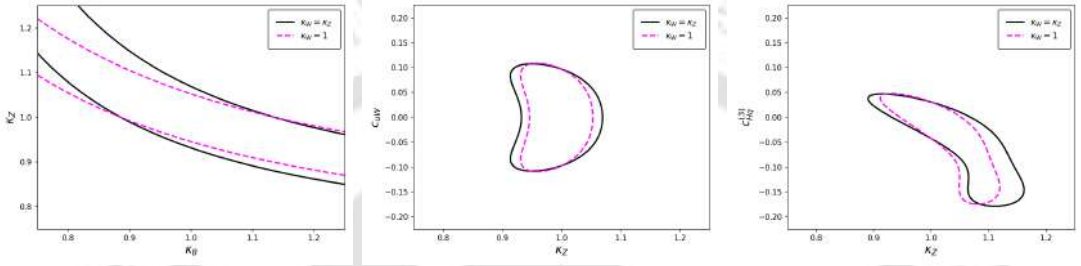

FIGURE 4.24: Shift in 68% C.L. limits depending on whether custodial symmetry is assumed.

4.F ML-based Discrimination

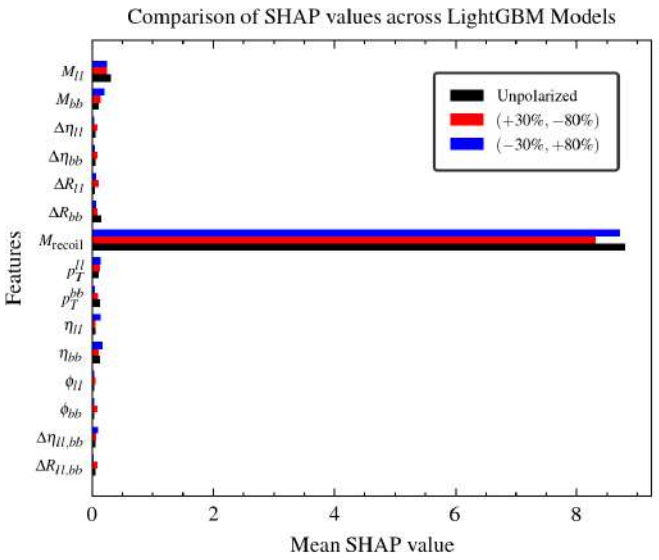

FIGURE 4.25: SHAP values for BDT models trained for signal-background segregation.

We train three BDT models using the `LightGBM` framework: one for the unpolarized case and two for the polarized beam configurations $(P_{e^+}, P_{e^-}) = (+30\%, -80\%)$ and

$(-30\%, +80\%)$. For each model, the dataset is split into equal halves for training and testing. The kinematic variables (features) used for training are as follows: Invariant mass of the dilepton system (M_{ll}) and the $b\bar{b}$ system (M_{bb}), recoil mass of the dilepton system (m_{Recoil}), angular separation between the leptons ($\Delta\eta_{ll}$, ΔR_{ll}), angular separation between the b-jets ($\Delta\eta_{bb}$, ΔR_{bb}), kinematic variables of the dilepton system: transverse momentum (p_T^{ll}), pseudorapidity (η_{ll}), and azimuthal angle (ϕ_{ll}), kinematic variables of the $b\bar{b}$ system: p_T^{bb}, η_{bb}, and ϕ_{bb}, and angular separation between the dilepton and $b\bar{b}$ systems: $\Delta\eta_{ll,bb}$, $\Delta R_{ll,bb}$. The recoil mass of the dilepton system is defined as:

$$m_{\text{Recoil}} = \sqrt{s - 2\sqrt{s}E_{ll} + M_{ll}^2}\,, \tag{4.46}$$

where E_{ll} is the total energy of the two leptons. The definitions of the other variables follow standard usage in collider physics literature. The polar angle of the final state, reconstructed from the dilepton system, is defined as:

$$\cos\theta_{\text{Recoil}} = \frac{p_z^{ll}}{|\overrightarrow{p}_{ll}|} \tag{4.47}$$

where p_z^{ll} is the longitudinal momentum of the dilepton system and $|\overrightarrow{p}_{ll}|$ is its total three-momentum magnitude. All input features are normalized using the `StandardScaler` module. The BDT models are trained with equal class weights for signal and background events, while testing is performed using weights proportional to the true event yields. The SHAP values for the trained models are shown in Fig. 4.25. Among all features, the recoil mass m_{Recoil} emerges as the most powerful discriminator. Therefore, we choose to replace the BDT model with a simple optimized selection cut on m_{Recoil}, achieving similar classification performance with greater interpretability.

4.G Couplings in Optimal Observable

As stated before, the differential cross-section for $e^+e^- \to Zh$ serves as the observable to estimate the NP couplings (WCs) optimally in the ILC. In the limit where background contamination is assumed negligible, the observable can be expressed as:

$$\mathcal{O}(\phi) = \left.\frac{d\sigma}{d\phi}\right|_{\texttt{observed}} = \epsilon_{\texttt{S}} \left.\frac{d\sigma}{d\phi}\right|_{\texttt{S,theory}} = \sum_i g_i f_i(\phi)\,, \tag{4.48}$$

Upon a semi-numeric evaluation with $\sqrt{s} = 250$ GeV, $m_Z = 91$ GeV, and $m_h = 125$ GeV, the couplings attached to the phase space variables as in Eq. (4.21) are furnished in Eq. (4.49)-(4.54).

$$\begin{aligned} g_0^L = {} & 2.0 \times 10^{-3} + 1.8 \times 10^{-3}\, C_{HW} + 7.7 \times 10^{-5}\, C_{HWB} \\ & + 4.4 \times 10^{-4}\, (C_{HW})^2 - 4.7 \times 10^{-4}\, (C_{HB})^2 + 7.7 \times 10^{-7}\, (C_{HWB})^2 \\ & - 2.3 \times 10^{-4}\, C_{HW} C_{HB} - 9.4 \times 10^{-6}\, C_{HB} C_{HWB} \\ & + 8.4 \times 10^{-5}\, (C_{H\tilde{W}})^2 + 5.4 \times 10^{-6}\, (C_{H\tilde{B}})^2 + 1.5 \times 10^{-7}\, (C_{H\tilde{W}B})^2 \\ & - 4.2 \times 10^{-5}\, C_{H\tilde{W}} C_{H\tilde{B}} + 7.0 \times 10^{-7}\, C_{H\tilde{W}} C_{H\tilde{W}B} \\ & - 1.8 \times 10^{-6}\, C_{H\tilde{B}} C_{H\tilde{W}B}\,, \end{aligned} \tag{4.49}$$

$$\begin{aligned} g_1^L = {} & 3.2 \times 10^{-19}\, C_{HW} - 3.2 \times 10^{-19}\, C_{HB} - 5.4 \times 10^{-20}\, C_{HWB} \\ & - 5.4 \times 10^{-20}\, (C_{HW})^2 - 2.7 \times 10^{-20}\, (C_{HB})^2 - 1.3 \times 10^{-19}\, C_{HW} C_{HB} \\ & - 4.7 \times 10^{-20}\, C_{HW} C_{HWB} + 2.4 \times 10^{-20}\, (C_{H\tilde{W}})^2 + 2.4 \times 10^{-20}\, (C_{H\tilde{B}})^2 \\ & + 2.5 \times 10^{-21}\, (C_{H\tilde{W}B})^2 - 4.7 \times 10^{-20}\, C_{H\tilde{W}} C_{H\tilde{B}} \\ & - 1.4 \times 10^{-20}\, C_{H\tilde{W}} C_{H\tilde{W}B} + 1.4 \times 10^{-20}\, C_{H\tilde{B}} C_{H\tilde{W}B}\,, \end{aligned} \tag{4.50}$$

$$\begin{aligned} g_2^L = {} & -3.7 \times 10^{-4} - 5.4 \times 10^{-20}\, C_{HW} + 5.4 \times 10^{-20}\, C_{HB} + 1.4 \times 10^{-20}\, C_{HWB} \\ & + 8.4 \times 10^{-5}\, (C_{HW})^2 - 5.4 \times 10^{-6}\, (C_{HB})^2 - 1.5 \times 10^{-7}\, (C_{HWB})^2 \\ & - 4.3 \times 10^{-5}\, C_{HW} C_{HB} - 7.0 \times 10^{-6}\, C_{HW} C_{HWB} - 1.8 \times 10^{-6}\, C_{HB} C_{HWB} \\ & + 8.4 \times 10^{-5}\, (C_{H\tilde{W}})^2 + 5.4 \times 10^{-6}\, (C_{H\tilde{B}})^2 + 1.5 \times 10^{-7}\, (C_{H\tilde{W}B})^2 \\ & - 4.3 \times 10^{-5}\, C_{H\tilde{W}} C_{H\tilde{B}} - 7.0 \times 10^{-6}\, C_{H\tilde{W}} C_{H\tilde{W}B} \\ & + 1.8 \times 10^{-6}\, C_{H\tilde{B}} C_{H\tilde{W}B}\,, \end{aligned} \tag{4.51}$$

$$
\begin{aligned}
g_0^R = {} & 1.4\times10^{-3} + 1.0\times10^{-4}\,C_{HW} + 9.1\times10^{-4}\,C_{HB} + 8.6\times10^{-4}\,C_{HWB} \\
& + 1.9\times10^{-6}\,(C_{HW})^2 + 1.5\times10^{-4}\,(C_{HB})^2 + 1.3\times10^{-4}\,(C_{HWB})^2 \\
& + 3.6\times10^{-7}\,(C_{H\tilde{W}})^2 + 2.8\times10^{-5}\,(C_{H\tilde{B}})^2 + 2.5\times10^{-5}\,(C_{H\tilde{W}B})^2 \\
& + 3.3\times10^{-5}\,C_{HW}C_{HB} + 3.2\times10^{-5}\,C_{HW}C_{HWB} + 2.8\times10^{-4}\,C_{HB}C_{HWB} \\
& + 6.3\times10^{-6}\,C_{H\tilde{W}}C_{H\tilde{B}} + 6.0\times10^{-6}\,C_{H\tilde{W}}C_{H\tilde{W}B} \\
& + 5.2\times10^{-5}\,C_{H\tilde{B}}C_{H\tilde{W}B}\,,
\end{aligned}
\tag{4.52}
$$

$$
\begin{aligned}
g_1^R = {} & -1.1\times10^{-19}\,C_{HW} + 1.1\times10^{-19}\,C_{HB} + 1.1\times10^{-19}\,C_{HWB} \\
& - 5.4\times10^{-20}\,(C_{HW})^2 + 6.1\times10^{-20}\,(C_{HB})^2 + 2.0\times10^{-20}\,(C_{HWB})^2 \\
& + 2.4\times10^{-20}\,(C_{H\tilde{W}})^2 + 1.0\times10^{-20}\,(C_{H\tilde{B}})^2 + 2.5\times10^{-21}\,(C_{H\tilde{W}B})^2 \\
& + 1.4\times10^{-19}\,C_{HW}C_{HB} + 3.4\times10^{-20}\,C_{HW}C_{HWB} - 6.8\times10^{-21}\,C_{HB}C_{HWB} \\
& - 4.7\times10^{-20}\,C_{H\tilde{W}}C_{H\tilde{B}} - 1.4\times10^{-20}\,C_{H\tilde{W}}C_{H\tilde{W}B} \\
& + 2.7\times10^{-20}\,C_{H\tilde{B}}C_{H\tilde{W}B}\,,
\end{aligned}
\tag{4.53}
$$

$$
\begin{aligned}
g_2^R = {} & -2.8\times10^{-4} - 2.7\times10^{-20}\,C_{HW} + 2.7\times10^{-20}\,C_{HB} - 1.4\times10^{-20}\,C_{HWB} \\
& + 3.6\times10^{-7}\,(C_{HW})^2 + 2.8\times10^{-5}\,(C_{HB})^2 + 2.5\times10^{-5}\,(C_{HWB})^2 \\
& + 3.6\times10^{-7}\,(C_{H\tilde{W}})^2 + 2.8\times10^{-5}\,(C_{H\tilde{B}})^2 + 2.5\times10^{-5}\,(C_{H\tilde{W}B})^2 \\
& + 6.3\times10^{-6}\,C_{HW}C_{HB} + 6.0\times10^{-6}\,C_{HW}C_{HWB} + 5.2\times10^{-5}\,C_{HB}C_{HWB} \\
& + 6.3\times10^{-6}\,C_{H\tilde{W}}C_{H\tilde{B}} + 6.0\times10^{-6}\,C_{H\tilde{W}}C_{H\tilde{W}B} \\
& + 5.2\times10^{-5}\,C_{H\tilde{B}}C_{H\tilde{W}B}\,.
\end{aligned}
\tag{4.54}
$$

Note that they are quadratic in C_i with cross-terms of different WCs coming from different operators. The optimal χ^2 analysis is done based on the above parametrization.

4.H Comparison with FCC-ee Limits

The electron-positron collision stage of the Future Circular Collider (FCC-ee) [322] is expected to run at a CM energy of $\sqrt{s} = 240$ GeV with a projected integrated luminosity of $\mathfrak{L}_{\rm int} = 10500$ fb^{-1}. However, the setup is expected to collide unpolarized beams only. In this section, we draw a comparison between the 95% C.L. limits on the SMEFT

operators for ILC 250 GeV with $\mathcal{L}_{\rm int} = 2000$ fb^{-1} for the unpolarized and polarized setup discussed in Tab. 4.12, with the limits from the FCC-ee run, tabulated in Tab. 4.18. The higher luminosity of the FCC-ee results in more sensitive bounds compared to the ILC runs.

WCs	**FCC-ee (240 GeV 10500 fb^{-1})**	**ILC (250 GeV 2000 fb^{-1})**	
		Unpolarized	**Polarized**
C_{HW}	$[-0.02, +0.02]$	$[-0.06, +0.06]$	$[-0.04, +0.04]$
C_{HWB}	$[-0.03, +0.03]$	$[-0.12, +0.12]$	$[-0.08, +0.08]$
C_{HB}	$[-0.06, +0.06]$	$[-0.28, +0.23]$	$[-0.07, +0.07]$
$C_{H\widetilde{W}}$	$[-0.47, +0.47]$	$[-0.98, +0.98]$	$[-0.83, +0.83]$
$C_{H\widetilde{W}B}$	$[-0.86, +0.86]$	$[-1.80, +1.80]$	$[-1.42, +1.42]$
$C_{H\widetilde{B}}$	$[-0.74, +0.74]$	$[-1.55, +1.55]$	$[-1.32, +1.32]$

TABLE 4.18: 95% CL bounds on CP-even (*top half*) and CP-odd (*bottom half*) operator coefficients from Zh production at the FCC-ee 240 GeV vs. ILC 250 GeV. For the polarized case, we choose $\mathfrak{L}_{\rm int} = 1000$ fb^{-1} for polarization setups $(+30\%, -80\%)$ and $(-30\%, +80\%)$ each.

4.I Correlated Sensitivities in the OOT

The two parameter χ^2 sensitivity contours are shown in Fig. 4.26 for both the unpolarized and the polarized beam configurations discussed in Tab. 4.12. For the two-parameter case, the 95% C.L. limit corresponds to $\chi^2 = 5.99$. The comparison between the unpolarized and combined setups clearly demonstrates the enhanced sensitivity achieved through beam polarization, emphasizing its crucial role in constraining SMEFT operators at future e^+e^- colliders.

4.J Spin Analyzing Power for $V \to f_1 f_2$

Considering the decay of a spin-1 boson (W/Z) to two fermions via a vertex of the form $\overline{f}_1\gamma^\mu(C_L P_L + C_R P_R) f_2 V_\mu$ with real $C_{L,R}$, the expressions for the spin analyzing

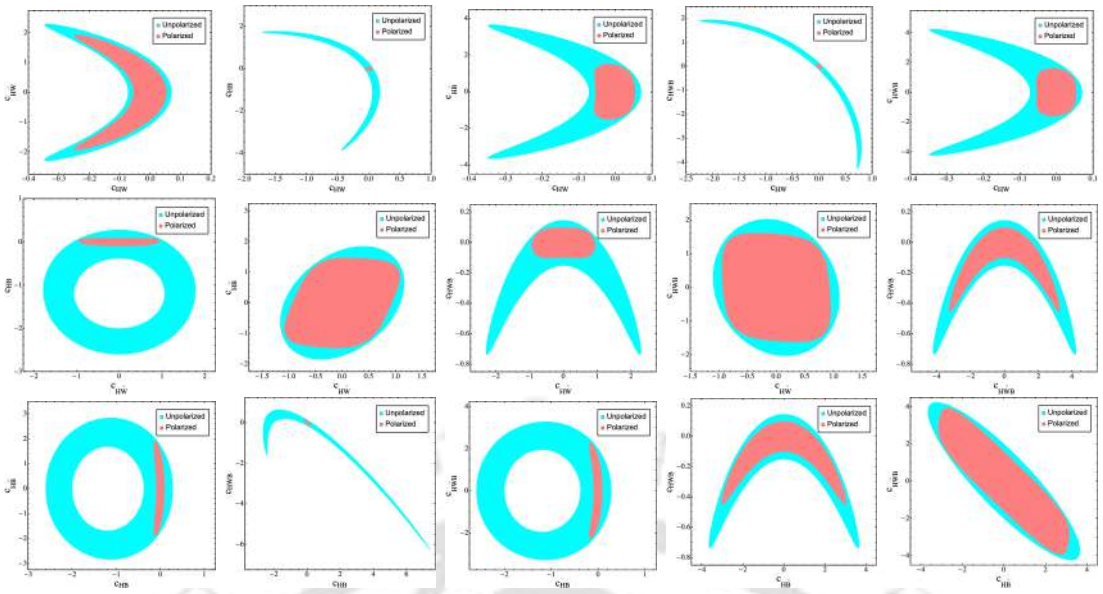

FIGURE 4.26: Two parameter optimal sensitivity plots from Zh production at the ILC 250 GeV for unpolarized and combined setup. For the unpolarized setup, $\mathfrak{L}_{\rm int} = 2000$ fb^{-1}, and for the polarized setup, each polarization configuration viz. $(+30\%, -80\%)$ and $(-30\%, +80\%)$ with $\mathfrak{L}_{\rm int} = 1000$ fb^{-1}, combines to an integrated luminosity of $\mathfrak{L}_{\rm int} = 2000$ fb^{-1}.

parameters α and δ are given by [373]:

$$\begin{aligned}\alpha =& \frac{2(C_R^2 - C_L^2)\sqrt{1 + (x_1^2 - x_2^2)^2 - 2(x_1^2 + x_2^2)}}{12C_LC_Rx_1x_2 + (C_R^2 + C_L^2)[2 - (x_1^2 - x_2^2)^2 + (x_1^2 + x_2^2)]},\\ \delta =& \frac{4C_LC_Rx_1x_2 + (C_R^2 + C_L^2)[(x_1^2 + x_2^2) - (x_1^2 - x_2^2)^2]}{12C_LC_Rx_1x_2 + (C_R^2 + C_L^2)[2 - (x_1^2 - x_2^2)^2 + (x_1^2 + x_2^2)]},\end{aligned} \tag{4.55}$$

where $x_i = m_i/m$, m_i is the mass of the final fermion, and m is the mass of the mother boson. At the high energy limit, the final fermions decayed from the W/Z are taken to be massless, $x_1 \to 0, x_2 \to 0$, then one obtains $\alpha \to (C_R^2 - C_L^2)/(C_R^2 + C_L^2)$ and $\delta \to 0$. Further, within the SM, in the decay of W, we have $C_R = 0$, hence $\alpha = -1$.

Chapter 5

Application to Flavor Physics

"Everything is vague to a degree you do not realize till you have tried to make it precise."
Bertrand Russell

Contents

The flavor sector of the SM has long stood as one of the most compelling frontiers for the discovery of NP, owing to the pronounced hierarchy in fermion masses and the non-trivial mixing between flavor and mass eigenstates. While neutrino oscillations have firmly established flavor violation in the neutral lepton sector, cLFV is strictly forbidden in the SM with massless neutrinos and remains extremely suppressed even after incorporating finite neutrino masses. In the quark sector, FCNCs arise only at the loop level and are highly suppressed, with top quark FCNC processes being of particular interest due to the large top quark mass. Consequently, any experimental observation of cLFV or top quark FCNCs would provide an unambiguous signal of physics beyond the SM.

In this context, the SMEFT four-fermion operators offer a powerful and model-independent avenue to study flavor violating effects. Their purely fermionic structure allows for direct contact interactions, enabling a transparent connection to heavy NP through tree-level UV completions. Future lepton colliders provide an ideal environment to probe such effects, leveraging clean experimental signatures and enhanced sensitivity.

This chapter explores the application of SMEFT to rare flavor violating processes at future lepton colliders. It is organized into two main studies. Sec. 5.1 focuses on cLFV within the lepton sector, examining the production of $\mu\tau$ and $e\tau$ final states at the proposed CLiC. By employing the OOT, we derive the ultimate statistical sensitivity to flavor violating four-fermion couplings, and demonstrate how beam polarization can suppress SM backgrounds and disentangle operator chiral structures. Sec. 5.2 extends the analysis to processes involving both lepton and quark sectors, investigating simultaneous cLFV and top-quark FCNC interactions. In particular, we study the flavor violating process $\mu^+e^- \to tq'$ (with $q' = u, c$) at the proposed asymmetric μTRISTAN collider. Using a cut-based analysis complemented by binned likelihood techniques, we obtain projected bounds on scalar, vector, and tensor structures, and translate these into constraints on rare top quark decay branching ratios. Together, these studies highlight the crucial role of next-generation lepton colliders in addressing the flavor puzzle and placing stringent constraints on the parameter space of BSM scenarios.

5.1 Charged Lepton Flavor Violation in SMEFT

Exploring optimal sensitivity of lepton flavor violating effective couplings at the e^+e colliders.
S. Jahedi, A. Sarkar.
Phys.Rev.D 110 (2024) 9, 9 (e-Print: 2408.00190 [hep-ph]).

A comprehensive array of experiments has been conducted across different scales to explore cLFV. However, none of these experiments have yielded substantial evidence supporting it. Consequently, upper limits have been established for cLFV branching ratios ($\mathcal{B}$'s) in decay processes, as well as cLFV couplings in the decays of charged leptons. The SINDRUM experiment puts an upper bound on $\mathcal{B}(\mu \to e\gamma)$ at 10^{-12} [110]. In case of τ-μ and τ-e conversions, the Belle experiment puts bound on $\mathcal{B}(\tau \to \mu\gamma) < 4.2\times10^{-8}$ and $\mathcal{B}(\tau \to e\gamma) < 5.6\times10^{-8}$ [109]. On the other hand, the MEG experiment provides an upper bound on $\mathcal{B}(\mu \to e\gamma)$ at 4.2×10^{-13} [83]. In the scenario of three body decays, the Belle experiment sets an upper bound on $\mathcal{B}(\tau \to 3e) < 2.7 \times 10^{-8}$ and $\mathcal{B}(\tau \to 3\mu) < 4.4 \times 10^{-8}$ [111]. All the limits are determined at 90% C.L. Neutral bosons decays into cLFV modes is also investigated at different collider experiments. The CMS experiment at the LHC has established that the branchings of the Higgs boson in the $e\mu$, $e\tau$, and $\tau\mu$ channels are constrained to be less than 3.5×10^{-4} [378],

6.1×10^{-3}, and 2.5×10^{-3} [379], respectively, at 95% C.L. The cLFV decays of Z boson have undergone measurement in the $e\mu$, $e\tau$, and $\mu\tau$ channels at the LEP by the OPAL and DELPHI collaborations [380, 381]. Nevertheless, the latest investigations of these decays at the LHC by the ATLAS collaboration have surpassed the preceding limits set by LEP [119, 382, 383]. LEP has further examined cLFV $2 \to 2$ processes and imposed restrictions on the cross sections associated with these processes. The OPAL analysis conducted at LEP presents confidence level boundaries on the cross sections for $e^+e^- \to \tau\mu,\ \tau e$, and μe processes at various CM energies, as detailed in Tab. 5.1.

CM energy $\sqrt{s}$ (GeV)	**Cross section (fb)**		
	$\tau\mu$	τe	μe
189	115	95	58
$192 \leq \sqrt{s} \leq 196$	116	144	162
$200 \leq \sqrt{s} \leq 209$	64	78	22

TABLE 5.1: Upper bound on different flavor violating cross sections from the OPAL experiment [13].

In this analysis, we investigate the production of muon-tau ($\mu\tau$) and electron-tau ($e\tau$) pairs at the CLiC [384], a proposed electron-positron collider. The absence of the QCD effects in the initial electron-positron beams proves invaluable for estimating potential NP against a significantly cleaner background. Additionally, the availability of partially polarized beams offers a distinct advantage in suppressing the SM background, thereby facilitating the dominance of the NP signal over the SM background. We consider the SMEFT framework [11, 14, 168, 169, 172, 273] to probe the cLFV through four-fermion effective operators, which we discuss in the next section. cLFV under the SMEFT framework has been studied at hadron colliders [385–389] and lepton colliders [390–393]. Due to heightened background contamination in the leptonic decay modes of τ lepton, our study centers on the hadronic decay modes of the τ lepton that manifest as light jets at high energy colliders. Despite the predominance of the hadronic modes in τ lepton decays, distinguishing τ jets from other hadronic activities proves challenging due to formidable background interference at both hadron and hadron-electron colliders. Hence, exploring such signals in the cleaner environments of lepton colliders offers a more favorable avenue for investigation. We perform the OOT [367–370] to estimate the optimal sensitivity of dimension 6 effective couplings through the signal process $e^+e^- \to l\tau$ ($l = e, \mu$).

The OOT has been utilized in constraining top quark couplings [394–399] and Higgs couplings [246, 334] at the e^+e^- colliders. Its application extends to the examination of top quark interactions at $\gamma\gamma$ colliders [400, 401], the measurement of top Yukawa couplings at the LHC [402], muon colliders [403], and $e\gamma$ colliders [404]. Recent studies of the OOT includes the investigation of Z couplings of heavy charged fermions at the e^+e^- colliders [232, 405, 406], explored neutral triple gauge couplings [407, 408], and investigated NP effects in flavor physics scenarios [409–412].

This study is organized as follows: In Sec. 5.1.1, we point out the relevant dimension 6 effective operators pertinent to our study and evaluate the upper bound on NP couplings from flavor violating τ lepton decays. We describe the collider simulation in Sec. 5.1.2. A brief overview of the OOT and optimal sensitivity are discussed in Sec. 5.1.3. Finally, in Sec. 5.1.4, we present summary and conclusion of our study.

5.1.1 cLFV via Dimension 6 SMEFT

The lack of signals in direct searches for new particle production at the LHC implies a gap in energy between the electroweak scale and the potential scale where the NP responsible for inducing cLFV may manifest. This leads us to work under the SMEFT framework, which involves introducing a series of higher dimensional operators along with the SM Lagrangian. The general definition of SMEFT Lagrangian is given by

$$\mathcal{L}_{\rm EFT} = \mathcal{L}_{\rm SM} + \sum_{i,\,d} \frac{C_i\,\mathcal{O}_i^{(d)}}{\Lambda^{d-4}}\,, \tag{5.1}$$

where Λ is the scale of NP, C_i's are the WCs through which the effects of NP are understood. $\mathcal{O}_i^{(d)}$'s are the d-dimensional operators constructed from SM fields and respect SM gauge symmetry. flavor violating dilepton production at the lepton colliders is primarily governed by three classes of SMEFT operators, presented in Tab. 5.2. In operators expressions, ℓ and e are the $SU(2)_L$ lepton doublets and iso-spin singlets, H is the Higgs doublet, and $W^I_{\mu\nu}$, $B_{\mu\nu}$ are the field strength tensors of the $SU(2)_L$ and $U(1)_Y$ gauge group.

Experimental constraints derived from the muon decay process $\mu \to 3e$ at the SINDRUM experiment [110], $\mu - e$ conversion [115], and $\mu \to e\gamma$ transition [83] have firmly restricted flavor violation between the first and second generations of leptons. However,

Higgs-current operators	Dipole operators	Four-fermion operators
$(\mathcal{O}^{(1)}_{H\ell})_{ij} : (H^\dagger i\overleftrightarrow{D}_\mu H)(\bar{\ell}_i\gamma^\mu\ell_j)$	$(\mathcal{O}_{eW})_{ij} : (\bar{\ell}_i\sigma^{\mu\nu}e_j)\tau^I H W^I_{\mu\nu}$	$(\mathcal{O}_{\ell\ell})_{ijkl} : (\bar{\ell}_i\gamma^\mu\ell_j)(\bar{\ell}_k\gamma^\mu\ell_l)$
$(\mathcal{O}^{(3)}_{H\ell})_{ij} : (H^\dagger i\overleftrightarrow{D}^I_\mu H)(\bar{\ell}_i\gamma^\mu\tau^I\ell_j)$	$(\mathcal{O}_{eB})_{ij} : (\bar{\ell}_i\sigma^{\mu\nu}e_j)H B_{\mu\nu}$	$(\mathcal{O}_{ee})_{ijkl} : (\bar{e}_i\gamma^\mu e_j)(\bar{e}_k\gamma^\mu e_l)$
$(\mathcal{O}_{He})_{ij} : (H^\dagger i\overleftrightarrow{D}_\mu H)(\bar{e}_i\gamma^\mu e_j)$		$(\mathcal{O}_{\ell e})_{ijkl} : (\bar{\ell}_i\gamma^\mu\ell_j)(\bar{e}_k\gamma^\mu e_l)$

TABLE 5.2: Three classes of dimension 6 operators contributing to the flavor violating dilepton production at the lepton colliders [11, 14].

the constraints pertaining to flavor violation between electrons/muons and tau leptons appear less stringent. Given these observations, we examine the $eel\tau$ couplings through $l\tau$ production at future e^+e^- colliders.

$e^+e^- \to l\tau$ ($l = \mu, e$) Production Among the various classes of operators listed in Tab. 5.2 to produce τl, the four-fermion operators result in contact interactions, as illustrated in left diagram of Fig. 5.2. Meanwhile, the dipole and Higgs-current operators contribute to the $Zl\tau$ and $\gamma l\tau$ vertices, respectively, as shown in right diagram Fig. 5.2. Considering that the couplings are of same order, at a fixed CM energy, the contribution of four-fermion operators to τl production dominates over the dipole/Higgs-current operators evidently due to the absence of s-channel suppression in case of this class of operators, and the dominance is amplified as we tend towards higher CM energies, as shown in Fig. 5.1. The contribution of Higgs-current operators to the τl production drops rapidly with increase in CM energy. Concerning the dipole operators, the cross section remains nearly constant throughout the range of $\sqrt{s}$, but for a similar value of WC, the cross section pertaining to four-fermion operators dominate over the dipole operators by $\mathcal{O}(100)$ at $\sqrt{s} = 3$ TeV. It should be noted that owing to their sensitivity, four-fermion operators are more strongly constrained from cLFV measurements in comparison to the other two classes. However, it is clear from Fig. 5.2 that only four-Fermi-type operators can address tree level decoupled NP concerned with $e^+e^- \to l\tau$ production process at the lepton colliders. For our analysis, we restrict ourselves to four-fermion operators only. Since, we study the processes at the e^+e^- collider, to further simplify the notation, we drop the ee indices associated with these operators and different index combinations contributing to same vertex are naturally assumed to be equal, detailed in Eq. (5.2) for $\mu\tau$ production. Same applies for $e\tau$ production as well.

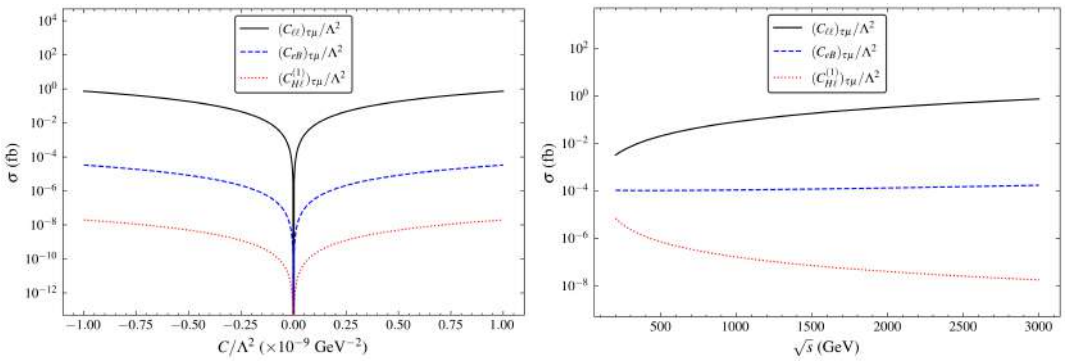

FIGURE 5.1: Left: Variation of cross section for the process $e^+e^- \to \mu^\pm\tau^\mp$ with the change in WCs (C/Λ^2) at $\sqrt{s} = 3$ TeV. Right: Variation of the cross section for the same process with change in CM energy, $\sqrt{s}$ (C/Λ^2 set to 1.0×10^{-9} GeV^{-2}).

$$\begin{aligned}
\left(C_{\ell\ell/\ell e/ee}\right)_{\tau\mu} &= \left(C_{\ell\ell/\ell e/ee}\right)_{\mu\tau ee} = \left(C_{\ell\ell/\ell e/ee}\right)_{ee\mu\tau} \\
&= \left(C_{\ell\ell/\ell e/ee}\right)_{e\tau\mu e} = \left(C_{\ell\ell/\ell e/ee}\right)_{\mu ee\tau}, \\
\left(C_{\ell\ell/\ell e/ee}\right)_{\tau e} &= \left(C_{\ell\ell/\ell e/ee}\right)_{e\tau ee} = \left(C_{\ell\ell/\ell e/ee}\right)_{eee\tau}, \\
\left(C_{\ell\ell/\ell e/ee}\right)_{\mu e} &= \left(C_{\ell\ell/\ell e/ee}\right)_{e\mu ee} = \left(C_{\ell\ell/\ell e/ee}\right)_{eee\mu}.
\end{aligned} \tag{5.2}$$

Considering the $\mu\tau$ production at the e^+e^- colliders, the four-fermion operators, following simplification and Fierz transformation, can be expressed as

$$\begin{aligned}
&(C_V^{LL})_{\tau\mu}\frac{1}{\Lambda^2}(\bar{e}\gamma_\alpha P_L e)(\bar{\mu}\gamma^\alpha P_L\tau), && (C_V^{RR})_{\tau\mu}\frac{1}{\Lambda^2}(\bar{e}\gamma_\alpha P_R e)(\bar{\mu}\gamma^\alpha P_R\tau), \\
&(C_V^{LR})_{\tau\mu}\frac{1}{\Lambda^2}(\bar{e}\gamma_\alpha P_L e)(\bar{\mu}\gamma^\alpha P_R\tau), && (C_V^{RL})_{\tau\mu}\frac{1}{\Lambda^2}(\bar{e}\gamma_\alpha P_R e)(\bar{\mu}\gamma^\alpha P_L\tau), \\
&(C_S^{LR})_{\tau\mu}\frac{1}{\Lambda^2}(\bar{e}P_L e)(\bar{\mu}P_R\tau), && (C_S^{RL})_{\tau\mu}\frac{1}{\Lambda^2}(\bar{e}P_R e)(\bar{\mu}P_L\tau),
\end{aligned} \tag{5.3}$$

where the WCs are defined as follows:

$$\begin{aligned}
(C_V^{LL})_{\tau\mu} &= (C_{\ell\ell})_{ee\mu\tau} + (C_{\ell\ell})_{\mu\tau ee} + (C_{\ell\ell})_{e\tau\mu e} + (C_{\ell\ell})_{\mu ee\tau} = 4(C_{\ell\ell})_{\tau\mu}, \\
(C_V^{RR})_{\tau\mu} &= (C_{ee})_{ee\mu\tau} + (C_{ee})_{\mu\tau ee} + (C_{ee})_{e\tau\mu e} + (C_{ee})_{\mu ee\tau} = 4(C_{ee})_{\tau\mu}, \\
(C_V^{LR})_{\tau\mu} &= (C_{\ell e})_{ee\mu\tau} = (C_{\ell e})_{\tau\mu}, \qquad (C_V^{RL})_{\tau\mu} = (C_{\ell e})_{\mu\tau ee} = (C_{\ell e})_{\tau\mu}, \\
(C_S^{LR})_{\tau\mu} &= -2(C_{\ell e})_{\mu ee\tau} = -2(C_{\ell e})_{\tau\mu}, \quad (C_S^{RL})_{\tau\mu} = -2(C_{\ell e})_{e\tau\mu e} = -2(C_{\ell e})_{\tau\mu}.
\end{aligned} \tag{5.4}$$

The helicity amplitudes, $\mathcal{M}(\lambda_{e^-}, \lambda_{e^+}; \lambda_{\mu^-}, \lambda_{\tau^+})$ for the process $e^+e^- \to \mu^+\tau^-$ induced by the four-fermion operators are given by[1]

$$\begin{aligned}
\mathcal{M}(+\lambda, -\lambda; +\lambda^{'}, -\lambda^{'}) &= -\frac{s}{\Lambda^2}\left[(C_V^{LL})_{\tau\mu}\delta_{\lambda,-1}\delta_{\lambda',-1} + (C_V^{RR})_{\tau\mu}\delta_{\lambda,1}\delta_{\lambda',1}\right](1+\cos\theta) \\
&\quad + \frac{s}{\Lambda^2}\left[(C_V^{LR})_{\tau\mu}\delta_{\lambda,-1}\delta_{\lambda',1} + (C_V^{RL})_{\tau\mu}\delta_{\lambda,1}\delta_{\lambda',-1}\right](1-\cos\theta), \\
\mathcal{M}(+\lambda, -\lambda; +\lambda^{'}, +\lambda^{'}) &= 0, \\
\mathcal{M}(+\lambda, +\lambda; +\lambda^{'}, -\lambda^{'}) &= 0, \\
\mathcal{M}(+\lambda, +\lambda; +\lambda^{'}, +\lambda^{'}) &= \frac{s}{\Lambda^2}\left[(C_S^{LR})_{\tau\mu}\delta_{\lambda,-1}\delta_{\lambda',-1} + (C_S^{RL})_{\tau\mu}\delta_{\lambda,1}\delta_{\lambda',1}\right],
\end{aligned} \tag{5.5}$$

where, θ is the scattering angle in CM frame. $\lambda, \lambda^{'} = -1(+1)$ denotes the left(right)-

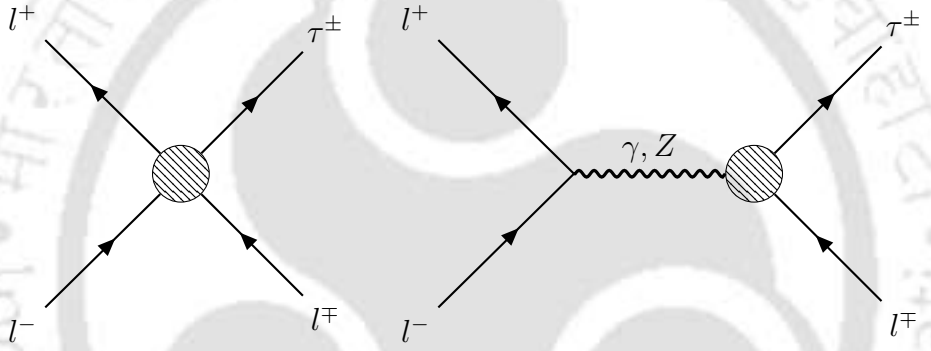

FIGURE 5.2: Feynman diagrams that induce $l^\mp\tau^\pm$ production at the lepton colliders; left: effective four-fermion contribution, right: dipole and Higgs-current contributions.

handed helicity of initial beam particle. The differential cross section with partial initial beam polarization ($-1 \le P_{e^\pm} \le +1$) is written as

$$\begin{aligned}
\frac{d\sigma(P_{e^-}, P_{e^+})}{d\phi} =& \frac{(1-P_{e^-})(1-P_{e^+})}{4}\left(\frac{d\sigma}{d\phi}\right)_{\rm LL} + \frac{(1-P_{e^-})(1+P_{e^+})}{4}\left(\frac{d\sigma}{d\phi}\right)_{\rm LR} \\
&+ \frac{(1+P_{e^-})(1-P_{e^+})}{4}\left(\frac{d\sigma}{d\phi}\right)_{\rm RL} + \frac{(1+P_{e^-})(1+P_{e^+})}{4}\left(\frac{d\sigma}{d\phi}\right)_{\rm RR}, \\
=& g_i f_i(\phi),
\end{aligned} \tag{5.6}$$

[1]These amplitudes are calculated in the massless limit of initial and final particles.

where $P_{e^-(e^+)}$ is the electron(positron) beam polarization and ϕ is the phase-space coordinate.

$$\begin{aligned}
g_1 =&(1-P_{e^-})\left(\frac{1}{\Lambda^4}\right)\left[(1+P_{e^+})(C_V^{LR})^2_{\tau\mu}+(1-P_{e^+})\{(C_V^{LL})^2_{\tau\mu}+(C_S^{LR})^2_{\tau\mu}\}\right]\\
&+(1+P_{e^-})\left(\frac{1}{\Lambda^4}\right)\left[(1-P_{e^+})(C_V^{RL})^2_{\tau\mu}+(1+P_{e^+})\left\{(C_V^{RR})^2_{\tau\mu}+(C_S^{RL})^2_{\tau\mu}\right\}\right],\\
g_2 =&(1-P_{e^-})(1+P_{e^+})\left(\frac{1}{\Lambda^4}\right)\left[(C_V^{LL})^2_{\tau\mu}-(C_V^{LR})^2_{\tau\mu}\right]\\
&+(1+P_{e^-})(1-P_{e^+})\left(\frac{1}{\Lambda^4}\right)\left[(C_V^{RL})^2_{\tau\mu}-(C_V^{RR})^2_{\tau\mu}\right],\\
g_3 =&(1-P_{e^-})(1+P_{e^+})\left(\frac{1}{\Lambda^4}\right)\left[(C_V^{LR})^2_{\tau\mu}+(C_V^{LL})^2_{\tau\mu}\right]\\
&+(1+P_{e^-})(1-P_{e^+})\left(\frac{1}{\Lambda^4}\right)\left[(C_V^{RL})^2_{\tau\mu}+(C_V^{RR})^2_{\tau\mu}\right],
\end{aligned} \tag{5.7}$$

and

$$f_1(\theta)=\frac{s}{256\pi^2},\quad f_2(\theta)=\frac{s}{128\pi^2}\cos\theta,\quad f_3(\theta)=\frac{s}{256\pi^2}\cos^2\theta. \tag{5.8}$$

This above decomposition (Eqs. (5.7)-(5.8)) is required to determine the optimal covariance matrix as we discuss in Sec. 5.1.3. The total cross section is evaluated as

$$\sigma(P_{e^-},P_{e^+})=\frac{s}{96\pi}(3g_1+g_2). \tag{5.9}$$

We show that variation of $\mu\tau$ cross section with three different flavor violating dimension 6 effective couplings for various choices of beam polarization in Fig. 5.3. For the $(\mathcal{O}_{\ell\ell})_{\tau\mu}$ operator, both currents are left-handed. Thus, using a left-polarized electron beam is advantageous for enhancing the cross section compared to an unpolarized beam (left plot of Fig. 5.3). Conversely, for the $(\mathcal{O}_{ee})_{\tau\mu}$ operator, both currents are right-handed, making a right-handed electron beam more beneficial for increasing the total cross section (right plot of Fig. 5.3). In the case of the $(\mathcal{O}_{\ell e})_{\tau\mu}$ operator, one current is left-handed and the other is right-handed. Therefore, regardless of the beam polarization, this operator contributes in the same manner (middle plot of Fig. 5.3).

Constraints from cLFV Processes As discussed in previous sections, the cLFV processes are constrained from a wide array of low-energy experiments. In this section,

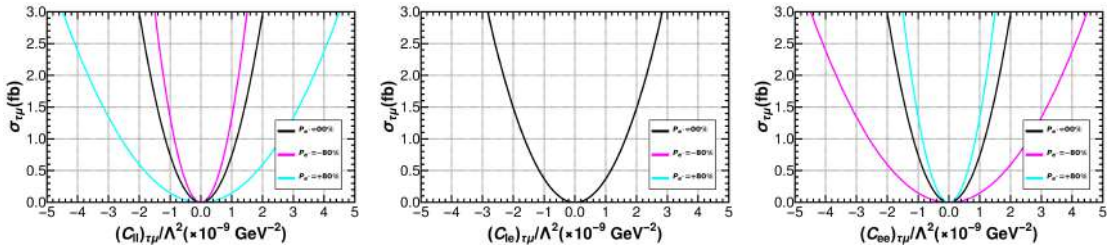

FIGURE 5.3: Variation of $\mu\tau$ cross section with various flavor violating effective couplings for different choices of beam polarization. Left: $(C_{\ell\ell})_{\tau\mu}/\Lambda^2$, middle: $(C_{\ell e})_{\tau\mu}/\Lambda^2$, right: $(C_{ee})_{\tau\mu}/\Lambda^2$.

we translate these experimental bounds to the cLFV operators. The four-fermion operators contributing to $l^{'} \to l\gamma$ processes (via leptonic loop) vanish when all the diagrams corresponding to this process are taken into account. Hence, bounds on the four-fermion operators are insensitive to $l^{'} \to l\gamma$ branching. The four-fermion operators are mostly constrained from flavor violating three body decays of μ and τ i.e. $l^{'} \to 3l$. These decay modes have been studied explicitly in all possible channels and the most recent bounds are quoted in Tab. 5.3. The $\mathcal{B}$s are parametrized in terms of EFT coefficients in Eq. (5.10). Since the phase space of three body decays are universal, the parametrization is done for the ratio of cLFV $l^{'} \to 3l$ decay to lepton flavor conserving $l^{'} \to l\nu^{'}\overline{\nu}$ decay. This removes common constant parameters and the parametrization is simplified. The branchings $\mathcal{B}(\tau^- \to \mu^-\nu_\tau\overline{\nu}_\mu)$ and $\mathcal{B}(\mu^- \to e^-\nu_\mu\overline{\nu}_e)$ are taken to be 0.174 and 1, respectively (based on combined fits by PDG [413]).

$$
\begin{aligned}
\frac{\mathcal{B}(\mu^- \to e^-e^+e^-)}{\mathcal{B}(\mu^- \to e^-\nu_\mu\overline{\nu}_e)} &\sim \frac{v^4}{\Lambda^4}\left\{4\left|(C_{\ell\ell})_{\mu e}\right|^2 + 4\left|(C_{ee})_{\mu e}\right|^2 + \left|(C_{\ell e})_{\mu e}\right|^2\right\},\\
\frac{\mathcal{B}(\tau^- \to e^-e^+e^-)}{\mathcal{B}(\tau^- \to \mu^-\nu_\tau\overline{\nu}_\mu)} &\sim \frac{v^4}{\Lambda^4}\left\{4\left|(C_{\ell\ell})_{\tau e}\right|^2 + 4\left|(C_{ee})_{\tau e}\right|^2 + \left|(C_{\ell e})_{\tau e}\right|^2\right\},\\
\frac{\mathcal{B}(\tau^- \to \mu^-e^+e^-)}{\mathcal{B}(\tau^- \to \mu^-\nu_\tau\overline{\nu}_\mu)} &\sim \frac{v^4}{\Lambda^4}\left\{4\left|(C_{\ell\ell})_{\tau\mu}\right|^2 + 4\left|(C_{ee})_{\tau\mu}\right|^2 + \left|(C_{\ell e})_{\tau\mu}\right|^2\right\}.
\end{aligned}
\tag{5.10}
$$

The bounds on operators contributing to $e^+e^- \to \mu e$ production, as presented in Tab. 5.3, are very stringent, therefore, it is very unlikely[2] that these operators will be probed in this particular channel even at CM energy as high as 3 TeV. Future high energy muon collider [414] could be a possibility to probe cLFV through this process with satisfactory

[2]Considering the allowed upper bound on, say, $(C_{\ell\ell})_{\mu e} = 8.26 \times 10^{-12}$, the cross section of $e^+e^- \to \mu e$ is $< 5 \times 10^{-5}$ fb (without any cuts), i.e. even $\mathfrak{L}_{\rm int} = 10$ ab^{-1} won't yield even a single event (< 0.5 events).

Observable	Upper Bounds	Bounds on EFT coefficients ($\mathbf{GeV^{-2}}$)
$\mathcal{B}(\mu^- \to e^- e^+ e^-)$	$< 1.0 \times 10^{-12}$ [110]	$\lvert(C_{\ell\ell})_{\mu e}\rvert / \Lambda^2 < 8.26 \times 10^{-12}$ $\lvert(C_{ee})_{\mu e}\rvert / \Lambda^2 < 8.26 \times 10^{-12}$ $\lvert(C_{\ell e})_{\mu e}\rvert \Lambda^2 < 1.65 \times 10^{-11}$
$\mathcal{B}(\tau^- \to e^- e^+ e^-)$	$< 2.7 \times 10^{-8}$ [111]	$\lvert(C_{\ell\ell})_{\tau e}\rvert / \Lambda^2 < 3.26 \times 10^{-9}$ $\lvert(C_{ee})_{\tau e}\rvert / \Lambda^2 < 3.26 \times 10^{-9}$ $\lvert(C_{\ell e})_{\tau e}\rvert / \Lambda^2 < 6.51 \times 10^{-9}$
$\mathcal{B}(\tau^- \to \mu^- e^+ e^-)$	$< 1.8 \times 10^{-8}$ [111]	$\lvert(C_{\ell\ell})_{\tau \mu}\rvert / \Lambda^2 < 2.66 \times 10^{-9}$ $\lvert(C_{ee})_{\tau \mu}\rvert / \Lambda^2 < 2.66 \times 10^{-9}$ $\lvert(C_{\ell e})_{\tau \mu}\rvert / \Lambda^2 < 5.32 \times 10^{-9}$

TABLE 5.3: Flavor bounds from lepton number violating observables and processes. $\mathcal{B}$ refers to branching ratio (Γ_i/Γ).

statistics. We would like to point out that the renomalization group equation (RGE) evolution on four-fermion effective couplings are small, given the upper bound from cLFV decays (see App. 5.B).

5.1.2 Collider Analysis: CLiC 3 TeV

In this section, we study the sensitivity of the flavor violating four-fermion effective operators at the CLiC with 3 TeV CM energy via $l\tau$ production. Since these operators are not flavor universal, we probe $(\mathcal{O}_{\ell\ell})_{\tau e}$, $(\mathcal{O}_{ee})_{\tau e}$ and $(\mathcal{O}_{\ell e})_{\tau e}$ operators with $e^{\mp}\tau^{\pm}$ production and $(\mathcal{O}_{\ell\ell})_{\tau\mu}$, $(\mathcal{O}_{ee})_{\tau\mu}$ and $(\mathcal{O}_{\ell e})_{\tau\mu}$ operators with $\mu^{\mp}\tau^{\pm}$ production. As discussed previously, our study centers on the hadronic decay modes of the τ lepton. Hence, the signal process in our case is $e^+e^- \to l\tau_h$ (+ missing energy, $\not{E}$, from the neutrino in τ decay). The dominant SM backgrounds come from $e^+e^- \to W^+W^-$, $e^+e^- \to \tau^+\tau^-$ and $e^+e^- \to \nu\bar{\nu}Z$.

The signal model is implemented in `FeynRules` [233]. The signal and background events are generated in `MG5_aMC` [235]. The generated MC events are fed into `Pythia8` [415] for parton showering (ISR, FSR, and hadronization effects). The showered events are further fed into `Delphes3` [237], where the detector resolution and efficiency factors are taken into account. The electron and muon efficiencies in different kinematic regions are tabulated in Tab. 5.4. The jet reconstruction task is done using `FastJet3` [238]. The

hadronic τ (τ jet) tagging efficiency is taken as 0.6 and the misstagging efficiency of light jets as τ is 0.01 (as per `Delphes3` default card).

Electrons	ε	**Muons**	ε
$p_T < 10.0$ GeV	0.00	$p_T < 10.0$ GeV	0.00
$p_T > 10.0$ GeV, $\lvert\eta\rvert \in [0.0, 1.5]$	0.95	$p_T > 10.0$ GeV, $\lvert\eta\rvert \in [0.0, 1.5]$	0.95
$p_T > 10.0$ GeV, $\lvert\eta\rvert \in (1.5, 2.5]$	0.85	$p_T > 10.0$ GeV, $\lvert\eta\rvert \in (1.5, 2.4]$	0.95
$\lvert\eta\rvert > 2.5$	0.00	$\lvert\eta\rvert > 2.4$	0.00

TABLE 5.4: Efficiency (ε) of electron and muon detection for different kinematic regions.

Cut-based Analysis The total cross sections at $\sqrt{s} = 3$ TeV for different polarization settings are tabulated in Tab. 5.5 for $l\tau$ and background processes at production level. The signal cross sections are noted for three benchmarks of EFT coefficients, adhering to the allowed bounds on these operators as stated in Tab. 5.3. As discussed previously, for signal process, the operators $(\mathcal{O}_{\ell\ell})_{\tau l}$ and $(\mathcal{O}_{ee})_{\tau l}$ have fixed chirality, they are very sensitive to the polarization settings, $P_{e^-} = \pm 80\%$. The operator $(\mathcal{O}_{\ell e})_{\tau lee}$ has mixed chirality and is unaffected by the different polarization tuning. The dominant backgrounds WW and $\nu\bar{\nu}Z$ are left chiral owing to the gauge structure of the SM, hence, polarization choice of $P_{e^-} = +80\%$ significantly reduce the background cross section and $P_{e^-} = -80\%$ choice enhance the SM background. The invariant mass, $M_{\mu\tau}/M_{e\tau}$ and H_T distributions for the signal benchmarks and the major backgrounds are plotted in Figs. 5.4 and 5.5. The invariant mass is defined as:

$$M_{l\tau} = \sqrt{(p_l + p_{\tau_h})^2}, \tag{5.11}$$

where, p_l and p_{τ_h} are the 4-momenta of the lepton and τ jet, respectively. The H_T variable is defined as:

$$H_T = \sum_{\text{visible}} p_T. \tag{5.12}$$

This is essentially the scalar sum of p_T of visible particles. There are different ways in which H_T is defined in the collider literature [2], but we will resort to the definition in Eq. (5.12). Additional distributions are shown in Figs. 5.15 and 5.16 of App. 5.A.

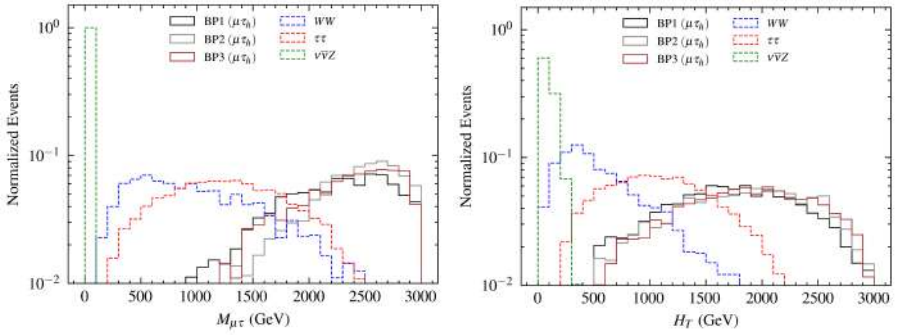

FIGURE 5.4: Kinematic distributions corresponding to signal and main background processes for $e^+e^- \to \mu\tau_h$ production at CLiC 3 TeV.

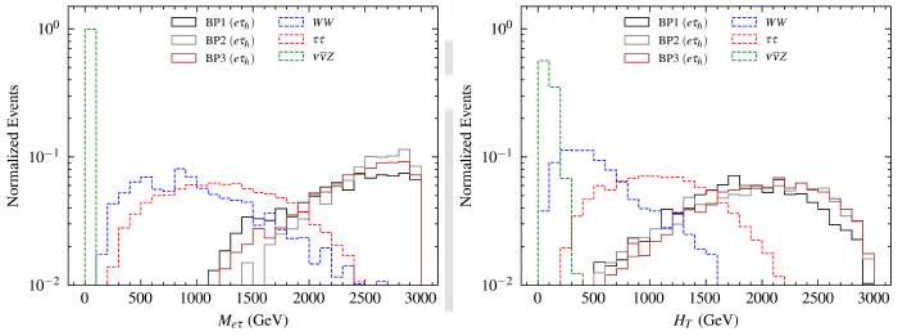

FIGURE 5.5: Kinematic distributions corresponding to signal and main background processes for $e^+e^- \to e\tau_h$ production at CLiC 3 TeV.

We perform a cut and count analysis based on the distributions. The cutflows are detailed in Tab. 5.6. We apply three sequential cuts as itemized below. Prior to $\mathcal{C}_0$, we apply detector resolution and efficiency criteria.

- $\mathcal{C}_0$: $N_{\mu/e} = 1$, $N_{\tau_h} = 1$.
- $\mathcal{C}_1$: $M_{\mu\tau}/M_{e\tau} > 2$ TeV.
- $\mathcal{C}_2$: $H_T > 1.5$ TeV.

Here, $N_{\mu/e}$ is the number of muons/electrons. For $\mu\tau$, N_e is set to 0 and for $e\tau$, N_μ is set 0. N_{τ_h} refers to the number of tau tagged jets. No additional jet is allowed. $M_{\mu\tau}/M_{e\tau}$ refers to the invariant mass of μ/e and τ jet. The signal process arises from a contact interaction with minimal branching, hence the invariant mass distribution is expected to peak close to the CM energy of the process, segregating it from the backgrounds which essentially peak at lower values. The invariant mass of $\nu\bar{\nu}Z$ is expected to peak entirely around the Z pole, and gets entirely wiped out by the invariant mass cut. The H_T distribution of the signal is shifted towards the higher end of the distribution and that of

the background is peaked towards the lower end, owing to the fact that the backgrounds mimicking $l\tau_h$ final state is usually accompanied by huge swarm of invisible particles, reducing the energies of the visible particles. Also, it should be noted that the effect of the H_T cut can also be replicated by a missing energy ($\not{E}$) cut instead, due to the same reason. After employing all the kinematical cuts on collider variables, we estimate the efficiency factor (ϵ) which is crucial to estimate the optimal sensitivity of NP couplings as we discuss next. The ϵ is defined as $\epsilon = \sigma^{\rm sig}/\sigma^{\rm prod}$, where $\sigma_{\rm prod}$ is the production cross section and $\sigma^{\rm sig}$ is the signal cross section for the chosen final state after implementing all the cuts along the branching ratios.The signal efficiency (ϵ_s) for three benchmark points (BPs) is as follows: for BP1, ϵ_s is 0.157; for BP2, ϵ_s is 0.190; and for BP3, ϵ_s is 0.182. The background efficiency (ϵ_b) for the dominant SM background is 0.01.

$\{(C_{\ell\ell})_{\tau\ell}/\Lambda^2, (C_{ee})_{\tau\ell}/\Lambda^2, (C_{\ell e})_{\tau\ell}/\Lambda^2\}$ ($\times 10^{-9}$ GeV^{-2})	**Cross section (fb)**		
	$P_{e^-} = 0\%$	$P_{e^-} = +80\%$	$P_{e^-} = -80\%$
BP1: $\{1.0, 0.0, 0.0\}$	0.74	0.15	1.33
BP2: $\{0.0, 1.0, 0.0\}$	0.74	1.33	0.15
BP3: $\{0.0, 0.0, 1.0\}$	0.37	0.37	0.37
Backgrounds	$P_{e^-} = 0\%$	$P_{e^-} = +80\%$	$P_{e^-} = -80\%$
W^+W^-	453.7	91.89	814.2
$\tau^+\tau^-$	12.23	11.70	12.76
$\nu\bar{\nu}Z$	2090	419.6	3751

TABLE 5.5: Total cross section of $e^+e^- \to l\tau$ ($l = e, \mu$) for different four-fermion couplings as well as SM backgrounds for different choices of beam polarization combination with $\sqrt{s} = 3$ TeV.

Signal Significance For signal significance we use the definition:

$$\mathfrak{Z} = \frac{S}{\sqrt{B}} = \frac{\sigma_S \times \mathfrak{L}_{\rm int}}{\sqrt{\sigma_B \times \mathfrak{L}_{\rm int}}} = \frac{\sigma_S \times \sqrt{\mathfrak{L}_{\rm int}}}{\sqrt{\sigma_B}} \tag{5.13}$$

Here, S, B, σ_S, σ_B and $\mathfrak{L}_{\rm int}$ are the number of signal and background events, the signal and background cross sections, and the integrated luminosity, respectively. $\mathfrak{Z}$ gives the number of sigmas, by which the NP signal, S, out-stands over the uncertainty in the SM background, $\sqrt{B}$. The significance plots (at 5σ level), based on the cut based analysis in the previous section, on the parameter spaces of the EFT coefficients are shown in Fig. 5.6 in two-parameter plane along with the exclusion from the flavor violating three body

Processes	$\mathcal{C}_0$: Selection cuts			$\mathcal{C}_1 : M_{\mu\tau} > 2$ TeV			$\mathcal{C}_2 : H_T > 1.5$ TeV		
	P_0	P_+	P_-	P_0	P_+	P_-	P_0	P_+	P_-
BP1 ($\mu\tau_h$)	0.238	0.048	0.427	0.157	0.032	0.281	0.116	0.024	0.208
BP2 ($\mu\tau_h$)	0.232	0.415	0.047	0.190	0.342	0.038	0.141	0.253	0.028
BP3 ($\mu\tau_h$)	0.118	0.118	0.118	0.087	0.087	0.087	0.067	0.067	0.067
Background	5.979	2.275	9.663	0.312	0.194	0.430	0.162	0.123	0.201

Processes	$\mathcal{C}_0$: Selection cuts			$\mathcal{C}_1 : M_{\mu\tau} > 2$ TeV			$\mathcal{C}_2 : H_T > 1.5$ TeV		
	P_0	P_+	P_-	P_0	P_+	P_-	P_0	P_+	P_-
BP1 ($e\tau_h$)	0.216	0.044	0.387	0.146	0.030	0.262	0.114	0.023	0.206
BP2 ($e\tau_h$)	0.208	0.372	0.042	0.174	0.313	0.035	0.133	0.239	0.027
BP3 ($e\tau_h$)	0.105	0.105	0.105	0.080	0.080	0.080	0.066	0.066	0.066
Background	5.134	1.957	8.295	0.252	0.161	0.342	0.133	0.104	0.162

TABLE 5.6: Cutflow cross sections (in fb) corresponding to signal and background for different beam polarization choices at the CLiC with $\sqrt{s} = 3$ TeV. Here, $P_0 \to P_{e^-} = 0\%$, $P_+ \to P_{e^-} = +80\%$ and $P_- \to P_{e^-} = -80\%$.

decays of τ. It is observed that due to the chiral structure of the operators, polarization plays an important role in probing the operators.

5.1.3 Optimal Observable Technique

The OOT is a convenient tool for determining the statistical sensitivity of any NP coupling in an optimal way. Here, we provide a brief overview of the mathematical framework of the OOT, which has already been explained in detail in previous studies [232, 368, 369]. Any observable such as the differential cross section that receives contributions from both the SM and BSM can be expressed as

$$\mathcal{O}(\phi) = \frac{d\sigma}{d\phi} = g_i f_i(\phi), \tag{5.14}$$

where g_i's are the function of NP coefficients and $f_i(\phi)$'s are the function of phase space variable ϕ. As our analysis is based on the process $e^+e^- \to \mu\tau$, the cosine of the emerging angle of the outgoing particle ($\cos\theta$) is the phase-space variable of our interest.

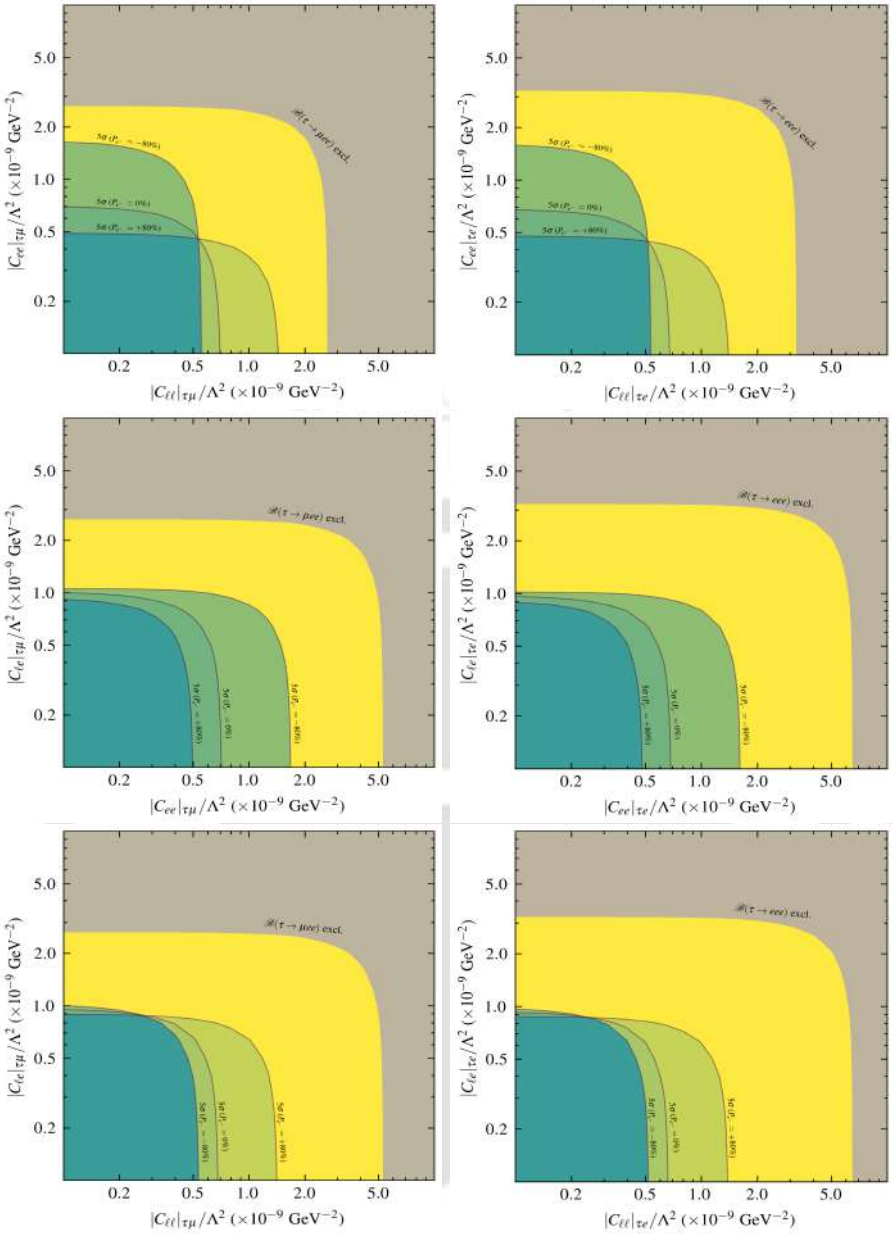

FIGURE 5.6: Significance plots corresponding to the process $e^+e^- \to l\tau_h$ at $\sqrt{s} = 3$ TeV and $\mathfrak{L}_{\text{int}} = 1000$ fb^{-1}. The solid lines refers to the 5σ signal significance for different polarization settings. The region excluded from τ branching ratios are also shown in the plots.

Alternative variables may be chosen instead of $\cos\theta$ depending on the specific observable/process being studied. Our goal is to determine g_i. This can be achieved by utilizing an appropriate weighting function ($w_i(\phi)$):

$$g_i = \int w_i(\phi)\mathcal{O}(\phi)d\phi, \tag{5.15}$$

In principle, various options for $w_i(\phi)$ are feasible, but there exists a particular selection for which the covariance matrix (V_{ij}) is optimal. This choice minimizes statistical uncertainties in NP couplings. For this specific selection, V_{ij} follows:

$$V_{ij} \propto \int w_i(\phi) w_j(\phi) \mathcal{O}(\phi) d\phi, \tag{5.16}$$

Hence, the weighting functions that fulfill the optimal condition $\delta V_{ij} = 0$ are

$$w_i(\phi) = \frac{M_{ij}^{-1} f_j(\phi)}{\mathcal{O}(\phi)}, \tag{5.17}$$

where,

$$M_{ij} = \int \frac{f_i(\phi) f_j(\phi)}{\mathcal{O}(\phi)} d\phi. \tag{5.18}$$

Next, the optimal covariance matrix takes shape as follows:

$$V_{ij} = \frac{M_{ij}^{-1}}{\mathfrak{L}_{\mathtt{int}}}. \tag{5.19}$$

Here, $\sigma_T = \int \mathcal{O}(\phi) d\phi$, and N represents the total number of events $(N = \sigma_T \mathfrak{L}_{\mathtt{int}})$. $\mathfrak{L}_{\mathtt{int}}$ denotes the integrated luminosity. The function χ^2, which dictates the optimal constraint on NP couplings, is defined as

$$\chi^2 = \sum_{ij} (g_i - g_i^0)(g_j - g_j^0) V_{ij}^{-1}, \tag{5.20}$$

where g_0's are 'seed values' that are dependent on the particular NP scenario. The limit set by $\chi^2 \leq n^2$ corresponds to $n\sigma$ standard deviations from these seed values (g_0), establishing the optimal limit for NP couplings while assuming the covariance matrix (V_{ij}) is minimized. Using the χ^2 function definition in Eq. (5.20), the optimal constraints on NP couplings have been investigated in subsequent sections.

Optimal Sensitivity of Effective Couplings In this section, we explore the optimal sensitivity of dimension 6 flavor violating effective couplings via $\tau\mu$ production at the e^+e^- collider with $\sqrt{s} = 3$ TeV and $\mathfrak{L}_{\text{int}} = 1000$ fb^{-1}. Using Eq. (5.20), optimal χ^2 variation with different NP couplings (one operator scenario) are shown in Fig. 5.7 for several choices of beam polarization and optimal limits (95% C.L.) are presented in Tab. 5.7. Given the CM energy and luminosity of a specific collider, the sensitivity of

a particular flavor violating NP coupling depends on the relative contribution to the $\tau\mu$ production, efficiency factor for a final state, and beam polarization. For unpolarized beam, the sensitivity of $(C_{\ell\ell})_{\tau\mu}/\Lambda^2$ and $(C_{\ell e})_{\tau\mu}/\Lambda^2$ appear to be similar as their contributions to the $\tau\mu$ production are equal. However, there is a slight betterment for $(C_{\ell\ell})_{\tau\mu}/\Lambda^2$ as the efficiency factor is relatively better for this coupling. Due to the spinor structure of $\mathcal{O}_{\ell\ell}$, $(C_{\ell\ell})_{\tau\mu}/\Lambda^2$ provides the maximum cross section for $P_{e^-} = -80\%$ choice, hence provides best sensitivity among these three polarization combination. Whereas, due to the similar reason, best sensitivity is achieved for $P_{e^-} = +80\%$ choice in case of $(C_{ee})_{\tau\mu}/\Lambda^2$. For $(C_{\ell e})_{\tau\mu}/\Lambda^2$, all polarization combinations have the same cross section, therefore, the sensitivity of this coupling are expected to be similar for all polarization combinations. However, due to the SM background reduction, $P_{e^-} = +80\%$ provides a delicate enhancement for this coupling. It is noteworthy to mention that, at $\sqrt{s} = 3$ TeV, the CLiC is expected to surpass the flavor sensitivity of NP couplings (from three body decays of τ lepton) with $\mathfrak{L}_{\rm int} = 1$ fb^{-1}. At $\mathfrak{L}_{\rm int} = 1000$ fb^{-1}, the sensitivity of these NP couplings could enhanced by one order compared to flavor violating tau decays.

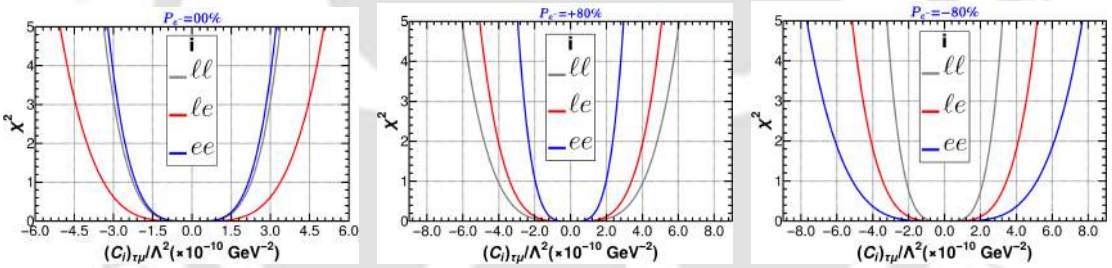

FIGURE 5.7: Optimal χ^2 variations for four-fermion effective couplings with different choices of beam polarization with $\sqrt{s} = 3$ TeV and $\mathfrak{L}_{\rm int} = 1000$ fb^{-1}. Left: unpolarized beam, middle: $\{P_{e^-} : P_{e^+} = +80\% : 00\%\}$, right: $\{P_{e^-} : P_{e^+} = -80\% : 00\%\}$.

Couplings	**Sensitivity (95% C.L.)** $\times\mathbf{10^{-10}}$		
(GeV^{-2})	$\boldsymbol{P_{e^-} = 00\%}$	$\boldsymbol{P_{e^-} = -80\%}$	$\boldsymbol{P_{e^-} = +80\%}$
$(C_{\ell\ell})_{\mu\tau}/\Lambda^2$	± 3.18	± 3.04	± 5.69
$(C_{\ell e})_{\mu\tau}/\Lambda^2$	± 4.75	± 4.82	± 4.70
$(C_{ee})_{\mu\tau}/\Lambda^2$	± 3.03	± 7.21	± 2.80

TABLE 5.7: Optimal sensitivity at 95% C.L. on dimension 6 flavor violating effective couplings at the CLiC with $\sqrt{s} = 3$ TeV CM energy and $\mathfrak{L}_{\rm int} = 1000$ fb^{-1} luminosity.

Now, we turn to discuss the effect of signal and background efficiency to estimate the sensitivity of NP couplings. If we increase[3] the ϵ_s by a factor of 2 by keeping ϵ_b fixed, the

[3]The enhancement (reduction) of ϵ_s (ϵ_b) can be achieved by using multivariate analysis [416, 417].

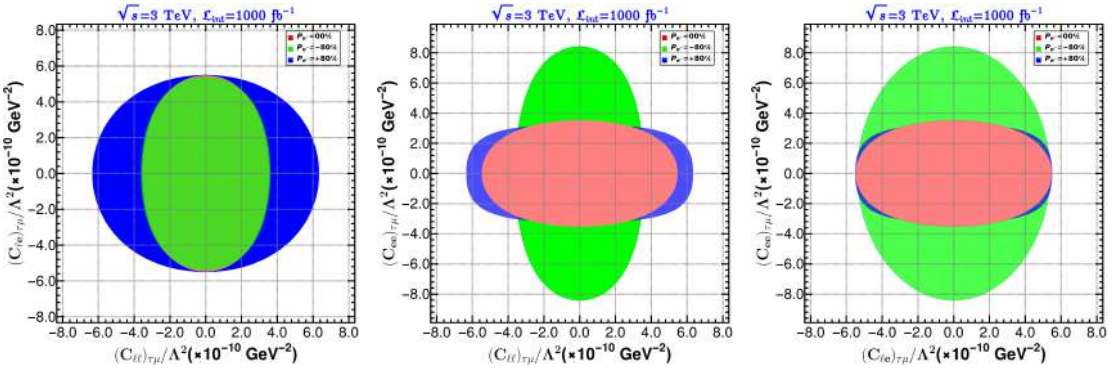

FIGURE 5.8: Optimal 95% C.L. region between two different dimension 6 effective couplings at $\sqrt{s} = 3$ TeV and $\mathfrak{L}_{\rm int} = 1000$ fb^{-1}. Left: $(C_{\ell\ell})_{\tau\mu}/\Lambda^2 - (C_{\ell e})_{\tau\mu}/\Lambda^2$ plane, middle: $(C_{\ell\ell})_{\tau\mu}/\Lambda^2 - (C_{ee})_{\tau\mu}/\Lambda^2$ plane, right: $(C_{\ell e})_{\tau\mu}/\Lambda^2 - (C_{ee})_{\tau\mu}/\Lambda^2$ plane.

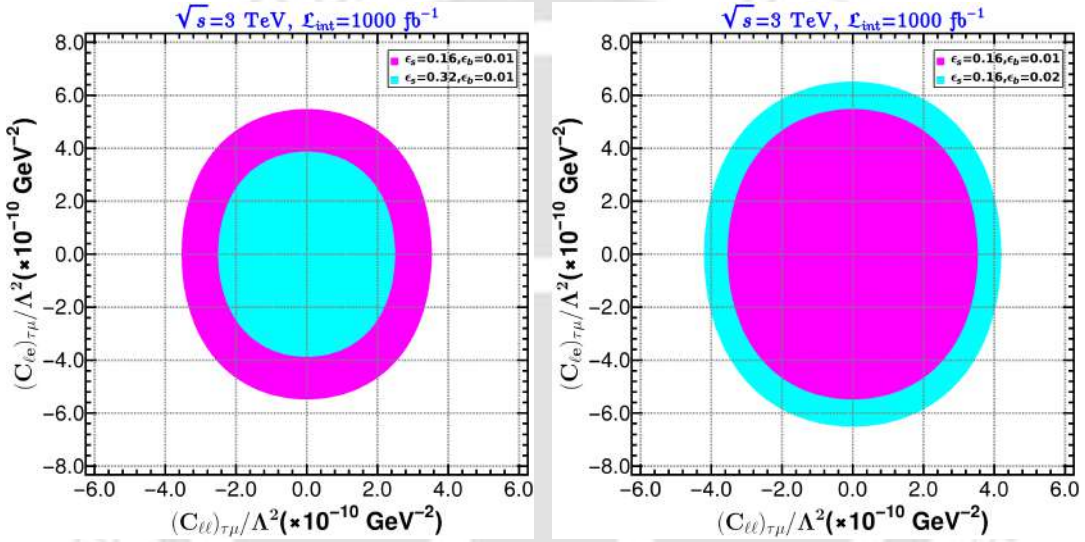

FIGURE 5.9: Variation of optimal 95% C.L. region with the change in the efficiency factors. Left: ϵ_s is enhanced by a factor of 2 by keeping ϵ_b fixed, right: ϵ_b is enhanced by a factor of 2 keeping ϵ_s fixed.

sensitivity of a particular NP coupling improves by 30% as shown in the left of Fig. 5.9. On the other hand, if we decrease ϵ_b by a factor of 2 by keeping ϵ_s constant, the sensitivity of the NP couplings enhances by 16% (right plot of Fig. 5.9). Therefore, we conclude that increasing ϵ_s is more economical than decreasing ϵ_b. In our analysis, ϵ_s is 15 times larger than ϵ_b, making the signal contribution five times greater than the background in the chosen final state. As a result, our analysis is signal-dominated, which is why changing ϵ_s is more effective than changing ϵ_b in estimating the sensitivity of the NP couplings. It is worthwhile to mention that the change in sensitivity of the NP couplings depends on the relative contribution of signal and background to the final state which means if there is a scenario where background dominates (unlike our scenario) compare to signal for a particular final state then change in ϵ_b will affect the change in sensitivity of the

NP couplings compare to the change in ϵ_s. In Fig. 5.8, we show the 95% C.L. allowed region in 2D parameter space for different choice of beam polarizations. We would like to highlight that, under the signal-only hypothesis ($\epsilon_b \to 0$), Δg is inversely proportional to the CM energy and inversely proportional to the square root of the luminosity (for the case of contact interaction). This suggests that a high energy lepton collider would be advantageous for estimating these type of couplings compared to high luminosity lepton colliders.

5.1.4 Summary and Conclusion

In this work, we have discussed the estimation of dimension 6 flavor violating effective couplings through $l\tau$ ($l = \mu, e$) production at future electron-positron colliders. After evaluating the upper limits on NP couplings from flavor violating tau decays, we have performed cut-based analysis using $l\tau_h$ as our final state signal. Invariant dilepton mass and H_T are the collider kinematical variables that play the crucial role to estimate the signal background estimation. After performing cut-based analysis, we have espoused the optimal observable technique to determine the optimal sensitivity of flavor violating effective couplings at the e^+e^- colliders. At 3 TeV CM energy, the CLiC could surpass the upper bound on effective couplings obtained from flavor violating tau decays at 1 fb^{-1} integrated luminosity. If we further increase the luminosity up to 1000 fb^{-1}, then the upper bound the NP couplings can be tighter by one order of magnitude compared to the flavor bound. The signal and background efficiencies play a very important role to estimate the optimal sensitivity of NP couplings. In our scenario, as we are able to reduce the non-interfering SM backgrounds maximally after employing prudent kinematical cuts therefore enhancing the signal efficiency is more beneficial to achieve better optimal precision of NP couplings. Judicious choice of beam polarization is advantageous for assessing the sensitivity of the NP couplings. For instance, left (right)-polarized electron beam improves sensitivity by approximately (4%) 8% for $(C_{\ell\ell})_{\tau\mu}/\Lambda^2$ ($(C_{ee})_{\tau\mu}/\Lambda^2$) compared to the unpolarized beam. On the contrary, there is minuscule improvement of the sensitivity estimation in case of $(C_{\ell e})_{\tau\mu}/\Lambda^2$ for $P_{e^-} = +80\%$ choice. The interplay between the signal and background plays a very important role to estimate the sensitivity of NP couplings. As far as four-fermion flavor violating operators of our concern, the optimal sensitivity is inversely proportional (for signal-only hypothesis) to CM energy, therefore, the high energy muon collider ($\sqrt{s}$ = 10, 14, and 30 TeV) is expected to

provide better estimation of these type of couplings. Although our analysis focuses on $\tau\mu$ production, a similar approach can be applied to τe production. While the effect of polarization will remain same, the sensitivity in estimating the NP couplings will have slight variations because of different efficiency factors.

5.2 Charged Lepton Flavor Violating Top FCNC

Lepton flavor violating top quark FCNC processes at the μTRISTAN.
A. Sarkar.
Phys.Rev.D 113 (2026) 9, 095010 (e-Print: 2506.18015 [hep-ph]).

One of the most intriguing feature of the SM is the flavor structure, with each type of fermion appearing in three generations. Flavor mixing arises through the Yukawa interactions, which couple the flavor and mass eigenstates. In the quark sector, such mixing appears in the charged current interactions and is suppressed by the Glashow Iliopoulos Maiani (GIM) mechanism [418]. In contrast, the SM originally contained no analogous mixing in the lepton sector.

In the quark sector, FCNC processes are forbidden at tree level and highly suppressed at loop level within the SM. These include radiative decays such as $b \to s\gamma$ ($B \to X_s\gamma$ [123–125], $B \to K^*\gamma$ [126, 127]), semileptonic decays $b \to sl^+l^-$ ($B \to Kl^+l^-$ [128, 129], $B \to K^*l^+l^-$ [129, 130], $B_s \to \phi l^+l^-$ [131]), neutral meson mixing ($B^0 - \overline{B}^0$ [132], $B_s^0 - \overline{B}_s^0$ [133], $D^0 - \overline{D}^0$ [134]), and rare kaon decays ($K^+ \to \pi^+\nu\overline{\nu}$ [135]), among others. Although these precision observables provide sensitive probes of potential new physics, in most cases, the current measurements are largely consistent with the Standard Model within experimental and theoretical uncertainties, and the flavor sector continues to offer strong constraints complementary to direct collider searches. Similar FCNC searches have also been conducted in the context of top quark production and decay [15, 136–140]. However, no significant deviations from the SM predictions have been observed so far, primarily due to limited precision in current top quark measurements. As the heaviest particle in the SM, the top quark offers a promising window into potential new physics. Consequently, FCNC studies involving the top quark are crucial for probing physics beyond the SM at current and future experimental frontiers.

As discussed previously, probing cLFV in tandem with top FCNCs provides a unique window into NP. While experimental measurements strongly constrain either cLFV processes, such as the stringent low-energy lepton bounds discussed in Sec. 5.1, or quark FCNCs individually, scenarios involving simultaneous violations in both the lepton and top quark sectors are relatively less restricted, allowing more freedom for phenomenological exploration.

Top quark FCNC processes have been investigated by phenomenological studies [412, 419–436] in various BSM scenarios, and within the EFT framework, in the context of both current and future collider experiments. Similarly, cLFV has also been extensively studied in the literature [13, 119, 378–383, 385–393, 437–449]. In this work, we aim to simultaneously address both phenomena by exploring charged lepton flavor violating top quark FCNC interactions through tq $(t\overline{q} + \bar{t}q)$ production, with $q = u, c$, at the μ^+e^- asymmetric collision stage of the proposed μTRISTAN collider [226]. Such charged lepton flavor violating top quark FCNC interactions can arise naturally in a variety of BSM scenarios. For instance, models with extended Higgs sectors, such as 2HDMs with flavor violating Yukawa couplings [450–452], can generate tree-level top FCNCs together with cLFV. Leptoquark models, which introduce colored scalar or vector particles coupling simultaneously to quarks and leptons, can induce both top quark FCNC transitions and cLFV processes, with their flavor structure determined by underlying symmetries or coupling hierarchies [453, 454]. Similarly, models with an additional Z' gauge boson that has flavor-dependent couplings to SM fermions can enhance top FCNC interactions while simultaneously generating cLFV [455, 456], without conflicting with stringent low-energy constraints. Additionally, such scenarios can also arise from composite Higgs models [457, 458]. In all these frameworks, interactions involving up-type quarks, particularly the top quark, are more natural, as down-type FCNCs are strongly constrained by precision B-physics measurements. This provides a theoretically well-motivated rationale for focusing on lepton flavor violating processes involving the top quark. For detailed BSM scenarios, refer App. 5.C. Experimental searches at the LHC [15, 140] and some phenomenological studies [459] have already explored charged lepton flavor violating top quark FCNC interactions in the context of low-energy experiments, hadron colliders, and same-flavor lepton colliders. However, different-flavor lepton colliders [460–462] offer a cleaner environment for probing cLFV due to reduced background contamination and the possibility of introducing flavor violation directly at the initial collision vertex.

The proposed μTRISTAN collider is an asymmetric muon–electron collider designed to operate within the existing TRISTAN [463] storage ring. It aims to collide ultra-cold μ^+ beams with energies of 1 TeV against high-intensity e^- beams of 30 GeV, achieving a center-of-mass energy of $\sqrt{s} = 346$ GeV. The baseline design targets an instantaneous luminosity of approximately $4.6 \times 10^{33}\,\mathrm{cm}^{-2}\,\mathrm{s}^{-1}$, enabling the accumulation of around $100\,\mathrm{fb}^{-1}$ of data over a few operational years. With potential upgrades to beam intensity and repetition rate, the integrated luminosity could be extended up to $1\,\mathrm{ab}^{-1}$, making the μTRISTAN a promising platform for probing rare processes and performing precision measurements. A follow-up stage envisions symmetric same-sign anti-muon collisions at a center-of-mass energy of $\sqrt{s} = 2$ TeV.

Several BSM phenomenological studies have been conducted for both stages of the μTRISTAN [102, 440–448, 464–471]. In particular, cLFV has been explored in the context of Z' models, heavy neutrino models, axion-like particle (ALP) searches, and effective operator frameworks, focusing predominantly on the lepton sector. In this work, we focus on the process $\mu^+e^- \to tq'$ (with $q' = u, c$), induced by charged lepton flavor violating top quark FCNC interactions. We construct simplified scalar, vector, and tensor four-fermion operators extracted from the SMEFT framework introduced earlier, following the modeling strategy used in [15, 140], as detailed later. Our analysis constrains these EFT operators and, in turn, the rare FCNC decay modes of the top quark involving cLFV. These bounds can be mapped onto a broad class of BSM scenarios that link the lepton and quark sectors, such as Z' and leptoquark models.

This study is organized as follows: In Sec. 5.2.1, we present the EFT framework adopted for this study and review existing constraints on the relevant operators. Sec. 5.2.2 details the collider analysis of the process $\mu^+e^- \to tq'$ at the μTRISTAN, based on a cut-based strategy, along with a discussion on the impact of beam polarization. In Sec. 5.2.3, we provide the projected sensitivities for the EFT operators and the corresponding limits on rare top quark decay branching ratios. Finally, we summarize our findings and conclusions in Sec. 5.2.4.

5.2.1 EFT Operators for cLFV Top FCNC

In the absence of direct evidence for new physics at current experiments, effective field theories have emerged as powerful tools for interpreting observed deviations and projecting sensitivities in a model-independent manner. As introduced in Sec. 5.1.1, SMEFT provides a systematic extension of the SM by incorporating higher-dimensional operators built from SM fields and respecting its gauge symmetries, without introducing additional degrees of freedom. While the leading contribution in SMEFT arises at dimension 5 through the Weinberg operator [99], its phenomenological impact is limited primarily to neutrino mass generation. In practice, the dominant and most widely studied effects begin at dimension 6, which have significant implications across various sectors of particle physics. A complete and non-redundant basis of dimension 6 operators is presented in [11].

Operator	**SMEFT operators**		**Simplified operators**	
	Symbol	**Structure**	**Symbol**	**Structure**
Scalar	$[\mathcal{O}^{(1)}_{\ell equ}]_{prst}$	$(\bar{\ell}^a_p e_r)\epsilon^{ab}(\bar{q}^b_s u_t)$	$\mathcal{O}^S_{e\mu tu}$ $\mathcal{O}^S_{e\mu tc}$	$(\bar{e}\mu)(\bar{t}u)$ $(\bar{e}\mu)(\bar{t}c)$
Vector	$[\mathcal{O}^{(1)}_{\ell q}]_{prst}$ $[\mathcal{O}^{(3)}_{\ell q}]_{prst}$ $[\mathcal{O}_{eu}]_{prst}$ $[\mathcal{O}_{\ell u}]_{prst}$ $[\mathcal{O}_{qe}]_{prst}$	$(\bar{\ell}_p\gamma_\alpha\ell_r)(\bar{q}_s\gamma^\alpha q_t)$ $(\bar{\ell}_p\gamma_\alpha\tau^I\ell_r)(\bar{q}_s\gamma^\alpha\tau^I q_t)$ $(\bar{e}_p\gamma_\alpha e_r)(\bar{u}_s\gamma^\alpha u_t)$ $(\bar{\ell}_p\gamma_\alpha\ell_r)(\bar{u}_s\gamma^\alpha u_t)$ $(\bar{e}_p\gamma_\alpha e_r)(\bar{q}_s\gamma^\alpha q_t)$	$\mathcal{O}^V_{e\mu tu}$ $\mathcal{O}^V_{e\mu tc}$	$(\bar{e}\gamma_\alpha\mu)(\bar{t}\gamma^\alpha u)$ $(\bar{e}\gamma_\alpha\mu)(\bar{t}\gamma^\alpha c)$
Tensor	$[\mathcal{O}^{(3)}_{\ell equ}]_{prst}$	$(\bar{\ell}^a_p\sigma_{\alpha\beta}e_r)\epsilon^{ab}(\bar{q}^b_s\sigma^{\alpha\beta}u_t)$	$\mathcal{O}^T_{e\mu tu}$ $\mathcal{O}^T_{e\mu tc}$	$(\bar{e}\sigma_{\alpha\beta}\mu)(\bar{t}\sigma^{\alpha\beta}u)$ $(\bar{e}\sigma_{\alpha\beta}\mu)(\bar{t}\sigma^{\alpha\beta}c)$

TABLE 5.8: SMEFT and corresponding simplified four-fermion operators contributing to the process $\mu^+e^- \to tq'$ ($q' = u, c$) at the μTRISTAN. The scalar and tensor operators include their Hermitian conjugates, although they are not shown explicitly in the table. Indices p, r represent lepton flavors, while s, t denote quark flavors. The simplified operators incorporate all relevant flavor combinations necessary for the considered processes.

The leading contributions to the process $\mu^+e^- \to tq'$ ($q' = u, c$) arise from three classes of four-fermion SMEFT operators: scalar ($\mathcal{O}^{(1)}_{\ell equ}$, including its Hermitian conjugate), vector ($\mathcal{O}^{(1)}_{\ell q}$, $\mathcal{O}^{(3)}_{\ell q}$, $\mathcal{O}_{eu}$, $\mathcal{O}_{\ell u}$, and $\mathcal{O}_{qe}$), and tensor ($\mathcal{O}^{(3)}_{\ell equ}$, also including its Hermitian conjugate), as summarized in Tab. 5.8. These operators are flavor-dependent, with lepton flavor indices denoted by p, r and quark flavor indices by s, t. Following the approach

in [15], we define simplified operators that capture the relevant flavor structures contributing to the process, abstracted from the full SMEFT basis. The mapping between the simplified and SMEFT operators is given by:

$$\begin{aligned}
\mathcal{O}^{S}_{e\mu tq'} &= [\mathcal{O}^{(1)}_{\ell equ}]_{e\mu tq'}\,, \\
\mathcal{O}^{V}_{e\mu tq'} &= [\mathcal{O}^{(1)}_{\ell q}]_{e\mu tq'} + [\mathcal{O}^{(3)}_{\ell q}]_{e\mu tq'} + [\mathcal{O}_{eu}]_{e\mu tq'} + [\mathcal{O}_{\ell u}]_{e\mu tq'} + [\mathcal{O}_{qe}]_{e\mu tq'}\,, \\
\mathcal{O}^{T}_{e\mu tq'} &= [\mathcal{O}^{(3)}_{\ell equ}]_{e\mu tq'}\,.
\end{aligned} \tag{5.21}$$

It should be noted that upon flavor expansion, the operators $[\mathcal{O}^{(1)}_{\ell q}]_{e\mu tq'}$ and $[\mathcal{O}^{(3)}_{\ell q}]_{e\mu tq'}$ yield identical Lorentz structures. However, due to the presence of SU(2) generators τ^I in $[\mathcal{O}^{(3)}_{\ell q}]_{e\mu tq'}$, the charged lepton interactions acquire an overall negative sign, while the neutrino interactions acquire a positive sign [140, 472, 473]. Consequently, the effective WCs contributing to the $\mathcal{O}_{\ell q}$-like Lorentz structure is given by:

$$\left(\frac{[C^{(-)}_{\ell q}]_{e\mu tq'}}{\Lambda^2}\right) = \left(\frac{[C^{(1)}_{\ell q}]_{e\mu tq'}}{\Lambda^2}\right) - \left(\frac{[C^{(3)}_{\ell q}]_{e\mu tq'}}{\Lambda^2}\right)\,. \tag{5.22}$$

Constraints on Operators Before presenting our sensitivity projections in context of the μTRISTAN, it is important to review the current experimental constraints on charged lepton flavor violating top quark FCNC interactions. The most stringent bounds to date are provided by a recent CMS analysis at $\sqrt{s} = 13$ TeV with an integrated luminosity of 138 fb^{-1} [15, 474]. This analysis combines searches for anomalous production via $q'g \to e\mu t$ and rare decay processes $t \to e\mu q'$, interpreting the results in the framework of effective four-fermion interactions involving scalar, vector, and tensor operators.

The limits are derived under the assumption that only one operator is active at a time and are quoted in terms of the effective WCs, $C^{X}_{e\mu tq'}/\Lambda^2$. These bounds can be translated into constraints on the branching ratio of the rare top decay $t \to e\mu q'$ ($q' = u, c$) using the following expression [140, 475]:

$$\mathcal{B}(t \to e\mu q') = \frac{m_t^5}{3072\,\pi^3\,\Gamma_t}\left[\left(\frac{C^{S}_{e\mu tq'}}{\Lambda^2}\right)^2 + 8\left(\frac{C^{V}_{e\mu tq'}}{\Lambda^2}\right)^2 + 48\left(\frac{C^{T}_{e\mu tq'}}{\Lambda^2}\right)^2\right], \tag{5.23}$$

where m_t and Γ_t are the top quark mass and total decay width, respectively. It is worth emphasizing that our analysis is performed strictly within the SMEFT framework, where

$SU(2)_L$ gauge invariance restricts the allowed chiral structures of the semileptonic operators. In particular, the scalar and tensor operators $\mathcal{O}^{(1)}_{\ell equ}$ and $\mathcal{O}^{(3)}_{\ell equ}$ generate fixed chirality combinations. Independent chiral structures that would arise in a general low-energy EFT are not present, unlike [453]. Consequently, for the fully integrated unpolarized decay width considered here, the scalar-tensor interference term vanishes due to the antisymmetric Lorentz structure of the tensor operator, and is therefore not included in our expressions. Since the contribution of these operators to Γ_t is negligible for small values of the WCs, it is treated as a fixed SM parameter. The resulting bounds are summarized in Tab. 5.9.

Operator	$\boldsymbol{C^X_{e\mu tq'}/\Lambda^2}$ **(TeV^{-2})**	$\boldsymbol{\mathcal{B}(t \to e\mu q')}$
$\mathcal{O}^S_{e\mu tu}$	0.24	7.00×10^{-8}
$\mathcal{O}^V_{e\mu tu}$	0.12	1.30×10^{-7}
$\mathcal{O}^T_{e\mu tu}$	0.06	2.50×10^{-7}
$\mathcal{O}^S_{e\mu tc}$	0.86	8.90×10^{-7}
$\mathcal{O}^V_{e\mu tc}$	0.37	1.31×10^{-6}
$\mathcal{O}^T_{e\mu tc}$	0.21	2.59×10^{-6}

TABLE 5.9: 95% C.L. exclusion limits on charged lepton flavor violating top quark FCNC operators and corresponding bounds on top quark rare decay branching ratios from the LHC at 13 TeV with 138 fb^{-1} [15].

As shown in Tab. 5.9, the existing CMS bounds constrain the WCs down to the level of $\mathcal{O}(10^{-2})$ TeV^{-2}, translating to upper limits on the rare top quark branching ratios as low as $\mathcal{O}(10^{-8})$. The constraints are generally stronger for the u-type operators compared to c-type, reflecting the parton distribution function (PDF) enhancement of the up quark in proton collisions. Among the three operator classes, the tensor operator coefficients are the most tightly constrained, as both the production cross section for $q'g \to e\mu t$ and the decay branching ratio of $t \to e\mu q'$ exhibit a stronger sensitivity to variations in tensor interactions compared to their scalar and vector counterparts. This is because, tensor operators tend to contribute more strongly than vector operators, which in turn are larger than scalar operators, because the way their Lorentz structures contract with fermion spinors and affect the kinematics leads to progressively larger decay rates or cross sections. This pattern is evident in Eq. (5.23), where the tensor contribution carries the largest weight, followed by vector and then scalar.

5.2.2 Collider Analysis: μTRISTAN

The Feynman diagrams corresponding to the process $\mu^+e^- \to tq'$ $(q' = u, c)$ are shown in Fig. 5.10. For the collider analysis, we focus on the leptonic decay channel of the top quark, $t \to b\ell\nu$, which leads to a final state consisting of two jets (one being a b-jet), a charged lepton, and missing transverse energy (MET). The dominant SM background arises from $\mu^+e^- \to l\nu jj$, primarily via the process $\mu^+e^- \to Wl\nu$, where the W boson decays hadronically. This background is reducible and can be significantly suppressed with appropriate kinematic selections, as discussed later. While the hadronic decay mode of the top quark $(t \to bjj)$ benefits from a larger branching ratio and relatively lower background contamination, it poses practical challenges in this analysis. Since our study involves comparing operator structures from different effective classes, angular observables, particularly the separation between the light quark (q') and the top quark, play a crucial role in distinguishing operator contributions. In the leptonic channel, this angular separation can be effectively approximated using the separation between the light jet and the b-jet. In contrast, the hadronic channel suffers from combinatorial ambiguities due to the presence of multiple light jets, making the reconstruction of the correct jet pairing and extraction of angular correlations considerably more difficult.

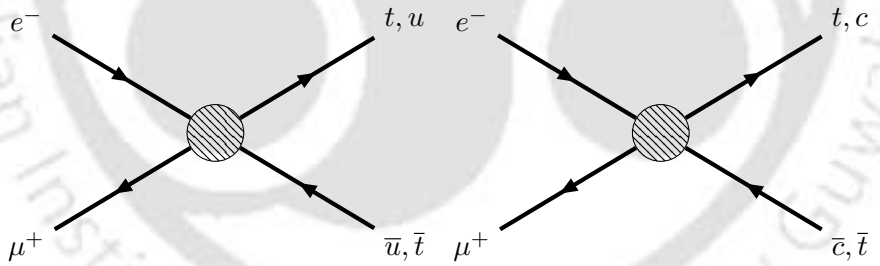

FIGURE 5.10: Feynman diagrams corresponding to $\mu^+e^- \to tq'$, $q' = u, c$ production at the μTRISTAN.

For our analysis, we define the following individual operator benchmark points, with all other WCs set to zero:

$$\begin{aligned}
&\text{BP}(S_u): \left(\frac{C^S_{e\mu tu}}{\Lambda^2}\right) = 0.01\ \text{TeV}^{-2}, \qquad \text{BP}(S_c): \left(\frac{C^S_{e\mu tc}}{\Lambda^2}\right) = 0.01\ \text{TeV}^{-2},\\
&\text{BP}(V_u): \left(\frac{C^V_{e\mu tu}}{\Lambda^2}\right) = 0.01\ \text{TeV}^{-2}, \qquad \text{BP}(V_c): \left(\frac{C^V_{e\mu tc}}{\Lambda^2}\right) = 0.01\ \text{TeV}^{-2},\\
&\text{BP}(T_u): \left(\frac{C^T_{e\mu tu}}{\Lambda^2}\right) = 0.01\ \text{TeV}^{-2}, \qquad \text{BP}(T_c): \left(\frac{C^T_{e\mu tc}}{\Lambda^2}\right) = 0.01\ \text{TeV}^{-2}.
\end{aligned} \tag{5.24}$$

All benchmark points respect the current exclusion limits summarized in Tab. 5.9. Although some of the operators are subject to weaker experimental constraints, we choose a uniform benchmark value across all cases to facilitate a consistent and direct comparison during the cut-based analysis, which will be discussed in subsequent sections.

Beam Polarization Effects As demonstrated in Sec. 5.1, beam polarization is a powerful diagnostic tool at lepton colliders. By tuning the polarization of the initial-state leptons, one can suppress SM backgrounds and selectively enhance signal contributions, thereby disentangling the effects of different operator classes based on their chirality. At the μTRISTAN, substantial beam polarization is anticipated for both μ^+ and e^- beams [226]. Surface muons, originating from π^+ decays, are naturally produced with nearly 100% polarization due to the V–A nature of weak interactions. When subjected to a longitudinal magnetic field of ~ 0.3 T, and accounting for possible beam emittance effects, a polarization of $P_{\mu^+} \sim \pm 0.80$ is expected. In less favorable scenarios, where the longitudinal magnetic field is absent, the polarization may reduce to $P_{\mu^+} \sim \pm 0.25$, which we adopt as the conservative benchmark for our analysis. On the electron side, technological developments at SuperKEKB [476] suggest that beam polarizations of $P_{e^-} = \pm 0.70$ are realistically achievable. The production cross section in the presence of beam polarizations translates to the following expression:

$$\begin{aligned}\sigma(P_{\mu^+}, P_{e^-}) = &\frac{(1-\overline{P_{\mu^+}})(1-P_{e^-})}{4}\sigma_{LL} + \frac{(1-\overline{P_{\mu^+}})(1+P_{e^-})}{4}\sigma_{LR} \\ &+ \frac{(1+\overline{P_{\mu^+}})(1-P_{e^-})}{4}\sigma_{RL} + \frac{(1+\overline{P_{\mu^+}})(1+P_{e^-})}{4}\sigma_{RR}\,,\end{aligned} \tag{5.25}$$

where $\overline{P}$ denotes the flipped sign of P. In addition, σ_{XY} denotes the polarized cross section defined as $\sigma_{XY} = \sigma(\mu^+_X e^-_Y \to tq')$, where $X, Y = L, R$, specify the chiralities of the initial state leptons. The scalar and tensor operators couple fields of opposite chiralities, whereas the vector operator couples fields of the same chirality. This chiral structure directly affects their response to beam polarization and underlies the polarization dependence observed in the signal rates.

The production cross sections for the signal processes $\mu^+e^- \to t(bl\nu)u$, mediated by scalar, vector, and tensor operators, along with the dominant SM background $\mu^+e^- \to l\nu jj$, are presented in Tab. 5.10 for various polarization configurations. Throughout this section, we denote beam polarization configurations using the shorthand $P_{\rm AB}$:

(P_{μ^+}, P_{e^-}), where A $= +, -$ corresponds to $P_{\mu^+} = +0.25, -0.25$, and B $= +, -$ corresponds to $P_{e^-} = +0.70, -0.70$. The unpolarized case $(P_{\mu^+}, P_{e^-}) = (0.00, 0.00)$ is denoted as $P_{\times\times}$. Using Eq. (5.25), the cross section can be written as

$$\sigma(P_{AB}) = \sum_{XY} M_{XY}^{AB}\, \sigma_{XY}\,, \tag{5.26}$$

where the matrix M is

$$M = \begin{bmatrix} 0.31875 & 0.05625 & 0.53125 & 0.09375 \\ 0.05625 & 0.31875 & 0.09375 & 0.53125 \\ 0.53125 & 0.09375 & 0.31875 & 0.05625 \\ 0.09375 & 0.53125 & 0.05625 & 0.31875 \end{bmatrix}. \tag{5.27}$$

The AB and XY sequences correspond to $\{++, +-, -+, --\}$ and $\{LL, LR, RL, RR\}$, respectively. For scalar and tensor operators, only σ_{LR} and σ_{RL} are non-zero. Furthermore, $\sigma_{LR} = \sigma_{RL}$, since the Hermitian conjugate operator carries the same coupling strength. In contrast, for the vector operator only σ_{LL} and σ_{RR} are non-zero, and the simplified operator definition in Eq. (5.21) implies $\sigma_{LL} = \sigma_{RR}$. Therefore, the chiral structure of the operators leads to the relations $\sigma(P_{++}) = \sigma(P_{--})$ and $\sigma(P_{+-}) = \sigma(P_{-+})$ for the signal cross sections. Among these, P_{++} yields lower SM background than P_{--}, making it a preferred benchmark configuration. Similarly, P_{+-} offers reduced background compared to P_{-+} and is thus also selected. Hence, our benchmark polarization choices are $P_{\times\times}$ (unpolarized), P_{++}, and P_{+-}. Importantly, polarization configurations affect operator sensitivity: P_{++}/P_{--} enhance scalar and tensor operator contributions while suppressing the vector ones. Conversely, P_{+-}/P_{-+} configurations enhance vector operator sensitivity while reducing scalar and tensor contributions. In addition to differentiating operator structures: scalar, vector, and tensor, beam polarization can also be exploited to disentangle the various SMEFT vector structures listed in Tab. 5.8. A detailed discussion of the role of polarization in distinguishing these vector operators is provided in App. 5.D.

Cut-based Analysis The model implementation is carried out using `FeynRules` [233]. The corresponding UFO model [234] files are exported and passed to `MG5_aMC` [235] to generate Monte Carlo events for both the EFT signal and SM background processes. In addition to the dominant background process $\mu^+e^- \to l\nu jj$, subleading contributions

Polarization (P_{μ^+}, P_{e^-})	**Signal**			**Background** $\sigma_{l\nu jj}$ **(fb)**
	$\sigma^{\mathrm{BP}(S_u)}_{t(l\nu b)q'}$ **(fb)**	$\sigma^{\mathrm{BP}(V_u)}_{t(l\nu b)q'}$ **(fb)**	$\sigma^{\mathrm{BP}(T_u)}_{t(l\nu b)q'}$ **(fb)**	
$P_{\times\times}$: Unpolarized	0.035	0.105	0.276	148.4
P_{++} : $(+0.25, +0.70)$	0.041	0.086	0.323	123.4
P_{+-} : $(+0.25, -0.70)$	0.029	0.123	0.228	242.1
P_{-+} : $(-0.25, +0.70)$	0.029	0.123	0.228	74.8
P_{--} : $(-0.25, -0.70)$	0.041	0.086	0.323	150.5

TABLE 5.10: Production cross sections for the signal process $\mu^+e^- \to t(l\nu b)u$, mediated by scalar, vector, and tensor operators, along with the dominant SM background $\mu^+e^- \to l\nu jj$, are presented for various beam polarization configurations.

can arise from processes such as $\mu^+e^- \to lljj$ and $\mu^+e^- \to llbb$, particularly due to non-identification of lepton or jet flavor misidentification. However, such contributions are highly suppressed and do not pass the event selection criteria; therefore, they are neglected in the analysis.

The generated events are passed to `Pythia8` [236] for parton showering, followed by detector simulation using `Delphes3` [237]. In the absence of a dedicated detector card for the μTRISTAN, we adopt the `ILCgen` [219] card, which provides a reasonable approximation of the expected detector performance at the μTRISTAN. For b-jet tagging, we employ the "tight" b-tagging configuration available in the `ILCgen` card. This model yields a b-tagging efficiency of approximately 53%, with mistagging rates of around 5% for charm jets and 0.5% for light-flavor jets (u, d, s, g). This tight tagging configuration effectively suppresses SM backgrounds, which rarely contain genuine b-jets. While the implementation of a c-tagging algorithm could in principle aid in distinguishing between u- and c-type operators, we refrain from doing so due to the limited discriminating power of current c-tagging techniques.

For signal event selection, we require events to contain exactly one charged lepton and two jets, with one b-tagged and one non-b-tagged jet:

$$N_l = 1, \quad N_b = 1, \quad N_j = 1. \tag{5.28}$$

Due to the asymmetric beam configuration at the μTRISTAN with μ^+ at 1 TeV and e^- at 30 GeV the final-state system is strongly boosted along the beam (z) direction.

In such setups, two primary analysis strategies are typically adopted: (i) reconstructing observables in the partonic center-of-mass frame, or (ii) relying on transverse and boost-invariant observables directly in the lab frame. We follow the latter approach, using kinematic variables such as the invariant mass of visible final-state particles, the transverse momentum of both visible (p_T) and invisible (MET) particles, rapidity differences, and azimuthal angular separations. Among these, we highlight two key invariant mass observables:

$$M_{bj} = \sqrt{(p_b + p_j)^2}\,, \qquad M_{lbj} = \sqrt{(p_l + p_b + p_j)^2}\,, \tag{5.29}$$

where p_l, p_b, and p_j denote the four-momenta of the lepton, b-jet, and light jet, respectively. Fig. 5.11 shows the distributions of M_{bj} (*left*) and $M_{\ell bj}$ (*right*) for the signal benchmarks and SM background in the process $\mu^+e^- \to t(l\nu b)q'$, with $q' = u, c$, at the μTRISTAN. The distributions are obtained after applying detector-level cuts along with the event selection criteria specified in Eq. (5.28), collectively referred to as the baseline cut, $\mathcal{C}_0$. Building on the baseline selection, we apply the following sequential kinematic

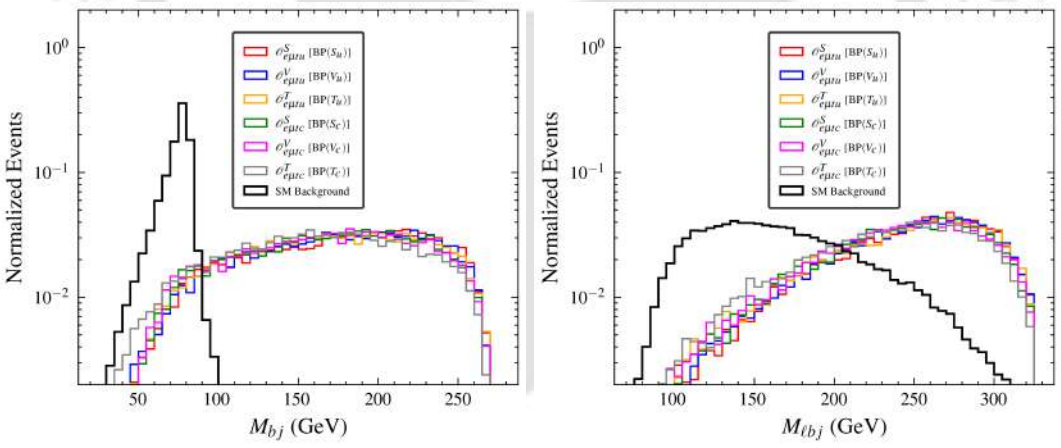

FIGURE 5.11: Invariant mass distributions after the baseline cut $\mathcal{C}_0$ for signal benchmarks and SM background in the process $\mu^+e^- \to t(l\nu b)q'$ with $q' = u, c$ at the μTRISTAN. M_{bj} (*left*) denotes the invariant mass of the b-jet and light jet system, while M_{lbj} (*right*) corresponds to the invariant mass of the lepton, b-jet, and light jet system.

cuts to further enhance the signal-to-background separation:

$$\mathcal{C}_1 : \; M_{bj} > 100 \text{ GeV}, \qquad \mathcal{C}_2 : \; M_{\ell bj} > 200 \text{ GeV}. \tag{5.30}$$

The dominant SM background arises from the process $\mu^+e^- \to W(jj)\,\ell\nu$, where the invariant mass of the jet pair peaks around the W boson mass. The cut $\mathcal{C}_1$ effectively

suppresses this background by requiring M_{bj} to lie above 100 GeV. Furthermore, because the signal process $\mu^+e^- \to tq$ originates from a contact interaction, it exhibits a harder kinematic spectrum, with visible final-state invariant masses peaking closer to the center-of-mass energy. In contrast, the background involves intermediate propagators, resulting in softer distributions. The additional cut $\mathcal{C}_2$, imposing $M_{\ell bj} > 200$ GeV, further discriminates against the background. The cutflow of cross sections for the signal benchmarks and the dominant SM background is summarized in Tab. 5.11. To quantify the observability of the signal, we define the statistical significance as:

$$\mathcal{Z}_{\mathfrak{L}_{\rm int}} = \frac{\sigma^{\rm S} \times \sqrt{\mathfrak{L}_{\rm int}}}{\sqrt{\sigma^{\rm S} + \sigma^{\rm B}}}, \tag{5.31}$$

where $\sigma^{\rm S}$ and $\sigma^{\rm B}$ denote the signal and background cross sections after cuts, respectively, and $\mathfrak{L}_{\rm int}$ is the integrated luminosity. The resulting signal significances for $\mathfrak{L}_{\rm int} = 1\,{\rm ab}^{-1}$ are also reported in Tab. 5.11. Despite the conservative choice of benchmark WCs, we find that the signal remains clearly distinguishable from the background. Owing to the strong suppression of the background through the optimized cutflow, even a modest increase in the EFT couplings leads to a marked improvement in significance.

Benchmarks	**Cutflow**			$\mathcal{Z}_{\mathbf{1\,ab^{-1}}}$
	σ_0 **(fb)**	σ_1 **(fb)**	σ_2 **(fb)**	
BP(S_u)	0.014	0.012	0.011	2.008
BP(V_u)	0.042	0.037	0.032	4.438
BP(T_u)	0.108	0.096	0.080	8.000
BP(S_c)	0.014	0.012	0.010	1.826
BP(V_c)	0.040	0.035	0.029	4.143
BP(T_c)	0.103	0.087	0.070	7.379
SM background	5.070	0.036	0.020	–

TABLE 5.11: Cutflow table showing the signal and background cross sections (σ_i) after each sequential cut $\mathcal{C}_i$, for various signal benchmarks and the dominant SM background. The final column, $\mathcal{Z}_{1\,{\rm ab}^{-1}}$, denotes the signal significance at the μTRISTAN collider with $\mathfrak{L}_{\rm int} = 1\,{\rm ab}^{-1}$.

Tab. 5.12 presents the cross sections after the final selection cut (σ_2) and the corresponding signal significances, $\mathcal{Z}_{1\,{\rm ab}^{-1}}$, for two polarization configurations: P_{++} and P_{-+}. As anticipated from the chiral structure of the effective operators, the scalar and tensor benchmarks yield higher significances under the P_{++} configuration, while the vector

operator shows enhanced signal significance for the P_{-+} setup.

Benchmarks	$\boldsymbol{P_{++}}$ **: (+0.25, +0.70)**		$\boldsymbol{P_{-+}}$ **: (−0.25, +0.70)**	
	$\boldsymbol{\sigma_2}$ **(fb)**	$\boldsymbol{\mathcal{Z}_{1\,\mathrm{ab}^{-1}}}$	$\boldsymbol{\sigma_2}$ **(fb)**	$\boldsymbol{\mathcal{Z}_{1\,\mathrm{ab}^{-1}}}$
BP(S_u)	0.013	2.373	0.009	2.065
BP(V_u)	0.026	3.965	0.037	5.397
BP(T_u)	0.094	8.922	0.066	7.571
BP(S_c)	0.012	2.228	0.008	1.886
BP(V_c)	0.024	3.748	0.034	5.126
BP(T_c)	0.082	8.241	0.058	7.034
SM background	0.017	–	0.010	–

TABLE 5.12: Cross sections after the final selection cut (σ_2) and corresponding signal significance, $\mathcal{Z}_{1\,\mathrm{ab}^{-1}}$, for various signal benchmarks and the SM background under polarization configurations P_{++} and P_{-+}.

5.2.3 Projected Sensitivity of Operators

In this section, we present the projected sensitivity to the effective operator coefficients, $C^X_{e\mu tq'}/\Lambda^2$, using a binned likelihood analysis. By leveraging the shape information of suitably chosen differential distributions, we go beyond total rate measurements and extract stronger constraints. This approach captures not only the overall event yield but also the distinct kinematic features of signal and background processes, thereby enhancing the sensitivity to new physics. We outline the statistical framework used to quantify these projections by constructing a binned likelihood using a differential observable, say φ. The expected number of events in the $\mathtt{r}^{\mathrm{th}}$ bin of φ is given by:

$$\mu_{\mathtt{r}}\left(C^X_{e\mu tq'}/\Lambda^2\right) = \mathfrak{L}_{\mathrm{int}}\left\{\sigma^{\mathrm{B}}_{\mathtt{r}} + \sigma^{\mathrm{S}}_{\mathtt{r}}\left(C^X_{e\mu tq'}/\Lambda^2\right)\right\}, \tag{5.32}$$

where $\mathfrak{L}_{\mathrm{int}}$ is the integrated luminosity, $\sigma^{\mathrm{B}}_{\mathtt{r}}$ is the background cross section in bin $\mathtt{r}$, and $\sigma^{\mathrm{S}}_{\mathtt{r}}$ is the signal cross section which depends on the operator coefficient, $C^X_{e\mu tq'}/\Lambda^2$. The corresponding likelihood function [9] is defined as a product of Poisson probabilities over all bins:

$$\mathscr{L}\left(C^X_{e\mu tq'}/\Lambda^2\right) = \prod_{\mathtt{r}=1}^{N} \frac{\left\{\mu_{\mathtt{r}}\left(C^X_{e\mu tq'}/\Lambda^2\right)\right\}^{n_{\mathtt{r}}} e^{-\mu_{\mathtt{r}}\left(C^X_{e\mu tq'}/\Lambda^2\right)}}{n_{\mathtt{r}}!}, \tag{5.33}$$

where the observable φ is divided into N bins, and $n_{\mathtt{r}}$ is the observed number of events in the $\mathtt{r}^{\text{th}}$ bin. Since no observed data exist for future colliders, the observed event counts are assumed to equal the expected background yields:

$$n_{\mathtt{r}} = \mathfrak{L}_{\text{int}}\, \sigma_{\mathtt{r}}^{\text{B}}\,. \tag{5.34}$$

The log-likelihood is then given by:

$$\log \mathscr{L}\left(C^X_{e\mu tq'}/\Lambda^2\right) = \sum_{\mathtt{r}=1}^{N} \left\{ n_{\mathtt{r}} \log \mu_{\mathtt{r}}\left(C^X_{e\mu tq'}/\Lambda^2\right) - \mu_{\mathtt{r}}\left(C^X_{e\mu tq'}/\Lambda^2\right) \right\} + \text{constant}\,. \tag{5.35}$$

To quantify the sensitivity, we define the profile likelihood ratio:

$$\begin{aligned} \lambda\left(C^X_{e\mu tq'}/\Lambda^2\right) &= \frac{\mathscr{L}\left(C^X_{e\mu tq'}/\Lambda^2\right)}{\mathscr{L}\left(\hat{C}^X_{e\mu tq'}/\Lambda^2\right)}\,, \\ \mathscr{Q}\left(C^X_{e\mu tq'}/\Lambda^2\right) &= -2\log\lambda\left(C^X_{e\mu tq'}/\Lambda^2\right), \end{aligned} \tag{5.36}$$

where $\hat{C}^X_{e\mu tq'}/\Lambda^2$ denotes the value of the operator coefficient that maximizes the likelihood. Since we are evaluating the sensitivity to new physics against the SM background, we perform the analysis around the null hypothesis, i.e., $\hat{C}^X_{e\mu tq'}/\Lambda^2 = 0$. The test statistic $\mathscr{Q}$ defined in Eq. (5.36) is used to derive projected bounds on the operator coefficient $C^X_{e\mu tq}/\Lambda^2$ at a given confidence level (C.L.).

According to Wilks' theorem [230], in the asymptotic limit, the distribution of $\mathscr{Q}$ approaches a chi-squared (χ^2) distribution with degrees of freedom equal to the number of parameters being tested. It is important to note that in the low-statistics regime, $\mathscr{Q}$ may deviate from the ideal χ^2 behavior, in which case the true distribution should be estimated using Monte Carlo simulations. However, such simulations are computationally demanding. For projection studies focused on assessing the reach of future colliders, the use of Wilks' theorem provides a reasonable and commonly adopted approximation. Using the Wilks' theorem, we translate the value of $\mathscr{Q}$ into confidence intervals on $C^X_{e\mu tq'}/\Lambda^2$. For instance, the critical values of the test statistic $\mathscr{Q}$ corresponding to the

68% and 95% C.L. are given by:

$$\begin{aligned}
\mathscr{Q}\left(C^X_{e\mu tq'}/\Lambda^2\right) &\leq \chi^2_{1,\,68\%} = 1.00\,,\\
\mathscr{Q}\left(C^X_{e\mu tq'}/\Lambda^2\right) &\leq \chi^2_{1,\,95\%} = 3.84\,,\\
\mathscr{Q}\left(C^X_{e\mu tq'}/\Lambda^2\right) &\leq \chi^2_{2,\,68\%} = 2.30\,,\\
\mathscr{Q}\left(C^X_{e\mu tq'}/\Lambda^2\right) &\leq \chi^2_{2,\,95\%} = 5.99\,,
\end{aligned} \tag{5.37}$$

where $\chi^2_{f,\,p\%}$ denotes the p^{th} percentile of the chi-squared distribution with f degrees of freedom. In the present analysis, the $f = 1$ thresholds are used when varying a single WC at a time, while the $f = 2$ thresholds are adopted when two WCs are simultaneously allowed to vary in the fit. These thresholds define the regions of parameter space that are consistent with the background-only hypothesis at the corresponding confidence levels.

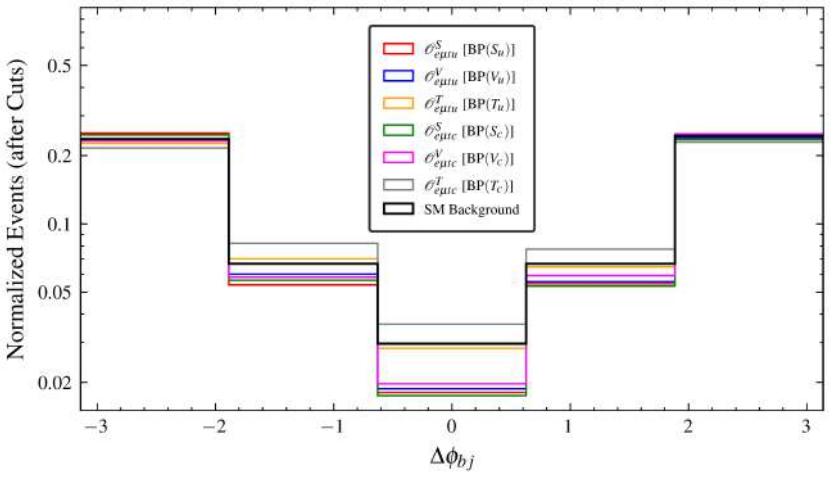

FIGURE 5.12: Normalized $\Delta\phi_{bj}$ distribution for signal benchmarks and the SM background, after applying the selection cuts in Eqs. (5.28) and (5.30).

For the sensitivity analysis, we employ the differential distribution $\Delta\phi_{bj}$, illustrated in Fig. 5.12, defined as:

$$\Delta\phi_{bj} = \phi_b - \phi_j\,, \tag{5.38}$$

where ϕ_b and ϕ_j denote the azimuthal angles of the b-jet and the light jet, respectively. As evident from Fig. 5.12, the azimuthal angle separation between jets exhibits notable sensitivity to the Lorentz structure of the effective operators, making it a powerful discriminator. We divide the $\Delta\phi_{bj}$ distribution into five equally spaced bins and perform a binned likelihood analysis to extract projected bounds on the operator coefficients, $C^X_{e\mu tq'}/\Lambda^2$. By scanning over these parameters and evaluating the test statistic $\mathscr{Q}$ for

each value, we determine the allowed parameter space consistent with the background-only hypothesis.

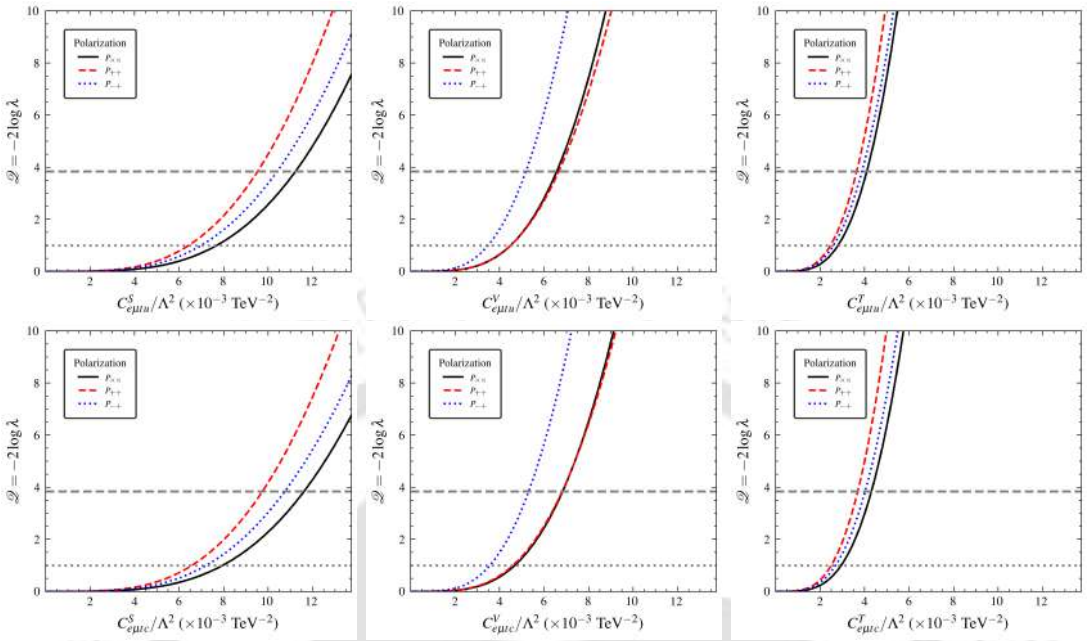

FIGURE 5.13: Single-parameter log-likelihood scans as functions of the WCs for scalar (*left*), vector (*middle*), and tensor (*right*) operators under different polarization configurations at the μTRISTAN with $\mathfrak{L}_{\rm int} = 1$ ab^{-1}. The *top* and *bottom* panels correspond to u- and c-type operators, respectively. Grey dashed (dotted) lines indicate the 95% (68%) C.L. limits.

Bounds on EFT Coefficients We present the variation of the test statistic $\mathscr{Q}$ as a function of the WCs in Fig. 5.13, corresponding to tq' production at the μTRISTAN with an integrated luminosity of 1 ab^{-1}. The projected 95% and 68% C.L. limits are indicated by grey dashed and dotted lines, respectively. The results are shown for three polarization configurations: unpolarized ($P_{\times\times}$), P_{++}, and P_{+-}.

For the scalar and tensor operators, both polarized setups P_{++} and P_{+-} offer improved sensitivity over the unpolarized case, with P_{++} yielding the strongest constraints. In contrast, for the vector operator, the P_{+-} configuration enhances sensitivity compared to the unpolarized scenario, while P_{++} does not improve and in some cases slightly worsens the reach. It is also noteworthy that, unlike at the LHC where up-quark PDFs significantly boost sensitivity to u-type operators over c-type ones, the lepton collider setup at the μTRISTAN ensures that both u- and c-type operator sensitivities are nearly comparable.

Operator	Luminosity	Polarization			LHC
		$P_{\times\times}$	P_{++}	P_{-+}	
$\mathcal{O}^S_{e\mu tu}$	100 fb^{-1}	0.0235	**0.0207**	0.0231	0.24
	1 ab^{-1}	0.0112	**0.0095**	0.0104	
$\mathcal{O}^V_{e\mu tu}$	100 fb^{-1}	0.0137	0.0144	**0.0115**	0.12
	1 ab^{-1}	0.0066	0.0067	**0.0052**	
$\mathcal{O}^T_{e\mu tu}$	100 fb^{-1}	0.0085	**0.0079**	0.0086	0.06
	1 ab^{-1}	0.0041	**0.0036**	0.0039	
$\mathcal{O}^S_{e\mu tc}$	100 fb^{-1}	0.0243	**0.0212**	0.0238	0.86
	1 ab^{-1}	0.0116	**0.0097**	0.0107	
$\mathcal{O}^V_{e\mu tc}$	100 fb^{-1}	0.0143	0.0148	**0.0118**	0.37
	1 ab^{-1}	0.0068	0.0068	**0.0053**	
$\mathcal{O}^T_{e\mu tc}$	100 fb^{-1}	0.0090	**0.0079**	0.0089	0.21
	1 ab^{-1}	0.0043	**0.0036**	0.0040	

TABLE 5.13: 95% C.L. limits on the WCs, $C^X_{e\mu tq'}/\Lambda^2$ (in TeV^{-2}) from tq' production at the μTRISTAN for integrated luminosities of a 100 fb^{-1} and 1 ab^{-1}, for different polarization setups. The last columns corresponds to the LHC bounds, detailed in Tab. 5.9. Best-case sensitivities in each row are highlighted in bold for clarity.

In Tab. 5.13, we present the projected 95% confidence level bounds on the WCs, $C^X_{e\mu tq'}/\Lambda^2$, derived from tq' production at the μTRISTAN for integrated luminosities of 100 fb^{-1} and 1 ab^{-1}, across different polarization configurations. Even with a relatively modest luminosity of 100 fb^{-1}, achievable within the early years of the μTRISTAN operation, the sensitivity surpasses current LHC limits by roughly an order of magnitude. With an integrated luminosity of 1 ab^{-1}, the bounds improve by more than a factor of two across all operator types and polarization configurations, highlighting the enhanced sensitivity and precision achievable at the μTRISTAN facility.

Bounds on Branching Ratios The projected bounds on the WCs, $C^X_{e\mu tq'}/\Lambda^2$, presented in Tab. 5.13, can be translated into upper limits on the branching ratios of rare top quark decays using Eq. (5.23). These projections are summarized in Tab. 5.14 for the process $\mu^+e^- \to tq'$ at the μTRISTAN, assuming integrated luminosities of 100 fb^{-1} and 1 ab^{-1} under different polarization configurations. The resulting bounds improve significantly over current LHC constraints, with branching ratio sensitivities reaching

2-3 orders of magnitude better, depending on the operator class and flavor structure. Notably, even at the early-stage luminosity of 100 fb^{-1}, the sensitivity outperforms existing limits, while the 1 ab^{-1} dataset offers substantially stronger exclusion potential. These improvements highlight the capability of the μTRISTAN collider to explore extremely rare flavor violating top decays with high precision, offering a promising avenue to uncover signals of new physics in the charged lepton and top quark sectors.

Operator	Luminosity	Polarization			LHC
		$P_{\times\times}$	P_{++}	P_{-+}	
$\mathcal{O}^S_{e\mu tu}$	100 fb^{-1}	6.3×10^{-10}	$\mathbf{4.9\times10^{-10}}$	6.1×10^{-10}	7.0×10^{-8}
	1 ab^{-1}	1.4×10^{-10}	$\mathbf{1.0\times10^{-10}}$	1.2×10^{-10}	
$\mathcal{O}^V_{e\mu tu}$	100 fb^{-1}	1.7×10^{-9}	1.9×10^{-9}	$\mathbf{1.2 \times 10^{-9}}$	1.3×10^{-7}
	1 ab^{-1}	4.0×10^{-10}	4.1×10^{-10}	$\mathbf{2.5\times10^{-10}}$	
$\mathcal{O}^T_{e\mu tu}$	100 fb^{-1}	4.0×10^{-9}	$\mathbf{3.4 \times 10^{-9}}$	4.1×10^{-9}	2.5×10^{-7}
	1 ab^{-1}	9.2×10^{-10}	$\mathbf{7.1\times10^{-10}}$	8.4×10^{-10}	
$\mathcal{O}^S_{e\mu tc}$	100 fb^{-1}	6.8×10^{-10}	$\mathbf{5.1\times10^{-10}}$	6.5×10^{-10}	8.9×10^{-7}
	1 ab^{-1}	1.5×10^{-10}	$\mathbf{1.1\times10^{-10}}$	1.3×10^{-10}	
$\mathcal{O}^V_{e\mu tc}$	100 fb^{-1}	1.9×10^{-9}	2.0×10^{-9}	$\mathbf{1.3 \times 10^{-9}}$	1.3×10^{-6}
	1 ab^{-1}	4.2×10^{-10}	4.2×10^{-10}	$\mathbf{2.6\times10^{-10}}$	
$\mathcal{O}^T_{e\mu tc}$	100 fb^{-1}	4.4×10^{-9}	$\mathbf{3.4 \times 10^{-9}}$	4.4×10^{-9}	2.6×10^{-6}
	1 ab^{-1}	1.0×10^{-9}	$\mathbf{7.1\times10^{-10}}$	8.8×10^{-10}	

TABLE 5.14: Projected limits on the branching ratios of rare top quark decay, $\mathcal{B}(t \to e\mu q')$, from tq' production at the μTRISTAN for integrated luminosities of 100 fb^{-1} and 1 ab^{-1}, for different polarization setups. The last column shows the current LHC bounds as listed in Tab. 5.9. Best-case sensitivities in each row are highlighted in bold for clarity.

Correlated Sensitivities In Fig. 5.14, we present the projected 95% C.L. correlated exclusion limits on the parameter spaces of different EFT operator classes, shown separately for u-type (left panels) and c-type (right panels) interactions. These bounds are derived from tq' production at the μTRISTAN, assuming an integrated luminosity of 1 ab^{-1} under various beam polarization configurations. The observed variations in the shape, orientation, and extent of the exclusion contours across different polarization setups reflect the chiral selectivity of the operators and the beam polarization. By appropriately tuning the beam polarization, one can enhance sensitivity in specific directions

of parameter space, thereby isolating dominant contributions from particular operator classes. This demonstrates the utility of polarization in boosting signal significance and providing a more refined probe of the underlying NP dynamics.

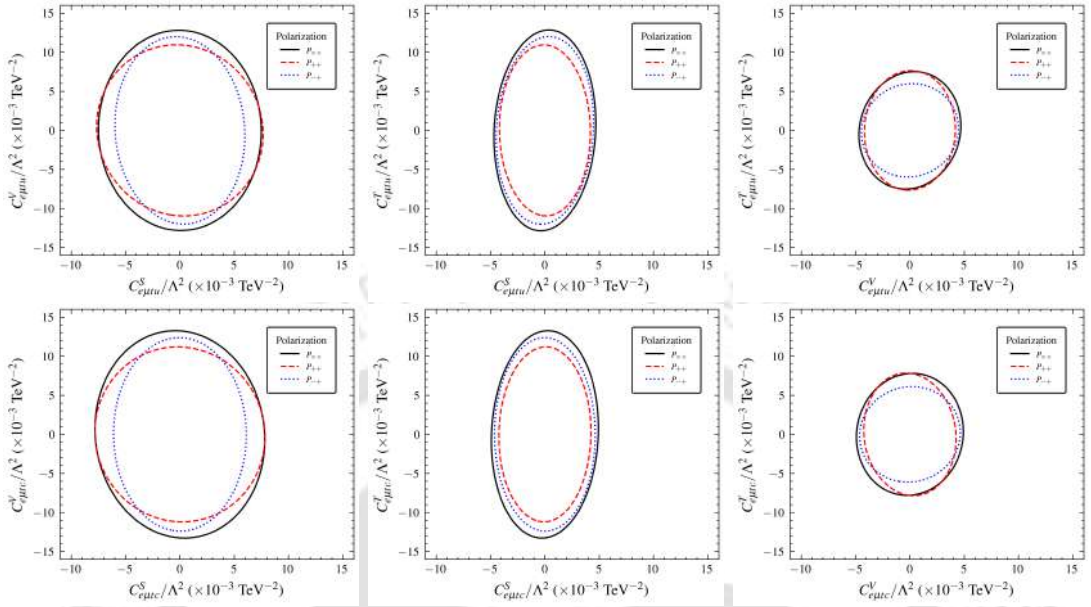

FIGURE 5.14: Correlated 95% C.L. exclusion contours for EFT operator parameter spaces of u-type (*top*) and c-type (*bottom*) classes from tq' production at the μTRISTAN, assuming an integrated luminosity of 1 ab^{-1}, for different beam polarization configurations.

5.2.4 Summary and Conclusion

In this section, we have studied charged lepton FCNC interactions involving the top quark at the proposed high-energy μ^+e^- collider stage of the μTRISTAN facility, operating at a CM energy of $\sqrt{s} = 346$ GeV. Focusing on the process $\mu^+e^- \to tq'$ with $q' = u, c$, we analyzed simplified scalar, vector, and tensor four-fermion operators derived from the SMEFT framework. These operators offer a model-independent parameterization of potential new physics responsible for cLFV and FCNC effects. Our collider analysis targeted the leptonic decay channel of the top quark and utilized a cut-based strategy to suppress the dominant SM backgrounds. We demonstrated that kinematic observables such as invariant mass and azimuthal angular separation between jets play a crucial role in enhancing signal sensitivity. The effect of initial-state beam polarization was studied in detail, revealing that it can significantly boost the sensitivity to specific operator structures and aid in disentangling their chiral nature. We employed a binned likelihood analysis using the distribution of $\Delta\phi_{bj}$ to derive projected 95% C.L. bounds

on the Wilson coefficients, $C^X_{e\mu tq'}/\Lambda^2$. Our results show that, even in the unpolarized configuration and with a modest integrated luminosity of 100 fb^{-1}, attainable within the early operational phase, the μTRISTAN can outperform existing LHC bounds by nearly an order of magnitude. With 1 ab^{-1} of data, the projected sensitivity improves by a further factor of 2–3. When translated into constraints on the rare decay branching ratios $\mathcal{B}(t \to e\mu q')$, this corresponds to improvements of up to three orders of magnitude over existing limits. Additionally, we presented correlated sensitivity projections in the Wilson coefficient parameter space, highlighting how different beam polarization configurations can be used to selectively enhance sensitivity in certain directions. This illustrates the unique potential of a polarized μ^+e^- collider in disentangling the contributions of different EFT operator classes. In summary, the μTRISTAN collider offers a clean and powerful environment to probe flavor violating interactions with high precision. Our analysis establishes that such a facility can play a leading role in exploring rare top FCNC processes involving cLFV, significantly extending the reach beyond current and near-future hadron collider capabilities. Furthermore, although we have framed our study in the language of effective operators, these interactions can arise in a broad range of BSM scenarios, including models with extended gauge sectors (e.g., Z'), scalar or vector leptoquarks, and compositeness frameworks. The bounds obtained in our analysis can thus be interpreted as constraints on these underlying theories, highlighting the utility of SMEFT-based collider studies in mapping out the viable parameter space of a wide class of new physics models.

Appendix: Application to Flavor Physics

5.A Additional Kinematical Distributions

The additional kinematic distributions of the signal and background processes are shown in Figs. 5.15 and 5.16. The detailed cutflow for the SM backgrounds is detailed in Tab. 5.15.

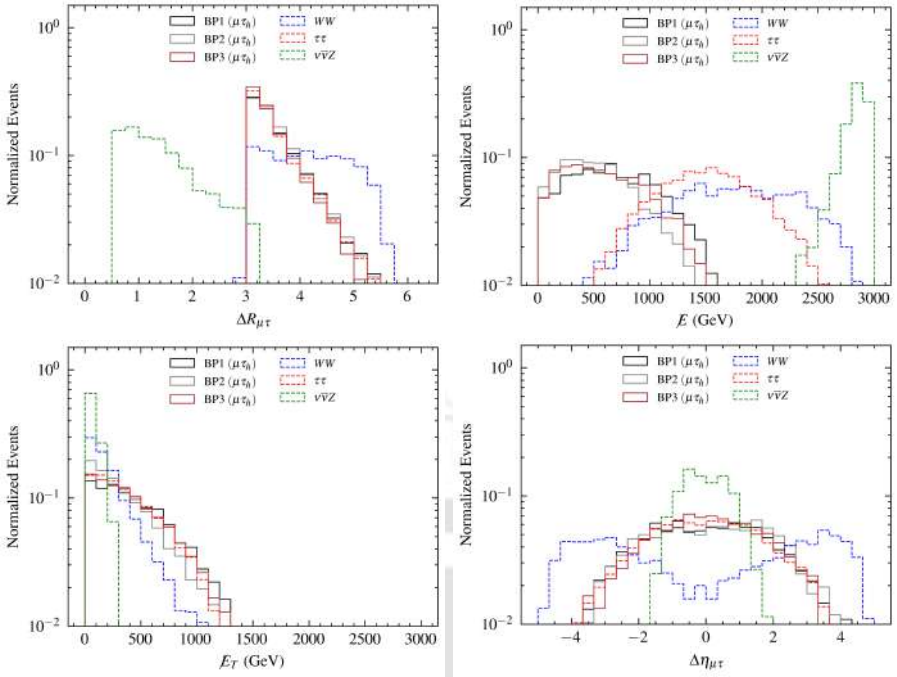

FIGURE 5.15: Additional kinematic distributions corresponding to signal and main background processes for $e^+e^- \to \mu\tau_h$ production at CLiC 3 TeV.

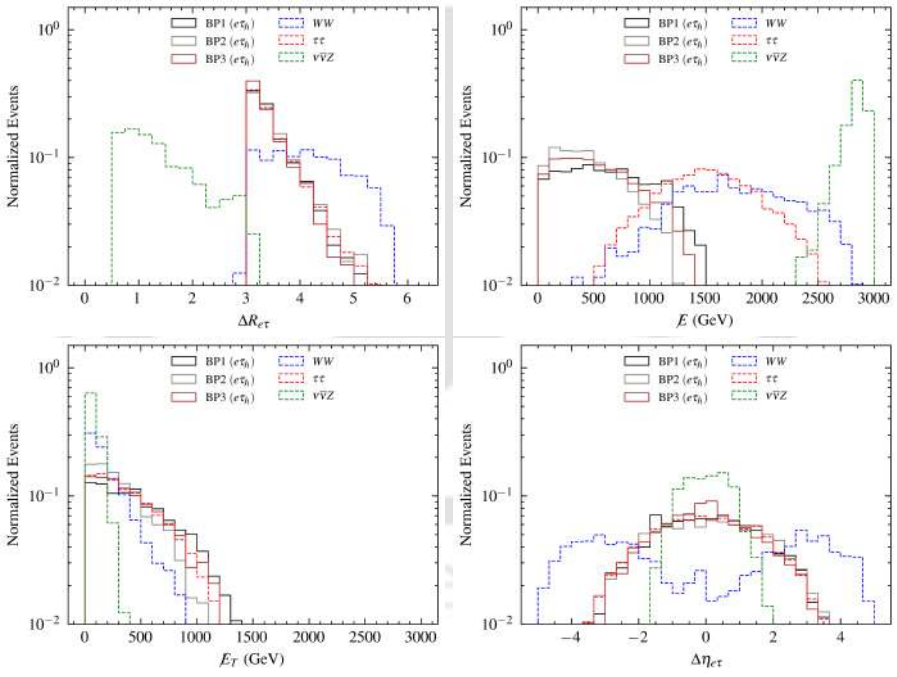

FIGURE 5.16: Additional kinematic distributions corresponding to signal and main background processes for $e^+e^- \to e\tau_h$ production at CLiC 3 TeV.

Processes	$\mathcal{C}_0$: Selection cuts			$\mathcal{C}_1 : M_{\mu\tau} > 2$ TeV			$\mathcal{C}_2 : H_T > 1.5$ TeV		
	P_0	P_+	P_-	P_0	P_+	P_-	P_0	P_+	P_-
$W^+W^-(\mu\tau_h)$	1.270	0.257	2.279	0.138	0.028	0.248	0.043	0.009	0.077
$\tau^+\tau^-(\mu\tau_h)$	1.420	1.358	1.481	0.174	0.166	0.182	0.119	0.114	0.124
$\nu\bar{\nu}Z(\mu\tau_h)$	3.289	0.660	5.903	0.000	0.000	0.000	0.000	0.000	0.000

Processes	$\mathcal{C}_0$: Selection cuts			$\mathcal{C}_1 : M_{\mu\tau} > 2$ TeV			$\mathcal{C}_2 : H_T > 1.5$ TeV		
	P_0	P_+	P_-	P_0	P_+	P_-	P_0	P_+	P_-
$W^+W^-(e\tau_h)$	1.021	0.207	1.832	0.106	0.021	0.190	0.031	0.006	0.056
$\tau^+\tau^-(e\tau_h)$	1.223	1.170	1.276	0.146	0.140	0.152	0.102	0.098	0.106
$\nu\bar{\nu}Z(e\tau_h)$	2.890	0.580	5.187	0.000	0.000	0.000	0.000	0.000	0.000

TABLE 5.15: Cutflow cross sections (in fb) corresponding to SM backgrounds ($l\tau_h$ + $\not{E}$) for different beam polarization choices at $\sqrt{s} = 3$ TeV. Here, $P_0 : P_{e^-} = 0\%$, $P_+ : P_{e^-} = +80\%$ and $P_- : P_{e^-} = -80\%$.

5.B Renormalization Group Equations

The RGEs corresponding to the SMEFT operators are represented as follows:

$$\frac{d[\mathcal{C}_i]}{d\log\mu} = \frac{1}{16\pi^2}\beta_i. \tag{5.39}$$

Here, $[\mathcal{C}_i] = C_i/\Lambda^2$ are the operator coefficients, μ is the renormalization scale, and β_i is the RGE β function corresponding to the operator $\mathcal{O}_i$. The RG equations for the SM gauge couplings are detailed in Eq. (5.40).

$$\begin{aligned}
\frac{dg}{d\log\mu} &= \frac{1}{16\pi^2}\left(-\frac{19}{6}g^3\right), \\
\frac{dg'}{d\log\mu} &= \frac{1}{16\pi^2}\left(\frac{41}{6}g'^3\right), \\
\frac{dg_s}{d\log\mu} &= \frac{1}{16\pi^2}\left(-7g_s^3\right).
\end{aligned} \tag{5.40}$$

The RG equation for the Top Yukawa coupling is shown in Eq. (5.41). All Yukawa couplings other than the one of the Top quark are considered as negligible.

$$\frac{dy_t}{d\log\mu} = \frac{y_t}{16\pi^2}\left(\frac{9}{2}y_t^2 - 8g_s^2 - \frac{9}{4}g^2 - \frac{17}{12}g'^2\right). \tag{5.41}$$

The general form of the β function corresponding to the cLFV four-fermion operators are detailed in Eqs. (5.42)-(5.44). Here, $[C_{ij}]_{prst} = (C_{ij})_{prst}/\Lambda^2$.

$$\begin{aligned}[\beta_{\ell\ell}]_{prst} = &\frac{1}{3}g'^2\left(2\,[C_{\ell\ell}]_{prww} + [C_{\ell\ell}]_{pwwr}\right)\delta_{st} + \frac{1}{3}g'^2\left(2\,[C_{\ell\ell}]_{wwst} + [C_{\ell\ell}]_{wtsw}\right)\delta_{pr} \\ &- \frac{1}{3}g^2\,[C_{\ell\ell}]_{pwwr}\,\delta_{st} + \frac{2}{3}g^2\,[C_{\ell\ell}]_{swwr}\,\delta_{pt} - \frac{1}{3}g^2\,[C_{\ell\ell}]_{wtsw}\,\delta_{pr} + \frac{2}{3}g^2\,[C_{\ell\ell}]_{wtpw}\,\delta_{sr} \\ &+ \frac{1}{3}g'^2\,[C_{\ell e}]_{prww}\,\delta_{st} + \frac{1}{3}g'^2\,[C_{\ell e}]_{wwst}\,\delta_{pr} + 6g^2\,[C_{\ell\ell}]_{ptsr} + 3\left(g'^2 - g^2\right)[C_{\ell\ell}]_{prst}\,,\end{aligned} \tag{5.42}$$

$$\begin{aligned}[\beta_{ee}]_{prst} = &\frac{2}{3}g'^2\left([C_{\ell e}]_{wwpr} + 4\,[C_{ee}]_{prww}\right)\delta_{st} + \frac{2}{3}g'^2\left([C_{\ell e}]_{stww} + 4\,[C_{ee}]_{wwst}\right)\delta_{pr} \\ &+ 6g'^2\,[C_{ee}]_{prst} + 6g'^2\,[C_{ee}]_{stpr}\,,\end{aligned} \tag{5.43}$$

$$\begin{aligned}[\beta_{\ell e}]_{prst} = &\frac{8}{3}g'^2\,[C_{\ell\ell}]_{prww}\,\delta_{st} + \frac{4}{3}g'^2\,[C_{\ell\ell}]_{pwwr}\,\delta_{st} + \frac{4}{3}g'^2\,[C_{\ell e}]_{prww}\,\delta_{st} + \frac{2}{3}g'^2\,[C_{\ell e}]_{wwst}\,\delta_{pr} \\ &+ \frac{8}{3}g'^2\,[C_{ee}]_{wwst}\,\delta_{pr} - 6g'^2\,[C_{\ell e}]_{prst}\,.\end{aligned} \tag{5.44}$$

Using the general form, we construct β function for each of the different operators. The equations are listed in Eqs. (5.45)-(5.50).

- **Operator Class:** $(\mathcal{O}_{\ell\ell})_{\tau\mu}$

$$\begin{aligned}[\beta_{\ell\ell}]_{ee\mu\tau} &= \frac{1}{3}\left(11g'^2 - 9g^2\right)[C_{\ell\ell}]_{ee\mu\tau} + \frac{1}{3}\left(g'^2 + 17g^2\right)[C_{\ell\ell}]_{e\tau\mu e} + \frac{1}{3}g'^2\,[C_{\ell e}]_{ee\mu\tau}\,, \\ [\beta_{\ell\ell}]_{\mu\tau ee} &= \frac{1}{3}\left(11g'^2 - 9g^2\right)[C_{\ell\ell}]_{\mu\tau ee} + \frac{1}{3}\left(g'^2 + 17g^2\right)[C_{\ell\ell}]_{\mu ee\tau} + \frac{1}{3}g'^2\,[C_{\ell e}]_{\mu\tau ee}\,, \\ [\beta_{\ell\ell}]_{\mu ee\tau} &= \frac{2}{3}g^2\,[C_{\ell\ell}]_{e\tau\mu e} + 6g^2\,[C_{\ell\ell}]_{\mu\tau ee} + 3\left(g'^2 - g^2\right)[C_{\ell\ell}]_{\mu ee\tau}\,, \\ [\beta_{\ell\ell}]_{e\tau\mu e} &= \frac{2}{3}g^2\,[C_{\ell\ell}]_{\mu ee\tau} + 6g^2\,[C_{\ell\ell}]_{ee\mu\tau} + 3\left(g'^2 - g^2\right)[C_{\ell\ell}]_{e\tau\mu e}\,.\end{aligned} \tag{5.45}$$

- **Operator Class:** $(\mathcal{O}_{\ell\ell})_{\tau e}$

$$\begin{aligned}[\beta_{\ell\ell}]_{eee\tau} &= \frac{1}{3}\left(11g'^2 - 9g^2\right)[C_{\ell\ell}]_{eee\tau} + \frac{1}{3}\left(g'^2 + 19g^2\right)[C_{\ell\ell}]_{e\tau ee} + \frac{1}{3}g'^2\,[C_{\ell e}]_{eee\tau}\,, \\ [\beta_{\ell\ell}]_{e\tau ee} &= \frac{1}{3}\left(11g'^2 - 9g^2\right)[C_{\ell\ell}]_{e\tau ee} + \frac{1}{3}\left(g'^2 + 19g^2\right)[C_{\ell\ell}]_{eee\tau} + \frac{1}{3}g'^2\,[C_{\ell e}]_{e\tau ee}\,.\end{aligned} \tag{5.46}$$

- **Operator Class:** $(\mathcal{O}_{ee})_{\tau\mu}$

$$\begin{aligned}
[\beta_{ee}]_{ee\mu\tau} &= \frac{26}{3}g'^2\,[C_{ee}]_{ee\mu\tau} + 6g'^2\,[C_{ee}]_{\mu\tau ee} + \frac{2}{3}g'^2\,[C_{\ell e}]_{\mu\tau ee}\,,\\
[\beta_{ee}]_{\mu\tau ee} &= \frac{26}{3}g'^2\,[C_{ee}]_{\mu\tau ee} + 6g'^2\,[C_{ee}]_{ee\mu\tau} + \frac{2}{3}g'^2\,[C_{\ell e}]_{ee\mu\tau}\,,\\
[\beta_{ee}]_{\mu ee\tau} &= 6g'^2\,[C_{ee}]_{\mu ee\tau} + 6g'^2\,[C_{ee}]_{e\tau\mu e}\,,\\
[\beta_{ee}]_{e\tau\mu e} &= 6g'^2\,[C_{ee}]_{e\tau\mu e} + 6g'^2\,[C_{ee}]_{\mu ee\tau}\,.
\end{aligned} \tag{5.47}$$

- **Operator Class:** $(\mathcal{O}_{ee})_{\tau e}$

$$\begin{aligned}
[\beta_{ee}]_{eee\tau} &= \frac{26}{3}g'^2\,[C_{ee}]_{eee\tau} + 6g'^2\,[C_{ee}]_{e\tau ee} + \frac{2}{3}g'^2\,[C_{\ell e}]_{e\tau ee}\,,\\
[\beta_{ee}]_{e\tau ee} &= \frac{26}{3}g'^2\,[C_{ee}]_{e\tau ee} + 6g'^2\,[C_{ee}]_{eee\tau} + \frac{2}{3}g'^2\,[C_{\ell e}]_{eee\tau}\,.
\end{aligned} \tag{5.48}$$

- **Operator Class:** $(\mathcal{O}_{\ell e})_{\tau\mu}$

$$\begin{aligned}
[\beta_{\ell e}]_{ee\mu\tau} &= -\frac{16}{3}g'^2\,[C_{\ell e}]_{ee\mu\tau} + \frac{8}{3}g'^2\,[C_{ee}]_{ee\mu\tau}\,,\\
[\beta_{\ell e}]_{\mu\tau ee} &= -\frac{14}{3}g'^2\,[C_{\ell e}]_{\mu\tau ee} + \frac{8}{3}g'^2\,[C_{\ell\ell}]_{\mu\tau ee} + \frac{4}{3}g'^2\,[C_{\ell\ell}]_{\mu ee\tau}\,,\\
[\beta_{\ell e}]_{\mu ee\tau} &= -6g'^2\,[C_{\ell e}]_{\mu ee\tau}\,,\\
[\beta_{\ell e}]_{e\tau\mu e} &= -6g'^2\,[C_{\ell e}]_{e\tau\mu e}\,.
\end{aligned} \tag{5.49}$$

- **Operator Class:** $(\mathcal{O}_{\ell e})_{\tau e}$

$$\begin{aligned}
[\beta_{\ell e}]_{eee\tau} &= -\frac{16}{3}g'^2\,[C_{\ell e}]_{eee\tau} + \frac{8}{3}g'^2\,[C_{ee}]_{eee\tau}\,,\\
[\beta_{\ell e}]_{e\tau ee} &= -\frac{14}{3}g'^2\,[C_{\ell e}]_{e\tau ee} + \frac{8}{3}g'^2\,[C_{\ell\ell}]_{e\tau ee} + \frac{4}{3}g'^2\,[C_{\ell\ell}]_{eee\tau}\,.
\end{aligned} \tag{5.50}$$

Fig. 5.17 shows the RGE flow of relevant operators obtained by solving Eqs. (5.45)-(5.50). The operators show very little variation to change in renormalization scale, hence, bounds obtained at lower energies will still be relevant even at higher energy scales.

5.C UV Completion of $e\mu tq$ Operators

In this section, we provide two specific BSM scenarios that generate sizeable $e\mu tq$ interactions and thereby source the EFT operators studied in this paper. We assume the presence of new flavour structures arising from BSM spurions that can naturally generate large off-diagonal entries in the lepton and quark sectors while suppressing diagonal

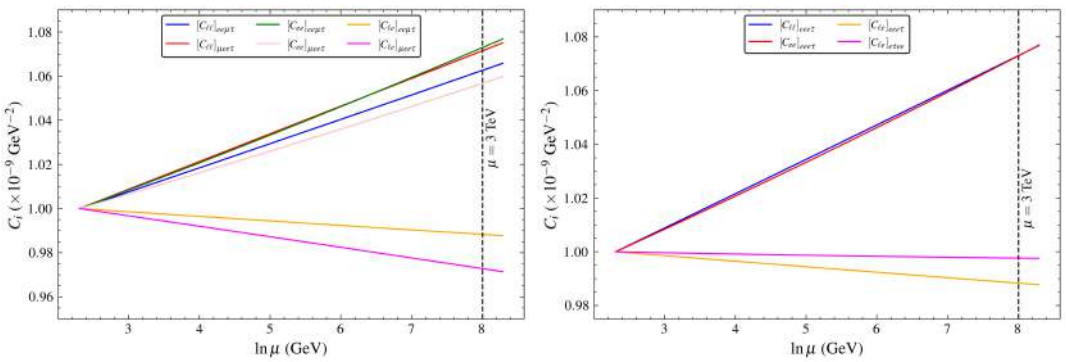

FIGURE 5.17: RGE flow for some of the cLFV operators (*Left:* $\mu\tau$ operators, *Right:* $e\tau$ operators). The black dashed line corresponds to the energy scale of the CLiC collider.

flavour structures. A simple theoretical motivation for such flavour structures arises from the presence of additional flavour spurions associated with the BSM sector. In this work we assume that the heavy states couple to SM fermions through new flavour matrices that are not aligned with the SM Yukawa structures. These spurions can naturally contain sizeable off-diagonal entries while keeping flavour-diagonal components suppressed. As a result, the effective flavour matrices X_ℓ and X_q may preferentially generate $(e\mu)$ and (tq) transitions, providing a natural origin for the $e\mu tq$ operators considered in this work.

Scalar leptoquark with flavourful couplings We consider a heavy scalar leptoquark $S \sim (3, 1, -1/3)$ under the SM gauge symmetry. Its most general renormalizable interactions with SM fermions, consistent with gauge invariance, are

$$\mathcal{L}_S = -\,\overline{q}_i\,(\mathcal{C}_q)_{ij}\,S\,\ell_j - \,\overline{u}_i\,(\mathcal{C}_u)_{ij}\,S\,e_j + \text{h.c.}\,, \tag{5.51}$$

where $\mathcal{C}_q$ and $\mathcal{C}_u$ are flavour matrices. We assume that these matrices originate from BSM flavour spurions that are not aligned with the SM Yukawa structures and can contain sizeable off-diagonal entries. The flavour structure of the couplings can be parametrized as

$$\mathcal{C}_q = \lambda\, X_q, \tag{5.52}$$

$$\mathcal{C}_u = \tilde{\lambda}\, X_u^\dagger, \tag{5.53}$$

where X_q and X_u denote BSM flavour spurions. These spurions are not required to follow the SM Yukawa hierarchy and may contain comparatively large off-diagonal entries,

particularly in the tq sector. Integrating out S at tree level generates the effective operator

$$\mathcal{L}_{\rm EFT} \supset -\frac{1}{M_S^2}\,(\bar{e}\,\mathcal{Y}_\ell\,\mu)(\bar{t}\,\mathcal{Y}_q\,q) + \text{h.c.}\,, \tag{5.54}$$

where $\mathcal{Y}_q$ inherits its flavour structure from the underlying spurions appearing in $\mathcal{C}_{q,u}$. The dominant flavour entry corresponds to the component generating the tq transition,

$$(\mathcal{Y}_q)_{tq} \sim (X_q)_{tq}, \tag{5.55}$$

while entries involving purely light generations remain suppressed according to the assumed flavour hierarchy. The tree-level matching coefficient therefore takes the schematic form

$$\mathbb{C}_{e\mu tq} \sim \frac{1}{M_S^2}\,(\mathcal{Y}_\ell)_{e\mu}\,(\mathcal{Y}_q)_{tq}\,, \tag{5.56}$$

highlighting the origin of the $e-\mu$ and $t-q$ flavour violation from the underlying spurion structure.

Flavorful Z' model with BSM flavour currents As an alternative, we consider a heavy neutral vector Z' coupled to flavourful fermion currents,

$$\mathcal{L}_{Z'} = Z'_\mu\left(g_q\,\overline{q}_i\gamma^\mu(\mathcal{G}_q)_{ij}q_j + g_\ell\,\overline{\ell}_i\gamma^\mu(\mathcal{G}_\ell)_{ij}\ell_j\right). \tag{5.57}$$

We assume that the flavour structure of these currents is controlled by BSM spurions,

$$\mathcal{G}_q = X_q X_q^\dagger, \tag{5.58}$$

$$\mathcal{G}_\ell = X_\ell X_\ell^\dagger, \tag{5.59}$$

where X_q and X_ℓ denote flavour matrices that can contain sizeable off-diagonal entries such as $(\mathcal{G}_q)_{tq}$ and $(\mathcal{G}_\ell)_{e\mu}$. Integrating out Z' yields at tree level

$$\mathcal{L}_{\rm EFT} \supset -\frac{g_q g_\ell}{M_{Z'}^2}\,(\bar{e}\gamma_\mu(\mathcal{G}_\ell)_{e\mu}\mu)\,(\bar{t}\gamma^\mu(\mathcal{G}_q)_{tq}q) + \text{h.c.}\,, \tag{5.60}$$

where the effective coefficient is controlled by the off-diagonal spurion entries generating the $e-\mu$ and $t-q$ transitions, while flavour-diagonal operators remain suppressed by the assumed structure of the BSM spurions.

5.D Disentangling Vector Chiral Structures

In this section, we explore the role of beam polarization in disentangling the different chiral structures of the vector operators in the SMEFT framework. While the simplified operator structures listed in Tab. 5.8 already exhibit kinematic distinctions from the scalar and tensor operators, the use of polarized beams provides an additional handle to separate the individual components of the vector operators. We select the following vector operator benchmarks relevant for $\mu^+e^- \to tu$ production:

$$\begin{aligned} \mathrm{BP}^{(u)}_{\ell Q}: \left(\frac{[C^{(-)}_{\ell q}]_{e\mu tu}}{\Lambda^2}\right) = 0.01\ \mathrm{TeV}^{-2}, \quad \mathrm{BP}^{(u)}_{\ell u}: \left(\frac{[C_{\ell u}]_{e\mu tu}}{\Lambda^2}\right) = 0.01\ \mathrm{TeV}^{-2}, \\ \mathrm{BP}^{(u)}_{eu}: \left(\frac{[C_{eu}]_{e\mu tu}}{\Lambda^2}\right) = 0.01\ \mathrm{TeV}^{-2}, \quad \mathrm{BP}^{(u)}_{qe}: \left(\frac{[C_{qe}]_{e\mu tc}}{\Lambda^2}\right) = 0.01\ \mathrm{TeV}^{-2}. \end{aligned} \tag{5.61}$$

For each benchmark, all other Wilson coefficients are set to zero. In this section, we focus exclusively on the u-type benchmarks, since an analogous analysis for c-type benchmarks would yield qualitatively similar results. The corresponding signal cross sections for $\mu^+e^- \to t(l\nu b)u$ production are presented in Tab. 5.16 for both the unpolarized case and various beam polarization configurations.

Polarization (P_{μ^+}, P_{e^-})	**Signal**			
	$\sigma^{\mathrm{BP}^{(u)}_{\ell q}}_{t(l\nu b)q}$ (fb)	$\sigma^{\mathrm{BP}^{(u)}_{u}}_{t(l\nu b)q}$ (fb)	$\sigma^{\mathrm{BP}^{(u)}_{\ell u}}_{t(l\nu b)q}$ (fb)	$\sigma^{\mathrm{BP}^{(u)}_{q^-}}_{t(l\nu b)q}$ (fb)
$P_{\times\times}$: Unpolarized	0.026	0.026	0.026	0.026
P_{++} : $(+0.25, +0.70)$	0.010	0.034	0.010	0.034
P_{+-} : $(+0.25, -0.70)$	0.056	0.006	0.056	0.006
P_{-+} : $(-0.25, +0.70)$	0.006	0.056	0.006	0.056
P_{--} : $(-0.25, -0.70)$	0.034	0.010	0.034	0.010

TABLE 5.16: Production cross sections for the signal process $\mu^+e^- \to t(l\nu b)u$, mediated by different vector operators are presented for various beam polarization configurations.

We observe that all operator structures contribute similarly in the unpolarized setup. The polarization configuration P_{+-} enhances the $\mathcal{O}^{(-)}_{\ell q}$ and $\mathcal{O}_{\ell u}$ contributions while suppressing $\mathcal{O}_{eu}$ and $\mathcal{O}_{qe}$, whereas the P_{-+} configuration exhibits the opposite behavior. We perform the collider simulation and likelihood-based sensitivity analysis following the same procedure outlined in Sec. 5.2.2 and 5.2.3. The resulting 95% C.L. limits on

the Wilson coefficients of the vector operators for tu production at the μTRISTAN, for integrated luminosities of 100 fb^{-1} and 1 ab^{-1} under different beam polarization configurations, are presented in Tab. 5.17. Observations from Tab. 5.13 indicate that the c-type operator structures are expected to exhibit similar sensitivity levels. This section highlights that beam polarization remains a crucial tool for distinguishing the chiral components of the vector operators.

Operator	**Luminosity**	**Polarization**		
		$\boldsymbol{P}_{\times\times}$	$\boldsymbol{P}_{++}$	$\boldsymbol{P}_{-+}$
$[\mathcal{O}_{LQ}^{(-)}]_{e\mu tu}$	100 fb^{-1}	0.0274	**0.0184**	0.0522
	1 ab^{-1}	0.0131	**0.0077**	0.0235
$[\mathcal{O}_{eu}]_{e\mu tu}$	100 fb^{-1}	0.0277	0.0566	**0.0171**
	1 ab^{-1}	0.0132	0.0235	**0.0077**
$[\mathcal{O}_{Lu}]_{e\mu tu}$	100 fb^{-1}	0.0272	**0.0188**	0.0511
	1 ab^{-1}	0.0130	**0.0079**	0.0231
$[\mathcal{O}_{Qe}]_{e\mu tu}$	100 fb^{-1}	0.0276	0.0569	**0.0168**
	1 ab^{-1}	0.0132	0.0239	**0.0076**

TABLE 5.17: 95% C.L. limits on the WCs of vector operators (up-type), C/Λ^2 (in TeV^{-2}) from tu production at the μTRISTAN for integrated luminosities of a 100 fb^{-1} and 1 ab^{-1}, for different polarization setups. Best-case sensitivities in each row are highlighted in bold for clarity.

Chapter 6

Application to Dark Matter

"Things seen are temporal, but the unseen is eternal."
Bible

Contents

One of the most compelling challenges in modern cosmology is the characterization of the dark sector, particularly the nature and origin of DM. While the SM successfully describes the visible Universe, it fails to accommodate a viable DM candidate within its particle content. Despite overwhelming astrophysical and cosmological evidence for its existence, the production mechanism of DM remains unknown. Although the WIMP paradigm has long guided experimental searches, the continued absence of a confirmed signal has motivated growing interest in alternative frameworks. Among these, FIMPs, produced via the freeze-in mechanism, provide a well-motivated scenario in which DM never attains thermal equilibrium with the SM bath.

In this context, the UV freeze-in scenario is particularly intriguing, as the DM relic abundance is governed by higher dimensional, non-renormalizable operators and is highly sensitive to the maximum temperature achieved during the reheating epoch. As a result, the present-day DM abundance carries imprints of the early Universe dynamics, offering a unique opportunity to probe epochs preceding BBN.

In this chapter, we investigate the potential of future lepton colliders to act as probes of the pre-BBN era. Working within the DMEFT framework, we establish a connection between collider observables and early Universe parameters such as the reheating temperature and inflaton dynamics. In particular, we focus on mono-photon (γ) signatures in context of photophilic DM scenarios, where the associated photon serves as a natural handle to efficiently suppress SM backgrounds, thereby enhancing the discovery potential at future lepton colliders. The discussion is structured as follows. In Sec. 6.1, we begin with a simplified scenario in which reheating dynamics is neglected, demonstrating how DMEFT operators serve as a direct window to reheating temperature by focusing on UV freeze-in production and its correlation with mono-γ signals at the ILC. Subsequently, in Sec. 6.2, we extend the analysis by explicitly incorporating reheating dynamics. By including the post-inflationary evolution of the inflaton field, we explore how the structure of the inflationary potential and the nature of inflaton-SM couplings (bosonic versus fermionic) significantly modify the viable parameter space for both scalar and fermionic DM candidates.

6.1 DMEFT as a Window to Reheating Temperature

Lepton collider as a window to reheating via freezing in dark matter detection. Part I.
B. Barman, S. Bhattacharya, S. Jahedi, D. Pradhan, A. Sarkar
Phys.Lett.B 869 (2025) 139863 (e-Print: 2406.11963 [hep-ph]).

High energy particle colliders are essential tools for NP search, where we can create heavy particles close or below the available CM energy. Our study attempts to address whether a correspondence can be established between collider signal and the early Universe cosmology, focusing particularly on the pre-BBN epoch. Through this approach, we can connect a large class of DM models and signals. Few attempts have been made before to probe FIMP DM at the colliders assuming the presence of a charged particle in the dark sector [477, 478]. In this work, we consider the direct production of FIMP DM at the colliders corresponding to low temperature reheating.

The cosmology of the early Universe has a profound impact on the production of exotic relics, for example, the DM, that constitutes about 26% of the matter-energy budget of the Universe [34]. While a particle DM candidate is well motivated to fit observations—having any intrinsic spin, minimal photon coupling, and stability on the order of the

Universe's lifetime, its exact production mechanism remains an open question. Beyond the standard thermal (WIMPs [63]) and non-thermal (FIMPs [64]) paradigms introduced earlier, other DM production mechanisms include axion misalignment [479, 480], production in inflaton decay [481], and gravitational production [482].

As established, the yield in a typical UV freeze-in scenario [66] becomes proportional to the temperature of the thermal bath. For the purposes of this section, we assume that reheating happens instantaneously, meaning the bulk of the DM is produced at the highest temperature of the Universe, usually known as the reheating temperature, $T_{\rm RH}$. Because this freeze-in occurs out of equilibrium, the DM retains the *memory* of the early Universe cosmology, allowing collider detections to serve as a direct probe of this instantaneous reheating epoch.

The organization of the section is as follows: In Sec. 6.1.1, we discuss the phenomenology of UV freeze-in DM. Following this, in Sec. 6.1.2, we explore the collider search strategies for photophilic DM. Finally, we establish the connection between collider observables and early Universe cosmology, summarizing our findings in Sec. 6.1.3.

6.1.1 UV Freeze-in via DMEFT Operators

The EFT approach [183, 483–487] to search for DM is economic in parameters and efficient in capturing the essential characteristics, focusing solely on the relevant degrees of freedom present at a certain scale. EFT methodologies are widely used, including condensed matter systems (see, [488]), and have emerged as a standard prescription for studying physics beyond the SM, but limited, if collider experiments reveal a direct manifestation of the heavy mediator, generating effective interactions. EFT is therefore valid when the CM energy of the collision remains lower than the heavy mediator mass. This is easier to achieve in lepton colliders than hadronic ones, since the partonic CM energy differs from the exact CM energy in the latter case.

At the colliders, as DM evades detection, the visible particles produced from the initial state radiation (ISR) in association with DM can provide vital clues via momentum or energy imbalance to search for DM. Mono-X, ($X \in \gamma$, j, Z, H) plus missing energy ($\not{E}$) final state is one of the popular probes to search for DM at colliders. The signal of our

interest is mono-γ, which has been studied extensively in lepton colliders [16, 189, 489–505]. Noticeably, the final state with ISR photon has similar $\not{E}$ event distribution to the huge SM neutrino background ($\nu\bar{\nu}\gamma$), making it difficult for signal-background separation (see App. 6.A). This motivates us to look for associated photon production, which we call *natural* mono-γ signal within the EFT framework. Effective operators with real spin-0 scalar (Φ), Dirac-type spin-1/2 fermionic (χ), and massive spin-1 gauge boson (X_α) DM leading to natural mono-γ searches are,

$$\mathcal{O}_2^s : \frac{C_\Phi}{\Lambda^2}(B_{\mu\nu}B^{\mu\nu} + W^I_{\mu\nu}\,W^{I\mu\nu})\,\Phi^2\,, \tag{6.1}$$

$$\mathcal{O}_3^f : \frac{C_\chi}{\Lambda^3}(B_{\mu\nu}B^{\mu\nu} + W^I_{\mu\nu}\,W^{I\mu\nu})\,(\overline{\chi}\chi)\,, \tag{6.2}$$

$$\mathcal{O}_2^V : \frac{C_V}{\Lambda^2}(B_{\mu\nu}B^{\mu\nu} + W^I_{\mu\nu}W^{I\mu\nu})\,X_\alpha\,X^\alpha\,, \tag{6.3}$$

$$\mathcal{O}_4^V : \frac{C'_V}{\Lambda^4}(B_{\mu\nu}B^{\mu\nu} + W^I_{\mu\nu}W^{I\mu\nu})\,X_{\alpha\beta}\,X^{\alpha\beta}\,, \tag{6.4}$$

where $W^I_{\mu\nu}$ ($i = 1, 2, 3$) and $B_{\mu\nu}$ are the electroweak field strength tensors corresponding to $SU(2)_L$ and $U(1)_Y$ respectively, $X_{\alpha\beta}$ represents the field strength tensor for the vector boson DM, and C_i are the dimensionless WCs. Unless otherwise stated, we consider $C_i = 1$ throughout this analysis[1]. Note that as all these operators are loop-generated when the NP is weakly coupled, they have an additional suppression of $1/(16\pi^2)$, therefore requiring the NP cutoff scale to be appropriately rescaled. For fermionic DM, there also exists a dimension-five operator, $\mathcal{O}_1^f \sim B_{\mu\nu}(\bar{\chi}\sigma^{\mu\nu}\chi)$, that can mimic a natural mono-photon-like signal via final state radiation (FSR). However, the phenomenology of such an operator is strongly constrained by DM relic abundance, pushing the corresponding NP scale beyond the reach of the collider set-up considered here. The presence of DM fields in pair implies $\mathcal{Z}_2$-symmetry that ensures absolute stability of the DM. These operators are well studied in the context of freeze-out, with a primary focus to constrain direct and indirect searches, complementing the LHC search bounds [506–508]. In the subsequent analysis, we will primarily concentrate on the spin-0 (scalar) and spin-1/2 (fermion) DM scenarios. We discuss DM production via freeze-in and derive the viable parameter space that complies with the observed DM abundance. The essential feature of freeze-in production is to consider that the DM number density was vanishingly small in the early Universe, then produced dynamically from the visible sector via DM-SM interactions,

[1]We assume that the operator relevant for DM production at early and present Universe is $\mathcal{O}_3^f$ for fermionic DM and $\mathcal{O}_2^s$ for scalar DM, and all the operators having lower mass dimension is absent. This makes the Higgs portal interaction $\Phi^2|H|^2$ to be zero as well.

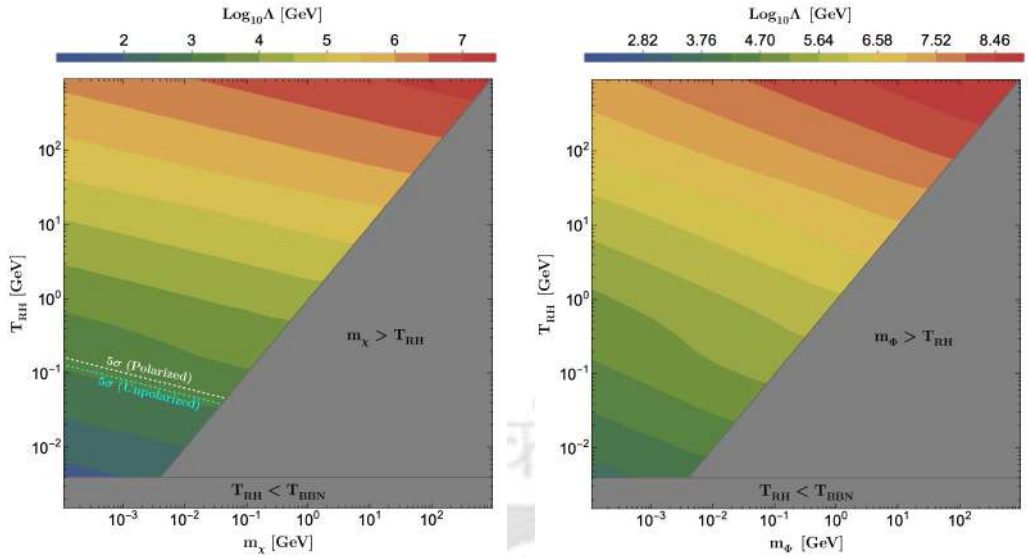

FIGURE 6.1: DM relic allowed parameter space for fermion (left) and scalar (right) DM, where the colour bar corresponds to Λ. The gray shaded regions are disallowed from the instantaneous decay approximation requiring $m_{\rm DM} \lesssim T_{\rm RH}$, as well as from the BBN bound $T_{\rm RH} \gtrsim 4$ MeV. In the left panel the cyan and white dashed contours shows 5σ significance for mono-$\gamma + \not{E}$ signal at the ILC, with $\sqrt{s} = 1$ TeV, $\mathfrak{L}_{\rm int} = 8$ ab^{-1} for unpolarized and polarized ($\{P_{e^+}, P_{e^-}\} = \{-20\%, +80\%\}$) beams respectively.

$\gamma\gamma \to$ DM DM in our case, emerging from Eq. (6.1) and (6.2). The DM-SM interaction strength is several orders of magnitude feebler than the weak interaction strength, so that the DM stays out of equilibrium. The limiting condition can be estimated by comparing the DM interaction rate $\Gamma_{2\to2} = n_{\rm DM}^{\rm eq} \langle\sigma v\rangle_{\rm DM\,DM\to\gamma\gamma}$ with the Hubble rate $\mathcal{H} = (\pi/3)\sqrt{g_\star/10}\,(T^2/M_P)$, where $\langle\sigma v\rangle$ is the thermally averaged DM production cross-section [509],

$$\left.\frac{\Gamma_{2\to2}}{\mathcal{H}}\right|_{T=T_{\rm RH}} \simeq \frac{1}{\sqrt{g_\star(T)}} \times \begin{cases} \mathcal{C}_0 \left(\frac{m_\Phi}{1\,\text{MeV}}\right) \left(\frac{T_{\rm RH}}{4\,\text{MeV}}\right)^2 \left(\frac{1\,\text{TeV}}{\Lambda}\right)^4 & \text{for scalar}\,, \\ \mathcal{C}_{1/2} \left(\frac{m_\chi}{1\,\text{MeV}}\right)^3 \left(\frac{T_{\rm RH}}{4\,\text{MeV}}\right)^2 \left(\frac{1\,\text{TeV}}{\Lambda}\right)^6 & \text{for fermion}\,, \end{cases} \tag{6.5}$$

Here, $\mathcal{C}_0 \simeq 1.39 \times 10^{-1}$ and $\mathcal{C}_{1/2} \simeq 8.94 \times 10^{-16}$, achieved by a conservative estimate of assuming DM number density to be the same as the equilibrium number density, i.e. $n_{\rm DM} \equiv n_{\rm DM}^{\rm eq} = (T/2\pi^2)\, m_{\rm DM}^2\, K_2\,(m_{\rm DM}/T)$. As one can infer, it is easy to satisfy the out-of-equilibrium condition for fermionic DM compared to the scalar case due to larger suppression (see Tab. 6.6 of App. 6.B). The very idea that we wish to investigate the collider signature of freeze-in, drives us to choose $\Lambda \sim \mathcal{O}$(TeV) such that the collider signal is significant enough, which in turn demands $m_{\rm DM} \sim \mathcal{O}$(MeV) to avoid overclosing the Universe. Because of the non-renormalizable nature of the interaction, we see, DM

yield features the typical UV nature [66] (see 6.B), where bulk of the DM is produced around the highest temperature. For DM production via $\gamma\,\gamma \to \mathrm{DM}\,\mathrm{DM}$ channel, an approximate analytical expression for DM yield $Y = n/s$ can be obtained by solving the corresponding Boltzmann equation (BEQ) (see App. 6.B)

$$Y_{\rm DM}(T) = \frac{270\,\sqrt{10}\,M_P}{g_{\star s}(T)\,\sqrt{g_\star(T)}\,\pi^8} \begin{cases} \frac{T_{\rm RH}^3 - T^3}{\Lambda^4} & \text{for scalar}\,, \\ \frac{288}{5}\,\frac{T_{\rm RH}^5 - T^5}{\Lambda^6} & \text{for fermion}\,, \end{cases} \tag{6.6}$$

considering $s \gg 4\,m_{\rm DM}^2$, where $g_\star$ and $g_{\star s}$ are the number of relativistic DOF contributing to energy and entropy density, respectively. Here, $T_{\rm RH}$ is the reheating temperature which, in the approximation of a sudden decay of the inflaton, corresponds to the maximal temperature reached by the SM thermal bath. Away from the sudden decay approximation for reheating, the bath temperature may rise to a temperature $T_{\rm max} \gg T_{\rm RH}$ [510]. It is plausible that the DM relic density may be established during this reheating period, in which case its abundance will significantly differ from freeze-in calculations assuming radiation domination. However, as the precise determination of such phenomenon depends on the details of the reheating mechanism (in particular, the shape of the inflationary potential during reheating), it is beyond the scope of the present study.

To fit the observed DM relic density, $Y_0\,m_{\rm DM} = (\Omega_{\rm DM}\,\rho_c/s_0) \simeq 4.3 \times 10^{-10}$ GeV, where Y_0, is the present day yield. Here $\rho_c \simeq 1.05 \times 10^{-5}\,h^2$ GeV/cm^3 is the critical energy density, $s_0 \simeq 2.69 \times 10^3$ cm^{-3} the present entropy density [241], and $\Omega h^2 \simeq 0.12$ is the observed abundance of DM relics [34]. From Eq. (6.6), it is clear that, for a given DM mass and effective scale, the yield is maximum at $T_{\rm RH} \gg T$, which is the quintessential feature of UV freeze-in. The DM abundance is governed by three independent parameters: $\{m_{\rm DM}, T_{\rm RH}, \Lambda\}$. The effective description of Eq. (6.1) and (6.2) remains valid under the hierarchy: $\Lambda > T_{\rm RH} \gtrsim m_{\rm DM}$, implying, the cut-off scale Λ stands as the highest scale of the theory (detailed in App. 6.F). In case of instantaneous decay approximation, maximum mass for the DM produced from the thermal bath can be $m_{\rm DM} \simeq T_{\rm RH}$. In order to produce the observed DM abundance, using Eq. (6.6) we

find

$$\Lambda \simeq \begin{cases} 5\,\text{TeV}\,\left(\frac{m_\Phi}{1\,\text{MeV}}\right)^{1/4}\left(\frac{T_{\rm RH}}{T_{\rm BBN}}\right)^{3/4} & \text{for scalar}\,, \\ 100\,\text{GeV}\,\left(\frac{m_\chi}{1\,\text{MeV}}\right)^{1/6}\left(\frac{T_{\rm RH}}{T_{\rm BBN}}\right)^{5/6} & \text{for fermion}\,, \end{cases} \tag{6.7}$$

which shows, in order to have $\Lambda \simeq \mathcal{O}(\text{TeV})$, we need to opt for low DM mass, as well as low $T_{\rm RH}$. It is easier to achieve for $\mathcal{O}_3^f$, because of larger suppression. We emphasize that the above estimation is approximate, as it accounts only for $\gamma\,\gamma \to \text{DM, DM}$ as the main production channel, and considers a constant $g_\star \approx g_{\star s} \simeq 3$ at $T_{\rm RH} = T_{\rm BBN}$. A complete numerical solution of the BEQ, including all possible DM production channels together with temperature evolution of the DOFs, has been performed in reality. The approximate estimation merely demonstrates that $\mathcal{O}_3^f$ is a favorable choice in the present scenario, and highlights the pronounced sensitivity of the DM abundance to the maximum temperature of the Universe, a quintessential feature of UV freeze-in. Note $T_{\rm BBN} \simeq 4$ MeV [511] corresponds to the lower bound on $T_{\rm RH}$, such that the accurate measurement of light element abundance during BBN is not hampered[2]. This order of magnitude estimation conforms well with the full numerical results as illustrated in Figure 6.1, showing relic density allowed parameter space in $T_{\rm RH} - m_{\rm DM}$ plane, where different shades of bands correspond to different values of Λ. A non-linear behavior in the DM relic-allowed region emerges in the color band around $T_{\rm RH} \sim 160$ MeV, driven by changes in the effective degrees of freedom of the SM bath across the QCD phase transition. Interestingly, 5σ significance for the mono-$\gamma + \not{E}$ signal produced by the DM at the ILC (with $\sqrt{s} = 1$ TeV, and integrated luminosity $\mathfrak{L}_{\rm int} = 8$ ab^{-1}) can be projected in this plane, as shown by the (cyan) white dashed lines for (un)polarized beams in the left panel plot, indicating the possibility of collider reach to probe the MeV-scale reheating era. We will elaborate on it soon. It is worth reminding that MeV-scale reheating is realizable in a minimal gravitational reheating scenario, where the SM bath is produced from inflaton scattering, mediated by graviton [514]. Since gravity interacts with all matter particles democratically, such a reheating process is inevitable and natural. The minimal scenario is however dismissed due to the excessive production of inflationary gravitational wave energy density around the time of BBN [515, 516]. As mentioned before, we refrain

[2]Since the DM-SM interaction is feeble here, the DM parameter space is safe from the CMB as well as INTEGRAL limit [512, 513], that constraints DM annihilation to photon final states.

from adhering to a specific reheating mechanism here, and simply consider $T_{\rm RH}$ as a free parameter.

6.1.2 Photophilic DM Search at the ILC

The photophilic DM provides mono-γ with missing energy signal as the innate choice, as shown in the left panel of Fig. 6.2.

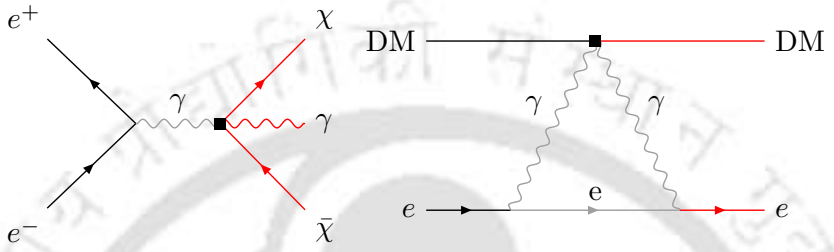

FIGURE 6.2: *Left:* Feynman graph for associated production of fermionic DM pair ($\chi\overline{\chi}$) with mono-γ at the e^+e^- collider. *Right:* Feynman diagram corresponds to the FIMP-electron (DM $-$ e) scattering.

For collider simulation we consider $\mathcal{O}_3^f$, since for $\mathcal{O}_2^s$, one needs $T_{\rm RH} < T_{\rm BBN}$ to have $\Lambda \lesssim \mathcal{O}(\text{TeV})$, as seen from Fig. 6.1. The choice of Λ is consistent with the LEP and the LHC mono-photon data (see App. 6.D and App. 6.E). For larger Λ, the signal significance diminishes as the production cross-section reduces. We perform detector-level analysis at the projected $\sqrt{s} = 1$ TeV and $\mathfrak{L}_{\rm int} = 8$ ab^{-1} which is expected to be the maximum reach of the ILC [330].

The model implementation is performed using `FeynRules` [233], and the signal and background Monte-Carlo (MC) events are generated using `MG5_aMC` [235]. The simulated events are then showered using `Pythia8` [415] to replicate initial and final state radiation effects, while further detector simulation is executed through `Delphes3` [237]. This toolchain serves as the standard simulation pipeline for all collider analyses throughout this chapter. The signal selection is ensured by only allowing events with a single photon with no associated leptons or jets. The dominant SM background stems from the $\nu\bar{\nu}\gamma$ channel, where the photon can be radiated from the electron leg in the W mediated t-channel (dominant), Z mediated s-channel, or from the W boson fusion process. The photon from the SM neutrino background is characterized by low *transverse momentum* (p_T), unlike the signal photon produced in association with a DM pair. To effectively segregate the signal from the SM background, we utilize the following kinematic variables:

- **Missing transverse energy (MET, $\not{E}_T$)**: Estimated from the momentum imbalance in the transverse direction associated with visible particles, providing an indication of missing particles not registered by the detector:

$$\not{E}_T = -\sqrt{\left(\sum p_x\right)^2 + \left(\sum p_y\right)^2}\,, \tag{6.8}$$

  where $p_{x,y}$ are the 3-momenta along the x and y directions, respectively, and the sum runs over all visible particles.

- **Missing energy (ME, $\not{E}$)**: The total energy carried away by the missing particles, defined at a lepton collider as:

$$\not{E} = \sqrt{s} - \sum_i E_i\,, \tag{6.9}$$

  where E_i are the energies of the detected visible particles. For our specific monophoton signal, this simplifies to $\not{E} = \sqrt{s} - E_\gamma$.

- **Pseudorapidity (η_γ)**: Defined from the photon emerging angle θ_γ as:

$$\eta_\gamma = -\ln\left[\tan\left(\frac{\theta_\gamma}{2}\right)\right]. \tag{6.10}$$

Thus, imposing a MET cut effectively mitigates a substantial portion of the dominant SM background. Applying a cut on ME to ensure the removal of the two peaks of the neutrino $\not{E}$ distribution reduces the background significantly, retaining most of the signal. Finally, implementing an absolute pseudorapidity cut $|\eta_\gamma| < 1.0$ finely tunes the elimination of non-transverse backgrounds. For the benchmarks illustrated in Tab. 6.1, the signal efficiency[3] ϵ_s is obtained to be 0.51 for a background rejection rate of 99%. The event topology in Fig. 6.3 shows the impact of these particular observables in separating the signal from the SM background. For details of simulation techniques, see App. 6.C.

The signal significance is calculated via [300]

$$\mathcal{S} = \sqrt{2\left[(S+B)\log\left(1+\frac{S}{B}\right) - S\right]}\,. \tag{6.11}$$

[3]We define $\epsilon_s = \sigma_{\texttt{sig}}/\sigma_{\texttt{prod}}$, where $\sigma_{\texttt{prod}}$ and $\sigma_{\texttt{sig}}$ are the signal cross-section before and after cut, respectively.

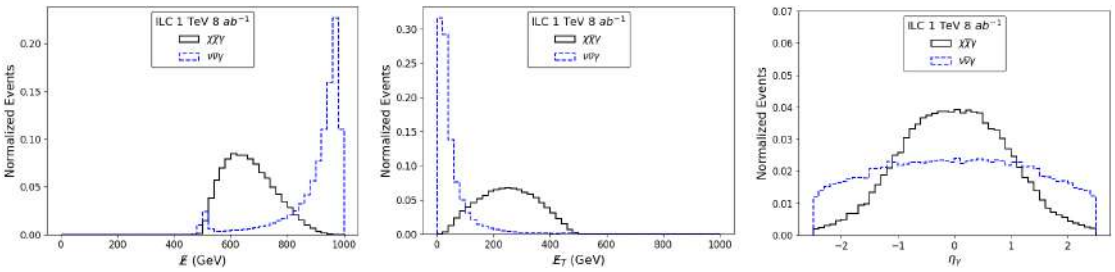

FIGURE 6.3: Normalised signal background event distributions for mono-γ final state. Left: ME ($\not{E}$), middle: MET ($\not{E}_T$), right: Pseudorapidity (η_γ). The signal corresponds to: m_χ=33 MeV, Λ=1.14 TeV.

Here S and B denote signal and background events, respectively. Signal significance ($\mathcal{S}$) undergoes enhancement after employing a series of cuts outlined in Tab. 6.1. Note that, for $S/B \ll 1$, one finds $\mathcal{S} \simeq S/\sqrt{B} \propto 1/\Lambda^6$. As the SM is a left chiral theory, judicious

Cutflow	$\boldsymbol{\nu\bar{\nu}\gamma}$ **(B)**	$\boldsymbol{\chi\bar{\chi}\gamma}$	
		Events (S)	**Significance ($\mathcal{S}$)**
Basic Cuts	18101325	4422	1.04
$\not{E}_T > 200.0$ GeV	725945	2957	3.47
$\not{E} \in [525, 750]$ GeV	289420	2694	5.00
$\lvert\eta_\gamma\rvert < 1.0$	219161	2395	5.10

Polarization $\{P_{e^+}, P_{e^-}\}$	$\boldsymbol{\nu\bar{\nu}\gamma}$ **(B)**	$\boldsymbol{\chi\bar{\chi}\gamma}$	
		Events (S)	**Significance ($\mathcal{S}$)**
$\{0\%, 0\%\}$	219161	2395	5.10
$\{+20\%, +80\%\}$	55052	2010	8.52
$\{-20\%, +80\%\}$	40711	2778	13.62
$\{+20\%, -80\%\}$	453639	2774	4.11
$\{-20\%, -80\%\}$	303079	2003	3.63

TABLE 6.1: *Upper:* Signal-background event counts and $\mathcal{S}$ for mono-γ signal for fermion DM, where m_χ=33 MeV and Λ=1.14 TeV. *Lower:* Same after final cut for different polarization combinations. The event counts correspond to $\sqrt{s} = 1$ TeV and $\mathfrak{L}_{\rm int} = 8$ ab^{-1}.

choice of beam polarizations, as e^+e^- machines are equipped with, can suppress the SM background, and enhance $\mathcal{S}$. Owing to the proposed polarizability of ILC, we study $\mathcal{S}$ for various polarization combinations, as outlined in Tab. 6.1. The detailed event analysis is summarized in App. 6.C. $\{P_{e^+}, P_{e^-}\} = \{-20\%, +80\%\}$ emerges as the most favorable combination, enhancing the signal while significantly reducing the background. Having

larger SM background and absence of polarization, probing the model at the LHC turns difficult.

6.1.3 Summary and Conclusion

Fig. 6.4 shows $\mathcal{S}$ in $\Lambda - m_\chi$ plane via coloured bands, which decreases with larger Λ, as the signal cross-section $\sim 1/\Lambda^6$. Also the significance diminishes with larger m_χ due to limited phase space. Following Eq. (6.6), each $\Lambda - m_\chi$ point indicate to a specific $T_{\rm RH}$ to satisfy the DM abundance, as shown by the reddish points, establishing a correlation between $\mathcal{S}$ and $T_{\rm RH}$. For higher DM masses, a lower $T_{\rm RH}$ is required to achieve the correct DM relic, which violates the lower bound on $T_{\rm RH}$ from BBN or the instantaneous reheating approximation itself (shown by black points). Therefore, it is possible to associate a signal significance of 5σ with MeV-scale reheating temperature and MeV-scale frozen in DM. This is what we represent in the left panel of Fig. 6.1, via the white (cyan) dashed line(s). Note that a significant part of our parameter space survives the projected 95% C.L. exclusion limit from the HL-LHC 14 TeV 3 ab^{-1} run (blue dashed line). An effective DM-electron interaction can also be realized at the 1-loop level

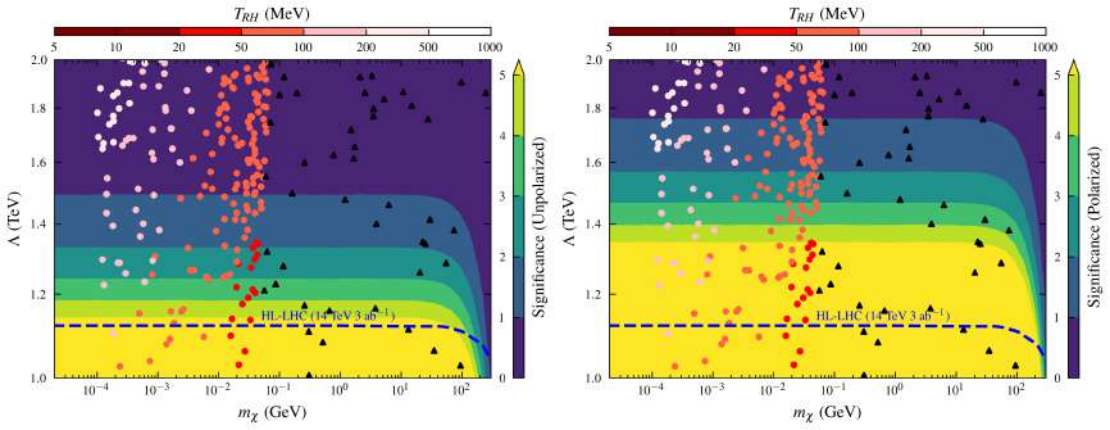

FIGURE 6.4: Observed DM abundance for $\mathcal{O}_3^f$ for different combinations of m_χ, Λ and $T_{\rm RH}$, shown via scattered reddish points. Black points are disallowed, requiring $T_{\rm RH} < T_{\rm BBN}$ or $m_\chi > T_{\rm RH}$ or both to produce the right abundance; in conflict with the BBN bound and instantaneous reheating approximation. The colour gradient shows the variation of $\mathcal{S}$ at ILC with $\sqrt{s} = 1$ TeV, and $\mathfrak{L}_{\rm int} = 8$ ab^{-1}, for unpolarized beams (left), and polarised beams $\{P_{e^+}, P_{e^-}\} = \{-20\%, +80\%\}$ (right). The blue dashed line represents the projected 95% C.L. exclusion limit from the HL-LHC ($\sqrt{s} = 14$ TeV, $\mathfrak{L}_{\rm int} = 3$ ab^{-1}) [8].

(right panel of Fig. 6.2), that leads to DM direct search via electron scattering, which is typically sensitive to MeV-scale DM [517]. However, in our case, the corresponding

scattering cross section turns out to be $\lesssim 10^{-51}\,\mathrm{cm}^2$, far beyond the reach of present experiments [518–523]. To summarize, we demonstrate the possibility to infer the reheat temperature of the universe from DM signal at future lepton colliders. This emerges for DMs undergoing UV freeze-in, establishing a one-to-one correspondence between $T_{\rm RH}$, $m_{\rm DM}$, and Λ to address the correct relic abundance. Specifically, we elucidate how the natural mono-γ signal of an MeV-scale photophilic fermionic DM can effectively point towards an MeV-scale $T_{\rm RH}$, safely segregated from SM ISR backgrounds. This analysis seeds a plethora of possibilities, such as incorporating the details of the early Universe dynamics [58], exploring different DM operators, and investigating other signals that could provide similar inferences.

6.2 DMEFT as a Window to Reheating Dynamics

Lepton collider as a window to reheating via freezing in dark matter detection. Part II.
B. Barman, S. Bhattacharya, S. Jahedi, D. Pradhan, A. Sarkar
JHEP 07 (2025) 157 (e-Print: 2410.18198 [hep-ph]).

Over the past few decades, our comprehension of cosmic history has undergone a remarkable transformation. Precise measurements of temperature anisotropies in the CMB have unveiled a Universe that is homogeneous and isotropic on large scales. These observations provide compelling evidence for an inflationary phase in the early Universe. Furthermore, the relative abundances of light elements align exceptionally well with theoretical expectations, reinforcing the predictions of BBN. These predictions, grounded in the well-understood physics of nuclear reactions, point to a hot and dense Universe in local thermal equilibrium during later stages. However, bridging these two extraordinary epochs, inflation and BBN, remains a formidable challenge. The energy scale of inflation is as high as $\sim 10^{16}$ GeV, while that of BBN is about 4 MeV. This immense range of energy (and therefore, time) scale is still poorly understood and remains largely unconstrained by observations. Nevertheless, it is necessary to have a closer look into the period between inflation and BBN and the dynamics of reheating as it holds the key to the state of the Universe that we observe today. Importantly, the process of reheating not only explains the cosmic origin of the matter that constitutes our physical world but also accounts for the production of relics beyond the SM, such as DM. Particle colliders and accelerator-based experiments possess the profound capability of replicating some

of the Universe's earliest epochs. Colliders, such as the LHC, have demonstrably established their exceptional efficacy in elucidating the intricate mechanisms underlying the EWSB, a phenomenon that transpired at an energy scale on the order of $\sim \mathcal{O}(10^2)$ GeV, as well as the QCD phase transition, which occurred at an energy scale of approximately $\sim \mathcal{O}(10^2)$ MeV. Thus, colliders emerge as promising instruments for the study of early Universe dynamics within the controlled environment of laboratories.

Stringent observational constraints [524–527] continue to motivate the FIMP paradigm [64, 528, 529]. Building upon the UV freeze-in framework [66] established in the previous section, the scenario becomes particularly intriguing when we move beyond the sudden decay approximation, because the DM yield becomes sensitive to the highest temperature $T_{\rm max}$ reached by the SM plasma [478, 510, 530–542], which is determined by the inflaton dynamics. Note that this is distinct from the reheating temperature, $T_{\rm rh}$[4], defined as the temperature at which the energy densities of inflaton and radiation are equal.

This section explores the potential to illuminate this reheating period through collider searches for DM. Having already established the efficacy of natural mono-γ signals at lepton colliders in overcoming substantial SM backgrounds, we apply this signature to probe the post-inflationary epoch. We consider that the entire DM relic was produced from the thermal bath during reheating, while the bath itself is assumed to be sourced by the perturbative decay of the inflaton field either into a pair of bosons or into a pair of fermions. Consequently, any potential DM signature could be directly correlated with (**I**) the maximum temperature reached during reheating and (**II**) the shape of the potential during this phase. This expands upon the preceding analysis in Sec. 6.1 (based on [57]), which considered instantaneous reheating and overlooked the evolution of the thermal bath. By explicitly incorporating the non-instantaneous decay of the inflaton field, the allowed parameter space for the DM opens up to a large extent and becomes accessible for collider probes.

The remainder of this section is organized as follows. The underlying particle physics model and effective operators are briefly summarized in Sec. 6.2.1. In Sec. 6.2.2 we detail the post-inflationary dynamics of the inflaton, together with DM production. We then discuss the collider analysis in Sec. 6.2.3, where we elaborate on the connection between collider signal and reheating dynamics. Finally, we conclude in Sec. 6.2.4.

[4] $T_{\rm RH}$ was used in Sec. 6.1 to denote the reheating temperature in the instantaneous reheating scenario, where it corresponds to the maximum temperature attained by the SM bath.

6.2.1 EFT Model for DM-SM Interactions

As established in the preceding sections, our focus is on DM production via UV freeze-in, utilizing non-renormalizable interactions involving a pair of SM and a pair of DM fields. This mechanism is particularly relevant when the accessible bath temperature significantly exceeds the dark sector particle masses. As previously discussed, searching for these interactions at lepton colliders relies on identifying momentum or energy imbalances. Building on the rationale detailed in Sec. 6.1.2, we continue to focus on the *natural* mono-γ signal to effectively separate the DM signature from the substantial SM neutrino background ($\nu\bar{\nu}\gamma$).

This restricts our analysis to the specific set of effective operators introduced earlier. For clarity in the context of post-inflationary reheating, we express them here with the NP scale denoted as $\Lambda_{\rm NP}$, to distinguish it from Λ_ϕ (the inflation scale)[5]:

$$\begin{aligned}
\mathcal{O}_2^s &: \frac{C_\Phi}{\Lambda_{\rm NP}^2}(B_{\mu\nu}B^{\mu\nu} + W^I_{\mu\nu}W^{I\mu\nu})\,\Phi^2\,,\\
\mathcal{O}_3^f &: \frac{C_\chi}{\Lambda_{\rm NP}^3}(B_{\mu\nu}B^{\mu\nu} + W^I_{\mu\nu}W^{I\mu\nu})\,(\overline{\chi}\chi)\,,\\
\mathcal{O}_2^V &: \frac{C_V}{\Lambda_{\rm NP}^2}(B_{\mu\nu}B^{\mu\nu} + W^I_{\mu\nu}W^{I\mu\nu})\,X_\alpha\,X^\alpha\,,\\
\mathcal{O}_4^V &: \frac{C'_V}{\Lambda_{\rm NP}^4}(B_{\mu\nu}B^{\mu\nu} + W^I_{\mu\nu}W^{I\mu\nu})\,X_{\alpha\beta}\,X^{\alpha\beta}\,.
\end{aligned} \tag{6.12}$$

Unless otherwise explicitly mentioned, we consider all the WCs to be unity. Note that as all these operators are loop generated when the NP is weakly coupled, they have an additional suppression of $1/(16\pi^2)$, therefore requiring the NP scale to be appropriately rescaled. The presence of DM fields in pair implies $\mathbb{Z}_2$-symmetry that ensures absolute stability of the DM. In the rest of the analysis, we will typically concentrate on the spin-0 (scalar) and spin-1/2 (fermion) scenarios, references to spin-1 possibilities at times. All the relevant annihilation cross-sections for DM production is reported in App. 6.G.

6.2.2 Post-Inflationary Inflaton Dynamics

In this section, we elaborate on the freeze-in production of DM during non-instantaneous reheating. We begin by discussing the post-inflationary dynamics of the inflaton that

[5]Such operators have been explored also in the context of freeze-out [507, 508, 543].

results in the generation of the radiation bath, which in turn acts as a source for DM. We consider the post-inflationary oscillation of the inflaton ϕ in a monomial potential

$$V(\phi) = \lambda \frac{\phi^n}{\Lambda_\phi^{n-4}} , \tag{6.13}$$

where λ is a dimensionless coupling and $\Lambda_\phi \lesssim 10^{16}$ GeV is the scale of inflation, bounded from above by CMB measurements of inflationary parameters [544][6]. Note that the NP generating Λ_ϕ is quite different from $\Lambda_{\rm NP}$ characterizing DM-SM interactions. The effective mass $m_\phi(a)$ for the inflaton is

$$m_\phi(a)^2 \equiv \frac{d^2V}{d\phi^2} = n\,(n-1)\,\lambda\,\frac{\phi^{n-2}}{\Lambda_\phi^{n-4}} \simeq n\,(n-1)\,\lambda^{\frac{2}{n}}\,\Lambda_\phi^{\frac{2\,(4-n)}{n}}\,\rho_\phi(a)^{\frac{n-2}{n}} . \tag{6.14}$$

For $n \neq 2$, m_ϕ has a field dependence leading to a time-dependent inflaton decay rate. The equation of motion for the oscillating inflaton condensate is [552]

$$\ddot{\phi} + (3\,\mathcal{H} + \Gamma_\phi)\,\dot{\phi} + V'(\phi) = 0 , \tag{6.15}$$

where $\mathcal{H}$ denotes the Hubble expansion rate, and Γ_ϕ is the inflaton decay rate. The evolution of the inflaton energy density $\rho_\phi \equiv \dot{\phi}^2/2 + V(\phi)$ is tracked with the BEQ:

$$\frac{d\rho_\phi}{dt} + \frac{6\,n}{2+n}\,\mathcal{H}\,\rho_\phi = -\frac{2\,n}{2+n}\,\Gamma_\phi\,\rho_\phi , \tag{6.16}$$

where $\mathcal{H} = \sqrt{(\rho_\phi + \rho_R)\,/(3\,M_P^2)}$. The inflaton equation of state is parametrized as $w \equiv p_\phi/\rho_\phi = (n-2)/(n+2)$ [552]. During reheating ($a_I \ll a \ll a_{\rm rh}$), the term $\mathcal{H}\,\rho_\phi$ typically dominates over $\Gamma_\phi\,\rho_\phi$, yielding the analytical solution:

$$\rho_\phi(a) \simeq \rho_\phi(a_{\rm rh})\left(\frac{a_{\rm rh}}{a}\right)^{\frac{6\,n}{2+n}} . \tag{6.17}$$

Since the Hubble rate during reheating is dominated by the inflaton energy density:

$$\mathcal{H}(a) \simeq \mathcal{H}(a_{\rm rh}) \times \begin{cases} \left(\frac{a_{\rm rh}}{a}\right)^{\frac{3\,n}{n+2}} & \text{for } a \leq a_{\rm rh} , \\ \left(\frac{a_{\rm rh}}{a}\right)^2 & \text{for } a_{\rm rh} \leq a . \end{cases} \tag{6.18}$$

[6]The potential in Eq. (6.13) can naturally arise in a number of inflationary scenarios, for example, the α-attractor T- or E-models [545–547], or the Starobinsky model [548–551]. Given a particular inflationary model, λ can be fixed from CMB measurements of the inflationary observables.

The evolution of the SM radiation energy density ρ_R is governed by [534]:

$$\frac{d\rho_R}{dt} + 4\,\mathcal{H}\,\rho_R = +\frac{2\,n}{2+n}\,\Gamma_\phi\,\rho_\phi\,. \tag{6.19}$$

The end of reheating occurs when $\rho_R(a_{\rm rh}) = \rho_\phi(a_{\rm rh}) = 3\,M_P^2\,\mathcal{H}(a_{\rm rh})^2$. To avoid affecting BBN predictions, the reheating temperature must satisfy $T_{\rm rh} > T_{\rm BBN} \simeq 4$ MeV [511, 553–557].

Reheating from Perturbative Inflaton Decay We consider reheating via the *perturbative* two-body decay of the inflaton at the minimum of its potential into a pair of complex scalar doublets φ or vector-like Dirac fermions Ψ[7]. The relevant Lagrangian density reads:

$$\mathcal{L}_{\rm int} \supset -\mu\,\phi\,|\varphi|^2 - y_\psi\,\overline{\Psi}\,\Psi\,\phi\,. \tag{6.20}$$

We assume these decay channels operate exclusively of one another.

Decay via the Fermionic Channel For decay into a pair of fermions, the rate is

$$\Gamma_\phi(a) = \frac{y_{\rm eff}^2}{8\pi}\,m_\phi(a)\,, \tag{6.21}$$

where $y_{\rm eff} \neq y_\psi$ (for $n \neq 2$) is the effective coupling averaged over oscillations [534, 563, 564]. The radiation energy density evolves as [565–567]:

$$\rho_R(a) \simeq \frac{3\,n}{7-n}\,M_P^2\,\Gamma_\phi(a_{\rm rh})\,\mathcal{H}(a_{\rm rh})\left(\frac{a_{\rm rh}}{a}\right)^{\frac{6(n-1)}{2+n}}\left[1-\left(\frac{a_I}{a}\right)^{\frac{2(7-n)}{2+n}}\right]. \tag{6.22}$$

Assuming instantaneous SM bath thermalization[8], the temperature reads

$$T(a) \simeq T_{\rm rh}\left(\frac{a_{\rm rh}}{a}\right)^{\alpha}, \tag{6.23}$$

with

$$\alpha = \begin{cases} \frac{3}{2}\,\frac{n-1}{n+2} & \text{for } n < 7\,, \\ 1 & \text{for } n > 7\,. \end{cases} \tag{6.24}$$

[7] Gauge-invariant interactions between the inflaton and SM fermions can be realized in a more realistic set-up [558–560]. We remain agnostic about the microscopic model and write an effective inflaton-SM interaction as in Refs. [534, 561, 562].

[8] A detailed study of thermalization can be found in Refs. [568–573].

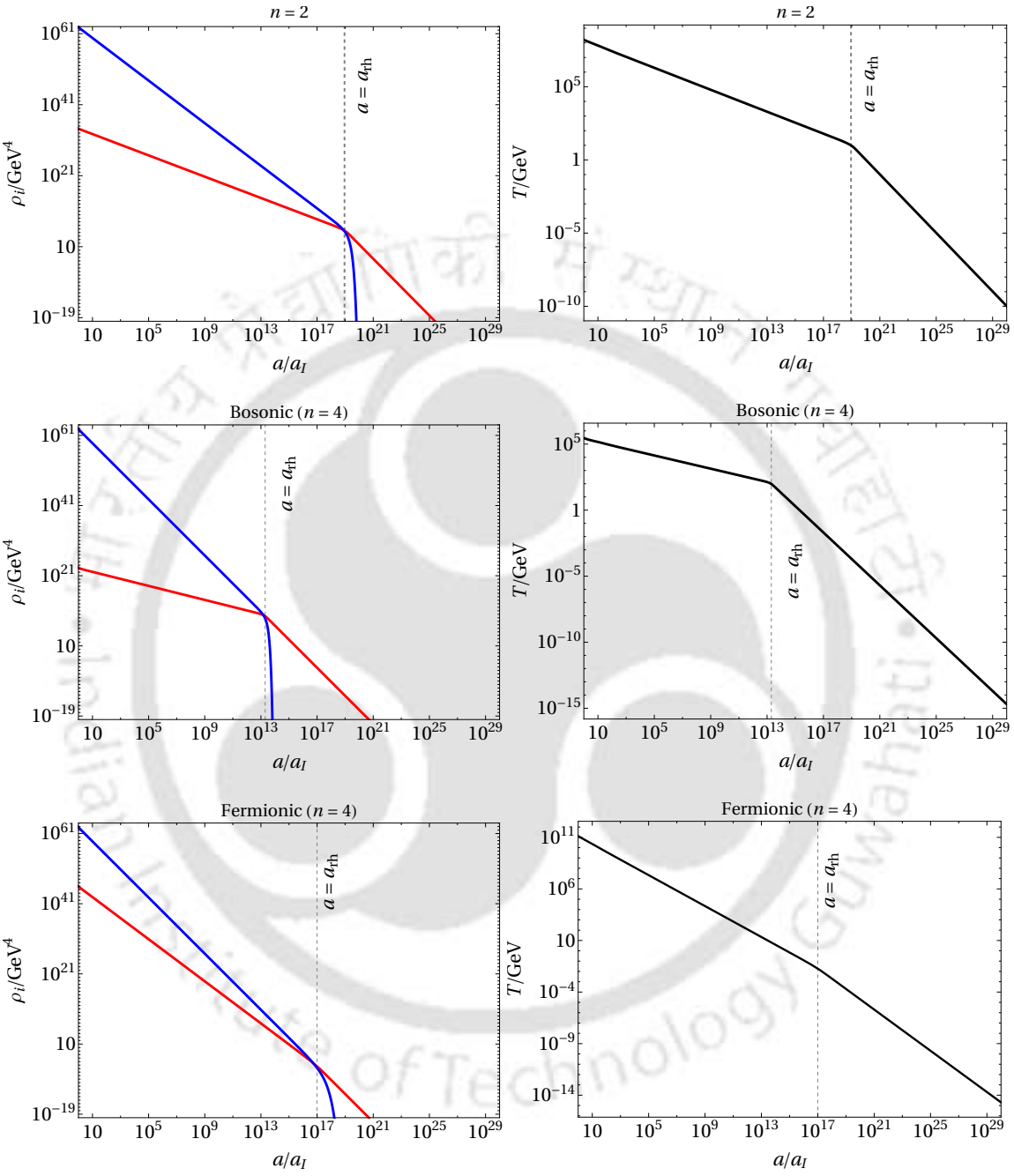

FIGURE 6.5: Left column: Evolution of inflaton and radiation energy density as a function of scale factor for bosonic and fermionic reheating scenario, with different choices of n. Right column: Corresponding SM bath temperature as a function of scale factor. Here we considered $T_{\rm rh} = 10$ GeV. The vertical dashed line in each figure shows the onset of radiation domination ($a = a_{\rm rh}$).

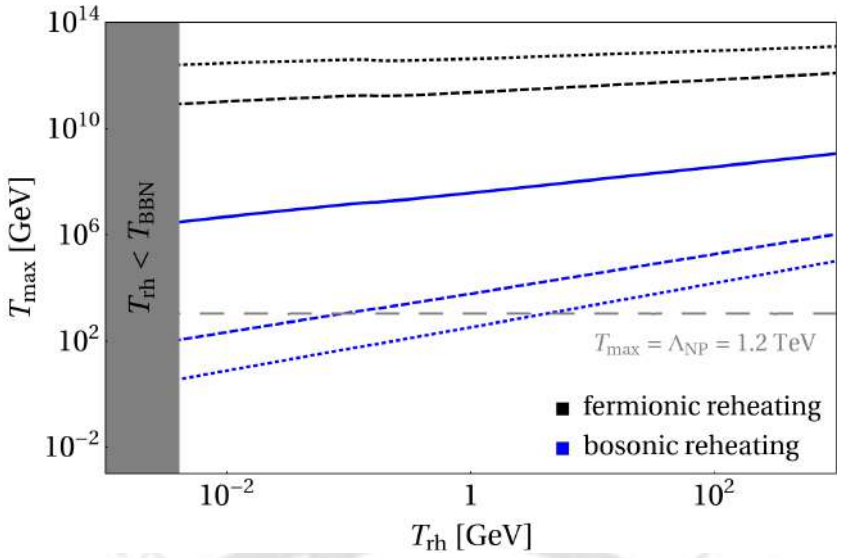

FIGURE 6.6: Maximum temperature during reheating $T_{\rm max}$, as a function of the reheating temperature $T_{\rm rh}$. The solid, dashed and dotted curves correspond to $n = 2$, 4, 6, respectively.

Trading the scale factor with temperature, the Hubble expansion rate during reheating is:

$$\mathcal{H}(T) \simeq \mathcal{H}(T_{\rm rh}) \left(\frac{T}{T_{\rm rh}}\right)^{\frac{3\,n}{2+n}\,\frac{1}{\alpha}} . \tag{6.25}$$

Decay via the Bosonic Channel If the inflaton decays solely into a pair of bosons, the rate is:

$$\Gamma_\phi(a) = \frac{\mu_{\rm eff}^2}{8\pi\, m_\phi(a)} , \tag{6.26}$$

where $\mu_{\rm eff} \neq \mu$ (if $n \neq 2$). The SM energy density scales as [565]:

$$\rho_R(a) \simeq \frac{3\,n}{1+2\,n}\, M_P^2\, \Gamma_\phi(a_{\rm rh})\, \mathcal{H}(a_{\rm rh}) \left(\frac{a_{\rm rh}}{a}\right)^{\frac{6}{2+n}} \left[1 - \left(\frac{a_I}{a}\right)^{\frac{2\,(1+2n)}{2+n}}\right] , \tag{6.27}$$

with the SM temperature and Hubble rate evolving similarly to Eqs. (6.23) and (6.25), but with

$$\alpha = \frac{3}{2}\,\frac{1}{n+2} . \tag{6.28}$$

The maximum temperature of the bath during reheating reads

$$T_{\rm max} \simeq T_{\rm rh} \begin{cases} (a_{\rm rh}/a_I)^{\frac{3\,(n-1)}{2\,(n+2)}} & \text{fermionic reheating} , \\ (a_{\rm rh}/a_I)^{\frac{3}{2\,(n+2)}} & \text{bosonic reheating} , \end{cases} \tag{6.29}$$

which can be several orders of magnitude larger than $T_{\rm rh}$ for $a_{\rm rh} \gg a_I$.

As seen in Fig. 6.5, the reheating process becomes more efficient over time for bosonic final states than for fermionic final states for $n > 2$. The effective description requires $\Lambda_{\rm NP} \gtrsim T_{\rm max}$ [533]. For our collider analysis, we require $\Lambda_{\rm NP} \gtrsim \sqrt{s} = 1$ TeV, specifically fixing $\Lambda_{\rm NP} = 1.2$ TeV. As demonstrated in Fig. 6.6, the hierarchy $\Lambda_{\rm NP} \gtrsim T_{\rm max}$ is satisfied only for bosonic reheating with $n = 4$, 6 and $T_{\rm rh}$ around the MeV scale. For fermionic reheating, $T_{\rm max}$ significantly exceeds $\Lambda_{\rm NP}$. Consequently, we restrict our subsequent analysis to the bosonic reheating framework. We also focus exclusively on perturbative reheating, restricting our analysis to $n < 8$, as gravitational reheating becomes efficient for $n \gtrsim 8$ [540, 574–576].

DM Genesis During Reheating We track DM production from the SM bath during reheating via UV freeze-in using the Boltzmann equation:

$$\frac{dn_{\rm DM}}{dt} + 3\,\mathcal{H}\,n_{\rm DM} = \gamma_{\rm DM}\,, \tag{6.30}$$

where γ is the reaction rate density, parametrized as [66, 530, 561, 577]:

$$\gamma_{\rm DM} = \frac{T^{k+6}}{\Lambda_{\rm NP}^{k+2}}\,. \tag{6.31}$$

Here $k = 2\,(d-5)$, where d is the dimension of the relevant effective operator ($d \geq 5$). Introducing a comoving number density $N_{\rm DM} \equiv n_{\rm DM}\,a^3$, Eq. (6.30) becomes:

$$\frac{dN_{\rm DM}}{da} = \frac{a^2\,\gamma_{\rm DM}}{\mathcal{H}}\,, \tag{6.32}$$

which is solved numerically with the initial condition $N_{\rm DM}(a_I) = 0$. To fit the observed relic density, we require:

$$Y_0\,m_{\rm DM} = \Omega h^2\,\frac{1}{s_0}\,\frac{\rho_c}{h^2} \simeq 4.3 \times 10^{-10}\ \text{GeV}, \tag{6.33}$$

where $Y_0 \equiv Y(T_0)$ and $Y(T) \equiv n_{\rm DM}(T)/s(T)$.

Depending on the mass scale, if $m_{\rm DM} \ll T_{\rm rh}$, DM is produced at the end of reheating, yielding:

$$N_{\rm DM}(a_{\rm rh}) \simeq \frac{2\sqrt{10}\,(n+2)}{\pi\, g_{\star s}(T_{\rm rh})}\,\frac{M_P\, T_{\rm rh}^{k+4}}{\Lambda_{\rm NP}^{k+2}}\, a_{\rm rh}^3 \times \begin{cases} \frac{1}{k-n\,(k+2)+10}\left[1-(a_I/a_{\rm rh})^{\frac{3\,(k+10-n\,(k+2)}{2n+4}}\right], & \text{fermionic reheating} \\ \frac{1}{4\,n-k-2}\left[1-(a_I/a_{\rm rh})^{\frac{12n-3k-6}{2n+4}}\right], & \text{bosonic reheating}\,, \end{cases} \tag{6.34}$$

and corresponding yield:

$$Y(a_{\rm rh}) \simeq \frac{45\sqrt{10}\,(n+2)}{\pi^3\, g_{\star s}(T_{\rm rh})^{3/2}}\,\frac{M_P\, T_{\rm rh}^{k+1}}{\Lambda_{\rm NP}^{k+2}} \times \begin{cases} \frac{1}{k-n\,(k+2)+10}\left[1-(a_I/a_{\rm rh})^{\frac{3\,(k+10-n\,(k+2)}{2n+4}}\right], & \text{fermionic reheating} \\ \frac{1}{4\,n-k-2}\left[1-(a_I/a_{\rm rh})^{\frac{12n-3k-6}{2n+4}}\right], & \text{bosonic reheating}\,. \end{cases} \tag{6.35}$$

For $T_{\rm rh} < m_{\rm DM} \ll T_{\rm max}$, DM is produced *during* reheating. Integrating to $a_{\rm DM} = a(T = m_{\rm DM})$ gives:

$$N_{\rm DM}(a_{\rm DM}) \simeq \frac{2\sqrt{10}\,(n+2)}{\pi\, g_{\star s}(m_{\rm DM})}\,\frac{M_P\, T_{\rm rh}^{k+4}}{\Lambda_{\rm NP}^{k+2}}\, a_{\rm rh}^3 \times \begin{cases} (T_{\rm rh}/m_{\rm DM})^{\frac{k-n(k+2)+10}{n-1}}\ \frac{1}{k-n\,(k+2)+10}\left[1-(a_I/a_{\rm DM})^{\frac{3\,(k+10-n\,(k+2)}{2n+4}}\right], & \text{fermionic reheating} \\ (T_{\rm rh}/m_{\rm DM})^{4n-k-2}\ \frac{1}{4\,n-k-2}\left[1-(a_I/a_{\rm DM})^{\frac{12n-3k-6}{2n+4}}\right], & \text{bosonic reheating}\,, \end{cases} \tag{6.36}$$

with yield:

$$Y(a_{\rm DM}) \simeq \frac{45\sqrt{10}\,(n+2)}{\pi^3\, g_{\star s}^{3/2}(m_{\rm DM})}\,\frac{M_P\, T_{\rm rh}^{k+4}}{m_{\rm DM}^3\,\Lambda_{\rm NP}^{k+2}} \times \begin{cases} (T_{\rm rh}/m_{\rm DM})^{\frac{6+k-n\,(k+4)}{n-1}}\ \frac{1}{k-n\,(k+2)+10}\left[1-(a_I/a_{\rm DM})^{\frac{3\,(k+10-n\,(k+2)}{2n+4}}\right], & \text{fermionic reheating} \\ (T_{\rm rh}/m_{\rm DM})^{2n-k-6}\ \frac{1}{4\,n-k-2}\left[1-(a_I/a_{\rm DM})^{\frac{12n-3k-6}{2n+4}}\right], & \text{bosonic reheating}\,. \end{cases} \tag{6.37}$$

The final yield at the end of reheating is $Y(a_{\rm rh}) \simeq Y(a_{\rm DM})\ (m_{\rm DM}/T_{\rm rh})^3\ (a_{\rm DM}/a_{\rm rh})^3$.

The analytical dependencies gathered in Fig. 6.7 show that for $m_{\rm DM} \ll T_{\rm rh}$, the slope

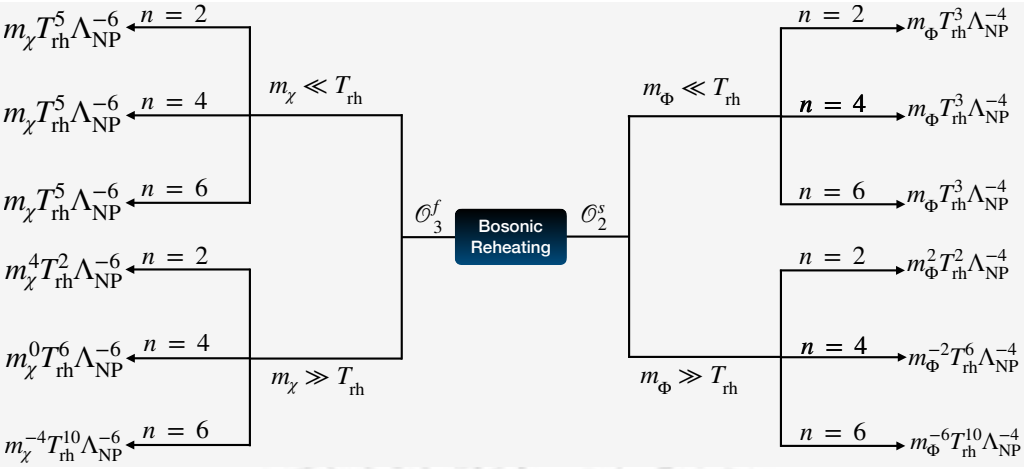

FIGURE 6.7: Summary of parameter dependence of relic abundance for scalar ($\mathcal{O}_2^s$) and fermionc ($\mathcal{O}_3^f$) dark matter, considering the bosonic reheating scenario for $n = 2, 4, 6$.

$T_{\rm rh}/m_{\rm DM}$ is negative. This is visible in the bottom panel of Fig. 6.8 for fermionic DM, but forbidden by BBN bounds for scalar DM. Conversely, for $T_{\rm rh} \ll m_{\rm DM} \ll T_{\rm max}$, the slope is positive, allowing viable parameter space for both scalar and fermionic DM. Unlike the sudden decay approximation analyzed in Sec. 6.1, explicitly incorporating the post-inflationary evolution of the thermal bath permits the production of DM with $m_{\rm DM} > T_{\rm rh}$, significantly opening up the accessible parameter space for both candidate types.

Limits from Indirect DM Search The relic density allowed parameter space is tightly constrained by Fermi-LAT [578], H.E.S.S [579], and Planck [580] observations. We have translated bounds on DM annihilation cross-section into bounds on $\Lambda_{\rm NP}$ and $m_{\rm DM}$. In Fig. 6.9, we show the constraints for scalar (left) and fermionic (right) DM annihilating into a photon pair. For scalar DM with $\Lambda_{\rm NP} = 2$ TeV, masses $m_\Phi > 1$ GeV are ruled out by Planck. The constraints on fermionic DM ($\mathcal{O}_3^f$) are relaxed due to higher dimensional suppression, leaving the corresponding parameter space viable. Based on these bounds, we select benchmark points consistent with both relic abundance and indirect detection limits for the collider analysis in the following section.

6.2.3 Testing Reheating Dynamics at Colliders

We now discuss the prospects of detecting DM produced during the epoch of reheating through the effective interactions given in Eq. (6.12). Feynman graphs corresponding

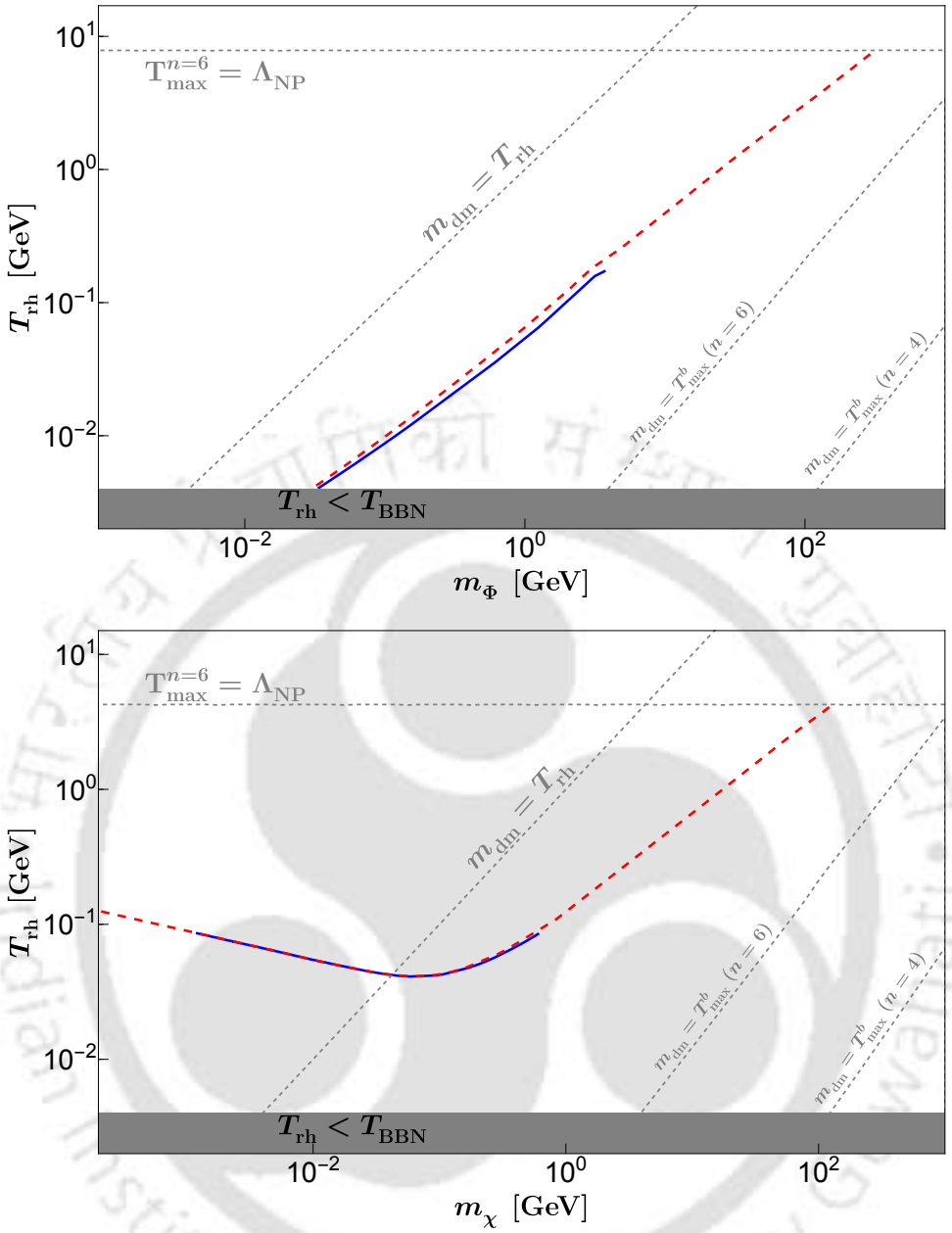

FIGURE 6.8: Viable parameter space for scalar (top) and fermionic DM (bottom), satisfying the observed relic abundance for the bosonic reheating scenario. The blue solid and red dashed lines correspond to $n = 4$ and $n = 6$, respectively. The gray shaded region is forbidden from BBN bound on $T_{\rm rh}$. We have fixed $\Lambda_{\rm NP} = 2.0$ (1.2) TeV for the scalar (fermionic) DM scenario, ensuring consistency with indirect search constraints and maintaining the validity of the EFT approach in the collider context, where $\sqrt{s} < \Lambda_{\rm NP}$.

associated production of DM pair with mono-γ (left) and `OSE` (right) at the e^+e^- collider, are shown in Fig. 6.10. As established in Sec. 6.1.2, detecting an excess in missing energy events over the SM backgrounds indicates the potential for DM discovery. We continue our signal-background analysis considering the proposed ILC [215] for a CM energy of $\sqrt{s} = 1$ TeV, utilizing the same detector simulation pipeline (`MG5_aMC`, `Pythia8`, and

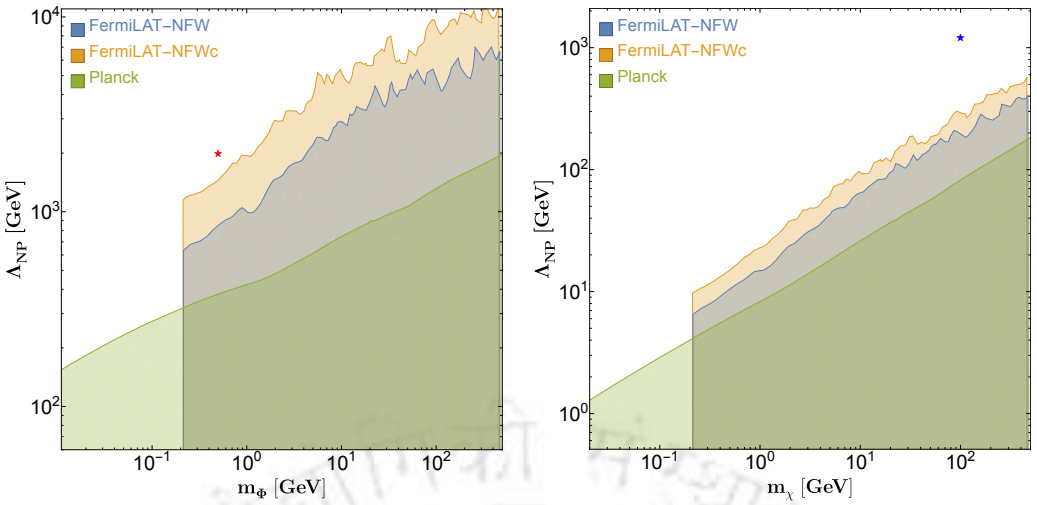

FIGURE 6.9: The figures depict the indirect search constraints on the thermally averaged annihilation cross-section, $\langle\sigma v\rangle_{\rm DM\ DM\to\gamma\gamma}$, based on current observational data, presented in the $m_{\rm DM} - \Lambda_{\rm NP}$ parameter plane for scalar (left) and fermionic (right) DM. The red (blue) star denotes the benchmark point utilized in the collider analysis for scalar (fermionic) DM.

`Delphes3`) described earlier.

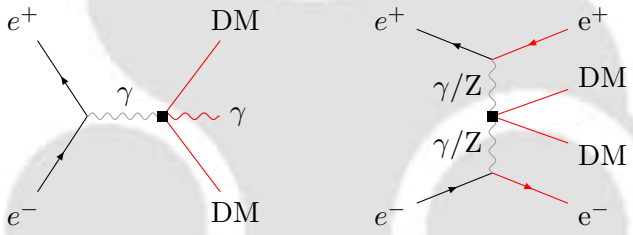

FIGURE 6.10: Feynman graphs showing associated production of DM pair with mono-γ (left) and `OSE` (right) at the e^+e^- collider.

Mono-γ Signal Analysis Identifying natural mono-γ events remains one of the most effective methods for segregating the signal from the SM background. We employ the identical cut-based strategy utilizing Missing Energy ($\not{E}$), Missing Transverse Energy ($\not{E}_T$), pseudorapidity (η_γ), and azimuthal angle (ϕ_γ)[9]. In Fig. 6.11, we illustrate the signal-background event distributions for these kinematic variables. The ISR photon from the SM background typically exhibits low p_T^γ, unlike the signal photon produced in association with the DM pair. This distinct feature in the MET distribution (top left of Fig. 6.11) enables clear differentiation. The missing energy distribution of the SM background (top right of Fig. 6.11) displays a double-peak behavior: the peak at $\not{E} \sim 1$ TeV is attributed to the W-mediated t-channel diagram, while the sub-dominant peak near

[9]The azimuthal angle of the photon is defined as $\phi_\gamma = \tan^{-1}\left(p_y^\gamma/p_x^\gamma\right)$, where, p_x^γ and p_y^γ are the x and y-component of the 4-momenta of the photon, respectively.

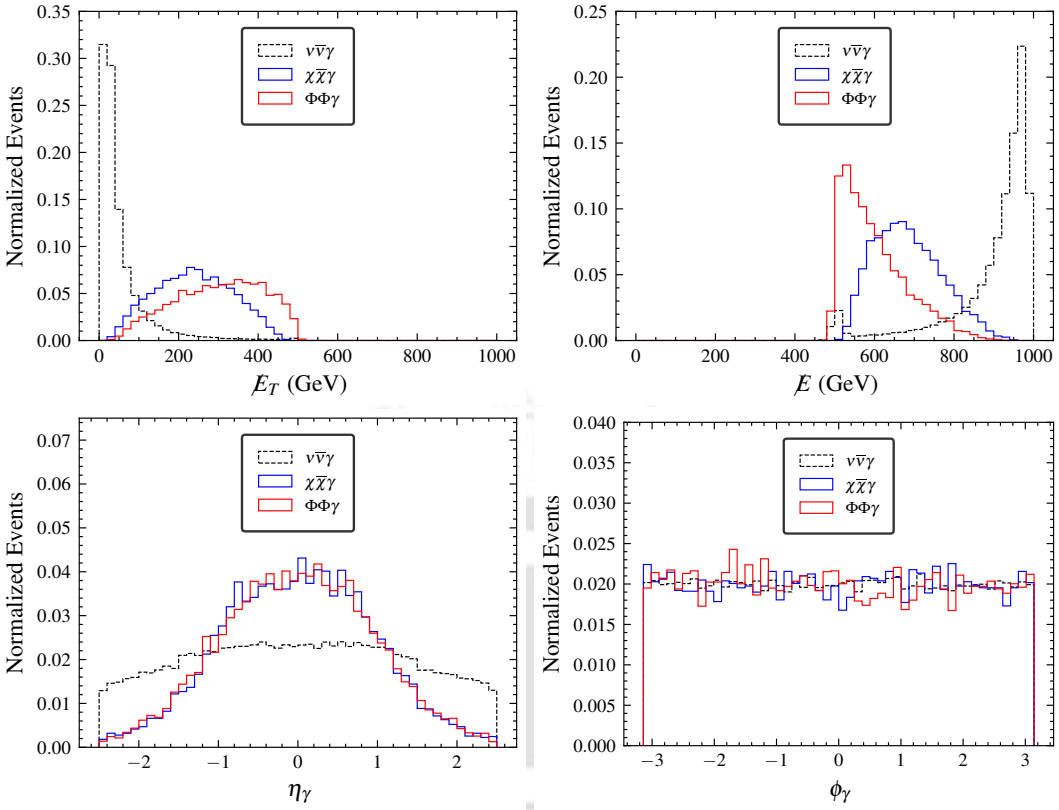

FIGURE 6.11: Event distribution for mono-γ plus missing energy signal and the SM background at the ILC with $\sqrt{s} = 1$ TeV. We choose $m_\chi = 100$ GeV, $\Lambda_{\rm NP} = 1.2$ TeV for the fermionic DM and $m_\Phi = 500$ MeV, $\Lambda_{\rm NP} = 2$ TeV for the scalar DM.

500 GeV is due to the Z-mediated s-channel diagram. The signal distribution, however, peaks near 500 GeV and exhibits a continuous decline, allowing a well-placed ME cut to eliminate a large portion of the background. Finally, an absolute pseudorapidity cut of $|\eta_\gamma| < 1.0$ refines the removal of non-transverse backgrounds. The azimuthal angle (ϕ_γ) is inefficient for discrimination (bottom right of Fig. 6.11).

The total polarized cross-section considering partial beam polarization ($-100\% < P_{e^\pm} < 100\%$) is given by [189, 215, 581]

$$\sigma(P_{e^+}, P_{e^-}) = \sum_{\lambda_{e^+}=\pm1} \sum_{\lambda_{e^-}=\pm1} \frac{(1+\lambda_{e^-}P_{e^-})\,(1+\lambda_{e^+}P_{e^+})}{4}\,\sigma_{\lambda_{e^-}\lambda_{e^+}}\,, \tag{6.38}$$

where $\lambda_i = -1(+1)$ is the left (right)-handed helicity. Employing a right-polarized electron beam and a left-polarized positron beam suppresses the SM background. Following the ILC Snowmass report [330], we choose $\{P_{e^+}, P_{e^-}\} = \{-20\%, +80\%\}$, which provides approximately a six-fold background suppression while enhancing the signal by 16%. Using the signal significance calculation defined in Eq. (6.11), the event counts and $\mathcal{S}$ are

listed in Table 6.2 (Table 6.3) for fermion (scalar) DM for the benchmark: $m_\chi(m_\Phi) = 100$ GeV (500 MeV) and $\Lambda_{\rm NP} = 1.2$ TeV (2 TeV) at $\mathfrak{L}_{\rm int} = 8$ ab^{-1}. We observe about a 99% reduction in the SM neutrino background while retaining around 50% of the signal in each case.

Cuts	$\{P_{e^+}, P_{e^-}\} = \{0\%, 0\%\}$			$\{P_{e^+}, P_{e^-}\} = \{-20\%, +80\%\}$		
	$\chi\bar{\chi}\gamma$	$\nu\bar{\nu}\gamma$	**Significance**	$\chi\bar{\chi}\gamma$	$\nu\bar{\nu}\gamma$	**Significance**
Basic cuts	2371	18061101	0.56	2747	3455860	1.48
$\not{E}_T > 190$ GeV	1595	790250	1.79	1808	447846	2.70
$\not{E} \in (510, 750)$ GeV	1462	406112	2.29	1659	142321	4.39
$\lvert\eta_\gamma\rvert < 1$	1291	272872	2.47	1462	79403	5.17

TABLE 6.2: Cutflow for signal and background events for mono-γ signal at the ILC with $\sqrt{s} = 1$ TeV and $\mathfrak{L}_{\rm int} = 8$ ab^{-1} for unpolarized ($\{P_{e^+}, P_{e^-}\} = \{0\%, 0\%\}$) and polarized ($\{P_{e^+}, P_{e^-}\} = \{+20\%, -80\%\}$) cases. Here, we consider fermionic DM with mass $m_\chi = 100$ GeV and $\Lambda_{\rm NP} = 1.2$ TeV.

Cuts	$\{P_{e^+}, P_{e^-}\} = \{0\%, 0\%\}$			$\{P_{e^+}, P_{e^-}\} = \{-20\%, +80\%\}$		
	$\Phi\Phi\gamma$	$\nu\bar{\nu}\gamma$	**Significance**	$\Phi\Phi\gamma$	$\nu\bar{\nu}\gamma$	**Significance**
Basic cuts	2945	18061101	0.69	3425	3455860	1.84
$\not{E}_T > 190$ GeV	2406	790250	2.70	2802	447846	4.18
$\not{E} \in (510, 750)$ GeV	2134	406112	3.34	2509	142321	6.63
$\lvert\eta_\gamma\rvert < 1$	1762	272872	3.37	2075	79403	7.33

TABLE 6.3: Same as Table 6.2, but for scalar DM with $m_\Phi = 500$ MeV and $\Lambda_{\rm NP} = 2$ TeV.

Opposite-sign Electron Signal Another possible collider signature can arise from the opposite sign electron (`OSE`) channel, where DM is produced through the fusion of neutral vector bosons (VBF) radiated from the initial state electrons (Fig. 6.2). Charged VBF can also produce a DM pair in association with SM neutrinos, resulting in no visible final state particles[10]. We focus exclusively on the neutral VBF production mode, strictly selecting events with two electrons and excluding any events with detected photons, jets, or muons. The dominating SM backgrounds are W^+W^- and $\tau^+\tau^-$ subsequent decay to electrons and neutrinos, alongside e^+e^-Z and $\nu\bar{\nu}Z$ production. The relevant kinematic variables are:

[10]The `OSE` signal can also appear from Z decay to electrons arising from "natural mono-Z" possibilities, however, this signal is subdominant and subjected to large background suppression.

- **Invariant di-electron mass (M_{ee})**:

$$M_{ee} = \sqrt{(p_{e^+} + p_{e^-})^2}\,, \tag{6.39}$$

  where p_{e^+} (p_{e^-}) is the 4-momenta of the detected positron (electron). This is crucial for identifying resonant production.

- **Difference in pseudorapidity ($\Delta\eta_{ee}$)**:

$$\Delta\eta_{ee} = (\eta_{e^+} - \eta_{e^-})\,. \tag{6.40}$$

- **Distance between the electron pair (ΔR_{ee})**:

$$\Delta R_{ee} = \sqrt{(\Delta\eta_{ee})^2 + (\Delta\phi_{ee})^2}\,, \tag{6.41}$$

  where $\Delta\phi_{ee}$ is the difference in the azimuthal angles.

To eliminate electrons from Z decay, we pre-select events with $M_{ee} > 100$ GeV, efficiently removing the Z-pole and discarding the $\nu\bar{\nu}Z$ background. The kinematic distributions are shown in Fig. 6.12. A cut demanding $\not{E} > 550$ GeV significantly kills the W^+W^- and e^+e^-Z backgrounds (top right of Fig. 6.12). Furthermore, a judicious cut of $|\Delta\eta_{ee}| > 1$ removes the central region of the distribution, eliminating most of the $\tau\tau$ background (top left of Fig. 6.12). Similar discrimination can be obtained using ΔR_{ee}.

Following these cuts, the signal and background events, along with $\mathcal{S}$, are listed in Table 6.4 (Table 6.5) for the unpolarized as well as the optimal polarization choice of $\{P_{e^+}, P_{e^-}\} = \{+20\%, +80\%\}$. This polarization suppresses the background by a factor of 1.5 while marginally enhancing the signal, resulting in a $\sim 96\%$ background reduction while retaining $\sim 55\%$ of the signal. The signal significance as a function of the integrated luminosity for different final states and combination of polarizations are illustrated in Fig. 6.13. We note that the scalar DM is expected to achieve 5σ signal significance at a lower integrated luminosity compared to the fermionic candidate. This is because the scalar DM emerges from a dimension-six operator in contrast to the fermionic DM (dimension-seven), resulting in less suppression for identical mass and NP scale benchmarks. This points toward the possibility of detecting the scalar candidate

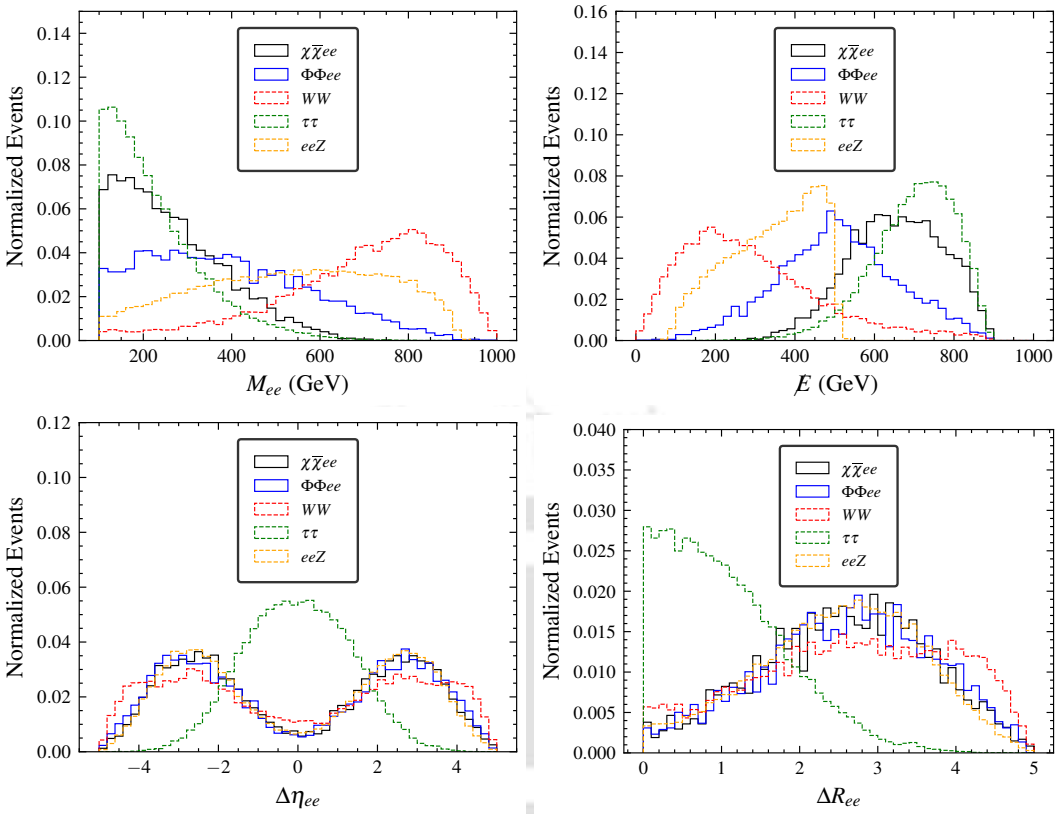

FIGURE 6.12: Event distribution of dilepton plus missing energy signal and corresponding SM background for $\sqrt{s} = 1$ TeV. We choose $m_\chi = 100$ GeV, $\Lambda_{\rm NP} = 1.2$ TeV for the fermionic DM and $m_\Phi = 100$ MeV, $\Lambda_{\rm NP} = 2$ TeV for the scalar DM.

Cuts	$\{P_{e^+}, P_{e^-}\} = \{0\%, 0\%\}$			$\{P_{e^+}, P_{e^-}\} = \{+20\%, +80\%\}$		
	$\chi\bar{\chi}ee$	**Backgrounds**	**Significance**	$\chi\bar{\chi}ee$	**Backgrounds**	**Significance**
Basic cuts	222	131699	0.61	235	80923	0.83
$\not{E} > 550$ GeV	178	15931	1.41	189	10255	1.86
$\lvert\Delta\eta_{ee}\rvert > 1$	121	4793	1.75	128	2876	2.38

TABLE 6.4: Cutflow for signal and background events for `OSE` signal at the ILC with $\sqrt{s} = 1$ TeV and $\mathfrak{L}_{\rm int} = 8$ ab^{-1} for unpolarized ($\{P_{e^+}, P_{e^-}\} = \{0\%, 0\%\}$) and polarized ($\{P_{e^+}, P_{e^-}\} = \{+20\%, +80\%\}$) cases. Here we consider fermionic DM with $m_\chi = 100$ GeV and $\Lambda_{\rm NP} = 1.2$ TeV.

Cuts	$\{P_{e^+}, P_{e^-}\} = \{0\%, 0\%\}$			$\{P_{e^+}, P_{e^-}\} = \{+20\%, +80\%\}$		
	$\Phi\Phi ee$	**Backgrounds**	**Significance**	$\Phi\Phi ee$	**Backgrounds**	**Significance**
Basic cuts	273	131699	0.75	279	80923	0.98
$\not{E} > 550$ GeV	103	15931	0.81	110	10255	1.09
$\lvert\Delta\eta_{ee}\rvert > 1$	68	4793	0.98	74	2876	1.38

TABLE 6.5: Same as Table 6.4 but for scalar DM with mass $m_\Phi = 500$ MeV and $\Lambda_{\rm NP} = 2$ TeV.

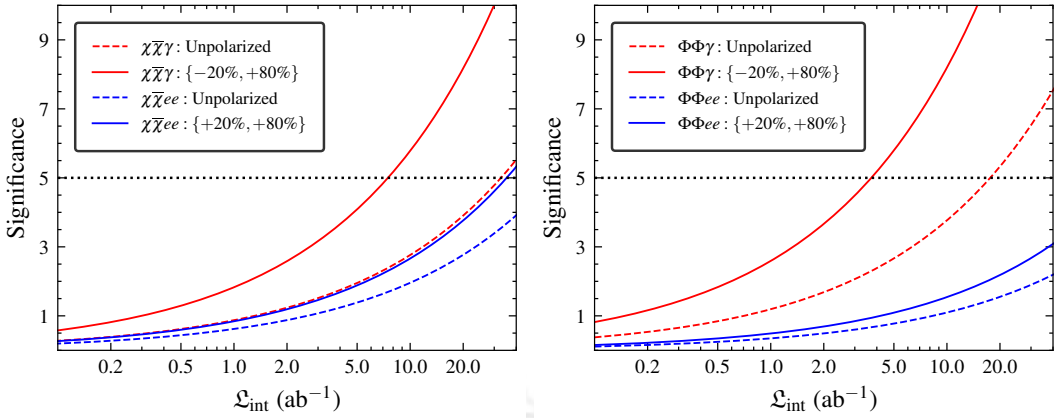

FIGURE 6.13: Signal significance as a function of integrated luminosity for a different combination of beam polarizations $\{P_{e^+}, P_{e^-}\}$ in case of fermionic DM (left) and scalar DM, (right). We choose $m_\chi = 100$ GeV and $\Lambda_{\rm NP} = 1.2$ TeV for the fermion DM and $m_\Phi = 500$ MeV and $\Lambda_{\rm NP} = 2$ TeV, with $\sqrt{s} = 1$ TeV. The dotted black line corresponds to 5σ significance.

during the early runs of the ILC, whereas the fermionic DM might only be probed during high-luminosity runs.

Similarly, the variation of signal significance with the DM mass $m_{\rm DM}$ for the relic density allowed points (for $n = 6$) is shown in Fig. 6.14. The significance drops with the increase in DM mass due to the limited final state phase space. Here we also denote the corresponding $T_{\rm rh}$ required to satisfy the observed DM abundance. As established earlier, only the bosonic reheating scenario is valid here, enabling us to establish a one-to-one correspondence between the DM mass, the reheating temperature (controlled by the reheating dynamics), and the signal significance at the ILC.

6.2.4 Summary and Conclusion

In this work, we have explored the ability of lepton colliders to shed light on the pre-BBN cosmology. To establish a one-to-one correspondence between collider and cosmological observables, we focused on DM genesis via UV freeze-in, which requires non-renormalizable interactions between DM and the visible sector, i.e., the SM. We considered DM production during the era of reheating, facilitated by DM-SM operators with mass dimensions six and seven—where the former pertains to spin-0 DM, and the latter to spin-1/2 DM. While the large effective NP scale required for UV freeze-in severely suppresses the collider signal cross-section, we demonstrated that leveraging natural mono-γ

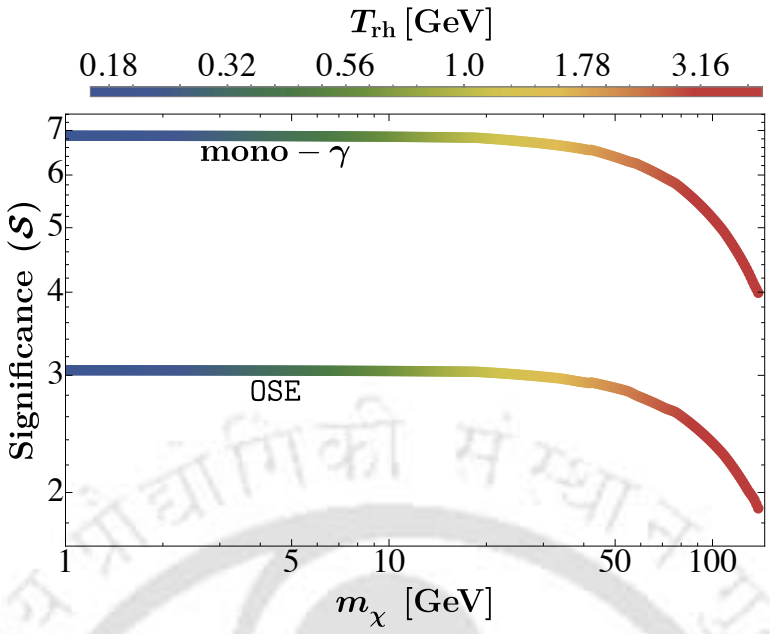

FIGURE 6.14: Signal significance as a function of DM mass for the fermionic DM. We choose $n = 6$, $\Lambda_{\rm NP} = 1.2$ TeV, $\sqrt{s} = 1$ TeV and $\mathfrak{L}_{\rm int} = 8$ ab^{-1}. The polarization combinations are $\{P_{e^+}, P_{e^-}\} = \{-20\%, +80\%\}$ ($\{+20\%, +80\%\}$) for mono-γ (OSE) signal. The bar legend denotes the corresponding reheating temperature required to satisfy the observed DM abundance.

and OSE signals allows for effective segregation from SM contamination using judicious missing energy and MET cuts at future lepton colliders.

As a concrete model for the pre-BBN cosmology, we assumed reheating occurred through the perturbative decay of the inflaton into either a pair of SM-like bosons or fermions, with the inflaton ϕ oscillating at the bottom of a monomial potential $V(\phi) \propto \phi^n$ during this period. Such monomial potentials are well-motivated from CMB measurements of inflationary observables, for example, the tensor-to-scalar ratio, spectral index or the amplitude of the tensor power spectrum. A detailed analysis of the reheating epoch allows us to explore beyond reheating temperature as $T_{\rm rh} < T_{\rm max}$. For significant collider signals to emerge over the SM background, the scale of NP needs to be around $\sim \mathcal{O}$(TeV). We found that in this scenario, the observed DM abundance can be achieved only through bosonic reheating, with a reheating temperature $T_{\rm rh} \sim \mathcal{O}$(MeV), such that the effective description of the DM-SM interaction remains valid during reheating (see Fig. 6.8). The scalar DM operator connecting to SM via field strength tensor gets highly suppressed from indirect search bounds from two photon annihilation channel. We study collider signal excess that can be achieved via mono photon signal for both scalar and fermionic DM in relic density and indirect search limited regions.

This implies that any signal excess detected, for instance, in the mono-γ channel (or opposite-sign electron channel) at the lepton collider (e.g., the ILC), could potentially indicate reheating via a bosonic channel and a low (MeV) reheating temperature (see Fig. 6.14). In conclusion, this analysis not only provides a method to probe freeze-in at colliders but also offers insight into the earliest epoch of the Universe, demonstrating the power of particle colliders in investigating the pre-BBN era.

Appendix: Application to Dark Matter

6.A Radiation γ vs. Vertex γ

We review two scenarios in our analysis. The first scenario (already discussed in the main text) involves the operator $\mathcal{O}_3^f$, where the photon from the lepton collider mono-γ signal originates directly from the effective vertex itself. In the alternate scenario, the photon is radiated from the incoming electron/positron leg. The later scenario is relevant to DM produced via leptophilic operators. One such operator is given by

$$\mathcal{O}_2^f = \frac{C_\chi}{\Lambda^2}(\bar{\ell}\gamma^\mu \ell + \bar{e}\gamma^\mu e)(\overline{\chi}\gamma_\mu \chi)\,. \tag{6.42}$$

We perform a comparative analysis between the vertex photon from $\mathcal{O}_3^f$ and the radiative photon from $\mathcal{O}_2^f$ along with the neutrino background. The kinematic distributions are shown in Fig. 6.15. It can be clearly seen that the radiative process is always overshadowed by the SM neutrino background, and hence, a clear distinction is extremely difficult using cut-based methods. To segregate these signal processes, we require polarization tuning (to suppress the background) as well as dedicated multivariate techniques.

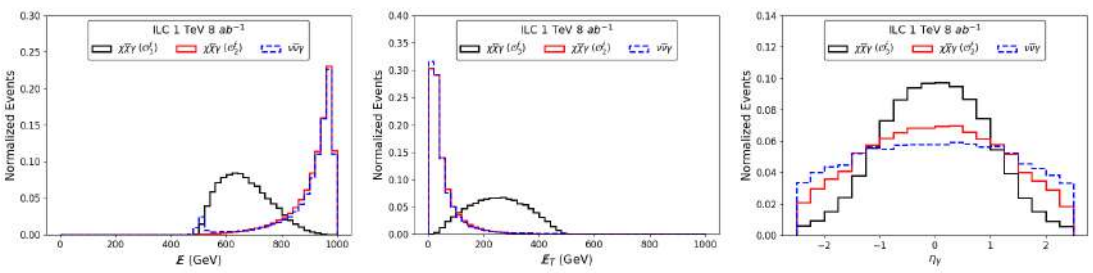

FIGURE 6.15: Signal background event distributions for different kinematic variables with the mono-γ final state signal. Left: MET ($\not{E}_T$), middle: ME ($\not{E}$), right: Pseudo-rapidity (η_γ). The signal corresponds to: m_χ=33 MeV and Λ=1.14 TeV.

6.B Reaction Density and Boltzmann Equation

The reaction density corresponding to 2-to-2 processes reads

$$\gamma_{22} = \int \prod_{i=1}^{4} d\Pi_i \, (2\pi)^4 \, \delta^{(4)}\Big(p_a + p_b - p_1 - p_2\Big) \, f_a^{\rm eq} f_b^{\rm eq} \, |\mathcal{M}_{a,b\to 1,2}|^2$$
$$= \frac{T}{32\pi^4} \, g_a g_b \int_{s_{\rm min}}^{\infty} ds \, \frac{\Big[\big(s - m_a^2 - m_b^2\big)^2 - 4 m_a^2 m_b^2\Big]}{\sqrt{s}} \sigma\,(s)_{a,b\to 1,2} \, K_1\left(\frac{\sqrt{s}}{T}\right) , \quad (6.43)$$

with a, b $(1, 2)$ as the incoming (outgoing) states and $g_{a,b}$ are corresponding degrees of freedom. Here $f_i^{\rm eq} \approx \exp\left(-E_i/T\right)$ is the Maxwell-Boltzmann distribution. The Lorentz invariant 2-body phase space is denoted by: $d\Pi_i = d^3 p_i / \Big[(2\pi)^3 \, 2E_i\Big]$. The amplitude squared (summed over final and averaged over initial states) is denoted by $|\mathcal{M}_{a,b\to 1,2}|^2$ for a particular 2-to-2 scattering process. The lower limit of the integration over s is $s_{\rm min} = \max\Big[(m_a + m_b)^2, (m_1 + m_2)^2\Big]$. The BEQ governing the DM number density

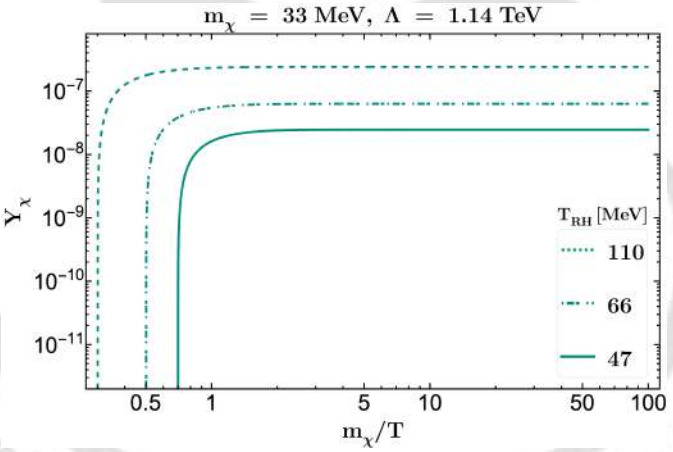

FIGURE 6.16: Yield of fermionic DM as a function of the dimensionless quantity m_χ/T, where different curves correspond to different choices of $T_{\rm RH} = \{47,\ 66,\ 110\}$ MeV, shown via solid, dot-dashed and dashed patterns, respectively. Here we have fixed $\Lambda = 1.14$ TeV and $m_\chi = 33$ MeV.

can be written in terms of the DM yield defined as a ratio of the DM number density to the entropy density in the visible sector, i.e., $Y_{\rm DM} = n_{\rm DM}/s$. The BEQ can then be expressed in terms of the reaction densities as

$$x \, \mathcal{H} \, s \, \frac{dY_{\rm DM}}{dx} = \gamma_{22} \, , \quad (6.44)$$

where $x \equiv m_{\rm DM}/T$, T being the temperature of the thermal bath and H is the Hubble parameter. In a radiation dominated Universe,

$$s(T) = \frac{2\,\pi^2}{45}\, g_{\star s}(T)\, T^3\,, \qquad \mathcal{H}(T) = \frac{\pi}{3}\sqrt{\frac{g_\star(T)}{10}}\,\frac{T^2}{M_P}\,, \tag{6.45}$$

where $g_{\star s}$ and $g_\star$ are the effective number of relativistic degrees of freedom contributing to the entropy and energy density respectively, while M_P is the reduced Planck mass. The typical UV nature of the DM yield is very much apparent from Fig. 6.16, where, as one can see, bulk of the DM production happens around $T_{\rm RH}$, for a given DM mass and NP scale. In Tab. 6.6 we quote the Γ/H ratio at $T = T_{\rm RH}$ for several benchmark values of DM mass, effective scale and reheating temperature, that correspond to the right DM abundance. For all cases we find $\Gamma_{2\to2}/H \ll 1$, showing the DM production happens out of equilibrium (for temperatures lower than $T_{\rm RH}$, this ratio is even smaller). In each case we also provide the value of the thermally averaged DM, DM $\to \gamma\gamma$ cross-section. This shows that our parameter space is safe from CMB bound on the annihilation cross-section of MeV-scale DM into mono-photon final states, that typically requires $\langle\sigma v\rangle \lesssim 10^{-16}$ GeV^{-2} [513, 582].

DM	$m_{\rm DM}$ (MeV)	Λ (TeV)	$T_{\rm RH}$ (MeV)	$\Gamma_{2\to2}/H\vert_{T=T_{\rm RH}}$	$\langle\sigma v\rangle_{\rm DM\ DM\to\gamma\gamma}$ (GeV^{-2})
Scalar (Φ)	0.101	73.621	439.54	2.00×10^{-3}	5.02×10^{-20}
	1.097	24.27	22.44	5.52×10^{-5}	1.11×10^{-20}
	10.139	68.549	45.29	6.48×10^{-6}	7.24×10^{-22}
	101.16	387.26	385.48	1.80×10^{-6}	5.19×10^{-23}
	1018.6	22233	47863	6.67×10^{-7}	7.16×10^{-26}
Fermion (χ)	0.186	1.101	111.69	1.52×10^{-4}	3.99×10^{-21}
	1.389	1.076	70.96	1.99×10^{-5}	4.28×10^{-22}
	12.8	1.248	54	2.18×10^{-6}	1.05×10^{-22}
	30.6	1.191	43	9.98×10^{-7}	6.44×10^{-23}
	40	1.204	42	8.58×10^{-7}	6.11×10^{-23}

TABLE 6.6: Table showing values of interaction rate to Hubble rate ratio and thermally averaged DM DM $\to \gamma\gamma$ cross-sections, at $T = T_{\rm RH}$, for benchmark points corresponding to right relic abundance. Note that these numbers are evaluated numerically by solving the Boltzmann equation.

6.C Details of the Collider Analysis

In this section, we detail out the event analysis configurations and strategy briefly explained in Sec. 6.1. A pure mono-γ signal is ensured by a no lepton no jet veto. The details of photon, lepton and jet identification and isolation will be detailed later. The signal process is $e^+e^- \to \chi\overline{\chi}\gamma$ and event generation is done in `MG5_aMC` at LO at CM energy of 1 TeV with the following pre-defined cuts on the γ kinematics: $p_T^\gamma > 10$ GeV and $|\eta_\gamma| < 2.5$. The dominant background process is $e^+e^- \to \nu\overline{\nu}\gamma$. The production level cross sections for the signal and the major background are listed for different CM energies in Tab. 6.7. The simulated events are showered in `Pythia8` to replicate ISR

CM energy, $\sqrt{s}$ (GeV)	**$\sigma_{\chi\overline{\chi}\gamma}$ (fb)**	**$\sigma_{\nu\overline{\nu}\gamma}$ (fb)**
250	0.0022	2743
500	0.0358	2120
1000	0.5889	2495

TABLE 6.7: Production cross sections for signal ($\chi\overline{\chi}\gamma$, for the benchmark: m_χ=33 MeV and Λ=1.14 TeV) and dominant background ($\nu\overline{\nu}\gamma$) at different CM energies of the ILC.

and FSR effects. The showered events are fed to `Delphes3` for detector simulation. The details of particle identification and isolation criteria used in `Delphes3` are listed below:

- **Photon**: Identification requires $p_T^\gamma > 10$ GeV and $|\eta_\gamma| < 2.5$. The identification efficiency for $|\eta_\gamma| \leq 1.5$ and $1.5 < |\eta_\gamma| \leq 2.5$ regions are 0.95 and 0.85 respectively. The photon isolation cone is taken to be $\Delta R = 0.5$ and the photon is isolated if the isolation p_T ratio is less than 0.12[11].

- **Lepton**: Identification requires $p_T^\ell > 10\,(10)$ GeV and $|\eta_\ell| < 2.5\,(2.4)$ for electron (muon). The identification efficiency for $|\eta_\gamma| \leq 1.5$ and $1.5 < |\eta_\gamma| \leq 2.5\,(2.4)$ regions for electrons (muons) are 0.95 (0.95) and 0.85 (0.95) respectively. The electron (muon) isolation cone is taken to be $\Delta R = 0.5\,(0.5)$ and the electron (muon) is isolated if the isolation p_T ratio is less than 0.12 (0.25).

- **Jet**: The jet clustering is done using the anti-k_T algorithm with jet radius, $R = 0.5$ and $p_T^j > 20$ GeV.

[11]The p_T isolation ratio is the sum of the p_T of all other species in the ΔR cone to the p_T of the photon.

The tracking efficiencies and momentum resolution functions are same as the default `Delphes3` card. These detector efficiencies combined consitute the 'Basic Cuts'. We additionally implement three more sequential cuts: $\not{E}_T > 200$ GeV, $\not{E} \in [525, 750]$ GeV, and $|\eta_\gamma| > 1.0$. The detailed cutflow of the signal and the dominant background for different polarization combination are detailed in Tab. 6.8 with associated Poissonian uncertainties. The benchmark is same as Tab. 6.1.

Cutflow		Polarization, $\{P_{e^+}, P_{e^-}\}$				
		$\{0\%, 0\%\}$	$\{+20\%, +80\%\}$	$\{-20\%, +80\%\}$	$\{+20\%, -80\%\}$	$\{-20\%, -80\%\}$
Basic Cuts	(S)	4422 ± 66	3710 ± 61	5124 ± 72	5124 ± 72	3701 ± 61
	(B)	18101325 ± 4254	4544778 ± 2132	3354590 ± 1832	37339851 ± 6111	24934392 ± 4993
$\not{E}_T > 200$ GeV	(S)	2957 ± 54	2484 ± 50	3419 ± 58	3434 ± 59	2479 ± 50
	(B)	725945 ± 852	344134 ± 587	413257 ± 643	1193090 ± 1092	831588 ± 912
$\not{E} \in [525, 750]$ GeV	(S)	2694 ± 51	2264 ± 48	3115 ± 56	3129 ± 56	2256 ± 47
	(B)	289420 ± 538	73299 ± 271	54545 ± 234	588283 ± 767	395508 ± 629
$\|\eta_\gamma\| > 1.0$	(S)	2395 ± 49	2010 ± 45	2778 ± 53	2774 ± 53	2003 ± 45
	(B)	219161 ± 468	55052 ± 235	40711 ± 202	453639 ± 674	303079 ± 550

TABLE 6.8: Signal (S), $\chi\overline{\chi}\gamma$ and dominant background (B), $\nu\overline{\nu}\gamma$ event counts with uncertainties in each step of the subsequent cuts for mono-γ final state signal (for the benchmark: m_χ=33 MeV and Λ=1.14 TeV) for different polarization combinations at the 1 TeV ILC with $\mathfrak{L}_{\rm int} = 8$ ab^{-1} and different possible beam polarizations.

Other Background Processes Other possible backgrounds arise from processes like $e^+e^- \to W^+W^-\gamma$, $e^+e^- \to ZZ\gamma$, $e^+e^- \to l^+l^-\gamma$, and $e^+e^- \to \gamma\gamma\gamma$, where the outgoing particles or decay products are undetected, resulting in missing energy. In Tab. 6.9, we provide an estimate on the backgrounds $W^+W^-\gamma$ and $ZZ\gamma$ for the cutflow in Tab. 6.8, and gauge their effect on the signal significance. We only show the numbers of the unpolarized case and the optimal polarization choice of $\{P_{e^+}, P_{e^-}\} = \{-20\%, +80\%\}$. The backgrounds $\ell^+\ell^-\gamma$ and $\gamma\gamma\gamma$ do not survive till the final cut and hence not listed. From the last two rows of Table 6.9, it is clear that the signal significance do not alter significantly and hence considering $\nu\overline{\nu}\gamma$ is good enough to obtain an estimate on the discovery limit.

6.D Recasting Limits from the LEP

The Large Electron–Positron Collider (LEP) has performed a number of studies concerning single photon events with missing energy [583, 584]. However, most of them were

Cutflow		**Polarization**, $\{P_{e^+}, P_{e^-}\}$	
		$\{0\%, 0\%\}$	$\{-20\%, +80\%\}$
Basic Cuts	$W^+W^-\gamma$	2136 ± 46	5814 ± 76
	$ZZ\gamma$	3805 ± 62	5429 ± 74
$\not{E}_T > 200.0$ GeV	$W^+W^-\gamma$	334 ± 18	1024 ± 32
	$ZZ\gamma$	522 ± 23	762 ± 28
$\not{E} \in [525.0, 750.0]$ GeV	$W^+W^-\gamma$	242 ± 16	738 ± 27
	$ZZ\gamma$	468 ± 22	676 ± 26
$\lvert\eta_\gamma\rvert > 1.0$	$W^+W^-\gamma$	175 ± 13	504 ± 22
	$ZZ\gamma$	348 ± 19	530 ± 23
Significance (only $\nu\nu\gamma$)		5.11 ± 0.10	13.62 ± 0.26
Significance (all backgrounds)		5.10 ± 0.10	13.45 ± 0.26

TABLE 6.9: Event counts of backgrounds $W^+W^-\gamma$ and $ZZ\gamma$ with uncertainties in each step of the subsequent cuts for mono-γ final state signal (for the benchmark: m_χ=33 MeV and Λ=1.14 TeV) and the final signal significance in presence and absence of these backgrounds at the 1 TeV ILC with $\mathfrak{L}_{\rm int} = 8$ ab^{-1} and two different beam polarizations.

aimed towards precision measurements within the SM or other exotic searches. One way to extract information from these existing studies is to recast them using identical set of resolutions and efficiencies as used in the original studies and feed MC generated events through the recasting framework. Such study has been done concerning the leptophilic operators in, for example, [16]. Here we provide an exclusion bound on the $m_\chi - \Lambda$ plane based on existing LEP data from mono-γ studies. LEP studies were done over a range of CM energies $\sqrt{s} = [180 - 209]$ GeV. The observed events, however, were reconstructed and presented in bins of x_γ, defined as $E_\gamma/E_{\rm beam}$, thus independent of CM energy of the collisions. For our analysis, we generate events at a reference CM mass energy of $\sqrt{s} = 200$ GeV, which, following the conclusion drawn in [16], does not invalidate the LEP data. The DELPHI detector at LEP had three angular regions (HPC, FEMC and STIC), and each region had a different set of trigger and reconstruction/identification efficiencies. The recasting of each of these regions, based on [583, 584], are detailed in Tab. 6.10. There is an additional photon identification efficiency of 90% valid for all regions. For STIC, since, the information provided by [583] is incomplete, we assume the overall efficiency to be 48% as done by [16]. In order to validate our framework, we plot the x_γ distribution of our generated MC events for the SM backgrounds on top of the

same from DELPHI MC studies. They are found to be in perfect agreement as shown in Fig. 6.17. The observed data as well as the DM signal corresponding to the benchmark $m_\chi = 1.37$ MeV, $\Lambda = 0.23$ TeV. To obtain an exclusion bound on the $m_\chi - \Lambda$ plane, we

Detector Regions	**Trigger Efficiency**	**Reconstruction Efficiency**	**Energy Smearing**
HPC $\theta_\gamma \in [90°, 45°]$ $x_\gamma \in [0.06, 1.10]$	$x_\gamma \in [0.06, 0.30]$ $(45.75 + 1.042\ E_\gamma)\%$ $\cup$ $x_\gamma \in [0.30, 1.10]$ $(74 + 0.1\ E_\gamma)\%$	$x_\gamma \in [0.06, 0.80]$ $(38 + 0.5\ E_\gamma)\%$ $\cup$ $x_\gamma \in [0.80, 1.10]$ 78%	Gaussian (σ_E/E_γ): $0.043 \oplus 0.32/\sqrt{E_\gamma}$ $+$ Lorentzian (Γ): $0.04\ E_\gamma$
FEMC $\theta_\gamma \in [32°, 12°]$ $x_\gamma \in [0.10, 0.90]$	$x_\gamma \in [0.10, 0.15]$ $(79 + 1.4\ E_\gamma)\%$ $\cup$ $x_\gamma \in [0.15, 0.90]$ 100%	$0.89(55 + 0.2E_\gamma)\%$	Gaussian (σ_E/E_γ): $0.03 \oplus 0.12/\sqrt{E_\gamma} \oplus 0.11/E_\gamma$ $+$ Lorentzian (Γ): $0.02\ E_\gamma$
STIC $\theta_\gamma \in [8°, 3.8°]$ $x_\gamma \in [0.30, 0.90]$	48%		Gaussian (σ_E/E_γ): $0.0152 \oplus 0.135/\sqrt{E_\gamma}$ $+$ Lorentzian (Γ): $0.02\ E_\gamma$

TABLE 6.10: Details of resolution and efficiencies for the LEP recast study. The θ_γ ranges are shown for one half of the detector only, but the same efficiencies apply for the other half as well. Additionally we implement angular cuts: $\theta_\gamma > (28 - 80x_\gamma)°$ and $\theta_\gamma > (9.2 - 9x_\gamma)°$ for FEMC and STIC regions respectively. For further details, see Ref. [16].

perform a $\Delta\chi^2$ test for the binned x_γ distribution. We exclude the first bin and consider other 19 bins for the analysis. The $\Delta\chi^2$ for this case is defined as:

$$\Delta\chi^2 = \sum_{i=1}^{19} \left(\frac{N_{\rm obs} - (S(m_\chi, \Lambda) + B)}{\sqrt{S(m_\chi, \Lambda) + B}} \right)^2 , \tag{6.46}$$

where, $N_{\rm obs}$ is the number of events observed in each bin, S and B are number of signal and background events post detector efficiencies. The DOF for the binned $\Delta\chi^2$ analysis is $N - M = 19 - 2 = 17$, where, N is the number of bins and M is the number of model parameters. For 17 dofs, the $\Delta\chi^2$ value corresponding to 68% C.L. and 95% C.L. are

19.514 and 27.587 respectively. Fig. 6.17 shows, for low mass regime, the Λ cutoff is around 180 GeV and 140 GeV at 68% C.L. and 95% C.L. respectively.

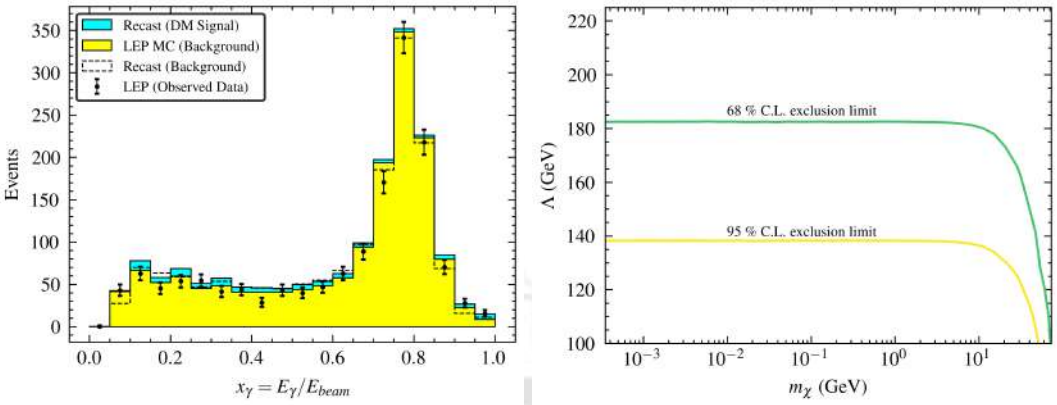

FIGURE 6.17: *Left:* Binned x_γ distribution for LEP studies corresponding to $\mathfrak{L}_{int} = 650\ \text{pb}^{-1}$. The DM signal corresponds to $\chi\overline{\chi}\gamma$ production for the benchmark $m_\chi = 1.37$ MeV, $\Lambda = 0.23$ TeV. *Right:* 68% C.L. and 95% C.L exclusion limits from LEP recast study on the $m_\chi - \Lambda$ plane.

6.E Recasting Limits from the LHC

In the previous segment, we successfully recast the LEP analysis to explore its implications for our model. Building on that foundation, our focus now shifts to recasting specific LHC studies that investigate particle production processes associated with MET. By leveraging existing analyses, we aim to establish robust constraints on our model, further refining its compatibility with current experimental data. Within this recast framework, we further provide projected 95% C.L. exclusion limits for the HL-LHC.

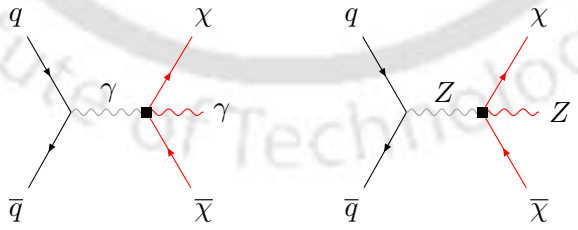

FIGURE 6.18: Feynman diagrams of mono-γ (*left*) and dilepton + MET (via Z decay to leptons, *right*) signals at the LHC.

Recasting LHC 13 TeV Analyses We consider two possible DM signal processes in the context of the LHC viz. mono-γ and dilepton + MET (mono-Z production followed by decay to leptons) shown in Fig. 6.18. There have been searches at the LHC regarding

these signal channels in the context of different models. In order to obtain a limit on our parameter space from the experimental results, we recast the experimental analysis in the context of our model using `CheckMATE2` [585], which is based on `Delphes3` and uses the CL_S method [586] to provide 95% C.L. exclusion limits. For the mono-γ process i.e. $pp \to \chi\overline{\chi}\gamma$, we recast the ATLAS analysis [587] at $\sqrt{s} = 13$ TeV (at an integrated luminosity of 36.1 fb^{-1}) using the `atlas_1704_03848` analysis of `CheckMATE2`. The signal regions are same as [587]. Event processes are generated at different benchmarks throughout the $m_\chi - \Lambda$ parameter space in `MG5_aMC`, showered in `Pythia8`, and then fed to `CheckMATE2` which recasts the experimental analysis results using custom `Delphes3` cards for different signal regions to provide the exclusion limits. For the mono-γ signal, $\Lambda < 800$ GeV is excluded by the LHC recast for the low mass regime. A similar analysis is done for dilepton + MET signal arising from the process $pp \to \chi\overline{\chi}Z(l^+l^-)$. We recast the ATLAS analysis [588] at $\sqrt{s} = 13$ TeV (at an integrated luminosity of 139 fb^{-1}) using the `atlas_1908_08215` analysis of `CheckMATE2`. The exclusion limit is less stringent compared to mono-γ case and is also shown in Fig. 6.19. We conclude that our analysis regime *i.e.* $\Lambda > 1$ TeV is safe from the bounds from the recast of experimental results of the LHC experiments.

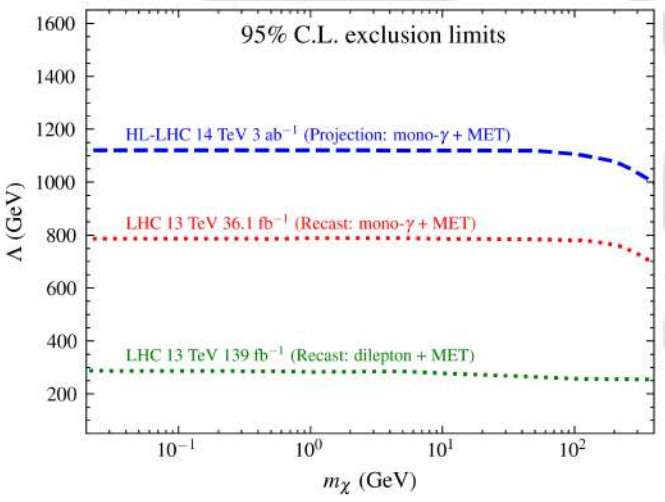

FIGURE 6.19: 95% C.L. exclusion limits from the LHC recast and HL-LHC projection study on the $m_\chi - \Lambda$ plane.

Projecting HL-LHC Limits To project exclusion limits for the future HL-LHC run at a CM energy of 14 TeV with an integrated luminosity of 3 ab^{-1}, we adopt the same signal regions (SRs) as those defined in Ref. [587]. Background event yields in each SR are estimated for 14 TeV and 3 ab^{-1} using `MG5_aMC`, in conjunction with the

`atlas_1704_03848` analysis card implemented in `CheckMATE2`. The expected 95% C.L. signal upper limit, S_{95}, in each SR is scaled by a factor of $\sqrt{R_B}$, where R_B is the ratio of background event yields at 14 TeV with 3 ab^{-1} to those at 13 TeV with 36.1 fb^{-1}. The exclusion is quantified using the parameter r, defined as: $r = (S - 1.64 \cdot \Delta S)/S_{95}$, where S and ΔS denote the predicted signal yield and its associated uncertainty for a given parameter point in a specific SR. A value of $r > 1$ indicates exclusion at 95% C.L. The projected HL-LHC exclusion reach is presented in Fig. 6.19. In the low-mass regime, the 95% C.L. exclusion limit extends up to $\Lambda \sim 1.1$ TeV.

6.F Validity of the EFT Approach

The effective theory realization of a NP scenario relies on a perturbative expansion of the production cross section in inverse powers of the NP scale, Λ. At the amplitude level, the EFT contribution can be expressed as

$$\mathcal{A} = \sum_d \widetilde{A}_d \left(\frac{p}{\Lambda}\right)^{d-4}, \tag{6.47}$$

where d denotes the canonical dimension of the effective operator and p represents the typical momentum scale of the process. The perturbative expansion is well-defined only if the expansion parameter is sufficiently small, i.e.

$$p < \Lambda, \tag{6.48}$$

ensuring the convergence of the series and thereby the validity of the EFT description [589]. A general requirement for EFT validity is that the cutoff scale should lie above the largest energy scale probed in the process under consideration. In the context of the early Universe, where DM production is governed by the thermal bath after reheating, the highest relevant energy scale is the reheating temperature $T_{\rm RH}$. The EFT description remains valid only if

$$\Lambda > T_{\rm RH} \gtrsim m_{\rm DM}, \tag{6.49}$$

ensuring that the mediator responsible for DM interactions is not kinematically accessible and that the EFT consistently captures the dynamics of DM production without reference to the details of the UV completion. At collider experiments, the same principle applies:

the EFT expansion is justified only if the accessible momenta remain below the cutoff scale. For lepton colliders, the maximum momentum transfer is set by the CM energy, $p \sim \sqrt{s}$. Thus, the validity condition reduces to

$$\sqrt{s} < \Lambda. \tag{6.50}$$

In the case of the ILC, where we consider $\sqrt{s} = 1$ TeV, the EFT analysis is self-consistent only if the new physics scale satisfies $\Lambda > 1$ TeV. This guarantees that higher-dimensional operator contributions remain perturbative, while the underlying UV completion remains safely decoupled at the energies probed by the collider.

6.G Relevant Annihilation Cross Sections

Here we report the annihilation cross-sections of a pair of SM states into a pair of spin-0 DM of mass m_Φ

$$\sigma_{\gamma\gamma\to\Phi\Phi} = \frac{s}{4\pi\Lambda_{\rm NP}^4}\sqrt{1-4\,m_\Phi^2/s}\,, \tag{6.51}$$

$$\sigma_{VV\to\Phi\Phi} = \frac{s}{9\pi\Lambda^4}\sqrt{\frac{1-4\,m_\Phi^2/s}{1-4\,m_V^2/s}}\left(1-4\,m_V^2/s+6\,(m_V^2/s)^2\right), \tag{6.52}$$

a pair of spin-1/2 DM of mass m_χ

$$\sigma_{\gamma\gamma\to\chi\overline{\chi}} = \frac{s^2}{4\pi\Lambda_{\rm NP}^6}(1-4\,m_\chi^2/s)^{3/2}\,, \tag{6.53}$$

$$\sigma_{VV\to\chi\overline{\chi}} = \frac{s^2}{9\pi\Lambda^6}\frac{(1-4\,m_\chi^2/s)^{3/2}}{(1-4\,m_V^2/s)^{1/2}}\left(1-4\,m_V^2/s+6(m_V^2/s)^2\right), \tag{6.54}$$

and into a pair of spin-1 DM of mass m_X

$$\sigma_{\gamma\gamma\to XX} = \frac{s^3}{240\pi\,\Lambda_{\rm NP}^4\,m_X^4}\sqrt{1-4\,m_X^2/s}\left(17-36\,m_X^2/s+292\,(m_X^2/s)^2\right), \tag{6.55}$$

$$\sigma_{VV\to XX} = \frac{s^3}{540\pi\Lambda_{\rm NP}^4 m_X^4}\sqrt{\frac{s-4m_X^2}{s-4m_V^2}}\Big[17-36(m_X^2/s)+292(m_X^2/s)^2-2(m_X^2/s)$$
$$\left(568(m_X^2/s)^2-24(m_X^2/s)+23\right)+4(m_X^2/s)^2\left(688(m_X^2/s)^2-84(m_X^2/s)+23\right)\Big], \tag{6.56}$$

where $V = \{W, Z\}$ represents the SM massive gauge bosons. These cross-sections are utilized to compute the reaction density $\gamma_{\rm DM}$ following Eq. (6.43) outlined in App. 6.B, substituting the upper limit of integration with $s = \Lambda_{\rm NP}^2$ to appropriately maintain EFT validity.

Chapter 7

Summary and Future Prospects

"We are still groping in the dark, but every now and then we strike a match."
Denis Diderot

In this thesis, we explored various applications of EFT frameowork as a powerful and model-independent tool to probe BSM physics at future sensitivities of collider experiments. Motivated by the absence of direct evidence for new resonances at the TeV scale, EFTs provide a systematic approach to encode the effects of heavy NP existing at a higher scale, via higher dimensional effective operators constructed from the fields of the lower energy theory, abiding by the low scale symmetry. The construction and implications of SM alongwith its shortcomings is discussed elaborately in Chap. 1, which helps us to take up a detailed overview of the construction and utility of EFTs, with particular emphasis on the SMEFT and DMEFT frameworks in Chap. 2, which have been used extensively in the research papers that constitute the following sections. The SMEFT framework allowed us to parametrize deviations in Higgs and flavor observables, while DMEFT enabled us to incorporate DM as an extension of the SM in a model-independent way. We detailed about the construction of operators of each framework and also introduced the idea of matching with UV complete scenarios. In Chap. 3, we presented a systematic discussion of collider phenomenology, including the essential differences between hadron and lepton colliders, particle detection strategies, and statistical methods used in data analysis. We provided a detailed description of the collider simulation pipeline, which forms the backbone of all phenomenological analyses carried out in this thesis. The main content of the research works included in this thesis staters

from Chap. 4. Here we discuss the applications of the concepts developed in context of Higgs physics, where we performed a comprehensive study of Higgs-gauge boson interactions using SMEFT. We focused our studies on the associated production of the Higgs boson with a Z boson (Zh production mode) at the HL-LHC and future lepton colliders like ILC and FCC-ee. By incorptating operators modifying $qqZ/qqZh$ structures as well as hVV modifiers of both CP-even and CP-odd kind, we quantified deviations in cross sections and kinematic observables from that of a pure SM case. A detailed collider analysis, including cut-based and machine learning techniques, demonstrated that future colliders can significantly improve sensitivity to anomalous Higgs couplings. Furthermore, we explored optimal observables and asymmetries, showing how presence of beam polarization and clean experimental environments of lepton colliders provide enhanced precision in extracting EFT coefficients. In Chap. 5, we investigated cLFV mediated via four-fermion interactions within the SMEFT framework. By studying processes such as $e^+e^- \to e\tau/\mu\tau$, we demonstrated that future facilities like CLiC can probe flavor violating operators with sensitivities far exceeding current bounds from τ decay branching ratio measurements. In addition, we analyzed top quark FCNC interactions in presence of cLFV at the proposed μTRISTAN collider, showing that such specialized setups can provide competitive and complementary constraints on rare top decays and FCNCs. A significant part of this thesis was devoted to connecting collider observables with early Universe physics using DMEFT, studied in Chap. 6. We studied UV freeze-in DM scenarios, where DM genesis occur via higher dimensional effective operators and the DM yield carries the seed of the early Universe dynamics. By incorporating reheating dynamics, we established a novel connection between collider signatures such as mono-γ and cosmological parameters like $T_{\rm RH}$ as well as the preferred inflaton decay mode. Our analysis demonstrated that future lepton colliders can act as indirect probes of the pre-BBN era, providing sensitivity to otherwise inaccessible regions of parameter space. We also performed detailed signal-background analyses and recast studies, highlighting the complementarity between collider searches, astrophysical constraints, and cosmological considerations. Overall, the results presented in this thesis reinforce the importance of EFTs as a unifying framework that bridges collider phenomenology and fundamental theoretical frameworks.

Future Prospects and Directions The work presented in this thesis opens several promising avenues for future research, some of which are outlined below:

- On the theoretical front, the high precision achievable at future colliders necessitates extending the EFT framework beyond dimension 6 operators. In particular, incorporating $O(\Lambda^4)$ corrections becomes essential, as such contributions, especially in processes like Higgs production can receive significant effects from dimension 8 SMEFT operators through their interference with the SM. A systematic inclusion of these effects will be crucial for consistent and precise interpretations in future studies.

- Another important direction is the exploration of EFT validity and its matching to UV complete models. Identifying specific UV scenarios that give rise to the observed operator structures can provide additional constraints on the allowed parameter space, thereby improving the precision with which EFT parameters are determined. In particular, UV completions that induce flavor violating interactions constitute a promising avenue, as the underlying flavor structure of such models can leave characteristic imprints on the EFT parameter space.

- In the collider analysis context, several improvements can be envisaged. The inclusion of higher order (NLO/NNLO) corrections in the simulation framework and inclusion of systematic uncertainties will be crucial for realistic projections. Furthermore, incorporation of modern machine learning techniques can not only enhance signal-background discrimination but also enable statistical inference, thereby providing a powerful framework for extracting EFT parameters in complex settings.

- Finally, in the context of DM, the connection between collider physics and cosmology can be further strengthened by exploring more general reheating scenarios, including non-standard expansion histories and specific inflationary models that govern the reheating dynamics. Such studies have the potential to transform collider experiments into probes of the earliest moments of the Universe. Additionally, incorporating gravitational wave signatures arising from early Universe dynamics can open new avenues for multi-messenger probes of NP, providing strong complementarity with collider-based searches.

In conclusion, the synergy between EFT techniques, collider experiments, and cosmological observations provides a compelling framework to explore BSM physics. With the advent of next-generation experiments and advancements in theoretical constructions, the prospects for uncovering NP avenues remain both promising as well as exciting.

Bibliography

[1] M. Cirelli, A. Strumia and J. Zupan, *Dark Matter*, 2406.01705.

[2] M.D. Schwartz, *TASI lectures on collider physics.*, in *Theoretical Advanced Study Institute in Elementary Particle Physics: Anticipating the Next Discoveries in Particle Physics*, pp. 65–100, 2018, DOI [1709.04533].

[3] L.R.F. Castillo, *The atlas and cms detectors*, in *The Search and Discovery of the Higgs Boson*, 2053-2571, pp. 4–1 to 4–8, Morgan Claypool Publishers (2015), DOI.

[4] ATLAS collaboration, *Measurements of WH and ZH production in the $H \to b\bar{b}$ decay channel in pp collisions at 13 TeV with the ATLAS detector*, *Eur. Phys. J. C* **81** (2021) 178 [2007.02873].

[5] CMS collaboration, *Observation of Higgs boson decay to bottom quarks*, *Phys. Rev. Lett.* **121** (2018) 121801 [1808.08242].

[6] ATLAS collaboration, *A detailed map of Higgs boson interactions by the ATLAS experiment ten years after the discovery*, *Nature* **607** (2022) 52 [2207.00092].

[7] CMS collaboration, *A portrait of the Higgs boson by the CMS experiment ten years after the discovery.*, *Nature* **607** (2022) 60 [2207.00043].

[8] O. Brüning and L. Rossi, eds., *The High Luminosity Large Hadron Collider: the new machine for illuminating the mysteries of Universe*, vol. 24 (2015), 10.1142/9581.

[9] Particle Data Group collaboration, *Review of particle physics*, *Phys. Rev. D* **110** (2024) 030001.

[10] P.F. de Salas, D.V. Forero, S. Gariazzo, P. Martínez-Miravé, O. Mena, C.A. Ternes et al., *2020 global reassessment of the neutrino oscillation picture*, *JHEP* **02** (2021) 071 [2006.11237].

[11] B. Grzadkowski, M. Iskrzynski, M. Misiak and J. Rosiek, *Dimension-Six Terms in the Standard Model Lagrangian*, *JHEP* **10** (2010) 085 [1008.4884].

[12] Y. Liao and X.-D. Ma, *Renormalization Group Evolution of Dimension-seven Baryon- and Lepton-number-violating Operators*, *JHEP* **11** (2016) 043 [1607.07309].

[13] OPAL collaboration, *Search for lepton flavor violation in e+ e- collisions at s**(1/2) = 189-GeV - 209-GeV*, *Phys. Lett. B* **519** (2001) 23 [hep-ex/0109011].

[14] W. Buchmuller and D. Wyler, *Effective Lagrangian Analysis of New Interactions and Flavor Conservation*, *Nucl. Phys. B* **268** (1986) 621.

[15] CMS collaboration, *Search for charged-lepton flavor violation in top quark production and decay in pp collisions at* $\sqrt{s}$ *= 13 TeV*, *JHEP* **06** (2022) 082 [2201.07859].

[16] P.J. Fox, R. Harnik, J. Kopp and Y. Tsai, *LEP Shines Light on Dark Matter*, *Phys. Rev. D* **84** (2011) 014028 [1103.0240].

[17] S. Weinberg, *A Model of Leptons*, *Phys. Rev. Lett.* **19** (1967) 1264.

[18] ATLAS collaboration, *Observation of a new particle in the search for the Standard Model Higgs boson with the ATLAS detector at the LHC*, *Phys. Lett. B* **716** (2012) 1 [1207.7214].

[19] CMS collaboration, *Observation of a New Boson at a Mass of 125 GeV with the CMS Experiment at the LHC*, *Phys. Lett. B* **716** (2012) 30 [1207.7235].

[20] P.W. Higgs, *Broken Symmetries and the Masses of Gauge Bosons*, *Phys. Rev. Lett.* **13** (1964) 508.

[21] E. Rutherford, *The scattering of alpha and beta particles by matter and the structure of the atom*, *Phil. Mag. Ser. 6* **21** (1911) 669.

[22] J.J. Thomson, *Cathode rays*, *Phil. Mag. Ser. 5* **44** (1897) 293.

[23] A. Einstein, *On a heuristic viewpoint concerning the production and transformation of light*, *Annalen der Physik* **17** (1905) 132.

[24] CDF collaboration, *Observation of top quark production in* $\bar{p}p$ *collisions*, *Phys. Rev. Lett.* **74** (1995) 2626 [hep-ex/9503002].

[25] D0 collaboration, *Observation of the top quark*, *Phys. Rev. Lett.* **74** (1995) 2632 [hep-ex/9503003].

[26] UA1 collaboration, *Experimental Observation of Isolated Large Transverse Energy Electrons with Associated Missing Energy at* $\sqrt{s}$ *= 540 GeV*, *Phys. Lett. B* **122** (1983) 103.

[27] UA2 collaboration, *Observation of Single Isolated Electrons of High Transverse Momentum in Events with Missing Transverse Energy at the CERN anti-p p Collider*, *Phys. Lett. B* **122** (1983) 476.

[28] UA1 collaboration, *Experimental Observation of Lepton Pairs of Invariant Mass Around 95-GeV/c**2 at the CERN SPS Collider*, *Phys. Lett. B* **126** (1983) 398.

[29] M. Kobayashi and T. Maskawa, *CP Violation in the Renormalizable Theory of Weak Interaction*, *Prog. Theor. Phys.* **49** (1973) 652.

[30] G. Bertone, D. Hooper and J. Silk, *Particle dark matter: Evidence, candidates and constraints*, *Phys. Rept.* **405** (2005) 279 [hep-ph/0404175].

[31] F. Zwicky, *On the Masses of Nebulae and of Clusters of Nebulae*, *Astrophys. J.* **86** (1937) 217.

[32] Y. Sofue and V. Rubin, *Rotation curves of spiral galaxies*, *Ann. Rev. Astron. Astrophys.* **39** (2001) 137 [astro-ph/0010594].

[33] E. Hayashi and S.D.M. White, *How Rare is the Bullet Cluster?*, *Mon. Not. Roy. Astron. Soc.* **370** (2006) L38 [astro-ph/0604443].

[34] Planck collaboration, *Planck 2018 results. VI. Cosmological parameters*, *Astron. Astrophys.* **641** (2020) A6 [1807.06209].

[35] Super-Kamiokande collaboration, *Study of the atmospheric neutrino flux in the multi-GeV energy range*, *Phys. Lett. B* **436** (1998) 33 [hep-ex/9805006].

[36] Super-Kamiokande collaboration, *Evidence for oscillation of atmospheric neutrinos*, *Phys. Rev. Lett.* **81** (1998) 1562 [hep-ex/9807003].

[37] SNO collaboration, *Direct evidence for neutrino flavor transformation from neutral current interactions in the Sudbury Neutrino Observatory*, *Phys. Rev. Lett.* **89** (2002) 011301 [nucl-ex/0204008].

[38] KamLAND collaboration, *First results from KamLAND: Evidence for reactor anti-neutrino disappearance*, *Phys. Rev. Lett.* **90** (2003) 021802 [hep-ex/0212021].

[39] F. Jegerlehner, *The hierarchy problem of the electroweak Standard Model revisited*, 1305.6652.

[40] G. Burdman, *New solutions to the hierarchy problem*, *Braz. J. Phys.* **37** (2007) 506 [hep-ph/0703194].

[41] N. Arkani-Hamed, S. Dimopoulos and G.R. Dvali, *The Hierarchy problem and new dimensions at a millimeter*, *Phys. Lett. B* **429** (1998) 263 [hep-ph/9803315].

[42] M. Sher, *Electroweak Higgs Potentials and Vacuum Stability*, *Phys. Rept.* **179** (1989) 273.

[43] G. Isidori, G. Ridolfi and A. Strumia, *On the metastability of the standard model vacuum*, *Nucl. Phys. B* **609** (2001) 387 [hep-ph/0104016].

[44] J. Elias-Miro, J.R. Espinosa, G.F. Giudice, G. Isidori, A. Riotto and A. Strumia, *Higgs mass implications on the stability of the electroweak vacuum*, *Phys. Lett. B* **709** (2012) 222 [1112.3022].

[45] G. Hiller, T. Höhne, D.F. Litim and T. Steudtner, *Vacuum stability in the Standard Model and beyond*, *Phys. Rev. D* **110** (2024) 115017 [2401.08811].

[46] S.M. Barr, *The Strong CP Problem in Unified Models*, *Phys. Rev. D* **23** (1981) 2434.

[47] S.M. Barr, *Solving the Strong CP Problem Without the Peccei-Quinn Symmetry*, *Phys. Rev. Lett.* **53** (1984) 329.

[48] M. Dine and A. Kusenko, *The Origin of the matter - antimatter asymmetry*, *Rev. Mod. Phys.* **76** (2003) 1 [hep-ph/0303065].

[49] A.D. Sakharov, *Violation of CP Invariance, C asymmetry, and baryon asymmetry of the universe*, *Pisma Zh. Eksp. Teor. Fiz.* **5** (1967) 32.

[50] W. Altmannshofer and P. Stangl, *New physics in rare B decays after Moriond 2021*, *Eur. Phys. J. C* **81** (2021) 952 [2103.13370].

[51] LHCb collaboration, *Tests of lepton universality using $B^0 \to K^0_S \ell^+ \ell^-$ and $B^+ \to K^{*+} \ell^+ \ell^-$ decays*, *Phys. Rev. Lett.* **128** (2022) 191802 [2110.09501].

[52] LHCb collaboration, *Test of lepton universality in beauty-quark decays*, *Nature Phys.* **18** (2022) 277 [2103.11769].

[53] LHCb collaboration, *Measurement of Form-Factor-Independent Observables in the Decay $B^0 \to K^{*0}\mu^+\mu^-$*, *Phys. Rev. Lett.* **111** (2013) 191801 [1308.1707].

[54] Heavy Flavor Averaging Group (HFLAV) collaboration, *Averages of b-hadron, c-hadron, and τ-lepton properties as of 2023*, *Phys. Rev. D* **113** (2026) 012008 [2411.18639].

[55] A. Del Popolo, *Nonbaryonic Dark Matter in Cosmology*, *Int. J. Mod. Phys. D* **23** (2014) 1430005 [1305.0456].

[56] A. Ibarra, M. Reichard and G. Tomar, *Probing dark matter electromagnetic properties in direct detection experiments*, *JCAP* **02** (2025) 072 [2408.15760].

[57] B. Barman, S. Bhattacharya, S. Jahedi, D. Pradhan and A. Sarkar, *Lepton collider as a window to reheating via freezing in dark matter detection. Part I*, *Phys. Lett. B* **869** (2025) 139863 [2406.11963].

[58] B. Barman, S. Bhattacharya, S. Jahedi, D. Pradhan and A. Sarkar, *Lepton collider as a window to reheating via freezing in dark matter detection. Part II*, *JHEP* **07** (2025) 157 [2410.18198].

[59] D. Feldman, Z. Liu and P. Nath, *The Stueckelberg Z-prime Extension with Kinetic Mixing and Milli-Charged Dark Matter From the Hidden Sector*, *Phys. Rev. D* **75** (2007) 115001 [hep-ph/0702123].

[60] Z. Bogorad and N. Toro, *Ultralight millicharged dark matter via misalignment*, *JHEP* **07** (2022) 035 [2112.11476].

[61] K. Griest, A.M. Cieplak and M.J. Lehner, *Experimental Limits on Primordial Black Hole Dark Matter from the First 2 yr of Kepler Data*, *Astrophys. J.* **786** (2014) 158 [1307.5798].

[62] W. Hu, R. Barkana and A. Gruzinov, *Cold and fuzzy dark matter*, *Phys. Rev. Lett.* **85** (2000) 1158 [astro-ph/0003365].

[63] G. Jungman, M. Kamionkowski and K. Griest, *Supersymmetric dark matter*, *Phys. Rept.* **267** (1996) 195 [hep-ph/9506380].

[64] L.J. Hall, K. Jedamzik, J. March-Russell and S.M. West, *Freeze-In Production of FIMP Dark Matter*, *JHEP* **03** (2010) 080 [0911.1120].

[65] S. Profumo, *An Introduction to Particle Dark Matter*, World Scientific (2017), 10.1142/q0001.

[66] F. Elahi, C. Kolda and J. Unwin, *UltraViolet Freeze-in*, *JHEP* **03** (2015) 048 [1410.6157].

[67] M.W. Goodman and E. Witten, *Detectability of Certain Dark Matter Candidates*, *Phys. Rev. D* **31** (1985) 3059.

[68] A.K. Drukier, K. Freese and D.N. Spergel, *Detecting Cold Dark Matter Candidates*, *Phys. Rev. D* **33** (1986) 3495.

[69] A. Bottino, V. de Alfaro, N. Fornengo, S. Mignola and S. Scopel, *On the neutralino as dark matter candidate. 2. Direct detection.*, *Astropart. Phys.* **2** (1994) 77 [hep-ph/9309219].

[70] LZ collaboration, *Dark Matter Search Results from 4.2 Tonne-Years of Exposure of the LUX-ZEPLIN (LZ) Experiment*, *Phys. Rev. Lett.* **135** (2025) 011802 [2410.17036].

[71] J.E. Gunn, B.W. Lee, I. Lerche, D.N. Schramm and G. Steigman, *Some Astrophysical Consequences of the Existence of a Heavy Stable Neutral Lepton*, *Astrophys. J.* **223** (1978) 1015.

[72] Fermi-LAT collaboration, *Fermi-LAT Observations of High-Energy γ-Ray Emission Toward the Galactic Center*, *Astrophys. J.* **819** (2016) 44 [1511.02938].

[73] C. Thorpe-Morgan, D. Malyshev, C.-A. Stegen, A. Santangelo and J. Jochum, *Annihilating dark matter search with 12 yr of Fermi LAT data in nearby galaxy clusters*, *Mon. Not. Roy. Astron. Soc.* **502** (2021) 4039 [2010.11006].

[74] O.S. Bruning, P. Collier, P. Lebrun, S. Myers, R. Ostojic, J. Poole et al., eds., *LHC Design Report Vol.1: The LHC Main Ring*, .

[75] O. Buning, P. Collier, P. Lebrun, S. Myers, R. Ostojic, J. Poole et al., eds., *LHC Design Report. 2. The LHC infrastructure and general services*, .

[76] M. Benedikt, P. Collier, V. Mertens, J. Poole and K. Schindl, eds., *LHC Design Report. 3. The LHC injector chain*, .

[77] Linear Collider Vision collaboration, *A Linear Collider Vision for the Future of Particle Physics*, 2503.19983.

[78] R.N. Mohapatra and G. Senjanovic, *Neutrino Mass and Spontaneous Parity Nonconservation*, *Phys. Rev. Lett.* **44** (1980) 912.

[79] W. Buchmuller, R.D. Peccei and T. Yanagida, *Leptogenesis as the origin of matter*, *Ann. Rev. Nucl. Part. Sci.* **55** (2005) 311 [hep-ph/0502169].

[80] G. Altarelli and F. Feruglio, *Neutrino masses and mixings: A theoretical perspective*, *Phys. Rept.* **320** (1999) 295.

[81] M. Magg and C. Wetterich, *Neutrino Mass Problem and Gauge Hierarchy*, *Phys. Lett. B* **94** (1980) 61.

[82] R. Foot, H. Lew, X.G. He and G.C. Joshi, *Seesaw Neutrino Masses Induced by a Triplet of Leptons*, *Z. Phys. C* **44** (1989) 441.

[83] MEG collaboration, *Search for the lepton flavour violating decay $\mu^+ \to e^+\gamma$ with the full dataset of the MEG experiment*, *Eur. Phys. J. C* **76** (2016) 434 [1605.05081].

[84] MEG II collaboration, *A search for $^+ \to e^+$ with the first dataset of the MEG II experiment*, *Eur. Phys. J. C* **84** (2024) 216 [2310.12614].

[85] R.S. Van Dyck, P.B. Schwinberg and H.G. Dehmelt, *New High Precision Comparison of electron and Positron G Factors*, *Phys. Rev. Lett.* **59** (1987) 26.

[86] T.S. Roussy et al., *An improved bound on the electron's electric dipole moment*, *Science* **381** (2023) adg4084 [2212.11841].

[87] Muon g-2 collaboration, *Measurement of the negative muon anomalous magnetic moment to 0.7 ppm*, *Phys. Rev. Lett.* **92** (2004) 161802 [hep-ex/0401008].

[88] Muon (g-2) collaboration, *An Improved Limit on the Muon Electric Dipole Moment*, *Phys. Rev. D* **80** (2009) 052008 [0811.1207].

[89] ATLAS collaboration, *Observation of the $\gamma\gamma \to \tau\tau$ Process in Pb+Pb Collisions and Constraints on the τ-Lepton Anomalous Magnetic Moment with the ATLAS Detector*, *Phys. Rev. Lett.* **131** (2023) 151802 [2204.13478].

[90] Belle collaboration, *An improved search for the electric dipole moment of the τ lepton*, *JHEP* **04** (2022) 110 [2108.11543].

[91] A.J. Buras, *Weak Hamiltonian, CP violation and rare decays*, in *Les Houches Summer School in Theoretical Physics, Session 68: Probing the Standard Model of Particle Interactions*, pp. 281–539, 6, 1998 [hep-ph/9806471].

[92] G. Isidori, Y. Nir and G. Perez, *Flavor Physics Constraints for Physics Beyond the Standard Model*, *Ann. Rev. Nucl. Part. Sci.* **60** (2010) 355 [1002.0900].

[93] R. Davis, Jr., D.S. Harmer and K.C. Hoffman, *Search for neutrinos from the sun*, *Phys. Rev. Lett.* **20** (1968) 1205.

[94] B. Pontecorvo, *Mesonium and Antimesonium*, *Sov. Phys. JETP* **6** (1958) 429.

[95] B. Pontecorvo, *Inverse Beta Processes and Nonconservation of Lepton Charge*, *Sov. Phys. JETP* **7** (1958) 172.

[96] B. Pontecorvo, *Neutrino Experiments and the Problem of Conservation of Leptonic Charge*, *Sov. Phys. JETP* **26** (1968) 984.

[97] Z. Maki, M. Nakagawa and S. Sakata, *Remarks on the unified model of elementary particles*, *Prog. Theor. Phys.* **28** (1962) 870.

[98] KATRIN collaboration, *Direct neutrino-mass measurement based on 259 days of KATRIN data*, *Science* **388** (2025) adq9592 [2406.13516].

[99] S. Weinberg, *Baryon and Lepton Nonconserving Processes*, *Phys. Rev. Lett.* **43** (1979) 1566.

[100] G. Anamiati, O. Castillo-Felisola, R.M. Fonseca, J.C. Helo and M. Hirsch, *High-dimensional neutrino masses*, *JHEP* **12** (2018) 066 [1806.07264].

[101] B. Fuks, J. Neundorf, K. Peters, R. Ruiz and M. Saimpert, *Probing the Weinberg operator at colliders*, *Phys. Rev. D* **103** (2021) 115014 [2012.09882].

[102] S. Bhattacharya, S. Datta and A. Sarkar, *Probing ΔL=2 lepton number violating SMEFT operators at the same-sign muon collider*, *Phys. Rev. D* **113** (2026) 055043 [2505.20936].

[103] KATRIN collaboration, *Direct neutrino-mass measurement with sub-electronvolt sensitivity*, *Nature Phys.* **18** (2022) 160 [2105.08533].

[104] K. Assamagan et al., *Upper limit of the muon-neutrino mass and charged pion mass from momentum analysis of a surface muon beam*, *Phys. Rev. D* **53** (1996) 6065.

[105] ALEPH collaboration, *An Upper limit on the tau-neutrino mass from three-prong and five-prong tau decays*, *Eur. Phys. J. C* **2** (1998) 395.

[106] A. Zee, *A Theory of Lepton Number Violation, Neutrino Majorana Mass, and Oscillation*, *Phys. Lett. B* **93** (1980) 389.

[107] E. Ma, *Pathways to naturally small neutrino masses*, *Phys. Rev. Lett.* **81** (1998) 1171 [hep-ph/9805219].

[108] BaBar collaboration, *Searches for Lepton Flavor Violation in the Decays $\tau^{\pm} \to e^{\pm}\gamma$ and $\tau^{\pm} \to \mu^{\pm}\gamma$*, *Phys. Rev. Lett.* **104** (2010) 021802 [0908.2381].

[109] Belle collaboration, *Search for lepton-flavor-violating tau-lepton decays to $\ell\gamma$ at Belle*, *JHEP* **10** (2021) 19 [2103.12994].

[110] SINDRUM collaboration, *Search for the Decay $\mu^+ \to e^+e^+e^-$*, *Nucl. Phys. B* **299** (1988) 1.

[111] K. Hayasaka et al., *Search for Lepton Flavor Violating Tau Decays into Three Leptons with 719 Million Produced Tau+Tau- Pairs*, *Phys. Lett. B* **687** (2010) 139 [1001.3221].

[112] A. Badertscher et al., *New Upper Limits for Muon - Electron Conversion in Sulfur*, *Lett. Nuovo Cim.* **28** (1980) 401.

[113] SINDRUM II collaboration, *Test of lepton flavor conservation in mu —> e conversion on titanium*, *Phys. Lett. B* **317** (1993) 631.

[114] SINDRUM II collaboration, *Improved limit on the branching ratio of mu —> e conversion on lead*, *Phys. Rev. Lett.* **76** (1996) 200.

[115] SINDRUM II collaboration, *A Search for muon to electron conversion in muonic gold*, *Eur. Phys. J. C* **47** (2006) 337.

[116] S. Davidson, B. Echenard, R.H. Bernstein, J. Heeck and D.G. Hitlin, *Charged Lepton Flavor Violation*, 2209.00142.

[117] BaBar collaboration, *Search for the reactions $e^+e^- \to \mu^+\tau^-$ and $e^+e^- \to e^+\tau^-$*, *Phys. Rev. D* **75** (2007) 031103 [hep-ex/0607044].

[118] ATLAS collaboration, *Search for the charged-lepton-flavor-violating decay $Z \to e\mu$ in pp collisions at $\sqrt{s} = 13$ TeV with the ATLAS detector*, *Phys. Rev. D* **108** (2023) 032015 [2204.10783].

[119] ATLAS collaboration, *Search for lepton-flavor-violation in Z-boson decays with τ-leptons with the ATLAS detector*, *Phys. Rev. Lett.* **127** (2022) 271801 [2105.12491].

[120] Belle collaboration, *Search for lepton flavor violating tau- decays into l- eta, l- eta-prime and l- pi0*, *Phys. Lett. B* **648** (2007) 341 [hep-ex/0703009].

[121] BaBar collaboration, *Search for Lepton Flavor Violating Decays $\tau^{\pm} \to \ell^{\pm}\pi^0$, $\ell^{\pm}\eta$, $\ell^{\pm}\eta'$*, *Phys. Rev. Lett.* **98** (2007) 061803 [hep-ex/0610067].

[122] Belle collaboration, *Search for lepton-flavor-violating τ decays into a lepton and a vector meson using the full Belle data sample*, *JHEP* **06** (2023) 118 [2301.03768].

[123] Belle collaboration, *Measurement of the $\bar{B} \to X_s\gamma$ Branching Fraction with a Sum of Exclusive Decays*, *Phys. Rev. D* **91** (2015) 052004 [1411.7198].

[124] BaBar collaboration, *Exclusive Measurements of $b \to s\gamma$ Transition Rate and Photon Energy Spectrum*, *Phys. Rev. D* **86** (2012) 052012 [1207.2520].

[125] BaBar collaboration, *Precision Measurement of the $B \to X_s\gamma$ Photon Energy Spectrum, Branching Fraction, and Direct CP Asymmetry $A_{CP}(B \to X_{s+d}\gamma)$*, *Phys. Rev. Lett.* **109** (2012) 191801 [1207.2690].

[126] Belle collaboration, *Evidence for Isospin Violation and Measurement of CP Asymmetries in $B \to K^*(892)\gamma$*, *Phys. Rev. Lett.* **119** (2017) 191802 [1707.00394].

[127] BaBar collaboration, *Measurement of Branching Fractions and CP and Isospin Asymmetries in $B \to K^*(892)\gamma$ Decays*, *Phys. Rev. Lett.* **103** (2009) 211802 [0906.2177].

[128] BELLE collaboration, *Test of lepton flavor universality and search for lepton flavor violation in $B \to K\ell\ell$ decays*, *JHEP* **03** (2021) 105 [1908.01848].

[129] BaBar collaboration, *Direct CP, Lepton Flavor and Isospin Asymmetries in the Decays $B \to K^{(*)}\ell^+\ell^-$*, *Phys. Rev. Lett.* **102** (2009) 091803 [0807.4119].

[130] Belle collaboration, *Measurement of the Differential Branching Fraction and Forward-Backward Asymmetry for $B \to K^{(*)}\ell^+\ell^-$*, *Phys. Rev. Lett.* **103** (2009) 171801 [0904.0770].

[131] LHCb collaboration, *Branching Fraction Measurements of the Rare $B_s^0 \to \phi\mu^+\mu^-$ and $B_s^0 \to f_2'(1525)\mu^+\mu^-$ Decays*, *Phys. Rev. Lett.* **127** (2021) 151801 [2105.14007].

[132] Belle-II collaboration, *Measurement of the B0 lifetime and flavor-oscillation frequency using hadronic decays reconstructed in 2019–2021 Belle II data*, *Phys. Rev. D* **107** (2023) L091102 [2302.12791].

[133] LHCb collaboration, *Precise determination of the B_s^0–$\overline{B}_s^0$ oscillation frequency*, *Nature Phys.* **18** (2022) 1 [2104.04421].

[134] LHCb collaboration, *Measurement of D^0–$\bar{D}^0$ Mixing Parameters and Search for CP Violation Using $D^0 \to K^+\pi^-$ Decays*, *Phys. Rev. Lett.* **111** (2013) 251801 [1309.6534].

[135] NA62 collaboration, *Measurement of the very rare $K^+ \to \pi^+\nu\bar{\nu}$ decay*, *JHEP* **06** (2021) 093 [2103.15389].

[136] CMS collaboration, *Search for flavor-changing neutral current interactions of the top quark mediated by a Higgs boson in proton-proton collisions at 13 TeV*, 2407.15172.

[137] ATLAS collaboration, *Search for flavour-changing neutral-current interactions of a top quark and a gluon in pp collisions at $\sqrt{s} = 13$ TeV with the ATLAS detector*, *Eur. Phys. J. C* **82** (2022) 334 [2112.01302].

[138] ATLAS collaboration, *Search for flavour-changing neutral-current couplings between the top quark and the photon with the ATLAS detector at s=13 TeV*, *Phys. Lett. B* **842** (2023) 137379 [2205.02537].

[139] ATLAS collaboration, *Search for flavor-changing neutral-current couplings between the top quark and the Z boson with proton-proton collisions at s=13 TeV with the ATLAS detector*, *Phys. Rev. D* **108** (2023) 032019 [2301.11605].

[140] ATLAS collaboration, *Search for charged-lepton-flavor violating $\mu\tau qt$ interactions in top-quark production and decay in pp collisions at s=13 TeV with the ATLAS detector at the LHC*, *Phys. Rev. D* **110** (2024) 012014 [2403.06742].

[141] CMS collaboration, *Search for Flavor-Changing Neutral Current Interactions of the Top Quark and Higgs Boson in Final States with Two Photons in Proton-Proton Collisions at $\sqrt{s} = 13$ TeV*, *Phys. Rev. Lett.* **129** (2022) 032001 [2111.02219].

[142] ATLAS collaboration, *Search for flavour-changing neutral-current couplings between the top quark and the Higgs boson in multi-lepton final states in 13 TeV pp collisions with the ATLAS detector*, *Eur. Phys. J. C* **84** (2024) 757 [2404.02123].

[143] S. Weinberg, *Phenomenological Lagrangians*, *Physica A* **96** (1979) 327.

[144] J. Gasser and H. Leutwyler, *Chiral Perturbation Theory to One Loop*, *Annals Phys.* **158** (1984) 142.

[145] W. Heisenberg and H. Euler, *Consequences of Dirac's theory of positrons*, *Z. Phys.* **98** (1936) 714 [physics/0605038].

[146] J. Schwinger, *On gauge invariance and vacuum polarization*, *Phys. Rev.* **82** (1951) 664.

[147] A.V. Manohar, *Effective field theories*, *Lect. Notes Phys.* **479** (1997) 311 [hep-ph/9606222].

[148] B. Henning, X. Lu and H. Murayama, *How to use the Standard Model effective field theory*, *JHEP* **01** (2016) 023 [1412.1837].

[149] A. Drozd, J. Ellis, J. Quevillon and T. You, *The Universal One-Loop Effective Action*, *JHEP* **03** (2016) 180 [1512.03003].

[150] I. Brivio and M. Trott, *The Standard Model as an Effective Field Theory*, *Phys. Rept.* **793** (2019) 1 [1706.08945].

[151] H.E. Haber and G.L. Kane, *The Search for Supersymmetry: Probing Physics Beyond the Standard Model*, *Phys. Rept.* **117** (1985) 75.

[152] G. Buchalla, O. Cata and C. Krause, *A Systematic Approach to the SILH Lagrangian*, *Nucl. Phys. B* **894** (2015) 602 [1412.6356].

[153] LHC Higgs Cross Section Working Group collaboration, *Handbook of LHC Higgs Cross Sections: 3. Higgs Properties*, 1307.1347.

[154] G. Buchalla, O. Catà and C. Krause, *Complete Electroweak Chiral Lagrangian with a Light Higgs at NLO*, *Nucl. Phys. B* **880** (2014) 552 [1307.5017].

[155] E.E. Jenkins, A.V. Manohar and P. Stoffer, *Low-Energy Effective Field Theory below the Electroweak Scale: Operators and Matching*, *JHEP* **03** (2018) 016 [1709.04486].

[156] CMS collaboration, *Measurement of the inclusive and differential WZ production cross sections, polarization angles, and triple gauge couplings in pp collisions at* $\sqrt{s}$ *= 13 TeV*, *JHEP* **07** (2022) 032 [2110.11231].

[157] CMS collaboration, *Measurement of* $W^{\pm}\gamma$ *differential cross sections in proton-proton collisions at* $\sqrt{s}$ *= 13 TeV and effective field theory constraints*, *Phys. Rev. D* **105** (2022) 052003 [2111.13948].

[158] J. de Vries, M. Postma, J. van de Vis and G. White, *Electroweak Baryogenesis and the Standard Model Effective Field Theory*, *JHEP* **01** (2018) 089 [1710.04061].

[159] S. Jahedi, I. Saha and A. Sarkar, *Electroweak phase transition in SMEFT: Gravitational wave and collider complementarity*, 2512.04168.

[160] L. Berthier and M. Trott, *Towards consistent Electroweak Precision Data constraints in the SMEFT*, *JHEP* **05** (2015) 024 [1502.02570].

[161] CMS collaboration, *Search for the lepton-flavor violating decay of the Higgs boson and additional Higgs bosons in the* $e\mu$ *final state in proton-proton collisions at* $\sqrt{s}$ *= 13 TeV*, *Phys. Rev. D* **108** (2023) 072004 [2305.18106].

[162] ATLAS collaboration, *Searches for lepton-flavour-violating decays of the Higgs boson into* $e\tau$ *and* $\mu\tau$ *in* $\sqrt{s} = 13$ *TeV pp collisions with the ATLAS detector*, *JHEP* **07** (2023) 166 [2302.05225].

[163] CMS collaboration, *Search for lepton-flavor violating decays of the Higgs boson in the* $\mu\tau$ *and* $e\tau$ *final states in proton-proton collisions at* $\sqrt{s}$ *= 13 TeV*, *Phys. Rev. D* **104** (2021) 032013 [2105.03007].

[164] J. Kley, T. Theil, E. Venturini and A. Weiler, *Electric dipole moments at one-loop in the dimension-6 SMEFT*, *Eur. Phys. J. C* **82** (2022) 926 [2109.15085].

[165] M. Thomas Arun, K. Deka and T. Srivastava, *Constraining SMEFT BSM scenarios with EWPO and* Δ_{CKM}, *Pramana* **99** (2025) 145 [2301.09273].

[166] A. Azatov, D. Ghosh and A.H. Singh, *Four-fermion operators at dimension 6: Dispersion relations and UV completions*, *Phys. Rev. D* **105** (2022) 115019 [2112.02302].

[167] A.B. Beneito, I, J. Gargalionis, J. Herrero-Garcia, A. Santamaria and M.A. Schmidt, *An EFT approach to baryon number violation: lower limits on the new physics scale and correlations between nucleon decay modes*, *JHEP* **07** (2024) 004 [2312.13361].

[168] L. Lehman, *Extending the Standard Model Effective Field Theory with the Complete Set of Dimension-7 Operators*, *Phys. Rev. D* **90** (2014) 125023 [1410.4193].

[169] S. Bhattacharya and J. Wudka, *Dimension-seven operators in the standard model with right handed neutrinos*, *Phys. Rev. D* **94** (2016) 055022 [1505.05264].

[170] K. Fridell, L. Gráf, J. Harz and C. Hati, *Probing lepton number violation: a comprehensive survey of dimension-7 SMEFT*, *JHEP* **05** (2024) 154 [2306.08709].

[171] C.W. Murphy, *Dimension-8 operators in the Standard Model Effective Field Theory*, *JHEP* **10** (2020) 174 [2005.00059].

[172] H.-L. Li, Z. Ren, J. Shu, M.-L. Xiao, J.-H. Yu and Y.-H. Zheng, *Complete set of dimension-eight operators in the standard model effective field theory*, *Phys. Rev. D* **104** (2021) 015026 [2005.00008].

[173] CMS collaboration, *Measurements of* pp $\to$ ZZ *production cross sections and constraints on anomalous triple gauge couplings at* $\sqrt{s} = 13$ *TeV*, *Eur. Phys. J. C* **81** (2021) 200 [2009.01186].

[174] ATLAS collaboration, *Evidence of pair production of longitudinally polarised vector bosons and study of CP properties in* $ZZ \to 4\ell$ *events with the ATLAS detector at* $\sqrt{s} = 13$ *TeV*, *JHEP* **12** (2023) 107 [2310.04350].

[175] C. Arzt, M.B. Einhorn and J. Wudka, *Patterns of deviation from the standard model*, *Nucl. Phys. B* **433** (1995) 41 [hep-ph/9405214].

[176] S. Bhattacharya and J. Wudka, *Effective theories with dark matter applications*, *Int. J. Mod. Phys. D* **30** (2021) 2130004 [2104.01788].

[177] J. Aebischer, W. Altmannshofer, E.E. Jenkins and A.V. Manohar, *Dark matter effective field theory and an application to vector dark matter*, *JHEP* **06** (2022) 086 [2202.06968].

[178] J.C. Criado, A. Djouadi, M. Perez-Victoria and J. Santiago, *A complete effective field theory for dark matter*, *JHEP* **07** (2021) 081 [2104.14443].

[179] G. Busoni, A. De Simone, E. Morgante and A. Riotto, *On the Validity of the Effective Field Theory for Dark Matter Searches at the LHC*, *Phys. Lett. B* **728** (2014) 412 [1307.2253].

[180] G. Busoni, A. De Simone, T. Jacques, E. Morgante and A. Riotto, *On the Validity of the Effective Field Theory for Dark Matter Searches at the LHC Part III: Analysis for the t-channel*, *JCAP* **09** (2014) 022 [1405.3101].

[181] G. Busoni, A. De Simone, J. Gramling, E. Morgante and A. Riotto, *On the Validity of the Effective Field Theory for Dark Matter Searches at the LHC, Part II: Complete Analysis for the s-channel*, *JCAP* **06** (2014) 060 [1402.1275].

[182] A. De Simone and T. Jacques, *Simplified models vs. effective field theory approaches in dark matter searches*, *Eur. Phys. J. C* **76** (2016) 367 [1603.08002].

[183] M. Duch, B. Grzadkowski and J. Wudka, *Classification of effective operators for interactions between the Standard Model and dark matter*, *JHEP* **05** (2015) 116 [1412.0520].

[184] H. Song, H. Sun and J.-H. Yu, *Complete EFT operator bases for dark matter and weakly-interacting light particle*, *JHEP* **05** (2024) 103 [2306.05999].

[185] G. Arcadi, A. Djouadi and M. Raidal, *Dark Matter through the Higgs portal*, *Phys. Rept.* **842** (2020) 1 [1903.03616].

[186] G. Arcadi, A. Djouadi and M. Kado, *The Higgs-portal for dark matter: effective field theories versus concrete realizations*, *Eur. Phys. J. C* **81** (2021) 653 [2101.02507].

[187] M. Escudero Abenza and T. Hambye, *The simplest dark matter model at the edge of perturbativity*, *Phys. Lett. B* **868** (2025) 139696 [2505.02408].

[188] P.J. Fox and E. Poppitz, *Leptophilic Dark Matter*, *Phys. Rev. D* **79** (2009) 083528 [0811.0399].

[189] B. Barman, S. Bhattacharya, S. Girmohanta and S. Jahedi, *Effective Leptophilic WIMPs at the e^+e collider*, *JHEP* **04** (2022) 146 [2109.10936].

[190] S. Bhattacharya, A. Ghosh, N. Mondal and A. Sarkar, *Lepton Collider as a Window to Reheating via Freezing Out Dark Matter Detection*, 2509.14340.

[191] J. Butterworth et al., *PDF4LHC recommendations for LHC Run II*, *J. Phys. G* **43** (2016) 023001 [1510.03865].

[192] S. Dulat, T.-J. Hou, J. Gao, M. Guzzi, J. Huston, P. Nadolsky et al., *New parton distribution functions from a global analysis of quantum chromodynamics*, *Phys. Rev. D* **93** (2016) 033006 [1506.07443].

[193] L.A. Harland-Lang, A.D. Martin, P. Motylinski and R.S. Thorne, *Parton distributions in the LHC era: MMHT 2014 PDFs*, *Eur. Phys. J. C* **75** (2015) 204 [1412.3989].

[194] NNPDF collaboration, *Parton distributions from high-precision collider data*, *Eur. Phys. J. C* **77** (2017) 663 [1706.00428].

[195] M. Greco, T. Han and Z. Liu, *ISR effects for resonant Higgs production at future lepton colliders*, *Phys. Lett. B* **763** (2016) 409 [1607.03210].

[196] J. Grames and M. Poelker, *Polarized Electron Sources*, in *Polarized Beam Dynamics and Instrumentation in Particle Accelerators: USPAS Summer 2021 Spin Class Lectures*, F. Méot, H. Huang, V. Ptitsyn and F. Lin, eds., pp. 261–284 (2022), DOI.

[197] T. Behnke, J.E. Brau, B. Foster, J. Fuster, M. Harrison, J.M. Paterson et al., eds., *The International Linear Collider Technical Design Report - Volume 1: Executive Summary*, 1306.6327.

[198] L.H. Thomas, *The motion of a spinning electron*, *Nature* **117** (1926) 514.

[199] V. Bargmann, L. Michel and V.L. Telegdi, *Precession of the polarization of particles moving in a homogeneous electromagnetic field*, *Phys. Rev. Lett.* **2** (1959) 435.

[200] C.D. Anderson, *The positive electron*, *Phys. Rev.* **43** (1933) 491.

[201] R. Schmidt, *The CERN SPS proton–antiproton collider*, in *Challenges And Goals For Accelerators In The XXI Century*, pp. 153–167 (2016), DOI.

[202] S. Holmes, R. Moore, J. Peoples and V. Shiltsev, *Accelerator physics at the Tevatron Collider: Introduction*, in *Accelerator Physics at the Tevatron Collider*, V. Lebedev and V. Shiltsev, eds., pp. 1–28 (2014), DOI.

[203] R. Assmann, M. Lamont and S. Myers, *A brief history of the LEP collider*, *Nucl. Phys. B Proc. Suppl.* **109** (2002) 17.

[204] ATLAS collaboration, *Measurement of the properties of Higgs boson production at $\sqrt{s} = 13$ TeV in the $H \to \gamma\gamma$ channel using 139 fb^{-1} of pp collision data with the ATLAS experiment*, *JHEP* **07** (2023) 088 [2207.00348].

[205] ATLAS collaboration, *Measurement of inclusive and differential cross sections in the $H \to ZZ^* \to 4\ell$ decay channel in pp collisions at $\sqrt{s} = 13$ TeV with the ATLAS detector*, *JHEP* **10** (2017) 132 [1708.02810].

[206] I. Zurbano Fernandez et al., *High-Luminosity Large Hadron Collider (HL-LHC): Technical design report*, .

[207] MAIA collaboration, *MAIA: A new detector concept for a 10 TeV muon collider*, 2502.00181.

[208] ILD collaboration, *The ILD detector at the ILC*, 1912.04601.

[209] M. Cacciari, G.P. Salam and G. Soyez, *The anti-k_t jet clustering algorithm*, *JHEP* **04** (2008) 063 [0802.1189].

[210] S. Mondal and L. Mastrolorenzo, *Machine learning in high energy physics: a review of heavy-flavor jet tagging at the LHC*, *Eur. Phys. J. ST* **233** (2024) 2657 [2404.01071].

[211] ATLAS, CMS collaboration, *Higgs Physics at HL-LHC*, in *30th International Workshop on Deep-Inelastic Scattering and Related Subjects*, 7, 2023 [2307.07772].

[212] ATLAS collaboration, *HL-LHC prospects for the measurement of Higgs boson pair production in the $b\bar{b}b\bar{b}$ final state and combination with the $b\bar{b}\gamma\gamma$ and $b\bar{b}\tau^+\tau^-$ final states at the ATLAS experiment*, .

[213] M. Ahmad et al., *CEPC-SPPC Preliminary Conceptual Design Report. 1. Physics and Detector*, .

[214] FCC collaboration, *The hadron collider FCC-hh: Extended conceptual design report*, .

[215] P. Bambade et al., *The International Linear Collider: A Global Project*, 1903.01629.

[216] ILC collaboration, H. Baer et al., eds., *The International Linear Collider Technical Design Report - Volume 2: Physics*, 1306.6352.

[217] C. Adolphsen et al., eds., *The International Linear Collider Technical Design Report - Volume 3.I: Accelerator \& in the Technical Design Phase*, 1306.6353.

[218] C. Adolphsen et al., eds., *The International Linear Collider Technical Design Report - Volume 3.II: Accelerator Baseline Design*, 1306.6328.

[219] H. Abramowicz et al., *The International Linear Collider Technical Design Report - Volume 4: Detectors*, 1306.6329.

[220] O. Brunner et al., *The CLIC project*, 2203.09186.

[221] CLICdp, CLIC collaboration, *The Compact Linear Collider (CLIC) - 2018 Summary Report*, *CERN Yellow Rep. Monogr.* **2** (2018) 1 [1812.06018].

[222] I. Agapov et al., *Future Circular Lepton Collider FCC-ee: Overview and Status*, in *Snowmass 2021*, 3, 2022 [2203.08310].

[223] International Muon Collider collaboration, *The Muon Collider*, 2504.21417.

[224] C. Aime et al., *Muon Collider Physics Summary*, 2203.07256.

[225] N. Bartosik et al., *Detector and Physics Performance at a Muon Collider*, *JINST* **15** (2020) P05001 [2001.04431].

[226] Y. Hamada, R. Kitano, R. Matsudo, H. Takaura and M. Yoshida, *μTRISTAN*, *PTEP* **2022** (2022) 053B02 [2201.06664].

[227] W.S. Cho, D. Kim, K. Kong, S.H. Lim, K.T. Matchev, J.-C. Park et al., *750 GeV Diphoton Excess May Not Imply a 750 GeV Resonance*, *Phys. Rev. Lett.* **116** (2016) 151805 [1512.06824].

[228] CMS collaboration, *Search for resonant production of high mass photon pairs using* $12.9\,\text{fb}^{-1}$ *of proton-proton collisions at* $\sqrt{s} = 13$ TeV *and combined interpretation of searches at 8 and 13 TeV*, Tech. Rep. , CERN, Geneva (2016).

[229] ATLAS collaboration, *Search for scalar diphoton resonances with 15.4 fb^{-1} of data collected at $\sqrt{s}$=13 TeV in 2015 and 2016 with the ATLAS detector*, Tech. Rep. , CERN, Geneva (2016).

[230] S.S. Wilks, *The Large-Sample Distribution of the Likelihood Ratio for Testing Composite Hypotheses*, *Annals Math. Statist.* **9** (1938) 60.

[231] M. Diehl and O. Nachtmann, *Optimal observables for measuring three gauge boson couplings in e+ e- —> W+ W-*, in *Physics with e+ e- Linear Colliders (The European Working Groups 4 Feb - 1 Sep 1995: Session 2)*, pp. 301–304, 3, 1996 [hep-ph/9603207].

[232] S. Bhattacharya, S. Jahedi and J. Wudka, *Probing heavy charged fermions at e^+e collider using the optimal observable technique*, *JHEP* **05** (2022) 009 [2106.02846].

[233] A. Alloul, N.D. Christensen, C. Degrande, C. Duhr and B. Fuks, *FeynRules 2.0 - A complete toolbox for tree-level phenomenology*, *Comput. Phys. Commun.* **185** (2014) 2250 [1310.1921].

[234] L. Darmé et al., *UFO 2.0: the 'Universal Feynman Output' format*, *Eur. Phys. J. C* **83** (2023) 631 [2304.09883].

[235] J. Alwall, M. Herquet, F. Maltoni, O. Mattelaer and T. Stelzer, *MadGraph 5 : Going Beyond*, *JHEP* **06** (2011) 128 [1106.0522].

[236] C. Bierlich et al., *A comprehensive guide to the physics and usage of PYTHIA 8.3*, *SciPost Phys. Codeb.* **2022** (2022) 8 [2203.11601].

[237] DELPHES 3 collaboration, *DELPHES 3, A modular framework for fast simulation of a generic collider experiment*, *JHEP* **02** (2014) 057 [1307.6346].

[238] M. Cacciari, G.P. Salam and G. Soyez, *FastJet User Manual*, *Eur. Phys. J. C* **72** (2012) 1896 [1111.6097].

[239] R. Brun and F. Rademakers, *ROOT — An object oriented data analysis framework*, *Nucl. Instrum. Meth. A* **389** (1997) 81.

[240] H.E. Logan, *TASI 2013 lectures on Higgs physics within and beyond the Standard Model*, 1406.1786.

[241] Particle Data Group collaboration, *Review of Particle Physics*, *PTEP* **2022** (2022) 083C01.

[242] CMS collaboration, *Constraints on anomalous HVV couplings from the production of Higgs bosons decaying to τ lepton pairs*, *Phys. Rev. D* **100** (2019) 112002 [1903.06973].

[243] I. Anderson et al., *Constraining Anomalous HVV Interactions at Proton and Lepton Colliders*, *Phys. Rev. D* **89** (2014) 035007 [1309.4819].

[244] P. Sharma and A. Shivaji, *Probing non-standard HVV (V = W, Z) couplings in single Higgs production at future electron-proton collider*, *JHEP* **10** (2022) 108 [2207.03862].

[245] A.I. Hernández-Juárez, G. Tavares-Velasco and A. Fernández-Téllez, *New evaluation of the HZZ coupling: Direct bounds on anomalous contributions and CP-violating effects via a new asymmetry*, *Phys. Rev. D* **107** (2023) 115031 [2301.13127].

[246] S. Dutta, K. Hagiwara and Y. Matsumoto, *Measuring the Higgs-Vector boson Couplings at Linear e^+e^- Collider*, *Phys. Rev. D* **78** (2008) 115016 [0808.0477].

[247] N. Desai, D.K. Ghosh and B. Mukhopadhyaya, *CP-violating HWW couplings at the Large Hadron Collider*, *Phys. Rev. D* **83** (2011) 113004 [1104.3327].

[248] N.D. Christensen, T. Han and Y. Li, *Testing CP Violation in ZZH Interactions at the LHC*, *Phys. Lett. B* **693** (2010) 28 [1005.5393].

[249] S. Dwivedi, D.K. Ghosh, B. Mukhopadhyaya and A. Shivaji, *Distinguishing CP-odd couplings of the Higgs boson to weak boson pairs*, *Phys. Rev. D* **93** (2016) 115039 [1603.06195].

[250] F.U. Bernlochner, C. Englert, C. Hays, K. Lohwasser, H. Mildner, A. Pilkington et al., *Angles on CP-violation in Higgs boson interactions*, *Phys. Lett. B* **790** (2019) 372 [1808.06577].

[251] J. Brehmer, F. Kling, T. Plehn and T.M.P. Tait, *Better Higgs-CP Tests Through Information Geometry*, *Phys. Rev. D* **97** (2018) 095017 [1712.02350].

[252] S. Banerjee, T. Mandal, B. Mellado and B. Mukhopadhyaya, *Cornering dimension-6 HVV interactions at high luminosity LHC: the role of event ratios*, *JHEP* **09** (2015) 057 [1505.00226].

[253] S. Banerjee, C. Englert, R.S. Gupta and M. Spannowsky, *Probing Electroweak Precision Physics via boosted Higgs-strahlung at the LHC*, *Phys. Rev. D* **98** (2018) 095012 [1807.01796].

[254] S. Banerjee, R.S. Gupta, J.Y. Reiness and M. Spannowsky, *Resolving the tensor structure of the Higgs coupling to Z-bosons via Higgs-strahlung*, *Phys. Rev. D* **100** (2019) 115004 [1905.02728].

[255] S. Banerjee, R.S. Gupta, J.Y. Reiness, S. Seth and M. Spannowsky, *Towards the ultimate differential SMEFT analysis*, *JHEP* **09** (2020) 170 [1912.07628].

[256] F.F. Freitas, C.K. Khosa and V. Sanz, *Exploring the standard model EFT in VH production with machine learning*, *Phys. Rev. D* **100** (2019) 035040 [1902.05803].

[257] F. Bishara, P. Englert, C. Grojean, G. Panico and A.N. Rossia, *Revisiting $Vh(\to b\bar{b})$ at the LHC and FCC-hh*, *JHEP* **06** (2023) 077 [2208.11134].

[258] F. Bishara, S. De Curtis, L. Delle Rose, P. Englert, C. Grojean, M. Montull et al., *Precision from the diphoton Zh channel at FCC-hh*, *JHEP* **04** (2021) 154 [2011.13941].

[259] P. Englert, *Improved Precision in $Vh(\to b\bar{b})$ via Boosted Decision Trees*, 2407.21239.

[260] S. Banerjee, R.S. Gupta, O. Ochoa-Valeriano, M. Spannowsky and E. Venturini, *A fully differential SMEFT analysis of the golden channel using the method of moments*, *JHEP* **06** (2021) 031 [2012.11631].

[261] S. Banerjee, R.S. Gupta, O. Ochoa-Valeriano and M. Spannowsky, *High energy lepton colliders as the ultimate Higgs microscopes*, *JHEP* **02** (2022) 176 [2109.14634].

[262] T. Biswas, A. Datta and B. Mukhopadhyaya, *Following the trail of new physics via the vector boson fusion Higgs boson signal at the Large Hadron Collider*, *Phys. Rev. D* **105** (2022) 055028 [2107.05503].

[263] J.Y. Araz, S. Banerjee, R.S. Gupta and M. Spannowsky, *Precision SMEFT bounds from the VBF Higgs at high transverse momentum*, *JHEP* **04** (2021) 125 [2011.03555].

[264] H.T. Li, B. Yan and C.P. Yuan, *Discriminating between Higgs Production Mechanisms via Jet Charge at the LHC*, *Phys. Rev. Lett.* **131** (2023) 041802 [2301.07914].

[265] B. Yan, *Determining Higgs boson width at electron-positron colliders*, *Phys. Lett. B* **822** (2021) 136709 [2105.04530].

[266] K.-P. Xie and B. Yan, *Probing the electroweak symmetry breaking with Higgs production at the LHC*, *Phys. Lett. B* **820** (2021) 136515 [2104.12689].

[267] Q. Bonnefoy, J. Kley, D. Liu, A.N. Rossia and C.-Y. Yao, *Aligned Yet Large Dipoles: a SMEFT Study*, 2403.13065.

[268] R. Alonso, E.E. Jenkins and A.V. Manohar, *A Geometric Formulation of Higgs Effective Field Theory: Measuring the Curvature of Scalar Field Space*, *Phys. Lett. B* **754** (2016) 335 [1511.00724].

[269] A. Crivellin, M. Ghezzi and M. Procura, *Effective Field Theory with Two Higgs Doublets*, *JHEP* **09** (2016) 160 [1608.00975].

[270] Anisha, S. Das Bakshi, J. Chakrabortty and S. Prakash, *Hilbert Series and Plethystics: Paving the path towards 2HDM- and MLRSM-EFT*, *JHEP* **09** (2019) 035 [1905.11047].

[271] F. del Aguila, S. Bar-Shalom, A. Soni and J. Wudka, *Heavy Majorana Neutrinos in the Effective Lagrangian Description: Application to Hadron Colliders*, *Phys. Lett. B* **670** (2009) 399 [0806.0876].

[272] A. Aparici, K. Kim, A. Santamaria and J. Wudka, *Right-handed neutrino magnetic moments*, *Phys. Rev. D* **80** (2009) 013010 [0904.3244].

[273] Y. Liao and X.-D. Ma, *Operators up to Dimension Seven in Standard Model Effective Field Theory Extended with Sterile Neutrinos*, *Phys. Rev. D* **96** (2017) 015012 [1612.04527].

[274] C. Degrande, C. Duhr, B. Fuks, D. Grellscheid, O. Mattelaer and T. Reiter, *UFO - The Universal FeynRules Output*, *Comput. Phys. Commun.* **183** (2012) 1201 [1108.2040].

[275] I. Brivio, *SMEFTsim 3.0 — a practical guide*, *JHEP* **04** (2021) 073 [2012.11343].

[276] C. Degrande, G. Durieux, F. Maltoni, K. Mimasu, E. Vryonidou and C. Zhang, *Automated one-loop computations in the standard model effective field theory*, *Phys. Rev. D* **103** (2021) 096024 [2008.11743].

[277] R.D. Ball et al., *Parton distributions with LHC data*, *Nucl. Phys. B* **867** (2013) 244 [1207.1303].

[278] SMEFiT collaboration, *Combined SMEFT interpretation of Higgs, diboson, and top quark data from the LHC*, *JHEP* **11** (2021) 089 [2105.00006].

[279] J. Ellis, M. Madigan, K. Mimasu, V. Sanz and T. You, *Top, Higgs, Diboson and Electroweak Fit to the Standard Model Effective Field Theory*, *JHEP* **04** (2021) 279 [2012.02779].

[280] I. Brivio, S. Bruggisser, N. Elmer, E. Geoffray, M. Luchmann and T. Plehn, *To profile or to marginalize - A SMEFT case study*, *SciPost Phys.* **16** (2024) 035 [2208.08454].

[281] Anisha, S. Das Bakshi, S. Banerjee, A. Biekötter, J. Chakrabortty, S. Kumar Patra et al., *Effective limits on single scalar extensions in the light of recent LHC data*, *Phys. Rev. D* **107** (2023) 055028 [2111.05876].

[282] A. Buckley, C. Englert, J. Ferrando, D.J. Miller, L. Moore, M. Russell et al., *Constraining top quark effective theory in the LHC Run II era*, *JHEP* **04** (2016) 015 [1512.03360].

[283] S. Bißmann, C. Grunwald, G. Hiller and K. Kröninger, *Top and Beauty synergies in SMEFT-fits at present and future colliders*, *JHEP* **06** (2021) 010 [2012.10456].

[284] C. Grunwald, G. Hiller, K. Kröninger and L. Nollen, *More synergies from beauty, top, Z and Drell-Yan measurements in SMEFT*, *JHEP* **11** (2023) 110 [2304.12837].

[285] ATLAS collaboration, *Measurements of differential cross-sections in four-lepton events in 13 TeV proton-proton collisions with the ATLAS detector*, *JHEP* **07** (2021) 005 [2103.01918].

[286] ATLAS collaboration, *Combined measurements of Higgs boson production and decay using up to* 139 fb^{-1} *of proton-proton collision data at* $\sqrt{s} = 13$ *TeV collected with the ATLAS experiment*, .

[287] ATLAS collaboration, *Combined effective field theory interpretation of Higgs boson and weak boson production and decay with ATLAS data and electroweak precision observables*, .

[288] J. de Blas, Y. Du, C. Grojean, J. Gu, V. Miralles, M.E. Peskin et al., *Global SMEFT Fits at Future Colliders*, in *Snowmass 2021*, 6, 2022 [2206.08326].

[289] E. Celada, T. Giani, J. ter Hoeve, L. Mantani, J. Rojo, A.N. Rossia et al., *Mapping the SMEFT at high-energy colliders: from LEP and the (HL-)LHC to the FCC-ee*, *JHEP* **09** (2024) 091 [2404.12809].

[290] C. Bissolotti, R. Boughezal and K. Simsek, *SMEFT probes in future precision DIS experiments*, *Phys. Rev. D* **108** (2023) 075007 [2306.05564].

[291] R. Boughezal, E. Mereghetti and F. Petriello, *Dilepton production in the SMEFT at O(1/Λ4)*, *Phys. Rev. D* **104** (2021) 095022 [2106.05337].

[292] E. da Silva Almeida, N. Rosa-Agostinho, O.J.P. Éboli and M.C. Gonzalez-Garcia, *Light-quark dipole operators at the LHC*, *Phys. Rev. D* **100** (2019) 013003 [1905.05187].

[293] V. Cirigliano, A. Crivellin, W. Dekens, J. de Vries, M. Hoferichter and E. Mereghetti, *CP Violation in Higgs-Gauge Interactions: From Tabletop Experiments to the LHC*, *Phys. Rev. Lett.* **123** (2019) 051801 [1903.03625].

[294] G. Panico, A. Pomarol and M. Riembau, *EFT approach to the electron Electric Dipole Moment at the two-loop level*, *JHEP* **04** (2019) 090 [1810.09413].

[295] T. Sjostrand, S. Mrenna and P.Z. Skands, *A Brief Introduction to PYTHIA 8.1*, *Comput. Phys. Commun.* **178** (2008) 852 [0710.3820].

[296] E. Conte, B. Fuks and G. Serret, *MadAnalysis 5, A User-Friendly Framework for Collider Phenomenology*, *Comput. Phys. Commun.* **184** (2013) 222 [1206.1599].

[297] F. Cascioli, T. Gehrmann, M. Grazzini, S. Kallweit, P. Maierhöfer, A. von Manteuffel et al., *ZZ production at hadron colliders in NNLO QCD*, *Phys. Lett. B* **735** (2014) 311 [1405.2219].

[298] L. Chen, J. Davies, G. Heinrich, S.P. Jones, M. Kerner, G. Mishima et al., *ZH production in gluon fusion at NLO in QCD*, *JHEP* **08** (2022) 056 [2204.05225].

[299] J.M. Campbell, J.W. Huston and W.J. Stirling, *Hard Interactions of Quarks and Gluons: A Primer for LHC Physics*, *Rept. Prog. Phys.* **70** (2007) 89 [hep-ph/0611148].

[300] G. Cowan, K. Cranmer, E. Gross and O. Vitells, *Asymptotic formulae for likelihood-based tests of new physics*, *Eur. Phys. J. C* **71** (2011) 1554 [1007.1727].

[301] Y. Coadou, *Boosted decision trees*, 2206.09645.

[302] A.S. Cornell, W. Doorsamy, B. Fuks, G. Harmsen and L. Mason, *Boosted decision trees in the era of new physics: a smuon analysis case study*, *JHEP* **04** (2022) 015 [2109.11815].

[303] T. Chen and C. Guestrin, *Xgboost: A scalable tree boosting system*, in *Proceedings of the 22nd ACM SIGKDD International Conference on Knowledge Discovery and Data Mining*, KDD '16, ACM, Aug., 2016, DOI.

[304] F. Pedregosa, G. Varoquaux, A. Gramfort, V. Michel, B. Thirion, O. Grisel et al., *Scikit-learn: Machine learning in Python*, *Journal of Machine Learning Research* **12** (2011) 2825.

[305] S. Lundberg and S.-I. Lee, *A unified approach to interpreting model predictions*, 2017.

[306] CMS collaboration, *Study of the Mass and Spin-Parity of the Higgs Boson Candidate Via Its Decays to Z Boson Pairs*, *Phys. Rev. Lett.* **110** (2013) 081803 [1212.6639].

[307] CMS collaboration, *Measurement of the Properties of a Higgs Boson in the Four-Lepton Final State*, *Phys. Rev. D* **89** (2014) 092007 [1312.5353].

[308] CMS collaboration, *Constraints on the spin-parity and anomalous HVV couplings of the Higgs boson in proton collisions at 7 and 8 TeV*, *Phys. Rev. D* **92** (2015) 012004 [1411.3441].

[309] CMS collaboration, *Limits on the Higgs boson lifetime and width from its decay to four charged leptons*, *Phys. Rev. D* **92** (2015) 072010 [1507.06656].

[310] CMS collaboration, *Combined search for anomalous pseudoscalar HVV couplings in VH($H \to b\bar{b}$) production and $H \to VV$ decay*, *Phys. Lett. B* **759** (2016) 672 [1602.04305].

[311] CMS collaboration, *Constraints on anomalous Higgs boson couplings using production and decay information in the four-lepton final state*, *Phys. Lett. B* **775** (2017) 1 [1707.00541].

[312] CMS collaboration, *Measurements of the Higgs boson width and anomalous HVV couplings from on-shell and off-shell production in the four-lepton final state*, *Phys. Rev. D* **99** (2019) 112003 [1901.00174].

[313] ATLAS collaboration, *Evidence for the spin-0 nature of the Higgs boson using ATLAS data*, *Phys. Lett. B* **726** (2013) 120 [1307.1432].

[314] ATLAS collaboration, *Study of the spin and parity of the Higgs boson in diboson decays with the ATLAS detector*, *Eur. Phys. J. C* **75** (2015) 476 [1506.05669].

[315] ATLAS collaboration, *Test of CP Invariance in vector-boson fusion production of the Higgs boson using the Optimal Observable method in the ditau decay channel with the ATLAS detector*, *Eur. Phys. J. C* **76** (2016) 658 [1602.04516].

[316] ATLAS collaboration, *Measurement of the Higgs boson coupling properties in the $H \to ZZ^* \to 4\ell$ decay channel at $\sqrt{s} = 13$ TeV with the ATLAS detector*, *JHEP* **03** (2018) 095 [1712.02304].

[317] ATLAS collaboration, *Measurements of Higgs boson properties in the diphoton decay channel with 36 fb^{-1} of pp collision data at $\sqrt{s} = 13$ TeV with the ATLAS detector*, *Phys. Rev. D* **98** (2018) 052005 [1802.04146].

[318] ATLAS collaboration, *Test of CP invariance in vector-boson fusion production of the Higgs boson in the $H \to \tau\tau$ channel in proton–proton collisions at s=13TeV with the ATLAS detector*, *Phys. Lett. B* **805** (2020) 135426 [2002.05315].

[319] ILC collaboration, *International Linear Collider Reference Design Report Volume 2: Physics at the ILC*, 0709.1893.

[320] ILC collaboration, *ILC Reference Design Report Volume 1 - Executive Summary*, 0712.1950.

[321] ILC collaboration, *ILC Reference Design Report Volume 4 - Detectors*, 0712.2356.

[322] FCC collaboration, *FCC-ee: The Lepton Collider: Future Circular Collider Conceptual Design Report Volume 2*, *Eur. Phys. J. ST* **228** (2019) 261.

[323] CEPC Study Group collaboration, *CEPC Conceptual Design Report: Volume 1 - Accelerator*, 1809.00285.

[324] CEPC Study Group collaboration, *CEPC Technical Design Report: Accelerator*, *Radiat. Detect. Technol. Methods* **8** (2024) 1 [2312.14363].

[325] CEPC Physics Study Group collaboration, *The Physics potential of the CEPC. Prepared for the US Snowmass Community Planning Exercise (Snowmass 2021)*, in *Snowmass 2021*, 5, 2022 [2205.08553].

[326] CLIC, CLICdp collaboration, *Updated baseline for a staged Compact Linear Collider*, 1608.07537.

[327] M. Aicheler, P. Burrows, M. Draper, T. Garvey, P. Lebrun, K. Peach et al., eds., *A Multi-TeV Linear Collider Based on CLIC Technology: CLIC Conceptual Design Report*, .

[328] L. Linssen, A. Miyamoto, M. Stanitzki and H. Weerts, eds., *Physics and Detectors at CLIC: CLIC Conceptual Design Report*, 1202.5940.

[329] P. Lebrun, L. Linssen, A. Lucaci-Timoce, D. Schulte, F. Simon, S. Stapnes et al., *The CLIC Programme: Towards a Staged e+e- Linear Collider Exploring the Terascale : CLIC Conceptual Design Report*, 1209.2543.

[330] ILC International Development Team collaboration, *The International Linear Collider: Report to Snowmass 2021*, 2203.07622.

[331] Linear Collider collaboration, *The Linear Collider Facility (LCF) at CERN*, 2503.24049.

[332] CLIC, CLICdp collaboration, P. Roloff, R. Franceschini, U. Schnoor and A. Wulzer, eds., *The Compact Linear e^+e^- Collider (CLIC): Physics Potential*, 1812.07986.

[333] K. Hagiwara and M.L. Stong, *Probing the scalar sector in e+ e- —> f anti-f H*, *Z. Phys. C* **62** (1994) 99 [hep-ph/9309248].

[334] K. Hagiwara, S. Ishihara, J. Kamoshita and B.A. Kniehl, *Prospects of measuring general Higgs couplings at e+ e- linear colliders*, *Eur. Phys. J. C* **14** (2000) 457 [hep-ph/0002043].

[335] S.S. Biswal, R.M. Godbole, R.K. Singh and D. Choudhury, *Signatures of anomalous VVH interactions at a linear collider*, *Phys. Rev. D* **73** (2006) 035001 [hep-ph/0509070].

[336] S.S. Biswal, D. Choudhury, R.M. Godbole and Mamta, *Role of polarization in probing anomalous gauge interactions of the Higgs boson*, *Phys. Rev. D* **79** (2009) 035012 [0809.0202].

[337] S.S. Biswal and R.M. Godbole, *Use of transverse beam polarization to probe anomalous VVH interactions at a Linear Collider*, *Phys. Lett. B* **680** (2009) 81 [0906.5471].

[338] R.M. Godbole, D.J. Miller and M.M. Muhlleitner, *Aspects of CP violation in the H ZZ coupling at the LHC*, *JHEP* **12** (2007) 031 [0708.0458].

[339] R. Godbole, D.J. Miller, K. Mohan and C.D. White, *Boosting Higgs CP properties via VH Production at the Large Hadron Collider*, *Phys. Lett. B* **730** (2014) 275 [1306.2573].

[340] R.M. Godbole, D.J. Miller, K.A. Mohan and C.D. White, *Jet substructure and probes of CP violation in Vh production*, *JHEP* **04** (2015) 103 [1409.5449].

[341] S.D. Rindani and P. Sharma, *Angular distributions as a probe of anomalous ZZH and gammaZH interactions at a linear collider with polarized beams*, *Phys. Rev. D* **79** (2009) 075007 [0901.2821].

[342] S.D. Rindani and P. Sharma, *Decay-lepton correlations as probes of anomalous ZZH and gammaZH interactions in e+e- –> ZH with polarized beams*, *Phys. Lett. B* **693** (2010) 134 [1001.4931].

[343] N. Craig, J. Gu, Z. Liu and K. Wang, *Beyond Higgs Couplings: Probing the Higgs with Angular Observables at Future e^+ e Colliders*, *JHEP* **03** (2016) 050 [1512.06877].

[344] M. Beneke, D. Boito and Y.-M. Wang, *Anomalous Higgs couplings in angular asymmetries of $H \to Z\ell^+\ell^-$ and e^+ $e^- \to HZ$*, *JHEP* **11** (2014) 028 [1406.1361].

[345] H. Khanpour and M. Mohammadi Najafabadi, *Constraining Higgs boson effective couplings at electron-positron colliders*, *Phys. Rev. D* **95** (2017) 055026 [1702.00951].

[346] T.V. Zagoskin and A.Y. Korchin, *Higgs boson ZZ couplings in Higgs-strahlung at the ILC*, *Phys. Rev. D* **98** (2018) 093008 [1804.10011].

[347] H.-D. Li, C.-D. Lü and L.-Y. Shan, *Sensitivity study of anomalous HZZ couplings at a future Higgs factory*, *Chin. Phys. C* **43** (2019) 103001 [1901.10218].

[348] H.-R. He, X. Wan and Y.-K. Wang, *Anomalous $H \to ZZ \to 4\ell$ decay and its interference effects on gluon–gluon contribution at the LHC*, *Chin. Phys. C* **44** (2020) 123101 [1902.04756].

[349] J. Nakamura, *Polarisations of the Z and W bosons in the processes $pp \to ZH$ and $pp \to W^{\pm}H$*, *JHEP* **08** (2017) 008 [1706.01816].

[350] W.H. Chiu, S.C. Leung, T. Liu, K.-F. Lyu and L.-T. Wang, *Probing 6D operators at future ee^+ colliders*, *JHEP* **05** (2018) 081 [1711.04046].

[351] G. Durieux, C. Grojean, J. Gu and K. Wang, *The leptonic future of the Higgs*, *JHEP* **09** (2017) 014 [1704.02333].

[352] K. Rao, S.D. Rindani and P. Sarmah, *Study of anomalous gauge-Higgs couplings using Z boson polarization at LHC*, *Nucl. Phys. B* **964** (2021) 115317 [2009.00980].

[353] W. Bizoń, F. Caola, K. Melnikov and R. Röntsch, *Anomalous couplings in associated VH production with Higgs boson decay to massive b quarks at NNLO in QCD*, *Phys. Rev. D* **105** (2022) 014023 [2106.06328].

[354] T. Corbett, O.J.P. Eboli, J. Gonzalez-Fraile and M.C. Gonzalez-Garcia, *Constraining anomalous Higgs interactions*, *Phys. Rev. D* **86** (2012) 075013 [1207.1344].

[355] T. Corbett, O.J.P. Eboli, J. Gonzalez-Fraile and M.C. Gonzalez-Garcia, *Robust Determination of the Higgs Couplings: Power to the Data*, *Phys. Rev. D* **87** (2013) 015022 [1211.4580].

[356] S. Bhattacharya, S. Biswas and A. Sarkar, *Higgs couplings in SMEFT via Zh production at the HL-LHC*, *Phys. Rev. D* **111** (2025) 115038 [2403.03001].

[357] Q.-H. Cao, L.-X. Xu, B. Yan and S.-H. Zhu, *Signature of pseudo Nambu–Goldstone Higgs boson in its decay*, *Phys. Lett. B* **789** (2019) 233 [1810.07661].

[358] T. Ogawa, J. Tian and K. Fujii, *Sensitivity to anomalous ZZH couplings at the ILC*, *PoS* **EPS-HEP2017** (2017) 322 [1712.09772].

[359] T. Barklow, K. Fujii, S. Jung, R. Karl, J. List, T. Ogawa et al., *Improved Formalism for Precision Higgs Coupling Fits*, *Phys. Rev. D* **97** (2018) 053003 [1708.08912].

[360] T. Barklow, K. Fujii, S. Jung, M.E. Peskin and J. Tian, *Model-Independent Determination of the Triple Higgs Coupling at e+e- Colliders*, *Phys. Rev. D* **97** (2018) 053004 [1708.09079].

[361] M. Fabbrichesi, R. Floreanini, E. Gabrielli and L. Marzola, *Stringent bounds on HWW and HZZ anomalous couplings with quantum tomography at the LHC*, *JHEP* **09** (2023) 195 [2304.02403].

[362] M. Del Gratta, F. Fabbri, P. Lamba, F. Maltoni and D. Pagani, *Quantum properties of $H \to VV^*$: precise predictions in the SM and sensitivity to new physics*, 2504.03841.

[363] M. Sullivan, *Constraining New Physics with $h \to VV$ Tomography*, 2410.10980.

[364] A. Bernal, P. Caban and J. Rembieliński, *Entanglement and Bell inequalities violation in $H \to ZZ$ with anomalous coupling*, *Eur. Phys. J. C* **83** (2023) 1050 [2307.13496].

[365] A. Subba, R.K. Singh and R.M. Godbole, *Looking into the quantum entanglement in $H \to ZZ^\star$ at LHC within SMEFT framework*, 2411.19171.

[366] CMS collaboration, *Constraints on anomalous Higgs boson couplings from its production and decay using the WW channel in proton–proton collisions at $\sqrt{s} =$ 13 TeV*, *Eur. Phys. J. C* **84** (2024) 779 [2403.00657].

[367] D. Atwood and A. Soni, *Analysis for magnetic moment and electric dipole moment form-factors of the top quark via e+ e- —> t anti-t*, *Phys. Rev. D* **45** (1992) 2405.

[368] J.F. Gunion, B. Grzadkowski and X.-G. He, *Determining the top - anti-top and Z Z couplings of a neutral Higgs boson of arbitrary CP nature at the NLC*, *Phys. Rev. Lett.* **77** (1996) 5172 [hep-ph/9605326].

[369] M. Diehl and O. Nachtmann, *Optimal observables for the measurement of three gauge boson couplings in e+ e- —> W+ W-*, *Z. Phys. C* **62** (1994) 397.

[370] M. Davier, L. Duflot, F. Le Diberder and A. Rouge, *The Optimal method for the measurement of tau polarization*, *Phys. Lett. B* **306** (1993) 411.

[371] K. Rao, S.D. Rindani and P. Sarmah, *Probing anomalous gauge-Higgs couplings using Z boson polarization at e+e− colliders*, *Nucl. Phys. B* **950** (2020) 114840 [1904.06663].

[372] K. Rao, S.D. Rindani, P. Sarmah and B. Singh, *Z polarization at an e^+e^- collider and properties of decay-lepton angular asymmetries*, *Proc. Indian Natl. Sci. Acad.* **90** (2024) 664 [2311.13473].

[373] F. Boudjema and R.K. Singh, *A Model independent spin analysis of fundamental particles using azimuthal asymmetries*, *JHEP* **07** (2009) 028 [0903.4705].

[374] R. Rahaman and R.K. Singh, *Breaking down the entire spectrum of spin correlations of a pair of particles involving fermions and gauge bosons*, *Nucl. Phys. B* **984** (2022) 115984 [2109.09345].

[375] A. Subba and R.K. Singh, *Role of polarizations and spin-spin correlations of W's in e-e+→W-W+ at s=250 GeV to probe anomalous W-W+Z/γ couplings*, *Phys. Rev. D* **107** (2023) 073004 [2212.12973].

[376] A. Subba and R.K. Singh, *Study of anomalous $W^-W^+\gamma/Z$ couplings using polarizations and spin correlations in $e^-e^+ \to W^-W^+$ with polarized beams*, *Eur. Phys. J. C* **83** (2023) 1119 [2305.15106].

[377] A. Atwal et al., *Future Collider Perspectives on Higgs CP Violation*, 2511.08359.

[378] CMS collaboration, *Search for lepton flavour violating decays of the Higgs boson to eτ and eμ in proton–proton collisions at $\sqrt{s} = 8$ TeV*, *Phys. Lett. B* **763** (2016) 472 [1607.03561].

[379] CMS collaboration, *Search for lepton flavour violating decays of the Higgs boson to μτ and eτ in proton-proton collisions at $\sqrt{s} = 13$ TeV*, *JHEP* **06** (2018) 001 [1712.07173].

[380] OPAL collaboration, *A Search for lepton flavor violating Z0 decays*, *Z. Phys. C* **67** (1995) 555.

[381] DELPHI collaboration, *Search for lepton flavor number violating Z0 decays*, *Z. Phys. C* **73** (1997) 243.

[382] ATLAS collaboration, *Search for the lepton flavor violating decay Z→eμ in pp collisions at $\sqrt{s}$ TeV with the ATLAS detector*, *Phys. Rev. D* **90** (2014) 072010 [1408.5774].

[383] ATLAS collaboration, *Search for charged-lepton-flavour violation in Z-boson decays with the ATLAS detector*, *Nature Phys.* **17** (2021) 819 [2010.02566].

[384] CLIC ACCELERATOR collaboration, M. Aicheler, P.N. Burrows, N. Catalan Lasheras, R. Corsini, M. Draper, J. Osborne et al., eds., *The Compact Linear Collider (CLIC) - Project Implementation Plan*, 1903.08655.

[385] T. Han, I. Lewis and M. Sher, *Mu-Tau Production at Hadron Colliders*, *JHEP* **03** (2010) 090 [1001.0022].

[386] S. Davidson, S. Lacroix and P. Verdier, *LHC sensitivity to lepton flavour violating Z boson decays*, *JHEP* **09** (2012) 092 [1207.4894].

[387] Y. Cai and M.A. Schmidt, *A Case Study of the Sensitivity to LFV Operators with Precision Measurements and the LHC*, *JHEP* **02** (2016) 176 [1510.02486].

[388] Y. Cai, M.A. Schmidt and G. Valencia, *Lepton-flavour-violating gluonic operators: constraints from the LHC and low energy experiments*, *JHEP* **05** (2018) 143 [1802.09822].

[389] A. Angelescu, D.A. Faroughy and O. Sumensari, *Lepton Flavor Violation and Dilepton Tails at the LHC*, *Eur. Phys. J. C* **80** (2020) 641 [2002.05684].

[390] B. Murakami and T.M.P. Tait, *Searching for lepton flavor violation at a future high energy e+e- collider*, *Phys. Rev. D* **91** (2015) 015002 [1410.1485].

[391] G.-C. Cho, Y. Fukuda and T. Kono, *Lepton flavor violation via four-Fermi contact interactions at the International Linear Collider*, *Phys. Lett. B* **789** (2019) 399 [1803.10475].

[392] S.M. Etesami, R. Jafari, M.M. Najafabadi and S. Tizchang, *Searching for lepton flavor violating interactions at future electron-positron colliders*, *Phys. Rev. D* **104** (2021) 015034 [2107.00545].

[393] W. Altmannshofer, P. Munbodh and T. Oh, *Probing lepton flavor violation at Circular Electron-Positron Colliders*, *JHEP* **08** (2023) 026 [2305.03869].

[394] B. Grzadkowski and Z. Hioki, *CP violating lepton energy correlation in e- e+ —> t anti-t*, *Phys. Lett. B* **391** (1997) 172 [hep-ph/9608306].

[395] B. Grzadkowski, Z. Hioki and M. Szafranski, *Four Fermi effective operators in top quark production and decay*, *Phys. Rev. D* **58** (1998) 035002 [hep-ph/9712357].

[396] B. Grzadkowski and Z. Hioki, *Probing top quark couplings at polarized NLC*, *Phys. Rev. D* **61** (2000) 014013 [hep-ph/9805318].

[397] B. Grzadkowski and J. Pliszka, *Testing top quark Yukawa interactions in e+ e- —> t anti-t Z*, *Phys. Rev. D* **60** (1999) 115018 [hep-ph/9907206].

[398] B. Grzadkowski and Z. Hioki, *Optimal observable analysis of the angular and energy distributions for top quark decay products at polarized linear colliders*, *Nucl. Phys. B* **585** (2000) 3 [hep-ph/0004223].

[399] S. Bhattacharya, S. Jahedi and J. Wudka, *Optimal determination of new physics couplings: a comparative study*, *JHEP* **12** (2023) 026 [2301.07721].

[400] B. Grzadkowski, Z. Hioki, K. Ohkuma and J. Wudka, *Optimal-observable analysis of possible new physics using the b quark in gamma gamma —> t anti-t —> bX*, *Phys. Lett. B* **593** (2004) 189 [hep-ph/0403174].

[401] B. Grzadkowski, Z. Hioki, K. Ohkuma and J. Wudka, *Optimal beam polarizations for new-physics search through gamma gamma —> t anti-t —> lX/bX*, *JHEP* **11** (2005) 029 [hep-ph/0508183].

[402] J.F. Gunion and J. Pliszka, *Determining the relative size of the CP even and CP odd Higgs boson couplings to a fermion at the LHC*, *Phys. Lett. B* **444** (1998) 136 [hep-ph/9809306].

[403] Z. Hioki, T. Konishi and K. Ohkuma, *Studying possible CP-violating Higgs couplings through top-quark pair productions at muon colliders*, *JHEP* **07** (2007) 082 [0706.4346].

[404] Q.-H. Cao and J. Wudka, *Search for new physics via single top production at TeV energy e gamma colliders*, *Phys. Rev. D* **74** (2006) 094015 [hep-ph/0608331].

[405] S. Bhattacharya, S. Jahedi, J. Lahiri and J. Wudka, *Optimal new physics estimation in the presence of standard model backgrounds*, *Phys. Rev. D* **111** (2025) 036004 [2312.12514].

[406] S. Jahedi, S. Bhattacharya and J. Wudka, *Probing Z Couplings of Heavy Charged Fermions at e^+e^- Colliders*, *Springer Proc. Phys.* **304** (2024) 1078.

[407] S. Jahedi and J. Lahiri, *Probing anomalous $ZZ\gamma$ and $Z\gamma\gamma$ couplings at the e^+e colliders using optimal observable technique*, *JHEP* **04** (2023) 085 [2212.05121].

[408] S. Jahedi, *Optimal estimation of dimension-8 neutral triple gauge couplings at the e^+e colliders*, *JHEP* **12** (2023) 031 [2305.11266].

[409] S. Bhattacharya, S. Nandi and S.K. Patra, *Optimal-observable analysis of possible new physics in $B \to D^{(*)}\tau\nu_\tau$*, *Phys. Rev. D* **93** (2016) 034011 [1509.07259].

[410] Z. Calcuttawala, A. Kundu, S. Nandi and S.K. Patra, *Optimal observable analysis for the decay $b \to s$ plus missing energy*, *Eur. Phys. J. C* **77** (2017) 650 [1702.06679].

[411] Z. Calcuttawala, A. Kundu, S. Nandi and S. Kumar Patra, *New physics with the lepton flavor violating decay $\tau \to 3\mu$*, *Phys. Rev. D* **97** (2018) 095009 [1802.09218].

[412] S. Bhattacharya, S. Jahedi, S. Nandi and A. Sarkar, *Probing flavor constrained SMEFT operators through tc production at the muon collider*, *JHEP* **07** (2024) 061 [2312.14872].

[413] Particle Data Group collaboration, *Review of Particle Physics*, *PTEP* **2022** (2022) 083C01.

[414] K.M. Black et al., *Muon Collider Forum report*, *JINST* **19** (2024) T02015 [2209.01318].

[415] T. Sjöstrand, S. Ask, J.R. Christiansen, R. Corke, N. Desai, P. Ilten et al., *An introduction to PYTHIA 8.2*, *Comput. Phys. Commun.* **191** (2015) 159 [1410.3012].

[416] TMVA collaboration, *TMVA - Toolkit for Multivariate Data Analysis*, physics/0703039.

[417] Y. Coadou, *Boosted Decision Trees and Applications*, *EPJ Web Conf.* **55** (2013) 02004.

[418] S.L. Glashow, J. Iliopoulos and L. Maiani, *Weak Interactions with Lepton-Hadron Symmetry*, *Phys. Rev. D* **2** (1970) 1285.

[419] W.-S. Hou and T. Modak, *Probing Top Changing Neutral Higgs Couplings at Colliders*, *Mod. Phys. Lett. A* **36** (2021) 2130006 [2012.05735].

[420] K. Fuyuto, W.-S. Hou and M. Kohda, *Z' -induced FCNC decays of top, beauty, and strange quarks*, *Phys. Rev. D* **93** (2016) 054021 [1512.09026].

[421] S. Bhattacharya, L. Kolay, D. Pradhan and A. Sarkar, *Up-type FCNC in presence of Dark Matter*, 2504.20045.

[422] S. Sun, Q.-S. Yan, X. Zhao and Z. Zhao, *Constraining rare B decays by $\mu^+\mu^- \to tc$ at future lepton colliders*, *Phys. Rev. D* **108** (2023) 075016 [2302.01143].

[423] M. Ghasemi Bostanabad and M. Mohammadi Najafabadi, *Machine learning approaches to top quark flavor-changing four-fermion interactions in trilepton signals at the LHC*, *Phys. Rev. D* **111** (2025) 112003 [2502.18667].

[424] O. Atkinson, C. Englert, M. Kirk and G. Tetlalmatzi-Xolocotzi, *Collider-flavour complementarity from the bottom to the top*, *Eur. Phys. J. C* **85** (2025) 258 [2411.00940].

[425] C.-H. Chen and T. Nomura, *Scotogenic top-quark FCNC decays*, *Phys. Rev. D* **106** (2022) 095005 [2204.01214].

[426] R. Gaitán, R. Martinez, J.H.M. de Oca and E.A. Garcés, *SM Higgs boson and $t \to cZ$ decays in the 2HDM type III with CP violation*, *Phys. Rev. D* **98** (2018) 035031 [1710.04262].

[427] L. Shi and C. Zhang, *Probing the top quark flavor-changing couplings at CEPC*, *Chin. Phys. C* **43** (2019) 113104 [1906.04573].

[428] M.A. Arroyo-Ureña, R. Gaitán, E.A. Herrera-Chacón, J.H. Montes de Oca Y. and T.A. Valencia-Pérez, *Search for the $t \to ch$ decay at hadron colliders*, *JHEP* **07** (2019) 041 [1903.02718].

[429] Y.-B. Liu and S. Moretti, *Probing the top-Higgs boson FCNC couplings via the $h \to \gamma\gamma$ channel at the HE-LHC and FCC-hh*, *Phys. Rev. D* **101** (2020) 075029 [2002.05311].

[430] Y. Liu, B. Yan and R. Zhang, *Loop induced top quark FCNC through top quark and dark matter interactions*, *Phys. Lett. B* **827** (2022) 136964 [2103.07859].

[431] P. Gutierrez, R. Jain and C. Kao, *Flavor changing top decays to charm and a Higgs boson with $\tau\tau$ at the LHC*, *Phys. Rev. D* **103** (2021) 115020 [2012.09209].

[432] S.-Y. Bie, G.-L. Liu and W. Wang, *Top rare decays $t \to cV$ in mirror twin Higgs models*, *Chin. Phys. C* **45** (2021) 013106 [2009.04858].

[433] S. Balaji, *CP asymmetries in the rare top decays $t \to c\gamma$ and $t \to cg$*, *Phys. Rev. D* **102** (2020) 113010 [2009.03315].

[434] M. Frank and I. Turan, *Rare decay of the top t —> c l anti-l and single top production at ILC*, *Phys. Rev. D* **74** (2006) 073014 [hep-ph/0609069].

[435] D. d'Enterria and V.D. Le, *Rare and exclusive few-body decays of the Higgs, Z, W bosons, and the top quark*, *J. Phys. G* **52** (2025) 053001 [2312.11211].

[436] S. Kala, L. Kolay, L. Mukherjee and S. Nandi, *Constraining anomalous Wtb and related SMEFT couplings using low-energy and electroweak precision observables*, 2505.07926.

[437] W. Altmannshofer and P. Munbodh, *Probing Lepton Flavor Violation at Linear Electron-Positron Colliders*, 2505.11653.

[438] A. Moreno-Sánchez and A. Palavrić, *Leptonic Flavor from Modular A_4: UV Mediators and SMEFT Realizations*, 2505.01535.

[439] A. Palavrić, *Discrete leptonic flavor symmetries: UV mediators and phenomenology*, *Phys. Rev. D* **110** (2024) 115025 [2408.16044].

[440] L. Calibbi, C. Hagedorn, M.A. Schmidt and J. Vandeleur, *Selection rules for charged lepton flavour violating processes from residual flavour groups*, 2505.24350.

[441] J. Kriewald, E. Pinsard and A.M. Teixeira, *High-energy cLFV at μTRISTAN: HNL extensions of the Standard Model*, *JHEP* **02** (2025) 116 [2412.04331].

[442] B. Batell, H. Davoudiasl, R. Marcarelli, E.T. Neil and S. Trojanowski, *Lepton-flavor-violating ALP signals with TeV-scale muon beams*, *Phys. Rev. D* **110** (2024) 075039 [2407.15942].

[443] L. Calibbi, T. Li, L. Mukherjee and Y. Yang, *Probing ALP lepton flavor violation at μTRISTAN*, *Phys. Rev. D* **110** (2024) 115009 [2406.13234].

[444] R. Ding, J. Li, M. Lu, Z. You, Z. Wang and Q. Li, *Study of charged Lepton Flavor Violation in electron muon interactions*, *JHEP* **01** (2025) 165 [2405.09417].

[445] J.L.G. Santiago, D. Portillo-Sánchez, G. Hernández-Tomé and J. Rendón, *Authentic Majorana versus singlet Dirac neutrino contributions to $\mu+\mu+\to\ell+\ell+$ ($\ell=e,\tau$) transitions*, *Phys. Rev. D* **110** (2024) 053006 [2405.02819].

[446] J. Heeck and M. Sokhashvili, *Lepton flavor violation by two units*, *Phys. Lett. B* **852** (2024) 138621 [2401.09580].

[447] A. Goudelis, J. Kriewald, E. Pinsard and A.M. Teixeira, *cLFV leptophilic Z' as a dark matter portal: prospects for colliders*, *Eur. Phys. J. C* **84** (2024) 804 [2312.14103].

[448] G. Lichtenstein, M.A. Schmidt, G. Valencia and R.R. Volkas, *Complementarity of μTRISTAN and Belle II in searches for charged-lepton flavour violation*, *Phys. Lett. B* **845** (2023) 138144 [2307.11369].

[449] S. Jahedi and A. Sarkar, *Exploring optimal sensitivity of lepton flavor violating effective couplings at the e+e- colliders*, *Phys. Rev. D* **110** (2024) 095021 [2408.00190].

[450] C.-H. Chen, C.-W. Chiang and C.-W. Su, *Top-quark FCNC decays, LFVs, lepton $g-2$, and W mass anomaly with inert charged Higgses*, *J. Phys. G* **51** (2024) 085001 [2301.07070].

[451] A. Crivellin, A. Kokulu and C. Greub, *Flavor-phenomenology of two-Higgs-doublet models with generic Yukawa structure*, *Phys. Rev. D* **87** (2013) 094031 [1303.5877].

[452] B.L. Gonçalves, M. Knauss and M. Sher, *Lepton flavor specific extended Higgs model*, *Phys. Rev. D* **107** (2023) 095001 [2301.08641].

[453] I. Doršner, S. Fajfer, A. Greljo, J.F. Kamenik and N. Košnik, *Physics of leptoquarks in precision experiments and at particle colliders*, *Phys. Rept.* **641** (2016) 1 [1603.04993].

[454] S. Davidson, D.C. Bailey and B.A. Campbell, *Model independent constraints on leptoquarks from rare processes*, *Z. Phys. C* **61** (1994) 613 [hep-ph/9309310].

[455] P. Langacker, *The Physics of Heavy Z' Gauge Bosons*, *Rev. Mod. Phys.* **81** (2009) 1199 [0801.1345].

[456] P. Langacker and M. Plumacher, *Flavor changing effects in theories with a heavy Z' boson with family nonuniversal couplings*, *Phys. Rev. D* **62** (2000) 013006 [hep-ph/0001204].

[457] K. Agashe, R. Contino and A. Pomarol, *The Minimal composite Higgs model*, *Nucl. Phys. B* **719** (2005) 165 [hep-ph/0412089].

[458] F. Feruglio, P. Paradisi and A. Pattori, *Lepton Flavour Violation in Composite Higgs Models*, *Eur. Phys. J. C* **75** (2015) 579 [1509.03241].

[459] W. Altmannshofer, Z. Balme, C.M. Donohue, S. Gori and S.V. Mukundhan, *Targets for Flavor-Violating Top Decay*, 2504.18664.

[460] M. Lu, A.M. Levin, C. Li, A. Agapitos, Q. Li, F. Meng et al., *The physics case for an electron-muon collider*, *Adv. High Energy Phys.* **2021** (2021) 6693618 [2010.15144].

[461] A.O. Bouzas and F. Larios, *Two-to-Two Processes at an Electron-Muon Collider*, *Adv. High Energy Phys.* **2022** (2022) 3603613 [2109.02769].

[462] A.O. Bouzas and F. Larios, *An electron-muon collider: what can be probed with it?*, *Rev. Mex. Fis. Suppl.* **4** (2023) 021128.

[463] S. Iwata, *TRISTAN experiment*, in *Adriatico Research Conference on Mesoscopic Systems and Chaos: A Novel Approach*, pp. 255–275, 12, 1993.

[464] P. Dehghani, M. Frank and B. Fuks, *Vector Boson Fusion Signatures of Superheavy Majorana Neutrinos at Muon Colliders*, 2506.06159.

[465] P.D. Bolton, F.F. Deppisch, S. Kulkarni, C. Majumdar and W. Pei, *Constraining the SMEFT Extended with Sterile Neutrinos at FCC-ee*, 2502.06972.

[466] C.H. de Lima, D. McKeen, J.N. Ng, M. Shamma and D. Tuckler, *Probing lepton number violation at same-sign lepton colliders*, *Phys. Rev. D* **111** (2025) 075002 [2411.15303].

[467] Y. Hamada, R. Kitano, R. Matsudo, S. Okawa, R. Takai, H. Takaura et al., *Higgs boson production at $\mu+\mu+$ colliders*, *Phys. Rev. D* **110** (2024) 113011 [2408.01068].

[468] L. Chen, S. Iguro and Y. Hamada, *Determining Weak-Mixing Angle at μTRISTAN*, 2406.04500.

[469] R. Okabe and S. Shirai, *Indirect probe of electroweak-interacting particles at the μTRISTAN $\mu+\mu+$ collider*, *Phys. Rev. D* **110** (2024) 035002 [2310.08434].

[470] H. Fukuda, T. Moroi, A. Niki and S.-F. Wei, *Search for WIMPs at future $\mu^+\mu^+$ colliders*, *JHEP* **02** (2024) 214 [2310.07162].

[471] P.S.B. Dev, J. Heeck and A. Thapa, *Neutrino mass models at μTRISTAN*, *Eur. Phys. J. C* **84** (2024) 148 [2309.06463].

[472] G. Durieux, F. Maltoni and C. Zhang, *Global approach to top-quark flavor-changing interactions*, *Phys. Rev. D* **91** (2015) 074017 [1412.7166].

[473] J. Aebischer, A.J. Buras and J. Kumar, *SMEFT ATLAS: The Landscape Beyond the Standard Model*, 2507.05926.

[474] F. Delzanno, K. Fuyuto, S. Gonzàlez-Solís and E. Mereghetti, *Global analysis of $\mu \to e$ interactions in the SMEFT*, *JHEP* **07** (2025) 283 [2411.13497].

[475] M. Chala, J. Santiago and M. Spannowsky, *Constraining four-fermion operators using rare top decays*, *JHEP* **04** (2019) 014 [1809.09624].

[476] Belle II SuperKEKB e- Polarization Upgrade Working Group collaboration, *Upgrading SuperKEKB with polarized e^- beams*, *PoS* **ICHEP2020** (2021) 699.

[477] G. Bélanger et al., *LHC-friendly minimal freeze-in models*, *JHEP* **02** (2019) 186 [1811.05478].

[478] M. Becker, E. Copello, J. Harz, J. Lang and Y. Xu, *Confronting dark matter freeze-in during reheating with constraints from inflation*, *JCAP* **01** (2024) 053 [2306.17238].

[479] J. Preskill, M.B. Wise and F. Wilczek, *Cosmology of the Invisible Axion*, *Phys. Lett. B* **120** (1983) 127.

[480] M. Dine and W. Fischler, *The Not So Harmless Axion*, *Phys. Lett. B* **120** (1983) 137.

[481] T. Moroi and W. Yin, *Light Dark Matter from Inflaton Decay*, *JHEP* **03** (2021) 301 [2011.09475].

[482] L.H. Ford, *Gravitational Particle Creation and Inflation*, *Phys. Rev. D* **35** (1987) 2955.

[483] J. Goodman, M. Ibe, A. Rajaraman, W. Shepherd, T.M.P. Tait and H.-B. Yu, *Constraints on Dark Matter from Colliders*, *Phys. Rev. D* **82** (2010) 116010 [1008.1783].

[484] M. Beltran, D. Hooper, E.W. Kolb and Z.C. Krusberg, *Deducing the nature of dark matter from direct and indirect detection experiments in the absence of collider signatures of new physics*, *Phys. Rev. D* **80** (2009) 043509 [0808.3384].

[485] Q.-H. Cao, C.-R. Chen, C.S. Li and H. Zhang, *Effective Dark Matter Model: Relic density, CDMS II, Fermi LAT and LHC*, *JHEP* **08** (2011) 018 [0912.4511].

[486] M.A. Fedderke, J.-Y. Chen, E.W. Kolb and L.-T. Wang, *The Fermionic Dark Matter Higgs Portal: an effective field theory approach*, *JHEP* **08** (2014) 122 [1404.2283].

[487] J.-H. Liang, Y. Liao, X.-D. Ma and H.-L. Wang, *Dark sector effective field theory*, *JHEP* **12** (2023) 172 [2309.12166].

[488] T. Brauner, S.A. Hartnoll, P. Kovtun, H. Liu, M. Mezei, A. Nicolis et al., *Snowmass White Paper: Effective Field Theories for Condensed Matter Systems*, in *Snowmass 2021*, 3, 2022 [2203.10110].

[489] Z.-H. Yu, Q.-S. Yan and P.-F. Yin, *Detecting interactions between dark matter and photons at high energy e^+e^- colliders*, *Phys. Rev. D* **88** (2013) 075015 [1307.5740].

[490] R. Essig, J. Mardon, M. Papucci, T. Volansky and Y.-M. Zhong, *Constraining Light Dark Matter with Low-Energy e^+e^- Colliders*, *JHEP* **11** (2013) 167 [1309.5084].

[491] K. Kadota and J. Silk, *Constraints on Light Magnetic Dipole Dark Matter from the ILC and SN 1987A*, *Phys. Rev. D* **89** (2014) 103528 [1402.7295].

[492] Z.-H. Yu, X.-J. Bi, Q.-S. Yan and P.-F. Yin, *Dark matter searches in the mono-Z channel at high energy e^+e^- colliders*, *Phys. Rev. D* **90** (2014) 055010 [1404.6990].

[493] A. Freitas and S. Westhoff, *Leptophilic Dark Matter in Lepton Interactions at LEP and ILC*, *JHEP* **10** (2014) 116 [1408.1959].

[494] S. Dutta, D. Sachdeva and B. Rawat, *Signals of Leptophilic Dark Matter at the ILC*, *Eur. Phys. J. C* **77** (2017) 639 [1704.03994].

[495] D. Choudhury and D. Sachdeva, *Model independent analysis of MeV scale dark matter. II. Implications from e^-e^+ colliders and direct detection*, *Phys. Rev. D* **100** (2019) 075007 [1906.06364].

[496] S.-I. Horigome, T. Katayose, S. Matsumoto and I. Saha, *Leptophilic fermion WIMP: Role of future lepton colliders*, *Phys. Rev. D* **104** (2021) 055001 [2102.08645].

[497] S. Kundu, A. Guha, P.K. Das and P.S.B. Dev, *EFT analysis of leptophilic dark matter at future electron-positron colliders in the mono-photon and mono-Z channels*, *Phys. Rev. D* **107** (2023) 015003 [2110.06903].

[498] S. Bhattacharya, P. Ghosh, J. Lahiri and B. Mukhopadhyaya, *Mono-X signal and two component dark matter: New distinction criteria*, *Phys. Rev. D* **108** (2023) L111703 [2211.10749].

[499] S.-F. Ge, K. Ma, X.-D. Ma and J. Sheng, *Associated production of neutrino and dark fermion at future lepton colliders*, *JHEP* **11** (2023) 190 [2306.00657].

[500] K. Ma, *Mono-γ production of a dark vector at future $e^+ e^-$ colliders**, *Chin. Phys. C* **46** (2022) 113104 [2205.05560].

[501] E. Singh, H. Bharadwaj and Devisharan, *Exploring new physics via effective interactions*, 2406.14389.

[502] D. Borah, N. Das, S. Jahedi and B. Thacker, *Collider and CMB complementarity of leptophilic dark matter with light Dirac neutrinos*, *JHEP* **01** (2025) 074 [2408.14548].

[503] P. Fayet, *Radiative Production of Gravitinos and Photinos in e+ e- Annihilation*, *Phys. Lett. B* **117** (1982) 460.

[504] J.R. Ellis and J.S. Hagelin, *Search for Photinos in e+ e- Annihilation*, *Phys. Lett. B* **122** (1983) 303.

[505] K. Grassie and P.N. Pandita, *Production of Photinos in $e^+e^- \to \gamma$ Photino Photino*, *Phys. Rev. D* **30** (1984) 22.

[506] A. Nelson, L.M. Carpenter, R. Cotta, A. Johnstone and D. Whiteson, *Confronting the fermi line with lhc data: An effective theory of dark matter interaction with photons*, *Phys. Rev. D* **89** (2014) 056011.

[507] C. Arina, A. Cheek, K. Mimasu and L. Pagani, *Light and Darkness: consistently coupling dark matter to photons via effective operators*, *Eur. Phys. J. C* **81** (2021) 223 [2005.12789].

[508] B.J. Kavanagh, P. Panci and R. Ziegler, *Faint Light from Dark Matter: Classifying and Constraining Dark Matter-Photon Effective Operators*, *JHEP* **04** (2019) 089 [1810.00033].

[509] P. Gondolo and G. Gelmini, *Cosmic abundances of stable particles: Improved analysis*, *Nucl. Phys. B* **360** (1991) 145.

[510] G.F. Giudice, E.W. Kolb and A. Riotto, *Largest temperature of the radiation era and its cosmological implications*, *Phys. Rev. D* **64** (2001) 023508 [hep-ph/0005123].

[511] S. Hannestad, *What is the lowest possible reheating temperature?*, *Phys. Rev. D* **70** (2004) 043506 [astro-ph/0403291].

[512] R. Laha, J.B. Muñoz and T.R. Slatyer, *integral constraints on primordial black holes and particle dark matter*, *Phys. Rev. D* **101** (2020) 123514.

[513] T. Siegert, F. Calore and P.D. Serpico, *Sub-GeV Dark Matter Annihilation: Limits from Milky Way observations with INTEGRAL*, *Mon. Not. Roy. Astron. Soc.* **528** (2024) 3433 [2401.03795].

[514] M.R. Haque and D. Maity, *Gravitational reheating*, *Phys. Rev. D* **107** (2023) 043531.

[515] D.G. Figueroa and E.H. Tanin, *Inconsistency of an inflationary sector coupled only to Einstein gravity*, *JCAP* **10** (2019) 050 [1811.04093].

[516] T. Opferkuch, P. Schwaller and B.A. Stefanek, *Ricci Reheating*, *JCAP* **07** (2019) 016 [1905.06823].

[517] R. Essig, J. Mardon and T. Volansky, *Direct Detection of Sub-GeV Dark Matter*, *Phys. Rev. D* **85** (2012) 076007 [1108.5383].

[518] DAMIC collaboration, *Constraints on Light Dark Matter Particles Interacting with Electrons from DAMIC at SNOLAB*, *Phys. Rev. Lett.* **123** (2019) 181802 [1907.12628].

[519] SENSEI collaboration, *SENSEI: Direct-Detection Results on sub-GeV Dark Matter from a New Skipper-CCD*, *Phys. Rev. Lett.* **125** (2020) 171802 [2004.11378].

[520] PandaX-II collaboration, *Search for Light Dark Matter-Electron Scatterings in the PandaX-II Experiment*, *Phys. Rev. Lett.* **126** (2021) 211803 [2101.07479].

[521] SuperCDMS collaboration, *Constraints on low-mass, relic dark matter candidates from a surface-operated SuperCDMS single-charge sensitive detector*, *Phys. Rev. D* **102** (2020) 091101 [2005.14067].

[522] CDEX collaboration, *Constraints on Sub-GeV Dark Matter–Electron Scattering from the CDEX-10 Experiment*, *Phys. Rev. Lett.* **129** (2022) 221301 [2206.04128].

[523] XENON collaboration, *First Dark Matter Search with Nuclear Recoils from the XENONnT Experiment*, *Phys. Rev. Lett.* **131** (2023) 041003 [2303.14729].

[524] L. Roszkowski, E.M. Sessolo and S. Trojanowski, *WIMP dark matter candidates and searches—current status and future prospects*, *Rept. Prog. Phys.* **81** (2018) 066201 [1707.06277].

[525] G. Arcadi, M. Dutra, P. Ghosh, M. Lindner, Y. Mambrini, M. Pierre et al., *The waning of the WIMP? A review of models, searches, and constraints*, *Eur. Phys. J. C* **78** (2018) 203 [1703.07364].

[526] J.H. Chang, R. Essig and A. Reinert, *Light(ly)-coupled Dark Matter in the keV Range: Freeze-In and Constraints*, *JHEP* **03** (2021) 141 [1911.03389].

[527] L. Darmé, A. Hryczuk, D. Karamitros and L. Roszkowski, *Forbidden frozen-in dark matter*, *JHEP* **11** (2019) 159 [1908.05685].

[528] J. McDonald, *Thermally generated gauge singlet scalars as selfinteracting dark matter*, *Phys. Rev. Lett.* **88** (2002) 091304 [hep-ph/0106249].

[529] N. Bernal, M. Heikinheimo, T. Tenkanen, K. Tuominen and V. Vaskonen, *The Dawn of FIMP Dark Matter: A Review of Models and Constraints*, *Int. J. Mod. Phys. A* **32** (2017) 1730023 [1706.07442].

[530] N. Bernal, F. Elahi, C. Maldonado and J. Unwin, *Ultraviolet Freeze-in and Non-Standard Cosmologies*, *JCAP* **11** (2019) 026 [1909.07992].

[531] N. Bernal, J. Rubio and H. Veermäe, *UV Freeze-in in Starobinsky Inflation*, *JCAP* **10** (2020) 021 [2006.02442].

[532] B. Barman, D. Borah and R. Roshan, *Effective Theory of Freeze-in Dark Matter*, *JCAP* **11** (2020) 021 [2007.08768].

[533] M.A.G. Garcia, K. Kaneta, Y. Mambrini and K.A. Olive, *Reheating and Post-inflationary Production of Dark Matter*, *Phys. Rev. D* **101** (2020) 123507 [2004.08404].

[534] M.A.G. Garcia, K. Kaneta, Y. Mambrini and K.A. Olive, *Inflaton Oscillations and Post-Inflationary Reheating*, *JCAP* **04** (2021) 012 [2012.10756].

[535] A. Ahmed and S. Najjari, *Ultraviolet freeze-in dark matter through the dilaton portal*, *Phys. Rev. D* **107** (2023) 055020 [2112.14261].

[536] Y. Mambrini and K.A. Olive, *Gravitational Production of Dark Matter during Reheating*, *Phys. Rev. D* **103** (2021) 115009 [2102.06214].

[537] K. Kaneta, P. Ko and W.-I. Park, *Conformal portal to dark matter*, *Phys. Rev. D* **104** (2021) 075018 [2106.01923].

[538] A. Ahmed, B. Grzadkowski and A. Socha, *Implications of time-dependent inflaton decay on reheating and dark matter production*, *Phys. Lett. B* **831** (2022) 137201 [2111.06065].

[539] B. Barman, N. Bernal, Y. Xu and O. Zapata, *Ultraviolet freeze-in with a time-dependent inflaton decay*, *JCAP* **07** (2022) 019 [2202.12906].

[540] M.R. Haque, D. Maity and R. Mondal, *WIMPs, FIMPs, and Inflaton phenomenology via reheating, CMB and ΔN_{eff}*, *JHEP* **09** (2023) 012 [2301.01641].

[541] N. Bernal, J. Harz, M.A. Mojahed and Y. Xu, *Graviton- and Inflaton-mediated Dark Matter Production after Large Field Polynomial Inflation*, 2406.19447.

[542] B. Barman, A. Basu, D. Borah, A. Chakraborty and R. Roshan, *Testing cogenesis during reheating with primordial gravitational waves*, 2410.19048.

[543] A. Nelson, L.M. Carpenter, R. Cotta, A. Johnstone and D. Whiteson, *Confronting the Fermi Line with LHC data: an Effective Theory of Dark Matter Interaction with Photons*, *Phys. Rev. D* **89** (2014) 056011 [1307.5064].

[544] Planck collaboration, *Planck 2018 results. X. Constraints on inflation*, *Astron. Astrophys.* **641** (2020) A10 [1807.06211].

[545] R. Kallosh and A. Linde, *Universality Class in Conformal Inflation*, *JCAP* **07** (2013) 002 [1306.5220].

[546] R. Kallosh, A. Linde and D. Roest, *Superconformal Inflationary α-Attractors*, *JHEP* **11** (2013) 198 [1311.0472].

[547] R. Kallosh and A. Linde, *Non-minimal Inflationary Attractors*, *JCAP* **10** (2013) 033 [1307.7938].

[548] A.A. Starobinsky, *A New Type of Isotropic Cosmological Models Without Singularity*, *Phys. Lett. B* **91** (1980) 99.

[549] A.A. Starobinsky, *Nonsingular Model of the Universe with the Quantum Gravitational de Sitter Stage and its Observational Consequences*, in *Second Seminar on Quantum Gravity*, 1981.

[550] A.A. Starobinsky, *The Perturbation Spectrum Evolving from a Nonsingular Initially De-Sitter Cosmology and the Microwave Background Anisotropy*, *Sov. Astron. Lett.* **9** (1983) 302.

[551] L.A. Kofman, A.D. Linde and A.A. Starobinsky, *Inflationary Universe Generated by the Combined Action of a Scalar Field and Gravitational Vacuum Polarization*, *Phys. Lett. B* **157** (1985) 361.

[552] M.S. Turner, *Coherent Scalar Field Oscillations in an Expanding Universe*, *Phys. Rev. D* **28** (1983) 1243.

[553] S. Sarkar, *Big bang nucleosynthesis and physics beyond the standard model*, *Rept. Prog. Phys.* **59** (1996) 1493 [hep-ph/9602260].

[554] M. Kawasaki, K. Kohri and N. Sugiyama, *MeV scale reheating temperature and thermalization of neutrino background*, *Phys. Rev. D* **62** (2000) 023506 [astro-ph/0002127].

[555] F. De Bernardis, L. Pagano and A. Melchiorri, *New constraints on the reheating temperature of the universe after WMAP-5*, *Astropart. Phys.* **30** (2008) 192.

[556] P.F. de Salas, M. Lattanzi, G. Mangano, G. Miele, S. Pastor and O. Pisanti, *Bounds on very low reheating scenarios after Planck*, *Phys. Rev. D* **92** (2015) 123534 [1511.00672].

[557] T. Hasegawa, N. Hiroshima, K. Kohri, R.S.L. Hansen, T. Tram and S. Hannestad, *MeV-scale reheating temperature and thermalization of oscillating neutrinos by radiative and hadronic decays of massive particles*, *JCAP* **12** (2019) 012 [1908.10189].

[558] C.-S. Chen and C.-M. Lin, *Type II Seesaw Higgs Triplet as the inflaton for Chaotic Inflation and Leptogenesis*, *Phys. Lett. B* **695** (2011) 9 [1009.5727].

[559] D. Borah, P.S.B. Dev and A. Kumar, *TeV scale leptogenesis, inflaton dark matter and neutrino mass in a scotogenic model*, *Phys. Rev. D* **99** (2019) 055012 [1810.03645].

[560] P. Meade and H. Ramani, *Unrestored Electroweak Symmetry*, *Phys. Rev. Lett.* **122** (2019) 041802 [1807.07578].

[561] K. Kaneta, Y. Mambrini and K.A. Olive, *Radiative production of nonthermal dark matter*, *Phys. Rev. D* **99** (2019) 063508 [1901.04449].

[562] A. Datta, R. Roshan and A. Sil, *Flavor leptogenesis during the reheating era*, *Phys. Rev. D* **108** (2023) 035029 [2301.10791].

[563] Y. Shtanov, J.H. Traschen and R.H. Brandenberger, *Universe reheating after inflation*, *Phys. Rev. D* **51** (1995) 5438 [hep-ph/9407247].

[564] K. Ichikawa, T. Suyama, T. Takahashi and M. Yamaguchi, *Primordial Curvature Fluctuation and Its Non-Gaussianity in Models with Modulated Reheating*, *Phys. Rev. D* **78** (2008) 063545 [0807.3988].

[565] N. Bernal and Y. Xu, *WIMPs during reheating*, *JCAP* **12** (2022) 017 [2209.07546].

[566] B. Barman, N. Bernal, Y. Xu and O. Zapata, *Bremsstrahlung-induced gravitational waves in monomial potentials during reheating*, *Phys. Rev. D* **108** (2023) 083524 [2305.16388].

[567] Y. Xu, *Ultra-high Frequency Gravitational Waves from Scattering, Bremsstrahlung and Decay during Reheating*, 2407.03256.

[568] S. Davidson and S. Sarkar, *Thermalization after inflation*, *JHEP* **11** (2000) 012 [hep-ph/0009078].

[569] A. Kurkela and G.D. Moore, *Thermalization in Weakly Coupled Nonabelian Plasmas*, *JHEP* **12** (2011) 044 [1107.5050].

[570] K. Harigaya and K. Mukaida, *Thermalization after/during Reheating*, *JHEP* **05** (2014) 006 [1312.3097].

[571] M. Drees and B. Najjari, *Energy spectrum of thermalizing high energy decay products in the early universe*, *JCAP* **10** (2021) 009 [2105.01935].

[572] M. Drees and B. Najjari, *Multi-species thermalization cascade of energetic particles in the early universe*, *JCAP* **08** (2023) 037 [2205.07741].

[573] K. Mukaida and M. Yamada, *Cascades of high-energy SM particles in the primordial thermal plasma*, *JHEP* **10** (2022) 116 [2208.11708].

[574] M.R. Haque and D. Maity, *Gravitational reheating*, *Phys. Rev. D* **107** (2023) 043531 [2201.02348].

[575] S. Clery, Y. Mambrini, K.A. Olive, A. Shkerin and S. Verner, *Gravitational portals with nonminimal couplings*, *Phys. Rev. D* **105** (2022) 095042 [2203.02004].

[576] R.T. Co, Y. Mambrini and K.A. Olive, *Inflationary gravitational leptogenesis*, *Phys. Rev. D* **106** (2022) 075006 [2205.01689].

[577] B. Barman, A. Ghoshal, B. Grzadkowski and A. Socha, *Measuring Inflaton Couplings via Primordial Gravitational Waves*, 2305.00027.

[578] Fermi-LAT collaboration, *Updated search for spectral lines from Galactic dark matter interactions with pass 8 data from the Fermi Large Area Telescope*, *Phys. Rev. D* **91** (2015) 122002 [1506.00013].

[579] H.E.S.S. collaboration, *Search for dark matter signals towards a selection of recently detected DES dwarf galaxy satellites of the Milky Way with H.E.S.S.*, *Phys. Rev. D* **102** (2020) 062001 [2008.00688].

[580] T.R. Slatyer, *Indirect dark matter signatures in the cosmic dark ages. I. Generalizing the bound on s-wave dark matter annihilation from Planck results*, *Phys. Rev. D* **93** (2016) 023527 [1506.03811].

[581] K. Fujii et al., *The role of positron polarization for the inital* 250 *GeV stage of the International Linear Collider*, 1801.02840.

[582] R. Laha, J.B. Muñoz and T.R. Slatyer, *INTEGRAL constraints on primordial black holes and particle dark matter*, *Phys. Rev. D* **101** (2020) 123514 [2004.00627].

[583] DELPHI collaboration, *Photon events with missing energy in e+ e- collisions at s**(1/2) = 130-GeV to 209-GeV*, *Eur. Phys. J. C* **38** (2005) 395 [hep-ex/0406019].

[584] DELPHI collaboration, *Search for one large extra dimension with the DELPHI detector at LEP*, *Eur. Phys. J. C* **60** (2009) 17 [0901.4486].

[585] D. Dercks, N. Desai, J.S. Kim, K. Rolbiecki, J. Tattersall and T. Weber, *CheckMATE 2: From the model to the limit*, *Comput. Phys. Commun.* **221** (2017) 383 [1611.09856].

[586] A.L. Read, *Presentation of search results: The CL_s technique*, *J. Phys. G* **28** (2002) 2693.

[587] ATLAS collaboration, *Search for dark matter at $\sqrt{s} = 13$ TeV in final states containing an energetic photon and large missing transverse momentum with the ATLAS detector*, *Eur. Phys. J. C* **77** (2017) 393 [1704.03848].

[588] ATLAS collaboration, *Search for electroweak production of charginos and sleptons decaying into final states with two leptons and missing transverse momentum in $\sqrt{s} = 13$ TeV pp collisions using the ATLAS detector*, *Eur. Phys. J. C* **80** (2020) 123 [1908.08215].

[589] A.V. Manohar, *Introduction to Effective Field Theories*, 1804.05863.